METAL-ORGANIC FRAMEWORKS AS INTRACELLULAR DELIVERY VECTORS

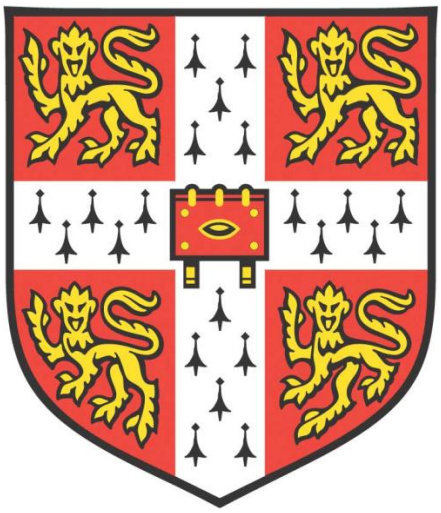

Salame Haddad

Trinity College

Department of Chemical Engineering & Biotechnology

University of Cambridge

This dissertation is submitted for the degree of Doctor of Philosophy

September 2018

If you tell the truth, you don't have to remember anything.

-Mark Twain

DECLARATION

This dissertation is the result of my own work and includes nothing which is the outcome of work done in collaboration except where specified in the text. It is not substantially the same as any that I have submitted, or, is being concurrently submitted for a degree or diploma or other qualification at the University of Cambridge or any other University or similar institution except as declared in the Preface and specified in the text. I further state that no substantial part of my dissertation has already been submitted, or, is being concurrently submitted for any such degree, diploma or other qualification at the University of Cambridge or any other University or similar institution except as declared in the Preface and specified in the text.

In accordance with the Department of Engineering guidelines, this thesis does not exceed 65,000 words, and it contains less than 150 figures.

_____

September 21st, 2018

Salame Haddad

AUTHOR PUBLICATIONS RELEVANT TO DISSERTATION

i. Abanades-Lazaro, I.; Haddad, S.; Sacca, S.; Orellana-Tavra, C.; Fairen-Jimenez, D.; Forgan, R. S. *Chem.* **2017**, *2*, 561–578.

ii. Orellana-Tavra, C.[§]; Haddad, S.[§]; Marshall, R. J.; Abanades-Lazaro, I.; Boix, G.; Imaz, I.; Maspoch, D.; Forgan, R. S.; Fairen-Jimenez, D. *ACS Appl. Mater. Interfaces*. **2017**, *9*, 35516-35525. [§]Authors contributed equally to this work.

iii. Abanades-Lazaro, I.; Haddad, S.; Rodrigo-Munoz, J. M.; Orellana-Tavra, C.; del Pozo, V.; Fairen-Jimenez, D.; Forgan, R. S. *ACS Appl. Mater. Interfaces*. **2018**, *10*, 5255-5268.

iv. Abanades-Lazaro, I.; Haddad, S.; Rodrigo-Munoz, J. M.; Marshall, R. J.; Sastre, B.; del Pozo, V.; Fairen-Jimenez, D.; Forgan, R. S. *ACS Appl. Mater. Interfaces*. **2018**, *10*, 31146-31157.

v. Haddad, S.; Abanades-Lazaro, I.; Fantham, M.; A. Mishra; Kaminski, G.; Kaminski, C. F.; Forgan, R. S.; Fairen-Jimenez, D. *In writing*.

ABSTRACT

Metal-organic frameworks (MOFs) have emerged as interesting candidates for intracellular carrier-based delivery. These hybrid materials are constituted of metal clusters linked together by organic ligands. The possibility to tune their physical and chemical properties both in the bulk and at the surface allows for the design of biocompatible delivery systems with high loading capacities and targeting abilities, combining the benefits of both organic and inorganic materials. The following dissertation focuses on developing and evaluating MOFs as intracellular delivery systems.

In the first instance, a zirconium-based MOF, UiO-66, was synthesised and utilised as an intracellular delivery vector for trehalose, a disaccharide with cryoprotective properties when present in the cytosol. This MOF demonstrated very high trehalose weight loadings compared to other trehalose delivery systems (up to *ca.* 50 wt %), release of the sugar from the framework over 5 h, and appropriate biocompatibility. To assess the delivery system's impact on cryopreservation, the viability of cells cryoprotected with trehalose-loaded UiO-66 was tested at 0 h, 24 h, and 48 h post-thaw, and showed no improvement compared to cells frozen with free trehalose or growth media alone. The absence of cryoprotective effect was hypothesised to be due to endosomal entrapment of the delivery system after cellular uptake through endocytosis.

The final fate of particles taken up by cells depends on the endocytosis pathways they go through. In order to confirm the hypothesis of MOF endosomal entrapment, the endocytosis of MOF particles was studied. In particular, the effects of surface chemistry of Zr-based MOFs on their endocytosis mechanisms were investigated. It was found that MOF surface chemistry had an important effect on cellular uptake behaviour, whereas particle size played a less important role. In particular, Zr-based MOFs synthesised using naphthalene-2,6-dicarboxylic acid and 4,4′-biphenyldicarboxylic acid as organic ligands, and UiO-66 particles surface-decorated with folic acid and PEG, promoted entry through the *caveolin*-pathway. This allowed the particles to potentially avoid endosomal entrapment and reach the cytosol, enhancing their therapeutic activity when loaded with drugs.

Equipped with an understanding of the cellular uptake of MOF particles, a range of mitochondrially-targeted UiO-66 particles capable of bypassing endosomal entrapment was prepared and tested. The UiO-66 particles were loaded with dichloracetic acid

(DCA), a small chemotherapeutic drug molecule that acts on mitochondria, and surface-functionalised with triphenylphosphonium, a known mitochondrial targeting agent. The system demonstrated a dramatic increase in efficacy, allowing a reduction in DCA effective dose of *ca.* 100-fold compared to the free drug, and *ca.* 10-fold compared to non-targeted, DCA-loaded UiO-66. Confocal microscopy revealed a distribution of the targeted nanoparticles around mitochondria. Super-resolution microscopy of cells treated with the system revealed important mitochondrial morphology changes associated with cell death as soon as 30 minutes after incubation. A whole transcriptome analysis of cells treated with the system indicated widespread changes in gene expression compared to both untreated cells and to cells treated with non-targeted, DCA-loaded UiO-66.

In summary, these studies demonstrated the advantages of MOFs as targeted intracellular delivery vectors. The ease with which their physicochemical properties can be tuned allows for the design of delivery systems able to bypass the critical drug delivery bottlenecks of endosomal entrapment and non-specific delivery.

ACKNOWLEDGEMENTS

First and foremost, to my supervisor, Dr. David Fairen-Jimenez, whose maddening attention to detail drove me to become a much better communicator of ideas, both orally and in writing. He has taught me a number of invaluable skills, both as a researcher and as a person. I am grateful for his guidance when I needed advice during my PhD, always pointing me in the right direction, helping me overcome obstacles when I was stuck, and giving me the freedom to pursue my own interests. I appreciate his genuine desire to make his students better all-round researchers and communicators, and challenging them to think and learn. I am especially grateful for his unconditional understanding when I needed to be away from Cambridge, even for extended periods of time.

To all my labmates in the Adsorption & Advanced Materials Lab, specifically Dr. Michelle Teplensky for the long science discussions and being a supportive friend, Dr. Claudia Orellana-Tavra for helping and training me, and Diana Vulpe for her daily encouragement while I was writing this thesis.

I would also like to thank my collaborator at the University of Glasgow, Dr. Isabel Abanades-Lazaro, from whom I have learnt many techniques. Her superhuman speed and drive have allowed me to generate so much data in the little time I was visiting Glasgow.

I am deeply grateful for Dr. Sergio Mercado-Argandona's mentorship and guidance during the early stages of my PhD, and for being a great friend. He has always helped me put things in perspective when things seemed tough.

To my friends in Cambridge and abroad, who despite the distance, have always been close through visits and phone calls.

Last but not least, I am extremely thankful to my family, especially my parents, who made sure I had unconditional support all along the way. To my dad, who supported my education without questions or compromise, and who pushed me to leave home to come to Cambridge when it was the last thing I wanted to do at the time. To my mom, who always selflessly pushed me forward towards a brighter future, and who made sure I always had wonderful food to remind me of home. Doing this PhD would not have been possible without both of you.

The Cambridge Trust is acknowledged for their financial support.

CONTENTS

1 INTRODUCTION 1

1.1 MOTIVATION 1

1.2 LITERATURE REVIEW 2

1.2.1 Relevance of Intracellular Delivery 2

1.2.2 Existing Carrier-Based Drug Delivery Systems (DDSs) 3

1.2.2.1 Organic Carriers 3

1.2.2.2 Inorganic Carriers 5

1.2.3 Metal-Organic Frameworks as Hybrid Materials 6

1.2.3.1 MOFs in Biomedical Applications 8

1.2.3.2 MOF Synthesis 10

1.2.3.3 Post-Synthetic Modification of MOFs 13

1.2.3.3.1 Post-Synthetic Modification of Zr-MOFs by Coordination to Metal SBUs 14

1.2.3.3.2 Post-synthetic Modification of Zr-MOFs Based on Covalent Chemistry 15

1.3 AIMS & OBJECTIVES 16

2 MATERIALS, SYNTHESIS, AND METHODS 17

2.1 MATERIALS 17

2.2 SYNTHESIS 18

2.2.1 Synthesis of Zr-L1 (UiO-66) 18

2.2.1.1 Synthesis of Zr-L1 for Delivery of Trehalose (Chapter 3) 18

2.2.1.2 Synthesis of *x*Zr-L1 with Different Particle Sizes (Chapter 4) 18

2.2.1.3 Synthesis of Zr-L1 for Mitochondrial Targeting (Chapter 5) 19

2.2.1.3.1 Triphenylphosphonium Attached Using Coordination Modulation 19

2.2.1.3.2 Triphenylphosphonium Attached Using Post-Synthetic Modification 20

2.2.2 Synthesis of Zr-L2−Zr-L6 (Chapter 4) 21

2.2.3 Synthesis of fTPP (Chapter 5) 21

2.3 METHODS 22

2.3.1 General Material Characterisation 22

2.3.1.1 Powder X-Ray Diffraction (PXRD) (Chapters 3, 4, and 5) 22

2.3.1.2 Scanning Electron Microscopy (SEM) (Chapters 3, 4, and 5) 22

2.3.1.3 Thermal Gravimetric Analysis (TGA) (Chapters 3, 4, and 5) 22

2.3.1.4 Dynamic Light Scattering (DLS) (Chapters 3, 4, and 5) 22

2.3.1.5 Zeta Potential Measurements (Chapters 4 and 5) 23

2.3.2 MOF Stability Assessment (Chapter 3) 23

2.3.3 Drug/Biomolecule loading into MOFs (Chapters 3, 4, and 5) 23

2.3.3.1 Trehalose Loading into UiO-66 (Chapter 3) 23

2.3.3.2 Calcein Loading into MOFs (Chapters 4 and 5) 23

2.3.4 Drug/Biomolecule release from MOF (Chapter 3) *24*
2.3.5 Cell Culture (Chapters 3, 4, and 5) *25*
2.3.5.1 Cell Line Maintenance 25
2.3.5.2 Preparation of Frozen Cell Stocks 25
2.3.5.3 Cell Thawing 25
2.3.6 MTS Cytotoxicity Assay (Chapters 3, 4, and 5) *26*
2.3.7 Confocal Microscopy (Chapters 4 and 5) *26*
2.3.7.1 Protocol for Lysosome Co-Localisation Experiments (Chapter 4) 26
2.3.7.2 Protocol for Mitochondria Co-Localisation Experiments (Chapter 5) 27
2.3.8 Super-Resolution Microscopy (Chapter 5) *27*
2.3.8.1 Image Analysis (Chapter 5) 28
2.3.9 Flow Cytometry (Chapters 4 and 5) *28*
2.3.9.1 Energy Dependence of Uptake Protocol (Chapters 4 and 5) 29
2.3.9.2 Endocytosis Inhibition Protocol (Chapters 4 and 5) 29
2.3.9.3 Cellular Uptake Efficiency Protocol (Chapter 4) 29
2.3.10 Microarray (Chapter 5) *30*
2.3.10.1 RNA extraction 30
2.3.10.2 Array Processing 30
2.3.10.3 Bioinformatics 30
3 INTRACELLULAR DELIVERY OF TREHALOSE FOR CRYOPRESERVATION APPLICATIONS 32
3.1 INTRODUCTION 32
3.1.1 Cryopreservation Process and Challenges *32*
3.1.2 Necessity of Cryoprotective Agents (CPAs) *34*
3.1.3 Trehalose as a CPA *36*
3.2 COLLABORATIVE WORK 38
3.3 RESULTS & DISCUSSION 39
3.3.1 Synthesis and Characterisation of Trehalose Delivery System *39*
3.3.2 Loading and Release of Trehalose from UiO-66 ..... *43*
3.3.3 In Vitro Testing of Biocompatibility and Cryoprotective Effect *48*
3.4 CONCLUSIONS 52
4 UPTAKE AND INTRACELLULAR FATE OF MOF NANOPARTICLES 54
4.1 INTRODUCTION 54
4.1.1 Importance of Understanding Endocytosis *54*
4.1.2 Endocytosis Pathways and Final Intracellular Fate of Particles *55*
4.2 COLLABORATIVE WORK 57
4.3 RESULTS & DISCUSSION 58
4.3.1 Effect of Size on Cellular Uptake by HeLa Cells *58*
4.3.2 Effect of Surface Chemistry on Cellular Uptake by HeLa Cells *66*

4.3.2.1 Cellular Uptake of Zr-Based Family of MOFs with Functionalised Linkers 71
4.3.2.2 Cellular Uptake of Post-Synthetically Modified Zr-L1 MOFs....78
4.4 CONCLUSIONS....83
5 TARGETED INTRACELLULAR DELIVERY TO MITOCHONDRIA....84
5.1 INTRODUCTION....84
5.1.1 Mitochondria in Cancer....84
5.1.2 Therapeutic Targets in Mitochondria....85
5.1.2.1 Modulators of the B-cell Lymphoma Protein 2 (BCL-2) Protein Family....86
5.1.2.2 Agents Targeting the Permeability Transition Pore Complex (PTPC)....86
5.1.2.3 Targeting Mitochondrial Metabolism....86
5.1.3 Triphenylphosphonium (TPP) as a Mitochondrial Targeting Agent....87
5.2 COLLABORATIVE WORK....88
5.3 RESULTS & DISCUSSION....89
5.3.1 Synthesis and Characterisation of Mitochondria-Targeting DDS....89
5.3.1.1 Functionalisation with TPP by Coordination Modulation....89
5.3.1.2 Functionalisation with TPP by Post-Synthetic Modification....102
5.3.1.3 Toxicity Time Course Study Using Three Candidate MOFs....107
5.3.2 Cellular Uptake Analysis Using Microscopy and Flow Cytometry....110
5.3.3 Effects of Treatments on Gene Expression of MCF7 cells....120
5.4 CONCLUSIONS....124
6 CONCLUSIONS AND FUTURE WORK....126
6.1 CONCLUSIONS....126
6.2 FUTURE WORK....129
6.2.1 Optimising Cryopreservation Procedure by Allowing Endosomal Escape....129
6.2.2 Elucidating the Biophysical and Biochemical Pathways Triggered by Nanoparticle Treatment....130
6.2.3 Designing a Nucleus-Targeting MOF-based delivery system....130
6.2.4 Using MOFs for CRISPR/Cas9 delivery....131
7 REFERENCES....132
8 APPENDICES....157

LIST OF TABLES

TABLE 2.1. DIFFERENT COMBINATIONS OF DCA AND TPP AMOUNTS USED IN THE SYNTHESIS OF ZR-L1 FOR MITOCHONDRIAL TARGETING. THE SUBSCRIPT NUMBERS IN THE SAMPLE NAMES REPRESENT THE NUMBER OF EQUIVALENTS OF REAGENTS USED. 20

TABLE 3.1. CONDITIONS USED TO TREAT CELLS BEFORE FREEZING. 49

TABLE 3.2. VALUES FOR THE VIABILITY OF HELA CELLS 0 H, 24 H, AND 48 H AFTER THAWING 51

TABLE 4.1. COLLOIDAL ANALYSIS OF ZR-L1 SAMPLES OF DIFFERENT PARTICLE SIZES (I.E. *X*ZR-L1) AS WELL AS THEIR CALCEIN UPTAKES. 58

TABLE 4.2. COLLOIDAL ANALYSIS OF ZR-BASED MOF SAMPLES WITH DIFFERENT SURFACE CHEMISTRY AS WELL AS THEIR CALCEIN UPTAKES. 67

TABLE 5.1. COLLOIDAL ANALYSIS OF DCA_X-TPP_Y-UIO-66 SAMPLES AS WELL AS THEIR DCA AND TPP LOADINGS. 93

TABLE 5.2. COLLOIDAL ANALYSIS OF SAMPLES WITH TPP POST-SYNTHETICALLY ATTACHED, AS WELL AS THEIR DCA AND TPP LOADINGS. 103

TABLE 5.3. NUMBER OF DIFFERENTIALLY EXPRESSED GENES BETWEEN CELLS TREATED WITH DIFFERENT CONDITIONS. 122

List of Figures

Figure 1.1. Schematic representation of the self-assembly process of MOFs from metals and organic ligands. 6

Figure 1.2. Growth of the number of crystalline structures included in the CSD (blue bars) and MOF entries (red bars) since 1972. 7

Figure 1.3. (a) UiO-66 SBU and (b) UiO-based family of isoreticular MOFs showing how porosity increases with the length of the organic ligand. 8

Figure 1.4. Schematic representation of crystal formation dependence on pH and capping agents. 12

Figure 1.5. Colloidal stability of UiO-66 particles synthesised as a function of modulator concentration and modulator acidity (pK_A). 13

Figure 1.6. Schematic representation of the use of solvent-assisted ligand exchange to incorporate a functionality (BODIPY) into MOF crystals. 15

Figure 1.7. Schematic illustration of the reaction scheme of the amidation by EDC hydrochloride and sulfo-NHS mediation 16

Figure 3.1. Schematic drawing of physical events and mechanisms of cryoinjury during freezing 34

Figure 3.2. Various theories to explain the mechanism of action of trehalose: (A) vitrification theory, (B) preferential exclusion theory, and (C) water replacement theory 37

Figure 3.3. PXRD patterns of synthesised UiO-66 (blue) compared with the calculated patterns (black). 39

Figure 3.4. SEM image of synthesised UiO-66 particles. Scale bar shown on image. 40

Figure 3.5. PXRD patterns of synthesised UiO-66 (blue), UiO-66 soaked in water for 9 days (red), and UiO-66 soaked in PBS for 9 days (purple). 41

Figure 3.6. (a) Calibration curve for BDC in PBS and (b) linker release from UiO-66 in PBS with time 42

Figure 3.7. TGA plot of desolvated UiO-66 between 450 ◦C and 550 ◦C. 43

FIGURE 3.8. (A) PXRD PATTERNS OF TREHALOSE, CALCULATED UIO-66, AND UIO-66 LOADED IN SOLUTIONS WITH DIFFERENT TREHALOSE CONCENTRATIONS, AND (B) MAGNIFIED PORTION OF THE CURVES BETWEEN THE ANGLES OF 10° AND 25°. 44

FIGURE 3.9. TGA PLOTS OF TREHALOSE, EMPTY UIO-66, AND TREHALOSE-LOADED UIO-66 PREPARED BY SOAKING UIO-66 IN DIFFERENT CONCENTRATIONS OF AQUEOUS TREHALOSE SOLUTIONS RANGING FROM 30 TO 500 MG/ML 45

FIGURE 3.10. (A) CALIBRATION CURVE USED TO DETERMINE TREHALOSE CONCENTRATIONS USING THE ANTHRONE METHOD, AND (B) LIQUID-PHASE ADSORPTION ISOTHERMS OF TREHALOSE ONTO UIO-66 DETERMINED USING DATA FROM TGA (BLUE) AND FROM MEASURING THE CONCENTRATION OF TREHALOSE INTO THE SUPERNATANT AFTER COMPLETE RELEASE IN WATER (RED) 46

FIGURE 3.11. TREHALOSE RELEASE FROM UIO-66 AS A FUNCTION OF TIME. 47

FIGURE 3.12. MTS VIABILITY ASSAY MEASURING ENZYMATIC METABOLIC ACTIVITY OF HELA CELLS AFTER 24 H INCUBATION WITH (A) TREHALOSE, AND (B) UIO-66 48

FIGURE 3.13. VIABILITY OF HELA CELLS MEASURED USING THE MTS ENZYMATIC METABOLIC ACTIVITY ASSAY AT 0 H (RED), 24 H (BLUE), AND 48 H (YELLOW) POST-THAW 51

FIGURE 3.14. VIABILITY OF HELA CELLS MEASURED USING THE MTS ENZYMATIC METABOLIC ACTIVITY ASSAY AFTER INCUBATION FOR 24 H WITH TREHALOSE-LOADED UIO-66 52

FIGURE 4.1. PXRD PATTERNS OF $_{X}$ZR-L1 MOFS COMPARED WITH THEIR CALCULATED PATTERN 59

FIGURE 4.2. (A) SEM IMAGES OF UIO-66 WITH DIFFERENT PARTICLE SIZES ($_{X}$ZR-L1), AND (B) PARTICLE SIZE DISTRIBUTION OF $_{X}$ZR-L1 PARTICLES AS DETERMINED FROM SEM IMAGES 60

FIGURE 4.3. NORMALISED INTRACELLULAR FLUORESCENCE OF HELA CELLS INCUBATED WITH ZR-L1 OF DIFFERENT PARTICLE SIZES 62

FIGURE 4.4. SIDE SCATTER VERSUS FORWARD SCATTER PLOTS OBTAINED FROM FLUORESCENCE-ACTIVATED CELL SORTING (FACS) OF (A) HELA CELLS, (B) HELA CELLS INCUBATED WITH $_{652}$ZR-L1, AND (C) HELA CELLS INCUBATED WITH $_{260}$ZR-L1 63

FIGURE 4.5. EFFECTS OF PHARMACOLOGICAL ENDOCYTOSIS INHIBITORS ON THE UPTAKE OF ZR-L1 WITH DIFFERENT PARTICLE SIZES, MEASURED BY FLOW CYTOMETRY..... 64

FIGURE 4.6. CHEMICAL STRUCTURES OF (A) THE ORGANIC LINKERS USED TO SYNTHESISE ZR-BASED MOFS WITH FUNCTIONALISED LINKERS, AND (B) THE SURFACE FUNCTIONALITIES ATTACHED TO ZR-L1..... 67

FIGURE 4.7. SEM IMAGES FOR A. ZR-BASED FAMILY, ZR-L2–ZR-L6 AND B. POST-SYNTHETICALLY MODIFIED ZR-L1-*FUNC* PARTICLES..... 69

FIGURE 4.8. NORMALISED INTRACELLULAR FLUORESCENCE OF HELA CELLS INCUBATED WITH ZR-L2 TO ZR-L6 72

FIGURE 4.9. EFFECTS OF PHARMACOLOGICAL ENDOCYTOSIS INHIBITORS ON THE UPTAKE OF ZR-BASED FAMILY OF MOFS COMPARED TO A CONTROL AT 37 °C, MEASURED BY FLOW CYTOMETRY 74

FIGURE 4.10. CONFOCAL MICROSCOPY IMAGES OF HELA CELLS INCUBATED WITH ZR-BASED MOFS (ZR-L2–ZR-L6) LOADED WITH CALCEIN (GREEN FLUORESCENCE), AND LYSO-TRACKER DEEP RED (RED), FOR 2 H. (B) MANDERS' OVERLAPPING COEFFICIENT FOR ALL THE MOF SAMPLES AND THE LYSOSOMAL MARKER 77

FIGURE 4.11. NORMALISED INTRACELLULAR FLUORESCENCE OF HELA CELLS INCUBATED WITH POST-SYNTHETICALLY SURFACE-MODIFIED ZR-L1-*FUNC*..... 78

FIGURE 4.12. EFFECTS OF PHARMACOLOGICAL ENDOCYTOSIS INHIBITORS ON THE UPTAKE OF POST-SYNTHETICALLY SURFACE-MODIFIED ZR-L1-*FUNC* MOFS, MEASURED BY FLOW CYTOMETRY 80

FIGURE 4.13. MTS VIABILITY ASSAY MEASURING ENZYMATIC METABOLIC ACTIVITY OF HELA CELLS AFTER 72 H INCUBATION WITH POST-SYNTHETICALLY FUNCTIONALISED ZR-L1-DCA-*FUNC* PARTICLES 82

FIGURE 5.1. CHEMICAL STRUCTURE OF DCA (DRUG) AND TPP (TARGETING AGENT), USED AS MODULATORS IN THE SYNTHESIS OF UIO-66. 89

FIGURE 5.2. PXRD PATTERNS OF SYNTHESISED MOFS COMPARED WITH THEIR CALCULATED PATTERN 90

FIGURE 5.3. TGA OF DCA_x-TPP_y-UIO-66 (BLACK), UIO-66 (BLUE), AND FREE TPP (PURPLE), UNDER AIR 91

FIGURE 5.4. TGA OF DCA_{10}-UIO-66 (BLACK) AND UIO-66 (BLUE) UNDER AIR. 92

FIGURE 5.5. SEM OF SYNTHESISED DCA_X-TPP_Y-UIO-66 PARTICLES 95

FIGURE 5.6. DCA_X-TPP_Y-UIO-66 PARTICLE SIZES DETERMINED FROM SEM AS A FUNCTION OF DCA AND TPP CONCENTRATIONS USED IN SYNTHESIS 96

FIGURE 5.7. DCA_X-TPP_Y-UIO-66 HYDRODYNAMIC DIAMETERS DETERMINED FROM DLS AS A FUNCTION OF DCA AND TPP CONCENTRATIONS USED IN SYNTHESIS. 98

FIGURE 5.8. MTS VIABILITY ASSAY MEASURING ENZYMATIC METABOLIC ACTIVITY OF MCF-7 (A-D) AND HEK-293 (E-H) CELLS AFTER 72 H INCUBATION WITH DCA_X-TPP_Y-UIO-66 PARTICLES 101

FIGURE 5.9. MTS VIABILITY ASSAY MEASURING ENZYMATIC METABOLIC ACTIVITY OF MCF-7 (A-F) AND HEK-293 (G-L) CELLS AFTER 72 H INCUBATION WITH DCA_X-UIO-66 PARTICLES TO WHICH TPP WAS POST-SYNTHETICALLY ATTACHED 105

FIGURE 5.10. MTS VIABILITY ASSAY MEASURING ENZYMATIC METABOLIC ACTIVITY OF MCF-7 CELLS AFTER 72 H INCUBATION WITH UIO-66 AND TPP@UIO-66 106

FIGURE 5.11. MTS VIABILITY ASSAY MEASURING ENZYMATIC METABOLIC ACTIVITY OF (A) MCF-7 AND (B) HEK-293 CELLS AFTER INCUBATION WITH DCA_5-UIO-66 (EMPTY RED SQUARES), DCA_5-TPP_5-UIO-66 (SOLID BLUE CIRCLES), AND $TPP_{(++)}$@(DCA_5-UIO-66) (SOLID RED SQUARES), FOR 4 H, 8 H, 24 H, 48 H, AND 72 H 108

FIGURE 5.12. CONFOCAL MICROSCOPY IMAGES OF (A) MCF-7 AND (B) HEK-293 CELLS INCUBATED FOR 2 H WITH FTPP@(DCA_5-UIO-66) (GREEN) 112

FIGURE 5.13. SIM IMAGES DEMONSTRATING CAL-$TPP_{(++)}$@DCA_5-UIO-66 (GREEN) INTERNALISATION INTO MCF-7 CELLS AFTER 30 MIN AND 8 H INCUBATION 114

FIGURE 5.14. SIM IMAGES SHOWING MCF-7 CELLS (A) UNTREATED, (B) TREATED WITH CAL@DCA_5-UIO-66, AND (C) TREATED WITH CAL-$TPP_{(++)}$@(DCA_5-UIO-66) FOR 8 H 115

FIGURE 5.15. IMAGES SHOWING MITOCHONDRIA SHAPE ANALYSIS USING CELL PROFILER 116

FIGURE 5.16. EFFECTS OF DIFFERENT TREATMENTS ON THE ECCENTRICITY OF MITOCHONDRIA IN MCF-7 CELLS 117

FIGURE 5.17. EFFECTS OF PHARMACOLOGICAL ENDOCYTOSIS INHIBITORS ON THE UPTAKE OF CAL@(DCA$_5$-UIO-66) (WHITE BARS) AND CAL-TPP$_{(++)}$@(DCA$_5$-UIO-66) (RED BARS) BY MCF-7 CELLS, MEASURED BY FLOW CYTOMETRY 119

FIGURE 5.18. PRINCIPAL COMPONENT ANALYSIS OF MCF-7 GENE EXPRESSION DATA ... 121

FIGURE 5.19. VENN DIAGRAM ANALYSIS OF A) UP-REGULATED AND B) DOWN-REGULATED DIFFERENTIALLY EXPRESSED GENES IN MICROARRAYS OF MCF-7 CELLS TREATED WITH DCA$_5$-UIO-66, DCA$_5$-TPP$_5$-UIO-66 AND TPP$_{(++)}$@(DCA$_5$-UIO-66) COMPARED TO AN UNTREATED CONTROL. 124

LIST OF ABBREVIATIONS AND ACRONYMS

Å – Angstrom

A2780 – Human ovarian cancer cells

BDC – 1,4-benzenedicarboxylate

BET – Brunauer-Emmett-Teller

Biot – Biotin

BTC – Benzene-1,3,5-tricarboxylate

Cal – Calcein

compound@MOF – compound loaded metal-organic framework

CPP – Cell penetrating peptide

DCA – Dichloroacetic acid

DLS – Dynamic light scattering

DMEM – Dulbecco's modified Eagle's medium

DMF – N,N-dimethylformamide

DNA – Deoxyribonucleic acid

Dox – Doxorubicin

EDTA – Ethylendiaminotetracetic acid

EPR – Enhanced permeability and retention

EST – Expressed sequence tags

FA – Folic acid

FBS – Foetal bovine serum

Fe – Iron

fTPP – Fluorescent variant of triphenylphosphonium

g – Gram

HEK 293 cells - human embryonic kidney cells

HeLa cells – Henrietta Lacks cells, human cervical cancer cells

ICP-OES – Ion-coupled plasma-optical emission spectroscopy

iPSCs – Induced pluripotent stem cells

kcal – Kilocalorie

Lact – poly(L-lactide)

M – Molar

mg – Milligrams

MIL – Materials Institute Lavoisier

mL – Millilitre

mm – Millimetre

mM – Millimolar

mmol – Millimole

MSNs – Mesoporous silica nanoparticles

MOF – Metal-organic framework

MTS – 3-(4,5-dimethylthiazol-2-yl)-5-(3-carboxymethoxyphenyl)-2-(4-sulfophenyl)-2H-tetrazolium salt

MTT – (3-(4,5-dimethylthiazol-2-yl)-2,5-diphenyltetrazolium bromide)

MW – Molecular weight

nm – Nanometres

nmol – Nanomole

NP(s) – Polymer-nanoparticle(s)

PBS – Phosphate buffered solution

PCN-224 – MOF with name that stands for porous coordination network 224

PEG – Polyethylene glycol

PEI – Polyethyleneimine

pmol – Picomole

PNIPAM – Poly(N-isopropylacrylamide)

PXRD – Powder X-ray diffraction

RT-PCR – Reverse-transcription quantitative polymerase chain reaction

RES – Reticuloendothelial system

RNA – Ribonucleic acid

SAGE – Serial analysis of gene expression

SBU – Secondary building unit

SEM – Scanning electron microscopy

SIM – Structured Illumination Microscopy

siRNA – Small interfering ribonucleic acid

TFA – Trifluoroacetic acid

TGA – Thermogravimetric analysis

TPP – Triphenylphosphonium

UiO – University of Oslo

ZIF – Zeolitic imidazolate framework

Zn – Zinc

Zr – Zirconium

α-CHC – α-cyano-4-hydroxycinnamic acid

μg – Micrograms

μL – Microliters

μm – Micrometer

μM – Micromolar

List of Appendices

Appendix 1 Statistical Significance of Viability Results after Cryopreservation from Chapter 3 158

Appendix 2 Endocytosis Pathway Studies Results from Chapter 4..... 159

Appendix 3 MTS Toxicity of DCA, TPP, and the Combination of Both from Chapter 5..... 161

1 INTRODUCTION

1.1 Motivation

Intracellular delivery of materials has become of critical importance to a variety of fields, including *ex vivo* cell-based therapies, genome-based approaches, and a range of fundamental research applications[1]. It also plays an important role in drastically enhancing the efficacy of treatment protocols *in vivo* by allowing the delivery of therapeutics to locations within the cell that are relevant to disease[2]. Despite its essential role in biological research and therapeutic applications, the intracellular delivery of therapeutic compounds and biomacromoleules remains a challenge. Intracellular delivery solutions are therefore required to overcome delivery hurdles and tap into the unfulfilled potential of these exciting applications.

Carrier-based approaches, involving the use of delivery vehicles to penetrate inside cells and deliver cargo, have proven attractive strategies for intracellular delivery[3–5]. These carrier-based systems can be broadly categorised into organic and inorganic materials[6]. Organic carriers have the advantage of biocompatibility, with their principle drawback being their low loading capacities[7]. Inorganic carriers on the other hand have well-defined porosity endowing them with high loading capacities. However, they display some issues with biocompatibility[6,8].

Metal-organic frameworks (MOFs) have emerged as interesting candidates for carrier-based delivery. These hybrid organic-inorganic materials are constituted of metal clusters linked together by organic ligands. The possibility to tune their physical and chemical properties both in the bulk and at the surface allows for the design of delivery

systems with high loading capacities, good biocompatibility, and targeting abilities, combining the benefits of both organic and inorganic materials[6,9,10]. The aim of this thesis is to investigate the use of MOFs as intracellular delivery vectors in a range of different applications.

1.2 Literature Review

1.2.1 Relevance of Intracellular Delivery

Intracellular delivery is a key step in various applications, ranging from cell-based therapy and gene editing to regenerative medicine and fundamental biology. A number of *ex vivo* cell-based therapies involving intracellular delivery have shown great promise in the treatment of human disease. Gene delivery to haematopoietic stem cells (HSCs) for example has allowed the correction of mutations involved in monogenic diseases, such as X-linked severe combined immunodeficiency, β-thalassaemia major, and metachromatic leukodystrophy[11]. In T-cell immunotherapy for cancer, T-cells with enhanced and/or novel function against tumour targets have been genetically engineered[11,12]. In regenerative medicine, efforts were made to generate induced pluripotent stem cells (iPSCs) without the need for potentially mutagenic viral vectors, by directly delivering reprogramming proteins fused with a cell penetrating peptide (CPP)[13]. Mout *et al.* were able to deliver CRISPR/Cas9-ribonucleoprotein intracellularly using gold nanoparticles (NPs) and demonstrated a 30 % gene editing efficiency[14]. In basic research applications, a large array of molecules are target materials for intracellular delivery. These include nucleic acids, peptides, metabolites, membrane impermeable drugs, cryoprotectants, exogenous organelles, and molecular probes[1]. For *in vivo* applications, the intracellular delivery of therapeutics can greatly enhance the therapeutic index of a drug, especially if delivery is targeted to specific molecular targets within sub-cellular locations/organelles[15].

The common theme in all these different biological applications is the need to safely and efficiently deliver cargo inside cells. For that, a number of approaches are available. Membrane-disruption-based approaches involve the introduction of temporary gaps in the plasma membrane to allow for the direct entry of materials into the cytosol[16]. This technique is very versatile in terms of its ability to rapidly deliver a diversity of materials to almost any cell type[17–19]. However, its main limitation is that it is only amenable to *in vitro* and *ex vivo* applications. It is also limited in terms of its

ability to target specific organelles within the cell – it is non-specific, and delivers almost any sub-micrometer material dispersed in solution into the cytosol[19]. Carrier-based approaches on the other hand involve the use of vectors to deliver relevant materials inside cells. They have the advantage of being appropriate for all types of applications (*in vitro*, *ex vivo*, *in vivo*). They can also allow for sub-cellular targeting by attaching targeting functionalities to the vector[2]. Though they are restricted in terms of feasible cargo materials and cell types[19], they are still very promising candidates to help develop intracellular delivery systems that can enable unprecedented flexibility in the capacity to manipulate cell function and probe the intracellular environment.

1.2.2 Existing Carrier-Based Drug Delivery Systems (DDSs)

To allow for efficient intracellular delivery, carrier-based systems need to be able to perform multiple functions. First, they must efficiently hold the cargo and protect it from degradation. Second, they must transport the cargo to the intracellular space and deliver it within the target destination. Third, they must deliver the cargo within the cell with appropriate spatiotemporal dynamics[19]. A number of synthetic carrier-based systems have traditionally been used for intracellular delivery. They can broadly be categorised into organic and inorganic materials. Organic materials include polymers, lipids, micelles, and hydrogels. Inorganic materials include the likes of zeolites and mesoporous silica nanoparticles[6].

1.2.2.1 Organic Carriers

This section describes the main types of organic carrier-based systems and identifies their key advantages and drawbacks. These include liposomes[20], polymers[21,22], micelles[23], and hydrogels[24].

Liposomes were first described in 1965[25] and were soon proposed as drug delivery systems[26]. They are among the most popular and well-studied drug carriers. They consist of vesicular structures with an aqueous core surrounded by a hydrophobic lipid bilayer, about 100–400 nm in size, created by the extrusion of phospholipids[27]. They are biocompatible materials, displaying no toxicity or antigenicity. Cargo included in liposomes is protected from the external media[28]. However, these materials have a number of drawbacks. Similar to biological membranes, they display low permeability to hydrophilic molecules and high permeability to lipophilic ones, which can cause

issues related to the fast release of highly hydrophobic cargo molecules[20]. Regarding clearance from the body, liposomes are rapidly eliminated from the blood and cleared by the reticulo-endothelial system (RES), mainly in the liver and spleen. This can be remedied by attaching PEG to the surface of liposomes, extending their blood circulation half-life from 30 min to 5 h[29,30].

Micelles represent another promising type of biomolecule carrier. They are amphiphilic macromolecule aggregates, self-assembled into a spherical shape, with a hydrophobic core and hydrophilic surface. Micelles are generally in the size range 10–100 nm, and are therefore large enough to avoid renal excretion (> 50 kDa), yet small enough to bypass filtration by the spleen[31]. They can allow to solubilise hydrophobic drugs by their incorporation into the micellar core. Genexol, the commercial name of a paclitaxel-loaded micelle, is a representative example of a very low solubility drug (0.3 μg/mL) being solubilised using micelles[32]. However, the poor physical stability of micelles upon entry into the bloodstream is one of their main drawbacks, with blood proteins disrupting micellar cohesion and prematurely releasing the cargo[31].

Polymer-drug conjugates are materials in which a low molecular weight (MW) therapeutic is attached to a polymeric carrier. Contrarily to free drugs which distribute randomly around the body causing unwanted side effects, polymer-drug conjugates can help to solubilise drugs, extend their circulation time to several hours, and facilitate passive targeting of tumours by the enhanced permeability and retention (EPR) effect[33]. Different polymer architectures can have different effects. For example, Paclitaxel conjugated with linear bis(PEG) and with dendritic polyamidoamine (PAMAM) G4 was shown to have 10-fold better solubility in both cases, but reduced activity (25-fold) for the linear PEG conjugate and increased activity (10-fold) for the dendritic conjugate compared to the free drug in A2780 human ovarian cancer cells[34].

Polymeric NPs are structures 10–100 nm in size and can also be considered polymer-drug conjugates. They are obtained from synthetic polymers such as polyacrylamide[35] and polyacrylate[36], or from natural polymers such as albumin[37], chitosan[38], and DNA[39]. Polymeric NPs such as poly(L-lactide) and polyglycolide are biodegradable and can undergo hydrolysis in the body, producing biodegradable metabolite monomers (lactic acid and glycolic acid). This makes this type of material non-toxic, non-immunogenic, and non-proinflammatory[40], whenever the monomers are non-toxic. A potential issue with biodegradable polymeric NPs is that they do not

always degrade into their monomeric components, but into a wide distribution of fragment sizes, making toxicity challenging to determine experimentally[41]. Although they are efficient carriers, with Park *et al*. demonstrating that poly(lactic-co-glycolic acid) NPs are able to greatly reduce the side effects of doxorubicin *in vivo* in mice, they do suffer from low drug weight loadings (5 % wt/wt in this case)[42].

1.2.2.2 Inorganic Carriers

Although less common and less well-developed, inorganic materials such as zeolites and mesoporous silica NPs (MSNs) have also been investigated as delivery systems. Their main advantage compared to organic carriers is that they are easier to synthesise reproducibly and at large scale owing to their crystallinity, which also endows them with high internal surface areas.

Zeolites are microporous crystalline materials based on a three-dimensional framework of SiO_4 and potentially AlO_4 tetrahedra that results in an extended uniform network of channels and pores[43]. The framework is negatively charged due to the AlO_4 tetrahedra. It is kept neutral overall by the extra-matrix alkaline ions. Water molecules are also loosely bound to the structure, but can be evacuated by heating, leaving a high available surface area and accessible pore volume. Various chemotherapeutic drugs, such as α-cyano-4-hydroxycinnamic acid (α-CHC)[44], and 5-fluorouracil[45] have been encapsulated in zeolites. Weight loadings were in the range of 10 wt %. Other drugs such as Ketoprofen, a non-steroidal anti-inflammatory drug, showed weight loadings of around 28.5 wt %[43]. The main drawback of zeolites is their limited physical (surface areas of at most *ca*. 1000 m^2/g; pore volumes *ca*. 0.3 cm^3/g; pore size ca. 2–10 Å) and chemical versatility, restricting the size and type of cargo molecules that can be loaded within the pores[6].

MSNs are mesporous materials with pore sizes in the 2–20 nm range, enabling them to hold biomolecules of different sizes, and making them attractive candidates for drug delivery[8,46–48]. They are synthesised *via* a template-directed method that yields well-defined pore networks. MSNs possess a high density of surface silanol groups, which can be modified with a wide range of organic functional groups. This allows to easily control the surface charge of the particles, to chemically link with functional molecules (e.g. targeting) inside and outside the pores, and to control the size of the pore entrance[49]. MSNs have high surface areas of up to > 900 m^2/g, and large pore

volumes of up to > 0.9 cm^3/g, allowing them to hold large quantities of cargo (loadings up to 50 wt %)[50]. A number of studies have been reported in the literature, showing MSNs' loading and release of a number of anti-inflammatory, antibiotic, osteogenic, and chemotherapeutic drugs[49,51]. A key drawback of MSNs is that the large surface density of silanol groups can cause the particles to interact with the phospholipid surface of red blood cell membranes, inducing hemolysis. They can also induce some metabolic changes[8].

1.2.3 Metal-Organic Frameworks as Hybrid Materials

MOFs are a class of three-dimensional, crystalline, porous solids consisting of metal clusters interconnected by organic linkers[10] (**Figure 1.1**). Li *et al*. synthesised the first MOF with accessible porosity in 1999, and termed it Zn(BDC).(DMF)(H_2O), where BDC = 1,4-benzenedicarboxylate and DMF = N,N-dimethylformamide[52].

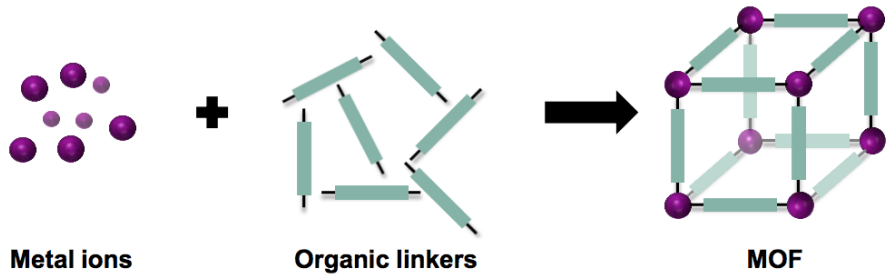

Figure 1.1. Schematic representation of the self-assembly process of MOFs from metals and organic ligands.

One of the key advantages of MOFs compared to their organic and inorganic counterparts is the ease with which their composition can be tuned. By simply varying the metal clusters and organic linkers (*e.g*. carboxylates, imidazolates, or phosphonates), MOFs can display highly diverse pore sizes (up to 6 nm), topologies, and physicochemical properties[9], which can be tailored to the properties of each individual drug and its medical application[6]. The flexibility offered by the different combinations of metal clusters and organic linkers has led to the discovery of tens of thousands of compounds[53]. **Figure 1.2** shows that the number of MOF entries in the Cambridge Structural Database (CSD) has substantially increased in the past decade, to an estimated 70,000 materials in 2017 (the number is regularly updated and currently stands at 82,000).

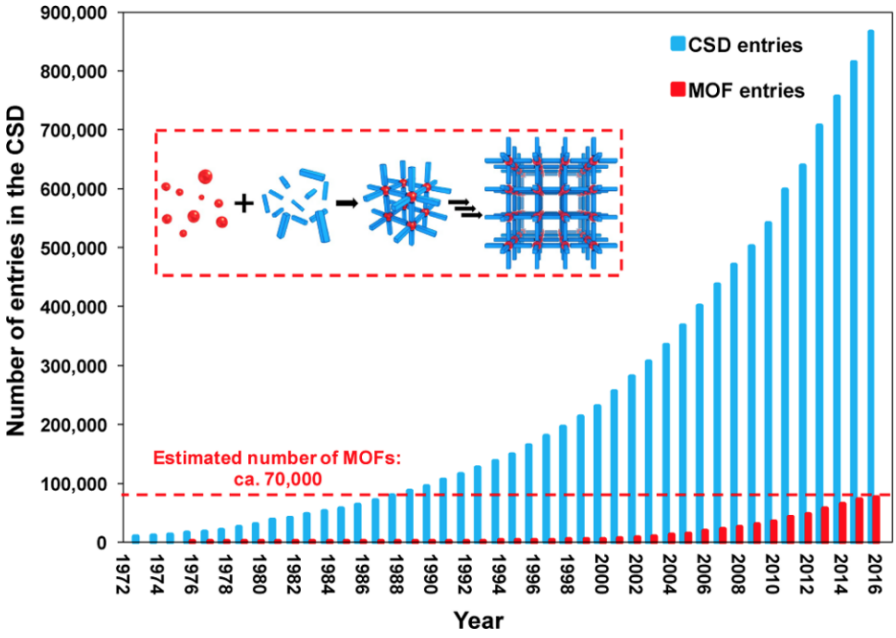

Figure 1.2. Growth of the number of crystalline structures included in the CSD (blue bars) and MOF entries (red bars) since 1972. Image adapted from Moghadam *et al*[53].

Among the most studied MOF models are MOF-5[54], HKUST-1[55] (Hong Kong University of Science and Technology), ZIF-8[56] (Zeolitic Imidazole Framework-8), the MIL family[57] (Materials of Institut Lavoisier), and the UiO family[58] (Universitetet i Oslo). They have been used as a platform to develop more complex derivative MOFs. Zirconium-based MOFs in particular have recently attracted interest as delivery systems due to their biocompatibility and high stability (thermal, chemical, and mechanical)[58–60], and will be the main focus of the upcoming sections dealing with MOF synthesis and surface modification (**Sections 1.2.3.2 and 1.2.3.3**). An attractive feature of Zr-based MOFs is their low stability in the presence of phosphate salts, which ensures that they are degraded *in vivo*, preventing accumulation of the carrier in the body.

UiO-66 ($[Zr_6O_4(OH)_4(BDC)_6]$) was the first Zr-based MOF to be discovered and is the most well-known and studied. It consists of SBUs formed by six-centre octahedral zirconium clusters (**Figure 1.3a**), linked together by BDC linkers, resulting in two main cavities (*ca*. 8 and 11 Å) and large porosity (S_{BET} = 1200 m^2/g; V_p = 0.5 cm^3/g)[58,61]. A range of organic ligands has been used to form an isoreticular series of Zr-based MOFs based on UiO-66, with porosity increasing with increasing linker length (**Figure 1.3b**). It is also possible to use linkers with pendant functionalities such as bromo, nitro, and amino, to tune the physicochemical properties of the MOF particles, and also to post-synthetically modify them[62,63].

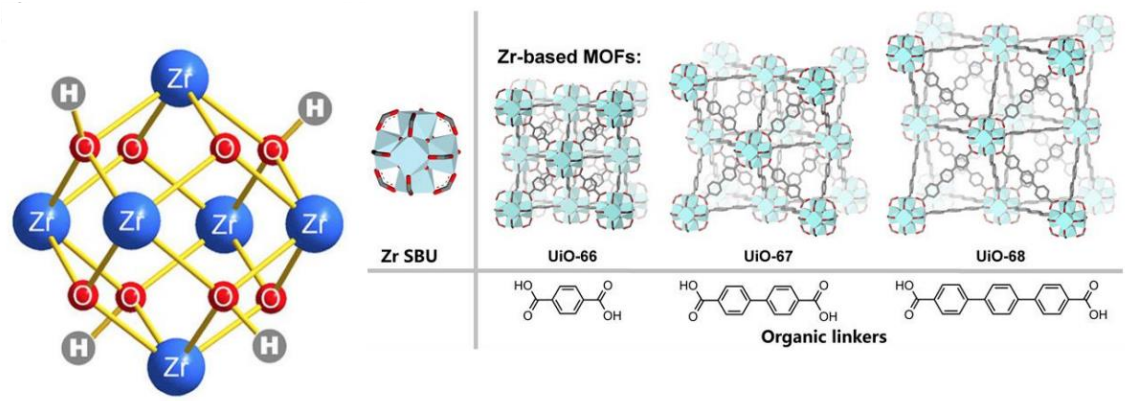

Figure 1.3. (a) UiO-66 SBU, adapted from Wang *et al.*[64] and (b) UiO-based family of isoreticular MOFs showing how porosity increases with the length of the organic ligand, adapted from Shearer *et al.*[65]

Since their discovery, MOFs have been used extensively in a variety of applications, ranging from catalysis, energy storage, sensors, and gas separation[6]. More recently, they have been investigated for their potential applications in drug delivery. A brief review of MOFs in this context will be outlined in the following section.

1.2.3.1 MOFs in Biomedical Applications

Ferey and co-workers first reported the use of iron-based MOFs in biomedical applications in 2006[66]. Since then, their use in healthcare applications has been extensively investigated[67]. Highlighting the interest of the cancer field, most studies involving MOFs for drug delivery have dealt with antitumour drugs. In one study for example, doxorubicin was encapsulated in MIL-100 (Fe) NPs at a weight loading of 9 %, and had a slow and progressive release profile of up to two weeks in phosphate buffered saline (PBS) at 37 °C[7]. In another, doxorubicin was loaded into ZIF-8 NPs (49 wt %), and 66 % of the drug was released in PBS over 30 days[68]. Lucena and co-workers demonstrated very high loading of the antitumoural 5-fluoroacil (5-FU) in Cu-BTC NPs (*ca.* 80 wt %). The drug-loaded NPs had higher antitumoural efficacy than free 5-FU, which was explained by the progressive release of the drug (*ca.* 82 % after 2 days)[69]. Nucleic acids have also been entrapped in MOFs to allow their protection from degradation until they reach the intracellular space. In one study by Lin *et al.*, small interfering RNA (siRNA) was attached to the surface of the zirconium aminotriphenyldicarboxylate UiO-type NPs by coordination to the surface metal sites. This protected the siRNA from nuclease degradation and enhanced its cellular uptake. The anticancer prodrug cisplatin was also loaded into the MOFs (12 wt %), and the

co-delivery of both the drug and the siRNA greatly enhanced the chemotherapeutic efficacy against the SKOV-3 ovarian cancer cell line[70]. MOFs have also been used to deliver challenging antiviral drugs, which due to their high polarity cannot cross the cell membrane efficiently. Cidofovir and the anti-HIV azidothymidine triphosphate (AZT-TP) were encapsulated in different MOFs of the MIL family, reaching loadings of up to 42 wt % in MIL-101(Fe)_NH_2 NPs. AZT-TP-loaded MOF NPs showed higher anti-HIV efficacy than the free drug[71]. Morris *et al*. have demonstrated the encapsulation in MOFs of nitric oxide (NO)[72], a neurotransmitter involved in the cardiovascular, nervous, and immune systems[73].

In terms of biocompatibility of MOFs, very limited literature is available regarding *in vitro* and *in vivo* toxicity. *In vitro* studies have been performed using a number of different cell lines, making comparison of results difficult. However, it generally seems that the toxicity is dependent on the choice of metal and organic ligand. This was demonstrated in a Horcajada and co-workers study in which they performed MTT (3-(4,5-dimethylthiazol-2-yl)-2,5-diphenyltetrazolium bromide) tests on a series of 14 MOFs with different metals (Fe, Zn, and Zr) and linkers (carboxylates and imidazolates), on two different cell lines (HeLa and murine macrophage cells J774). The materials demonstrated low toxicity comparable to other commercialised nanoparticulate systems, with the least toxic MOF being the Fe carboxylate, and the most toxic being the Zn imidazolate NPs. The hydrophobic-hydrophilic balance proved to be an important parameter, with the more hydrophilic ligands being the least toxic[74].

Regarding *in vivo* toxicity, Maspoch and co-workers assessed the cytotoxicity of 16 different MOFs on HepG2 and MCF-7 cells *in vitro*, and on zebrafish embryos *in vivo*, and found a strong correlation between *in vitro* and *in vivo* toxicities. Toxicity was chiefly attributed to leached metal ions, with the most toxic ions being Cu^{II}, Mn^{II}, and Fe^{III}, and the least toxic being Co^{II}, Ni^{II}, and Mg^{II} [75]. In another study, Horcajada and co-workers assessed the *in vivo* toxicity of three different porous iron carboxylate MOFs (MIL-88A, MIL-88B_$4CH_3$, and MIL-100) in rats for up to three months by studying their distribution, metabolism, and excretion. They found that the MOFs were degraded into their constituent components, allowing the excretion of the organic linker in the urine and faeces. They found no differences between treated and control groups, except for a transient increase in weight of the liver and spleen, attributed to the rapid sequestration of MOFs by the reticuloendothelial system (RES). Both organs however

kept their function intact. Altogether the results showed the suitability of the biodegradable non-toxic iron carboxylate MOFs for biological applications[76].

Having shown the interesting potential of MOFs for biomedical applications, the following sections will discuss their synthesis and post-synthetic modification in order to better understand the characteristics that make them remarkable candidates for intracellular delivery.

1.2.3.2 MOF Synthesis

The synthesis of Zr-based MOFs is usually done under solvothermal conditions, which involves the heating of a solution of metal and ligand over time. This leads to more controlled particle growth and nucleation than other synthesis methods such as microwave-assisted, electrochemical, mechanochemical, and sonochemical syntheses[77]. Coordination modulation - first introduced by Fischer and co-workers – involves the use of a monodentate ligand (modulator) with similar chemical functionality to the multidentate organic linker in the synthesis process[78]. The modulator competes with the organic linker for coordination to the metal clusters, which renders it a tool to control particle size and composition[65,79,80]. Behrens and co-workers first reported that modulators could be used for size control of UiO-66 in 2011[81].

The modulator can act in two different ways. On the one hand, it can form complexes with zirconium cations in solution, causing the framework construction to proceed through an exchange between the linker and the modulator at the coordination sites of the Zr ion. In this case, a higher concentration of monocarboxylic acid would reduce the possibility of the dicarboxylic acid linker coordinating to Zr ions in solution, thus disfavouring nucleation and allowing a smaller number of nuclei to grow into larger crystals. Although the exchange between the modulator and the linker still happens, the timescale for growth is much larger than the rate associated with nucleation[81]. On the other hand, the modulator can act as a capping agent, permanently coordinating to metal sites at the surface of growing crystals and thus inhibiting their growth[80,82,83]. The size of synthesised crystals is therefore dependent on the dynamic and kinetic balances between the two effects. A number of studies have found particle size to vary differently in different concentration ranges, indicating a more or less pronounced importance for each effect (capping and nucleation-preventing) depending on the modulator concentration range. For example, Guo *et al*. found that Dy(BTC)H_2O particle size decreases as the modulator concentration (sodium acetate) is increased to

3.5 eq, after which it increases[83]. Schaate *et al*. also found particle size of UiO-66 to decrease with increasing benzoic acid concentration up to 3 eq, after which particle size increases[81]. Particle size can therefore be tuned by varying the concentration of monocarboxylic acid modulator. This is especially important for biomedical applications, where it is imperative that the size of the delivery system be less than 500 nm for cellular uptake and less than 200 nm for *in vivo* applications to ensure circulation through small capillaries without blockage (> 10 nm to avoid filtration by the kidneys)[84].

The role and effect of a given modulator and its concentration are however difficult to predict due to the presence of additional factors affecting crystal growth[83,85]. Guo *et al*. for example have demonstrated that the pH of the reaction mixture also has an effect on particle size[83]. They found that it is possible to control particle size even in the absence of a coordinating modulator by simply making the pH more basic. By adding triethylamine (TEA), an organic base that does not have a carboxylate group to act as a capping agent, particle size decreased to a couple of micrometres. This is because a higher pH facilitates deprotonation of the linker, increasing the nucleation rate and allowing crystals to grow. Using a coordinating modulator that affects the pH of the reaction mixture while also acting as a capping agent, such as sodium acetate for example, therefore adds an additional factor to take into consideration when considering its effect on crystal growth. **Figure 1.4** shows a proposed crystal formation mechanism for Dy(BTC)H_2O MOF[83]. At lower pH values, both deprotonation of the linker and nucleation are slow, leading to large crystals. At higher pH, deprotonation and nucleation are faster, leading to smaller microcrystals. In the presence of a capping agent at high pH, crystal growth is restricted even further, resulting in yet smaller nanocrystals.

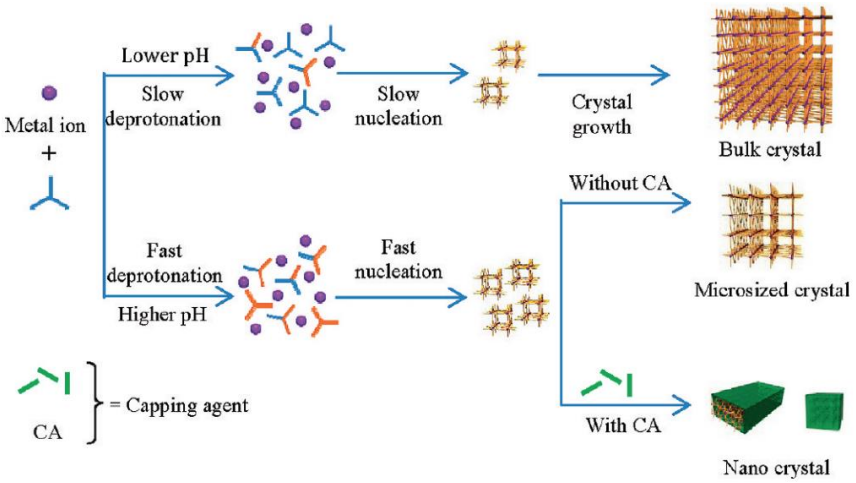

Figure 1.4. Schematic representation of crystal formation dependence on pH and capping agents. Blue and orange colours represent protonated and deprotonated COO- groups of the organic linker. Adapted from Guo *et al.*[83]

A number of studies have shown the key role that modulator concentration plays on the number of defects in UiO-66[58,61,65,86]. Most of these defects exist due to terephtalic acid linkers being replaced by modulator molecules throughout the structure[87,88]. Coordination modulation can therefore also be used to modify the bulk chemistry of MOFs. At the nanoscale, these bulk chemistry changes can also affect the surface properties of the particles, which in turn can affect their colloidal stability. NPs that are stable in aqueous media are essential for healthcare applications. In a systematic study of the effect of monocarboxylic acid modulators on the size and colloidal stability of UiO-66, Mirkin and co-workers found that modulators with lower pK_a values increase the colloidal stability of MOF particles[80]. This is because molecules with lower pK_a values are more likely to be deprotonated during synthesis, and so compete better with the organic linker for attachment to the zirconium positions, which in turn creates defects. These defects increase the surface charge as measured by the zeta potential, thereby increasing the repulsion between NPs and enhancing their colloidal stability. Using formic acid (FA, pK_a = 3.77), dichloroacetic acid (DCA, pK_a = 1.36), and trifluoroacetic acid (TFA, pK_a = 0.23), they were able to synthesise colloidally stable UiO-66 particles (the BDC linker has a first pK_a = 3.51 and a second pK_a = 4.82), as determined by DLS. On the other hand, particles synthesised using acetic acid (AA, pK_a = 4.76) aggregated considerably for similar modulator concentrations (**Figure 1.5**).

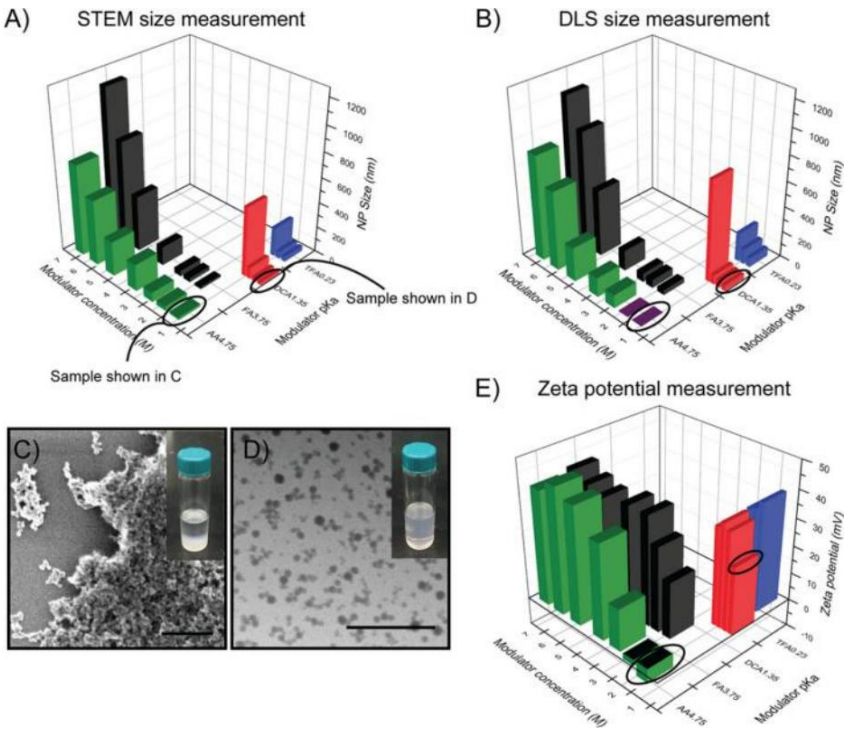

Figure 1.5. Colloidal stability of UiO-66 particles synthesised as a function of modulator concentration and modulator acidity (pK_a). Modulators used were acetic acid AA (green), formic acid FA (black), dichloroacetic acid DCA (red), and trifluoroacetic acid TFA (blue). (A) STEM size measurements. (B) DLS size measurements; purple bars indicate highly aggregated samples for which the size could not be determined using DLS. STEM image and digital photographs of UiO-66 dispersed in water, synthesised with (C) AA (1.2 M) and (D) DCA (0.58 M). (E) Zeta potential measurements. Adapted from Mirkin *et al*.[80]

In summary, coordination modulation can be used to tune the size, surface chemistry, and colloidal stability of MOFs, among other properties. Monocarboxylic acids with lower pK_a values are more effective modulators due to their ability to better compete with the organic linker for coordination to the metal node. They can control particle size by modulating the nucleation rate and by capping crystal growth, and yield more defective, and hence more colloidally stable particles.

1.2.3.3 Post-Synthetic Modification of MOFs

As discussed earlier, the properties of MOFs in solution (e.g. chemical and colloidal stability) are largely dependent on their surface chemistry. Having the ability to modify the surface chemistry is therefore an attractive tool, especially as it also allows for the addition of targeting agents to NP surfaces. Control of surface chemistry can be done during the synthesis step by coordination modulation, as discussed in

Section 1.2.3.2. However, incorporation of a molecule into the MOF structure using coordination modulation and obtaining a functional delivery system can be challenging, as it also has an effect on crystal growth and consequently on the particle size. Additionally, molecules coordinating to metal positions are not restricted to the surface of MOF NPs, but are also present in the bulk[81]. Modifying the surface of particles after they are formed, using post-synthetic modification (PSM), is an alternative technique that can allow to maintain a constant particle size[89]. Additionally, by choosing a functionality that is too large to fit through the pore windows, modification can be limited to the surface of MOF NPs[63]. Tight control of particle size and surface chemistry is particularly relevant for intracellular delivery as a number of studies have revealed a strong correlation between the physical parameters of NPs and cellular processes[90–94]. PSM can be done using a number of different approaches, which can be broadly categorised into (i) approaches that rely on coordinating functionalities to the surface metal clusters, and (ii) ones that rely on covalently attaching functionalities to reactive groups on the linker.

1.2.3.3.1 Post-Synthetic Modification of Zr-MOFs by Coordination to Metal SBUs

Zirconium SBUs are susceptible to nucleophilic attack, which allows the use of nucleophilic functional groups such as carboxylates[95], phosphates[96], and imidazolates[97], to attach functionalities to the surface of Zr MOFs through coordination to the unsaturated Zr positions. The functionality can attach to unsaturated Zr SBUs or can displace linkers by solvent assisted ligand exchange (SALE). When the reagent is too large to fit through the pores, functionalisation is restricted to the outer surface of the MOFs.

Xie *et al*. incorporated carboxyl-functionalised diiodo-substituted BODIPYs into UiO-66 using SALE by heating in DMF at 65 °C for 24 h (**Figure 1.6**). The measured BET area of 1422 m^2/g confirmed attachment to the external surface rather than filling of the pores. A high loading was obtained, with I_2-BODIPY forming 35 % of the weight of the material. The resulting material was assessed for photothermal and photodynamic therapy (PDT) and was shown to generate singlet oxygen very efficiently, which could kill cancer cells effectively[98]. Zhou *et al*. post-synthetically attached folic acid (FA) to the surface of PCN-224 particles 90 nm in size in order to actively target folate receptor (FAR) abundant tumour cells. FA was attached through its carboxylic acid functionality. They tested the material on the FAR abundant HeLa

cell line and showed an improvement in PDT efficacy compared to non-functionalised PCN-224, whereas tests on a control FAR-negative cell line (A549) showed no improvement[95]. Mirkin *et al*. took advantage of the ability of phosphates to coordinate to Zr SBUs to modify a number of UiO-66 series with the phospholipid 1,2-dioleoyl-sn-glycero-3-phosphate (DOPA). The hydrophobic ligand allowed the usually hydrophilic MOF to be suspended in chloroform[64].

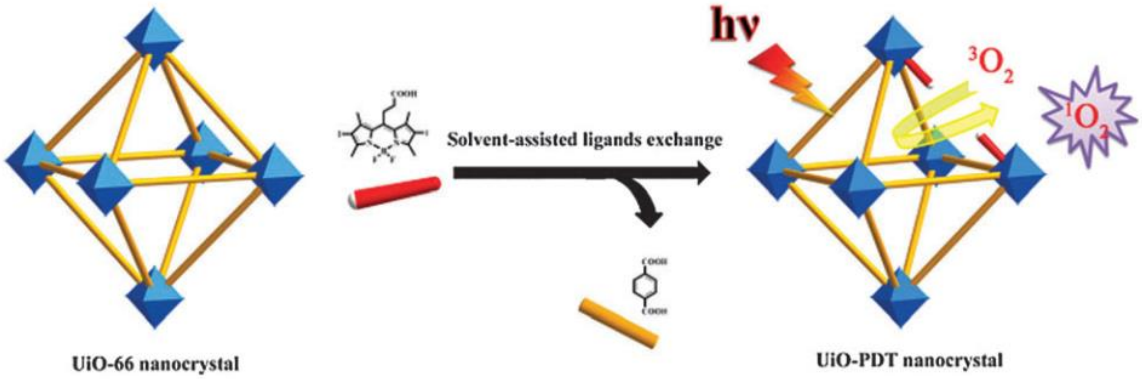

Figure 1.6. Schematic representation of the use of solvent-assisted ligand exchange to incorporate a functionality (BODIPY) into MOF crystals. Adapted from Wang et al.[98]

1.2.3.3.2 Post-synthetic Modification of Zr-MOFs Based on Covalent Chemistry

MOF surfaces can also be modified post-synthesis by covalently attaching molecules to pendant functional moieties on the organic linker. Wuttke *et al*. demonstrated the attachment of NH_2-PEG5000 to externally exposed carboxyl groups of the linker by a water-based carbodiimide mediated reaction (**Figure 1.7**). The functionalized MOF nanoparticles showed increased colloidal stability in aqueous media and displayed efficient uptake by cells, with no cytotoxic effects up to 24 h[99]. While this was done on Fe-based MIL-100 particles, the same principle can be applied to Zr-based MOFs. Mirkin *et al*. covalently functionalised UiO-66 with oligonucleotides. They did so by utilising click chemistry between DNA appended with dibenzylcyclooctyne and azide-functionalised UiO-66-N_3. In aqueous NaCl, the NPs exhibited enhanced stability and cellular uptake when compared to non-functionalised UiO-66 of similar particle size[100]. Sada *et al*. attached poly(N-isopropylacrylamide) (PNIPAM) chains to the amino groups on UiO-66-NH_2 through amide coupling. They obtained a thermoresponsive material that allows for controlled release through conformational changes of PNIPAM, which switches between ‘open’ and ‘closed’ states at lower and higher temperatures respectively[101].

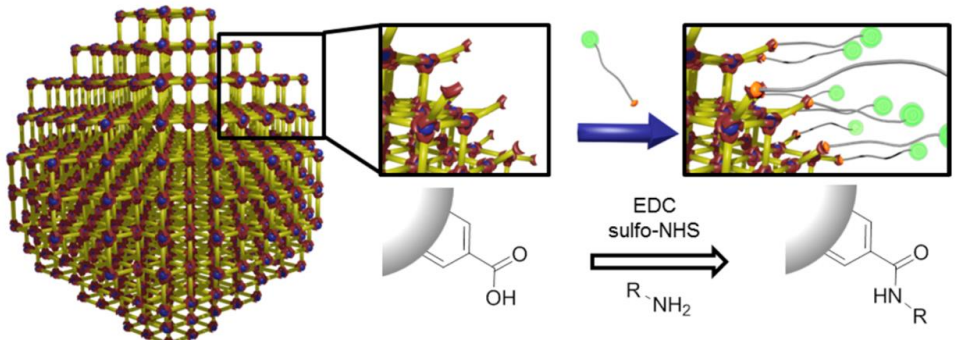

Figure 1.7. Schematic illustration of the reaction scheme of the amidation by EDC hydrochloride and sulfo-NHS mediation. Adapted from Zimpel *et al*.[99]

In summary, surface modification can be performed using a number of methods in order to tune and enhance a vast number of properties of the delivery system, such as colloidal dispersion, *in vivo* stability, and targeting ability, among others. Most surface modifications are done post-synthetically in order to be able to better control particle size. The use of large functionalities restricts attachment to the surface of the particles. Surface functionalisation allows for better design of delivery systems that are biologically relevant.

1.3 Aims & Objectives

The overall aim of the work discussed in this dissertation is to utilise a class of porous materials, metal-organic frameworks (MOFs), for the intracellular delivery of biomaterials. In order to accomplish the described aim, the following objectives were pursued in three separate chapters:

1. Synthesise and characterise Zr-based MOFs that are suitable for intracellular delivery applications.
2. Load different biomolecules into crystalline MOFs both during synthesis and post-synthetically.
3. Investigate the trafficking of MOFs by HeLa cells and their final intracellular fate by studying endocytosis pathways of uptake.
4. Post-synthetically functionalise the surface of MOFs with a targeting agent in order to deliver biomolecules to specific intracellular locations.
5. Determine the efficiency of MOFs as targeted intracellular delivery vectors compared to the free drug/biomolecule using *in vitro* studies on HeLa, MCF-7, and HEK-293 cells.

2 MATERIALS, SYNTHESIS, AND METHODS

2.1 Materials

Zirconium tetrachloride ($ZrCl_4$, 99.5%), terephthalic acid (BDC, 98%), and dimethyl sulfoxide (DMSO) were purchased from Alfa Aesar (UK). Dichloroacetic acid (≥99 %), HCl (37 %), benzoic acid (99.5 %), α-cyano-4-hydroxycinnamic acid (α-CHC, 98 %), calcein disodium salt, nystatin, chlorpromazine, rottlerin, sucrose (99.5 %), 4-carboxybutyl triphenylphosphonium bromide (TPP, 98 %), 3-(diphenylphosphino)propionic acid (97 %), 1-bromopyrene (96 %), triethylamine (TEA, 99.5 %), acetic acid (≥99%), dimethylformamide (DMF, 99.8%), ethanol (99.8 %) methanol (99.9%), and acetone (99.9%) were purchased from Sigma-Aldrich (UK).

HeLa, MCF-7 and HEK-293 cells were obtained from the ATCC. Dulbecco's modified Eagle's medium (DMEM), foetal bovine serum (FBS), L-glutamine, penicillin, and streptomycin were purchased from Invitrogen (UK). Phosphate-buffered saline (PBS), trypsin–EDTA, Lysotracker®-Deep Red, CellLight™ Mitochondria-GFP BacMam 2.0, HCS Mitochondrial Health kit, 2-Mercaptoethanol, Hoechst 33342 (H33342), and CellMask™ Orange were purchased from Life Technologies™ (UK). DRAQ5™ was purchased from Abcam. CellTiter 96® AQueous One Solution Cell Proliferation Assay (MTS) was obtained from Promega (UK). RNeasy Micro kit, QIAshredder, and RNAprotect Cell Reagent were obtained from QIAGEN.

All chemicals and biochemicals used were of analytical grade.

2.2 Synthesis

The results presented in this dissertation were obtained using an isoreticular zirconium-based family of MOFs. Six different linkers were used to synthesise the family of Zr-based MOFs. The linkers were named L1 to L6: L1 = terephtalic acid (BDC); L2 = 2-bromoterephtalic acid (Br-BDC); L3 = 2-nitroterephtalic acid (NO2-BDC); L4 = 2-aminoterephtalic acid (NH2-BDC); L5 = naphthalene-2,6-dicarboxylic acid (NDC); L6 = 4,4'-biphenyldicarboxylic acid (BPDC). The synthesised MOFs were named Zr-Lx, where x denotes the identifier of the linker. Zr-L1 corresponds to UiO-66.

Synthesis of Zr-L2 to Zr-L6 was done by Dr. Ross J. Marshall and Dr. Isabel Abanades Lazaro under the supervision of Dr. Ross Forgan (School of Chemistry, University of Glasgow, UK). Synthesis of the range of Zr-L1 with different particle sizes used in Chapter 4 was done by Mr. Gerard Boix and Dr. Inhar Imaz from Dr. Daniel Maspoch's group (Catalan Institute of Nanoscience and Nanotechnology ICN2, CSIC and The Barcelona Institute of Science and Technology, Campus UAB, Spain).

2.2.1 Synthesis of Zr-L1 (UiO-66)

Different synthetic methods were used to obtain the various samples of Zr-L1 used across this thesis.

2.2.1.1 Synthesis of Zr-L1 for Delivery of Trehalose (Chapter 3)

UiO-66 was synthesised according to Zhu *et al.*[96]: $ZrCl_4$ (2 mmol), terephtalic acid (2 mmol), benzoic acid (20 mmol), and 37 % HCl (0.33 mL, 4 mmol) were ultrasonically dissolved in 36 mL DMF. The mixture was put in a Teflon-lined steel autoclave and was heated in a reaction oven at 120 °C for 48 h. After cooling down to room temperature, the mixture was centrifuged in a bench-top centrifuge (Sigma 3-16PK, DKB Labcare Ltd, Buckinghamshire, UK) at 5500 rpm for 10 minutes, then washed twice with DMF to remove unreacted reagents. It was finally washed twice with ethanol to remove all traces of DMF, and then activated in a vacuum oven at 80 °C overnight in order to remove all guest molecules from the framework.

2.2.1.2 Synthesis of *x*Zr-L1 with Different Particle Sizes (Chapter 4)

(Work done by Gerard Boix and Inhar Imaz from Dr. Daniel Maspoch's group at the Institut Catala de Nanociencia i Nanotecnologia in Barcelona).

In a typical *x*Zr-L1 synthesis, 5 mL of a DMF solution of terephthalic acid (BDC; 20 mg, 0.12 mmol) was added to 10 mL of a DMF solution containing varying amounts of acetic acid (HAc) and $ZrCl_4$ (28 mg, 0.12 mmol) in a 26 mL glass vial with strong magnetic stirring. Once the addition was completed, the stirring was stopped and the vials were sealed and introduced into an oven at 120 °C for 24 hours. The resulting powders were collected by centrifugation (6701 rcf in 50-mL Falcon tubes), re-dispersed in 10 mL of DMF and precipitated by centrifugation. This two-step washing process was repeated two more times with DMF to remove the unreacted BDC. UiO-66 particles were further washed three times with methanol and left under stirring at 50 ºC for 24 hours to remove the DMF. The collected UiO-66 particles were finally dried at room temperature under vacuum overnight. The concentrations of acetic acid used to synthesize the UiO-66 particles of each size were: for 50 ± 2 nm, [HAc] = 10 µl (11.6 mM); for 75 ± 3 nm, [HAc] = 120 µL (139.8 mM); for 92 ± 2 nm, [HAc] = 230 µL (267.9 mM); for 260 ± 21 nm, [HAc] = 460 µL (535.7 mM); for 652 ± 23 nm, [HAc] = 2.75 mL (3.2 M).

2.2.1.3 Synthesis of Zr-L1 for Mitochondrial Targeting (Chapter 5)

2.2.1.3.1 Triphenylphosphonium Attached Using Coordination Modulation

(Work done in collaboration with Dr. Isabel Abanades-Lazaro in Dr. Ross Forgan's group, School of Chemistry, University of Glasgow).

In a typical synthesis, 5 mL of a DMF solution of $ZrCl_4$ (156.75 mg, 0.675 mmol) was added to 5 mL of a DMF solution containing terephtalic acid (BDC; 112 mg, 0.675 mmol) and varying amounts of dichloroacetic acid (DCA) and 4-carboxybutyltriphenylphosphonium bromide (TPP) in a 26 mL glass vial. HCl (60 µL, 0.675 mmol) was added to the mixture, which was then sealed and placed in an oven at 120 °C for 24 hours. The resulting powders were collected by centrifugation at 5500 rpm for 15 minutes, re-dispersed in 10 mL DMF and precipitated by centrifugation. This two-step washing process was repeated once more with DMF to remove the unreacted BDC. UiO-66 particles were further washed two times with methanol and were then left to dry at room temperature under vacuum overnight. The concentrations of DCA and TPP used are shown in Table 2.1.

Table 2.1. Different combinations of DCA and TPP amounts used in the synthesis of Zr-L1 for mitochondrial targeting. The subscript numbers in the sample names represent the number of equivalents of reagents used.

Sample name	**DCA**	**TPP**
DCA_{1}-TPP_{1}-UiO-66	55 µL (1 eq)	299.2 mg (1 eq)
DCA_{10}-TPP_{1}-UiO-66	550 µL (10 eq)	299.2 mg (1 eq)
DCA_{1}-TPP_{5}-UiO-66	55 µL (1 eq)	1496 mg (5 eq)
DCA_{5}-TPP_{1}-UiO-66	275 µL (5 eq)	299.2 mg (1 eq)
DCA_{5}-TPP_{5}-UiO-66	275 µL (5 eq)	1496 mg (5 eq)
DCA_{1}-$TPP_{2.5}$-UiO-66	55 µL (1 eq)	748 mg (2.5 eq)
$DCA_{2.5}$-TPP_{1}-UiO-66	137.5 µL (2.5 eq)	299.2 mg (1 eq)
DCA_{1}-UiO-66	55 µL (1 eq)	0
$DCA_{2.5}$-UiO-66	137.5 µL (2.5 eq)	0
DCA_{5}-UiO-66	275 µL (5 eq)	0
DCA_{10}-UiO-66	550 µL (10 eq)	0
DCA_{20}-UiO-66	1100 µL (20 eq)	0

2.2.1.3.2 Triphenylphosphonium Attached Using Post-Synthetic Modification

For the post-synthetic attachment of TPP to $DCA_{2.5}$-UiO-66, DCA_{5}-UiO-66, and DCA_{10}-UiO-66, 40 mg of MOF were dispersed in 20 mL methanol. Separately, 40 mg or 10 mg TPP (0.090 mmol or 0.023 mmol respectively) were dissolved in 20 mL methanol containing triethylamine (TEA; 0.2 mL, 1.43 mmol). The two solutions were mixed together and then stirred at room temperature overnight. The particles were centrifuged and washed three times with methanol, and were then dried at room temperature in a vacuum desiccator. Obtained particles were named $TPP_{(++)}$@(DCA_{x}-UiO-66) or $TPP_{(+)}$@(DCA_{x}-UiO-66), depending on whether they were functionalised using 40 mg or 10 mg of TPP respectively (x is either 2.5, 5, or 10). $DCA_{2.5}$-UiO-66 was also functionalised utilising 1 mg of TPP (0.009 mmol) using the same procedure. The resulting sample was named TPP@($DCA_{2.5}$-UiO-66). The post-

synthetic attachment of fTPP to DCA_5-UiO-66 was done using the same procedure as for $TPP_{(++)}$@(DCA_5-UiO-66).

2.2.2 Synthesis of Zr-L2−Zr-L6 (Chapter 4)

(Work done by Dr. Ross J. Marshall and Dr. Isabel Abanades-Lazaro in Dr. Ross Forgan's group at the University of Glasgow).

Zr–L2 to Zr–L4 nanoparticles were obtained following the protocol from Zhu *et al.*[96] with minor modifications. $ZrCl_4$ (0.466g, 2.00 mmol), the required linker (1.93 mmol), (L2-L4), benzoic acid (2.44 g, 20.00 mmol) and 0.33 mL of HCl 37 % were ultrasonically dissolved in 36 mL of DMF. The mixture was placed in a 50 mL autoclave and heated at 120 °C for 48 h. After cooling down to room temperature, the mixture corresponding to each MOF was harvested by centrifugation at 5500 rpm for 20 min and washed twice with DMF at room temperature in order to remove the unreacted linker. The same procedure was repeated with acetone in order to remove the DMF solvent from the sample. Finally, the solids were dried at 37 °C in a vacuum oven overnight.

Zr–L5 and Zr–L6 nanoparticles were obtained via solvothermal reaction conditions modifying a reported protocol[102]. Zirconyl chloride octahydrate (213 mg, 0.66 mmol) was dissolved in 25 mL DMF. Separately, the required linker (NDC and BPDC for Zr-L5 and Zr-L6 respectively) (352 mg, 1.63 mmol) was dissolved in 15 mL of DMF. Both reagent solutions were mixed together in a 100 mL jar, then acetic acid (2.6 mL) was added to the reaction mixture, which was stirred and placed in the oven at 120 °C for 24 h. After cooling, the nanoparticles were harvested by centrifugation (4500 rpm, 20 min), and purified by successive dispersion–centrifugation cycles with DMF (x2) and methanol (x3). The solids were dried in a high vacuum desiccator for 24 h.

2.2.3 Synthesis of fTPP (Chapter 5)

Synthesis of fTPP was done according to a protocol from Tomas-Gamasa *et al*[103]. 1-(bromomethyl)pyrene (1744 mg, 5.92 mmol) and 3-(diphenylphosphino)propionic acid (2296 mg, 8.88 mmol) were dissolved in 64 mL toluene, and were then left to reflux overnight. The resulting yellow precipitate was hot-filtered, washed once with methanol, and then left to dry in a rotary evaporator, giving rise to a pale yellow solid (3.223 g, 98 %).

2.3 Methods

2.3.1 General Material Characterisation

2.3.1.1 Powder X-Ray Diffraction (PXRD) (Chapters 3, 4, and 5)

Room temperature powder XRD (PXRD) was performed on all loaded and unloaded samples using a Bruker-D8 theta/theta machine with CuKα1 (λ = 1.5405 Å) radiation and a LynxEye position sensitive detector in Bragg Brentano parafocusing geometry. Steps were performed for 2θ = 2° to 50° at a step rate of 0.07°/s.

2.3.1.2 Scanning Electron Microscopy (SEM) (Chapters 3, 4, and 5)

Samples from Chapters 3 and 4 were scattered onto spectroscopically pure carbon tabs (TAAB Ltd UK) mounted on aluminium stubs. They were coated with 15 nm of gold in a Quorum Emitech K575X sputter coater to make them electrically conductive. They were imaged in an FEI XL30 FEGSEM, operated at 5 keV, using an Everhart Thornley secondary electron detector (Work done by Dr. Jeremy Skepper at the Cambridge Advanced Imaging Centre).

Samples from Chapter 5 were coated with Pd for 50 seconds using Polaron SC7640 sputter coater and imaged using a Carl Zeiss Sigma Variable Pressure Analytical SEM with Oxford Microanalysis. Particle size distribution was analysed manually using ImageJ software (Work done in collaboration with Dr. Isabel Abanades-Lazaro in Dr. Ross Forgan's group at the University of Glasgow).

2.3.1.3 Thermal Gravimetric Analysis (TGA) (Chapters 3, 4, and 5)

TGA was performed using a TA instruments Q500 series thermal gravimetric analyser. The sample (1–3 mg) was held on a platinum pan under continuous flow of air, using a heating rate of 5 ˚C/min, from room temperature up to 800 °C, with a 10 min hold at 100 °C.

2.3.1.4 Dynamic Light Scattering (DLS) (Chapters 3, 4, and 5)

Colloidal analysis was performed using a Zetasizer Nano ZS potential analyser equipped with non-invasive backscatter optics and a 50 mW laser at 633 nm. Measurements were performed at high resolution.

2.3.1.5 Zeta Potential Measurements (Chapters 4 and 5)

Zeta potential measurement cuvettes (Malvern DTS1070) were flushed once with ethanol, four times with distilled water, and then once with the media in which the measurement was to be made (either growth media or water). 1 mL of MOF suspension at a concentration of *ca*. 0.1 mg/mL was added to the cuvette, and the measurement was performed. Obtained data was analysed using the Malvern Zetasizer software.

2.3.2 MOF Stability Assessment (Chapter 3)

The stability of UiO-66 was studied by soaking 5 mg of MOF in 10 mL of various solvents and studying the resulting PXRD patterns 10 days later. Further information on the kinetics of degradation of UiO-66 was obtained by performing a degradation study in PBS. This was done by soaking 10 mg of activated UiO-66 in 500 mL of PBS at 37 °C and measuring the linker (i.e. BDC) release. All experiments were done in triplicate. A calibration curve for BDC was built using several concentrations of BDC in PBS in the range of 0–15 μg/mL. At each time point in the degradation study up to 24 h, the suspension was centrifuged; 1 mL of supernatant was taken out of the tube and replaced with 1 mL of fresh PBS. The absorbance of the collected sample was read on an absorbance microplate reader (SPECTROstar Nano, BMG Labtech, Aylesbury, Bucks, UK) at a wavelength of 240 nm, and the amount of BDC released was determined.

2.3.3 Drug/Biomolecule loading into MOFs (Chapters 3, 4, and 5)

2.3.3.1 Trehalose Loading into UiO-66 (Chapter 3)

40 mg UiO-66 were suspended in 40 mL of aqueous solutions of trehalose (Concentrations: 30, 50, 70, 100, and 500 mg/mL). The solutions were left to stir at room temperature for 4 days. After this loading period, the solutions were centrifuged at 5500 × g in a SIGMA 3-16PK Centrifuge for 20 min and the supernatant was discarded. The crystalline samples were then dried at 37 °C for 24 h.

2.3.3.2 Calcein Loading into MOFs (Chapters 4 and 5)

For *x*Zr-L1 samples with different particle sizes (Chapter 4), 25 mg MOF were dispersed in 10 mL of a methanolic calcein solution (1 mg/mL). The mixture was dispersed by sonication, and was then left under orbital shaking in an incubator at 37 °C for 4 days. After this loading period, the solutions were centrifuged at 5500 × g in a

SIGMA 3-16PK Centrifuge for 20 min and the supernatant was discarded. The MOF particles were washed 3–4 times with methanol until no further calcein was observed to be released. The crystalline samples were then dried at 37 °C for 24 h.

For Zr-L2−Zr-L6 particles (Chapter 4), 50 mg MOF were dispersed in 25 mL of a 1 mg/mL methanolic solution of calcein and left to shake at 37 °C for 1 day. The MOFs were harvested and washed as described for *x*Zr-L1 particles.

The amounts of loaded calcein were determined by taking 5 mg of calcein-loaded MOFs and soaking them in 1.5 mL PBS for 2 days until all the calcein was released. The total amount of released calcein was measured using UV-vis at a wavelength of 498 nm.

For DCA_5-UiO-66 and $TPP_{(++)}$@(DCA_5-UiO-66) (Chapter 5), 10 mg of MOF were dispersed in 5 mL of a methanolic solution of calcein (1 mg/mL), and left to stir at room temperature for 1 day. The MOFs were harvested and dried as described previously.

2.3.4 Drug/Biomolecule release from MOF (Chapter 3)

Release experiments were conducted over 1 day at 37 °C in an incubator. Samples of trehalose-loaded MOF were loaded into 1.5 mL Eppendorf tubes with 1 mL PBS. At each time point, samples were removed from the 37 °C shaking incubator, centrifuged at 16000 × g for 50 s, and the supernatant was collected for trehalose concentration measurement. The removed supernatant in the Eppendorf tubes was replaced with 1 mL fresh PBS, and the samples were placed back into the incubator at 37 °C until the following time point. Trehalose is a disaccharide that does not absorb light in the UV or visible range. In order to measure its concentration in solution, the anthrone assay was used. Concentrated sulphuric acid was used to dehydrate trehalose to form furfural. Furfural condensed with anthrone (10- keto-9,10 dihydroanthracene) to form a bluish-green complex which absorbs light at a wavelength of 620 nm. The colour formed when trehalose was treated with anthrone depended on the temperature and the time of heating, as well as the concentrations of sulphuric acid and anthrone used. Different acid concentrations, heating times, and volumetric ratios of anthrone to sample were tested. The following procedure was eventually used:

1 g of anthrone was dissolved in 100 mL of concentrated sulphuric acid. A stock solution of 1000 µg/mL trehalose in distilled water was prepared, and a range of

concentrations of 0–1000 μg/mL was set up. The anthrone solution and the standards were chilled in a fridge at 4 °C prior to use. 200 μL of chilled standard solution were mixed with 800 μL of anthrone solution (ratio 1:4) in an Eppendorf tube (Eppendorf UK Ltd., Cambridge, UK). All work was done on a rack of ice. The mixture was vortexed and then placed in a heating block at 100 °C for 20 minutes, after which the absorbance was read on a spectrophotometer at 620 nm. A standard curve was built and used to determine unknown trehalose concentrations.

2.3.5 Cell Culture (Chapters 3, 4, and 5)

2.3.5.1 Cell Line Maintenance

Cells were maintained at 37 °C and 5% CO_2 in high rich glucose (4500 mg/L) DMEM supplemented with 10% (v/v) FBS, 2 mM L-glutamine, 100 units/mL penicillin, and 100 μg/mL streptomycin, in a 75 cm^2 cell culture plate. This growth medium is termed complete growth medium in the remainder of the dissertation. The cells were passaged three times a week (at about 80 % confluence) by removing cell culture media, washing once with PBS, incubating with 1 mL of trypsin-EDTA for 5 min at 37 °C and 5 % CO_2, neutralising trypsin-EDTA activity by adding 5 mL of complete cell culture media, and then seeding the cells in a new 75 cm^2 plate at a density of 2.1×10^6 cells/cm^2.

2.3.5.2 Preparation of Frozen Cell Stocks

Cells were cultured and harvested by trypsinisation as described in Section 2.3.5.1. They were then counted using a haemocytometer. The cell suspension was then transferred to a 15 mL centrifuge tube and centrifuged at 1200 rpm for 5 min. The supernatant was discarded and the cell pellet resuspended in freezing medium (90 % FBS and 10 % DMSO) at a final concentration of 10^6 cells/mL. Aliquots of 1 mL of cells in freezing media were added to 2 mL cryogenic vials. Vials were then placed in a Nalgene freezing container (Rochester, NY, USA) at -80 °C overnight to provide a cooling rate of 1 °C/min, after which the vials were transferred to a liquid nitrogen tank at -196 °C.

2.3.5.3 Cell Thawing

Frozen cell stocks were removed from the liquid nitrogen bath and immediately placed in a water bath at 37 °C for rapid thawing. As soon as all the ice crystals had thawed, the cell suspensions were transferred a 15 mL centrifuge tube.

5 mL of complete growth medium were slowly added to the cell suspensions. The total solution was then transferred to tissue culture flasks (25 cm^2), and the cells were allowed to grow at 37 °C and 5 % CO_2 for 24 h, after which the media was replaced with fresh complete growth media. Cells were then maintained as described in Section 2.3.5.1.

2.3.6 MTS Cytotoxicity Assay (Chapters 3, 4, and 5)

The cytotoxicity of trehalose, DCA, and empty and loaded MOFs was investigated using the CellTiter 96® Aqueous Non-Radioactive Cell Proliferation Assay (Promega, UK). The day before the experiment, cells were seeded in a 96-well plate at a density of 10^4 cells/well. The following day, the different MOFs and drugs were dispersed in complete medium and a range of concentrations was prepared (0–1 mg/mL), of which 100 µL were added to each well and incubated for 4–72 h at 37 ºC with 5% CO_2. At the end of the incubation period, the treatment solutions were removed. The cells were washed once with PBS, and then 100 µL of fresh growth media was added to each well. To measure the toxicity, 20 µL of MTS solution were added to each well. The plate was then covered with aluminium foil, and placed at 37 ºC and 5% CO_2 for 75 min. Then, 100 µL of solution from each well were transferred to a new 96-well plate. The plate was read by UV/Vis spectroscopy (Spectro StarNano, BMG Labtech) at 490 nm.

2.3.7 Confocal Microscopy (Chapters 4 and 5)

2.3.7.1 Protocol for Lysosome Co-Localisation Experiments (Chapter 4)

HeLa cells were seeded in a NUNC™ imaging four-well plate at a density of 10^5 cells/mL (0.9 mL of a 1.1 x 10^5 cells/mL complete growth media solution) and incubated overnight at 37 ºC and 5% CO_2. The following day, cells were washed once with PBS, and incubated with 0.25 mg/mL of calcein-loaded MOFs in complete growth media for 2 h. Subsequently, cells were washed with PBS twice to remove the MOFs, and incubated with LysoTracker Deep-Red (50 nM) for another 30 min. Cells were then washed with trypan blue (0.4 %) to quench any external fluorescence, followed by three times with PBS. Then, fresh medium without phenol red was added to the cells (0.5 mL), and the four-well plate was imaged using a Leica TCS SP5 confocal microscope. The microscope was equipped with 405 diode, argon, and HeNe lasers. Laser excitation wavelengths used were 488 nm and 640 nm to excite the fluorescence emissions of

MOF and lysosomes respectively. Leica LAS AF software was used to process the images. The images were then analysed using a co-localization plug-in on ImageJ software (JaCOP) in order to determine the Manders' overlapping coefficient. This coefficient varies from 0 to 1, for non-overlapping signal to completely overlapping, respectively, and expresses the fraction of intensity in a channel that is located in pixels where there is above zero (or threshold) intensity in the other colour channel.

2.3.7.2 Protocol for Mitochondria Co-Localisation Experiments (Chapter 5)

MCF-7 and HEK-293 cells were seeded in a NUNC™ imaging four-well plate at a density of 5 x 10^4 cells/mL (0.9 mL of a 5.5 x 10^4 cells/mL complete growth media solution) and incubated overnight at 37 ºC and 5% CO_2. The following day, cells were transfected with 12 µL of CellLight® Mitochondria-RFP BacMam 2.0 and were allowed to continue growing for 16 h. After this, media was removed from the wells, and the cells were incubated for 2 h with 0.1 mg/mL of MOFs functionalised with a fluorescent variant of triphenylphosphonium (TPP). Subsequently, cells were washed with PBS twice to remove the MOFs, and 0.3 mL of 5 µM DRAQ5™ in PBS were added to each well. After 15 min incubation at room temperature in the dark, cells were imaged using a Leica TCS SP5 confocal microscope. The microscope was equipped with 405 diode, argon, and HeNe lasers. Laser excitation wavelengths used were 405 nm, 561 nm, and 640 nm to excite the fluorescence emissions of MOF, mitochondria, and DNA, respectively. Leica LAS AF software was used to analyse and process the images.

2.3.8 Super-Resolution Microscopy (Chapter 5)

(Work done in collaboration with Marcus Fantham from Professor Clemens Kaminski's group at the University of Cambridge)

MCF-7 cells were seeded in a NUNC™ imaging four-well plate at a density of 5 x 10^4 cells/mL (0.9 mL of a 5.5 x 10^4 cells/mL complete growth media solution) and incubated overnight at 37 ºC and 5% CO_2. The following day, cells were transfected with 12 µL of CellLight® Mitochondria-RFP BacMam 2.0 and were allowed to continue growing for 16 h. After this, media was removed from the wells, and the cells were incubated with 0.1 mg/mL of calcein-loaded MOFs in complete growth media for 0.5 h or 8 h. Subsequently, cells were washed with PBS twice to remove the MOFs, and 0.3 mL of 5 µM DRAQ5™ in PBS were added to each well. After 15 min incubation at

room temperature in the dark, cells were imaged using a custom built 3-color Structured Illumination Microscopy (SIM) setup that has previously been described[104]. The structured illumination patterns were generated by a spatial light modulator (SLM: SXGA-3DM, Forth Dimension Displays). A 60×/1.2NA water immersion lens (UPLSAPO 60XW, Olympus) focused the structured illumination pattern onto the sample. This lens also captured the samples' fluorescence emission light, which was imaged onto a sCMOS camera (C11440, Hamamatsu). Laser excitation wavelengths used were 488 nm (iBEAM-SMART-488, Toptica), 561 nm (OBIS 561, Coherent), and 640 nm (MLD 640, Cobolt), to excite the fluorescence emission of MOF, mitochondria, and DNA, respectively. Images were acquired using custom SIM software previously published[104]. Nine raw images were collected at each plane and recombined using a custom implementation of fairSIM[105].

2.3.8.1 Image Analysis (Chapter 5)

(Work done by Marcus Fantham from Professor Clemens Kaminski's group at the University of Cambridge)

Visualisation of cells reconstructed in 3D was performed with FPBioimage (Fantham & Kaminsky – 2017), and can be accessed online at http://aam.ceb.cam.ac.uk/mitoMOF.

Mitochondria eccentricity was assessed using a custom designed pipeline for Cell Profiler[106]. Briefly, the tool performed the following actions: Extract the mitochondria channel from the central slice of the reconstructed SIM image; apply a median filter window size 7 to remove elements of noise; run the 'IdentifyPrimaryObjects' plugin to extract mitochondria as objects from the image; run the 'MeasureObjectSizeShape' plugin to gather statistics on detected objects; filter objects with an area less than 20 pixels (34 μm^2); export filtered mitochondria objects to a spreadsheet. The eccentricity column was exported from the spreadsheet for further statistical analysis. The one-way ANOVA test was performed using GraphPad Prism version 7.04 for Windows to assess the statistical difference of mitochondria eccentricity between different experimental conditions.

2.3.9 Flow Cytometry (Chapters 4 and 5)

In all flow cytometry experiments, cells were seeded in a 24-well plate at a density of 5 x 10^4 cells/well and allowed to grow for 24 h at 37 ºC and 5 % CO_2. After

that, cells were incubated with 0.5 mL of solution containing the appropriate treatment for the appropriate amount of time, depending on the experiment. After incubation with the treatment solutions, media was aspirated from the wells and the cells were washed twice with PBS. The cells were then harvested by adding 0.1 mL of trypsin-EDTA and incubated for 5 min at 37 ºC and 5 % CO_2. The trypsin was neutralised by the addition of 0.4 mL of complete growth media, and the solutions were transferred to Eppendorf tubes. Cells were recovered by centrifugation at 1200 rpm for 5 min, and re-suspended in 100 µL of growth media without phenol red. Finally, the samples were analysed in a Cytek DxP8 analyser cytometer within 30 min. Analysis of the data was done using FlowJo software.

2.3.9.1 Energy Dependence of Uptake Protocol (Chapters 4 and 5)

After seeding the cells and allowing them to grow for 24 h as described in Section 2.3.9, cells were pre-treated with 0.5 mL of growth media at either 37 ºC or 4 ºC for 30 min. After this period, 0.7 mL of a 0.5 mg/mL solution of calcein-loaded MOF in growth media was added to the wells, and the cells were incubated for a further 1.5 h. Following treatment, the cells were collected and analysed as described in Section 2.3.9.

2.3.9.2 Endocytosis Inhibition Protocol (Chapters 4 and 5)

After allowing cells to grow for 24 h as described in Section 2.3.9, cells were pre-treated with 0.5 mL of sucrose (102.7 mg/mL, 0.3M), chlorpromazine (31.9 µg/mL, 100 µM), nystatin (0.250 mg/mL, 0.27 mM), and rottlerin (2.6 µg/mL, 5 µM), for 30 min at 37 ºC. After this period, 0.7 mL of a 0.5 mg/mL solution of calcein-loaded MOF in growth media was added to the wells, and the cells were incubated for a further 1.5 h. Following treatment, the cells were collected and analysed as described in Section 2.3.9.

2.3.9.3 Cellular Uptake Efficiency Protocol (Chapter 4)

After seeding the cells and allowing them to grow for 24 h as described in Section 2.3.9, cells were incubated with 0.7 mL of a 0.5 mg/mL solution of calcein-loaded MOF for 2 h. Free calcein in an amount equivalent to the one loaded in the MOFs was used as a control. Following treatment, the cells were collected and analysed as described in Section 2.3.9.

2.3.10 Microarray (Chapter 5)

2.3.10.1 RNA extraction

MCF-7 cells were seeded in 12-well plates at a density of 10^5 cells/well, and were allowed to grow overnight at 37 ºC and 5 % CO_2. The media was then aspirated, and replaced with 1 mL of a 0.25 mg/mL solution of MOF or free DCA. Cells were incubated for 72 h, after which the wells were washed twice with PBS, and the RNA was extracted using QIAGEN's RNeasy RNA Extraction Mini Kit following the manufacturer's instructions. The RNA concentration was adjusted to 50 ng/mL, and the solutions were used for microarray analysis.

2.3.10.2 Array Processing

(Work done by Cambridge Genomic Services, University of Cambridge)

RNA was assessed for concentration and quality using a SpectroStar (BMG Labtech, Aylesbury, UK) and a Bioanalyser (Agilent Technologies, Cheadle, UK). Microarray experiments were performed at Cambridge Genomic Services, University of Cambridge, using a species specific Gene 2.1 ST Array Plate (Affymetrix, Wooburn Green, UK) in combination with WT PLUS amplification kit (Affymetrix) according to the manufacturer's instructions. Briefly, 100 ng Total RNA was amplified along with inline PolyA spike in control RNA, using the WT PLUS amplification kit (Affymetrix). Successfully amplified samples were labelled using the GeneChip WT terminal labelling kit (Affymetrix) using the in line hybridization controls. Plate arrays were processed on the GeneTitan instrument (Affymetrix) using the GeneTitan Hybridization, Wash and Stain kit (Affymetrix). Samples were hybridized to the array, washed, stained and scanned using the array specific parameters provided by Affymetrix. Finally basic visual quality control was performed using Command Console Viewer (Affrymetrix) prior to bioinformatic quality control.

2.3.10.3 Bioinformatics

(Work done by Cambridge Genomic Services, University of Cambridge)

GCCN-STT correction was applied to the raw data using the Affymetrix powertools in order to correct probes for GC content bias and adjust the dynamic range of the array to give better spread of intensity in order to identify differentially expressed genes. After scanning the files generated by the scanner (CEL files), GCCN-STT corrected files were loaded in R using the oligo package from bioconductor[107]. No

background correction or normalisation was applied at this stage. In order to assess the quality of the data, plots of the control probes were generated along with boxplot, MAplot and intensity distribution plot. Variation within biological replicates was also investigated using clustering methods. The raw data was then processed using the Robust Multichip Analysis (RMA) method[108]. The data was background corrected, normalised using quantile, and summarized. Once the data was processed, the comparisons were performed using the limma package[109] and the results corrected for multiple testing using False Discovery Rate (FDR)[110].

3 Intracellular Delivery of Trehalose for Cryopreservation Applications

3.1 Introduction

Cryopreservation is the process of preserving biological material by freezing at extreme temperatures, most commonly -196 °C. Unprotected freezing is normally lethal, and a cryoprotective agent (CPA) is required to protect cells from freezing stresses. This chapter seeks to investigate the use of UiO-66 as a vehicle to encapsulate and intracellularly deliver trehalose, a naturally-occurring disaccharide able to protect cells from freezing stresses during cryopreservation. Section 3.1.1 describes the challenges and stresses that cells face during cryopreservation. Section 3.1.2 describes how CPAs can protect cells from these freezing stresses, and specifies how toxicity is their main drawback. Section 3.1.3 details how trehalose acts as a safe CPA when present inside cells.

3.1.1 Cryopreservation Process and Challenges

Cryopreservation consists of freezing cells, proteins, or other biological material to sub-zero temperatures. This process allows the preservation of cells for

prolonged periods of time by halting all biological activity, including the biochemical reactions that lead to cell death and DNA degeneration. Preserving cells in a stable state is a fundamental requirement in biological and medical science, agriculture, and biotechnology, as it enables standardisation of experimental work over time, and secures lifesaving banks of cells and tissue ready for transplantation at the time of need[111].

However, experimental findings show that the preservation process itself can damage cells, as they are put under significant stress at sub-zero temperatures. The challenge to cells during freezing is not their ability to withstand storage at extremely low temperatures; rather, it is the lethality of an intermediate zone of temperature (-5 °C to -60 °C) through which they have to pass twice: once during freezing, and once during thawing[112]. During freezing, the series of physical events that takes place in and around the cells is as follows: as the cells are cooled to -5 °C, both the extra- and intracellular media remain unfrozen. Between -5 °C and -15 °C, ice only forms in the external medium because the plasma membrane blocks the growth of ice crystals into the cytoplasm. As a result, cells tend to become supercooled, even in the presence of external ice[113]. As the temperature is decreased further, the supercooled water inside the cells has a higher chemical potential than the water in the partially frozen and hence more concentrated external medium. This drives the water to diffuse out of the cell, and to freeze externally. The subsequent physical events occurring in the cells between -15 °C and -60 °C depend on the cooling rate and directly affect their survival. Mazur *et al.* put forward the "Two-factor hypothesis" to describe the interrelationship between the cooling rate and cryosurvival, and to propose mechanisms for the injury that occurs to cells during cryopreservation[113].

The first factor in Mazur's hypothesis relates to the formation of intracellular ice. If the cooling rate is sufficiently low or the permeability of the cell to water sufficiently high, water can move down the chemical potential gradient from the more dilute intracellular solution to the concentrated extracellular medium[114], as illustrated in **Figure 3.1**. If, however, the cooling rate is too high or the permeability of the cells too low, intracellular water is not lost fast enough to maintain equilibrium and accumulates inside the cells. The cells subsequently attain osmotic equilibrium by freezing intracellularly. This formation of ice crystals within the cells causes lethal mechanical injury to the cell membrane and intracellular components. The second factor in Mazur's hypothesis relates to the concentration of solutes in and around the cells. This is also

highly dependent on the cooling rate. When the cooling rate is too low, cells are lethally damaged even though intracellular ice formation is avoided. This is because the cells are exposed to major alterations in the intra- and extracellular solutions over long periods of time, before they eventually reach the glassy state in which they will be stored. As ice crystals grow in the extracellular environment, the solutes surrounding the cells become increasingly concentrated in an ever-decreasing solvent volume. This freeze-dehydration causes a number of deleterious events known as solution effects, and include dehydration, extreme volume shrinkage, changes in pH, and the precipitation of solutes. These solution effects cause changes in the structure of cell membranes, loss or fusion of membrane bilayers, and organelle disruption[114]. Karow and Webb explain solution effects injury as a consequence of the extraction of bound water from intracellular components for incorporation into ice crystals, ridding proteins of lattice-arranged bound water essential to the integrity of their structures[115]. CPAs can help to overcome the discussed challenges arising from the formation of intracellular ice and solution effects.

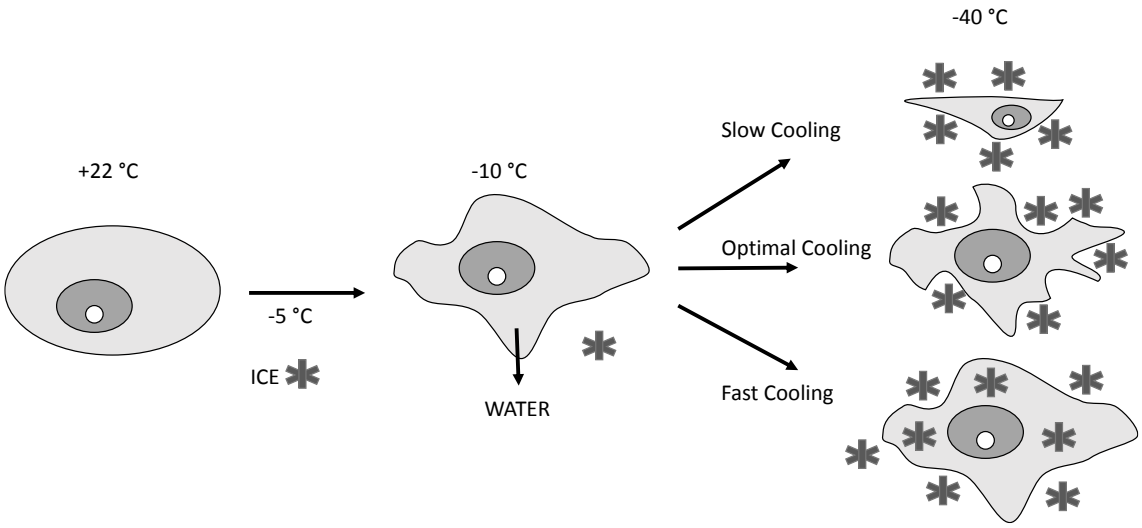

Figure 3.1. Schematic drawing of physical events and mechanisms of cryoinjury during freezing. Adapted from *Gao & Critser*[112].

3.1.2 Necessity of Cryoprotective Agents (CPAs)

The cooling rate is one key factor that determines the extent of injury cells will undergo during freezing. The optimal cooling rate for cells should be low enough to avoid lethal intracellular ice formation but high enough to minimise exposure time to solution effects. However, cooling at the optimal rate is not enough to provide protection to cells. Most cells also require the presence of a CPA[116]. A number of

hypotheses have been put forward as to how CPAs protect cells during freezing. Their mode of action is likely to be multi-factorial, with their main protective action being their ability to prevent the excessive concentration of electrolytes that otherwise occurs during the freezing process. At sub-zero temperatures, ice crystals form and the solutes become confined to a decreasing volume of solution. The total solute concentration in the unfrozen portion is solely determined by the sub-zero temperature[117]. Consequently, if the only constituent of the freezing medium is electrolytes, salt concentrations will reach very high levels as the temperature decreases and ice crystals form. In contrast, in a medium that contains electrolytes in addition to a large proportion of non-electrolytes, the salt concentration will be much lower. This could prevent the attainment of the critical salt concentration at which damage occurs whilst the whole system is sufficiently cooled to reach a 'glassy matrix'[114]. This is the main way that CPAs offer protection to cells.

There are two types of CPAs: permeating and non-permeating. When CPAs are non-permeating, they only affect the extracellular salt concentration. This can impose osmotic stresses on the cells even before freezing. Trehalose is an example of a non-permeating CPA. On the other hand, when CPAs are permeating, they affect both the extra- and intracellular salt concentrations[118]. When cells are put in a hypertonic permeating CPA solution, water exits the cells and its volume shrinks. However, the CPA also enters the cells, and after a brief period of equilibration, the normal cell volume is restored. The osmotic stress imposed by the permeating CPA is therefore much less than that imposed by the non-permeating one. In addition, when a high concentration of permeating CPA is used, part of the extracellular and intracellular water is replaced by the CPA. Hence, the amount of ice formed is lower[119], the non-frozen fraction remains larger, the cells suffer less volume shrinkage, and the electrolyte concentration in the freezing medium and in the cells remains lower than what it would be in the absence of the CPA[114]. This is the primary mechanism by which permeating CPAs offer cryoprotection. Permeating CPAs operate on a colligative basis, meaning that it is not the nature of the CPA but its concentration relative to the solutes inside and outside the cells that matters[120]. Any molecule can act as an effective permeating CPA provided that it is inherently non-toxic at high concentrations, has a low molecular weight, is highly soluble in aqueous electrolyte solutions, and has the ability to permeate cells[121]. Molecules with such properties are rare, with some common examples being glycerol, dimethylsulfoxide (DMSO), and ethylene glycol.

As mentioned above, CPAs at high enough concentrations should be able to suppress all types of freezing injury. In practice however, the toxicity of these CPAs acts as a key limiting factor, preventing the use of fully protective levels of additive[122]. Currently, dimethyl sulfoxide (DMSO) is the most widely used CPA. However, there have been a number of toxicity issues reported with its use. DMSO has been found to significantly decrease the viability of adult and embryonic stem cells[123,124], as well as alter the genome-wide methylation profile of cells[125]. Several studies have found that transplants with DMSO-cryopreserved stem cells cause side-effects in patients[126]. The overall incidence of DMSO toxicity is approximately 1 in 70 transplants and most cases are cardiovascular or respiratory in nature[127]. Some of these toxic side-effects include severe neurotoxicity[128], respiratory depression[129], and epileptic seizures[130]. Less severe side effects such as nausea, vomiting, and abdominal cramps are seen in up to 50 % of patients[127]. DMSO toxicity can be overcome by washing cells prior to implantation, but the additional wash steps cause cells to be lost and significantly increase the complexity of the cell delivery method[131]. In addition, washing the cells does not completely eliminate the risk of toxicity due to residual DMSO. A crucial need therefore exists for biocompatible and non-toxic CPAs that would eliminate the wash step altogether, saving time and resources.

3.1.3 Trehalose as a CPA

Trehalose is a non-reducing disaccharide in which the two glucose units are linked in an α-α-1,1,-glycosidic linkage. It is classified as a kosmotrope, meaning that the interaction between trehalose and water is much stronger than the interaction between two water molecules. This gives trehalose very useful cryoprotective properties. This naturally encountered sugar is found in extremely high concentrations in organisms capable of surviving dehydration. In cysts of brine shrimp, trehalose represents approximately 15 % of the dry weight of the embryos[132]. *Aphelenchus avenae*, a species of nematode, converts as much as 20 % of its dry weight into trehalose when dehydrated[133]. Other species that produce trehalose include bacteria, yeast, and tardigrades[134]. Mammals however are unable to produce trehalose endogenously and are therefore unable to survive the stresses of freezing and dehydration[135].

The exact mechanism by which trehalose provides protection during freezing and dessication is not completely understood, but a number of hypotheses have been put

forward to explain its remarkable properties. Vitrification theory (**Figure 3.2A**) states that trehalose forms a glassy matrix and physically shields proteins and cells from injury. Preferential exclusion theory (**Figure 3.2B**) states that trehalose restructures water around itself and away from the protein, decreasing its hydrated radius, and also decreases the availability of freezable water. Water replacement theory (**Figure 3.2C**) states that trehalose replaces water and directly interacts with the protein by forming hydrogen bonds, maintaining the three-dimensional structure and stabilising biomolecules[135]. These theories provide explanations for trehalose's remarkable role in the stabilisation of the bilipid membrane and intracellular proteins[136], as well as in the prevention of the formation of ice[135].

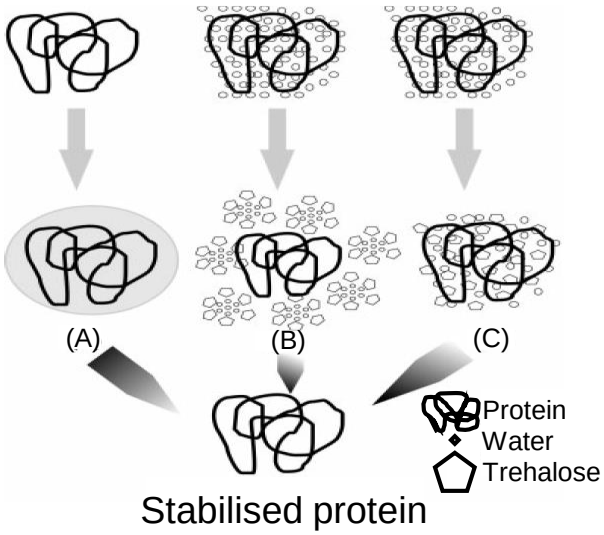

Figure 3.2. Various theories to explain the mechanism of action of trehalose: (A) vitrification theory, (B) preferential exclusion theory, and (C) water replacement theory. Adapted from Jain & Roy[135].

Several studies have demonstrated that trehalose effectively protects nucleated mammalian cells when used at intracellular concentrations between 100 mM and 200 mM[137–139]. However, its main drawback is that it does not readily permeate cells, with only low concentrations (< 0.5 %) being absorbed by passive diffusion or active endocytic mechanisms[140]. Efforts have therefore focused on finding ways to deliver trehalose inside the cell. Eroglu *et al.* used a genetically engineered mutant of *Staphylococcus aureus* α-hemolysin to create pores in the cellular membrane. These engineered pores are capable of being toggled between an open and closed state by the addition of micromolar concentrations of Zn^{2+} ions[137]. Using an extracellular

concentration of 200 mM trehalose in the freezing medium, they were able to successfully recover more than 70 % of cells post-thaw. Beattie *et al*. successfully introduced small concentrations of trehalose into pancreatic islet cells by taking advantage of a membrane phase transition at low temperatures. By cryopreserving with a combination of trehalose and DMSO, the recovery of cells was much higher than with DMSO alone (92 % vs 58 % respectively)[141]. Lynch *et al*. used an amphipathic polymer to permeabilise the cell membrane of erythrocytes and introduce trehalose into the cells[22]. Other studies have demonstrated the loading of trehalose by fluid-phase endocytosis[142], microinjection[138], and internal trehalose synthesis *via* genetic engineering[143]. Holovati *et al*. introduced trehalose inside erythrocytes using trehalose-loaded liposomes[144]. Other attempts were made using osmotic and thermal shock[145]. However, intracellular concentrations in erythrocytes in all the studies did not exceed 50 mM, which is below the threshold necessary for cryosurvival.

This chapter aims to investigate the use of UiO-66 as a potential intracellular delivery system for trehalose, which is unable to permeate cells on its own. Synthesis of the trehalose delivery system and its characterisation were performed, and subsequent biocompatibility studies were performed using the MTS viability assay. After the completion of these initial assessments, the system was tested as a CPA on HeLa cells.

3.2 Collaborative Work

SEM was performed at the Department of Physiology, University of Cambridge by Dr. Jeremy Skepper.

3.3 Results & Discussion

3.3.1 Synthesis and Characterisation of Trehalose Delivery System

UiO-66 was synthesised and activated following the protocol outlined in **Section 2.2.1.1**. PXRD studies were then performed on the resulting material in order to confirm successful synthesis. **Figure 3.3** shows the PXRD pattern for the synthesised UiO-66 compared with the pattern predicted from single crystal structures using Mercury software[146]. The positions of the main peaks in the synthesised structure at $2\theta = 7.4°$, 8.6°, and 12.1° perfectly matched those in the simulated structure. Additionally, other observable peaks above $2\theta = 12.1°$ were also in agreement with the simulated structure, indicating successful synthesis of UiO-66. The results also demonstrated that the crystal structure of UiO-66 was maintained after being exposed to the activation temperature of 80 °C for 48 hours, consistent with its reported thermal stability[59,96,147].

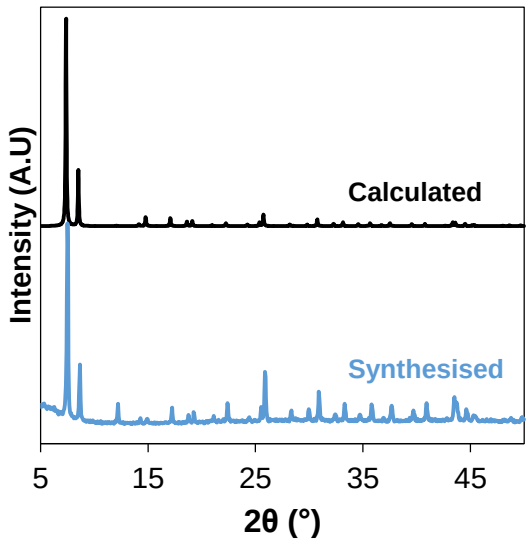

Figure 3.3. PXRD patterns of synthesised UiO-66 (blue) compared with the calculated patterns (black).

The particle size distribution of UiO-66 was investigated using SEM images of the synthesised materials, shown in **Figure 3.4**. The mean particle size and standard deviation were determined averaging across 100 particles. The average diameter of the particles was 136 ± 27 nm, which is within the size that cells can take up[148], indicating the suitability of the NPs as an intracellular delivery system. The colloidal stability of UiO-66 particles suspended in PBS and cell culture media was also assessed using DLS.

The measured hydrodynamic diameter reflects the dimension of the NP together with the layer of surface-bound solvent. The average particle size in PBS was 19432 ± 132 nm, which is significantly larger than the sizes determined from SEM images. This indicates that the synthesised UiO-66 particles tend to aggregate in PBS. For UiO-66 particles in cell culture media however, the average particle size was 206 ± 15 nm. The likely reason for their lower susceptibility to aggregation compared to PBS is the formation of a "protein corona" on the external surface of the MOF particles, resulting from the adsorption of different kinds of proteins from the growth media[149].

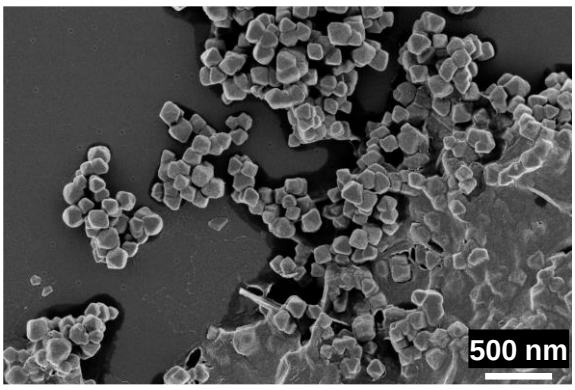

Figure 3.4. SEM image of synthesised UiO-66 particles. Scale bar shown on image.

In order to assess the chemical stability of UiO-66 in PBS and water, the particles were soaked in both solvents for 9 days, after which their crystallinity was measured using PXRD. Stability in aqueous media for extended periods of time is important as the loading process is done by soaking the MOFs in a solution of trehalose over a period of 4 days. **Figure 3.5** shows the measured PXRD patterns of the solvent-soaked UiO-66 as well as the as-synthesised particles for comparison. The main diffraction peaks of UiO-66 at 2θ of 7.4°, 8.6°, and 12.1° were present in the water-soaked material, confirming the material maintained its crystallinity after 9 days in water. For the PBS-soaked UiO-66 however, all the main peaks were absent. This indicates that the material was therefore amorphous after soaking in PBS for 9 days, likely due to the degradation and collapse of the MOF framework.

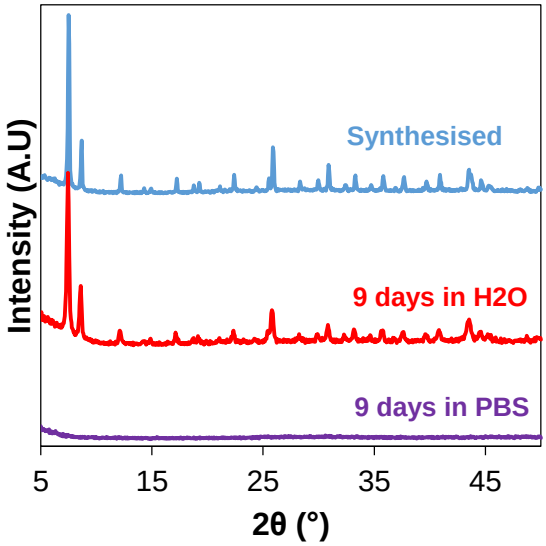

Figure 3.5. PXRD patterns of synthesised UiO-66 (blue), UiO-66 soaked in water for 9 days (red), and UiO-66 soaked in PBS for 9 days (purple).

The degradation of UiO-66 in PBS was further studied by investigating the release of organic linker, terephtalic acid (BDC), from the structure over time. For that, a calibration curve for BDC in PBS was prepared, and is shown in **Figure 3.6a**. Ideally, release studies should be done under sink conditions using a sheer volume of solvent, usually about 5 to 10 times greater than the volume present in the saturated solution. Otherwise, when the concentration gets close to saturation, the dissolution rate decreases significantly, which could falsely lead to conclude that the release is slower than what it actually is. The release study was done such that the total amount of BDC that could potentially be released (5.9 mg) would not saturate the solution (500 mL). The maximum concentration that could potentially be reached was 11.8 µg/mL, whereas the saturation concentration of BDC is 15 µg/mL. It was expected that at every time point, the concentration of BDC would be less than 5 times the saturation concentration, and that sink conditions would be satisfied. The percentage by weight of linker released from UiO-66 over time is shown in **Figure 3.6b**. After the first time point at 30 minutes, *ca.* 85 % of the BDC was already released from the structure, after which no further release was detected. These results show that degradation of the structure occurred at a time point less than 30 minutes. The high concentration of BDC at the first time point meant that the experiment was not done under sink conditions, and that the effective release rate was probably even faster, further pointing towards a very rapid degradation of the UiO-66 structure. Other studies have found similar results, showing that PBS leads to a rapid framework collapse of the MOFs due to the replacement of the

carboxylate linkers by phosphate groups present in the PBS solution[6,70,150–153]. UiO-66 in particular might be very prone to fast degradation in PBS due to the strong affinity of Zr atoms for phosphate groups. Interestingly, the total amount of linker released corresponds to *ca.* 90 % of the expected weight of linker present in the sample of UiO-66. Additional experiments were performed to determine whether partial release occurred due to some linker molecules still being attached to the framework, or whether there were ligands missing in the starting structure.

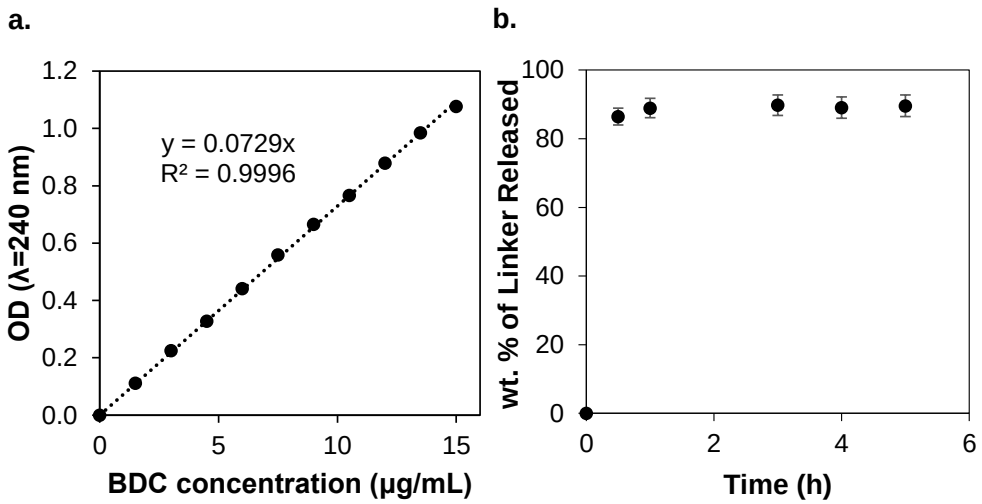

Figure 3.6. (a) Calibration curve for BDC in PBS and (b) linker release from UiO-66 in PBS with time. Error bars represent the standard error of three replicates.

In order to determine whether the synthesised UiO-66 had missing linkers in the framework, thermal gravimetric analysis (TGA) of UiO-66 was performed. **Figure 3.7** shows the TGA plot of UiO-66 between 450 °C and 550 °C. There was a significant weight loss due to the loss of benzene rings between 450 °C and 530 °C, and the sample was left with 46 % of the original weight. It is known that loss of benzene fragments occurs at 500 °C and is completed by 550 °C[61], which means that the residual material at the end of the TGA experiment was ZrO_2. If there were 12 BDC ligands attached to the $Zr_6O_4(OH)_4$ cluster, a weight loss of 59.5 % would have been observed. The actual weight loss between the dehydrated and desolvated UiO-66 and the residual ZrO_2 was approximately 54 %. This suggests that the as-synthesised material is slightly defective, having about 11 ligands per inorganic $Zr_6O_4(OH)_4$ cluster. This is consistent with the results of the linker degradation in PBS in which 90 % of the expected linker was released into solution.

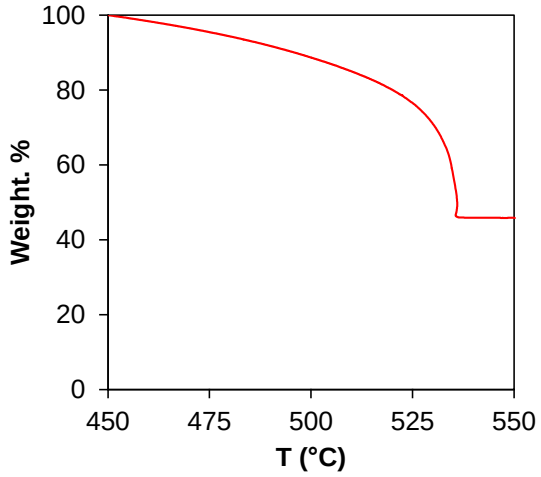

Figure 3.7. TGA plot of desolvated UiO-66 between 450 ◦C and 550 ◦C.

3.3.2 Loading and Release of Trehalose from UiO-66

In order to load trehalose into UiO-66, the synthesised NPs were soaked in aqueous trehalose solutions of varying concentrations (0–500 mg/mL) for 4 days, after which they were collected by centrifugation and dried. The crystallinity of the loaded UiO-66 was checked by PXRD. **Figure 3.8a** shows the patterns for the trehalose-loaded UiO-66, the UiO-66 pattern predicted from single crystal structures, and the pattern for free trehalose. All the main peaks associated with UiO-66 were present in the PXRD patterns, confirming that UiO-66 crystallinity was not affected during the loading procedure at all loading concentrations. At the highest trehalose concentration of 500 mg/mL, some small additional peaks were visible at 2θ of 12.5°, 13.8°, and 15.1° among others (**Figure 3.8b**). These peaks occurred at the same positions as some of the peaks of the crystalline trehalose material. They indicate that some trehalose is crystallising on the outer surface of the material. Trehalose is hypothesised to be mostly confined to the external surface of the UiO-66 NPs due to it being too large (6–10 Å) to fit through the UiO-66 windows (5–7 Å). It is also noteworthy that the characteristic peaks of UiO-66 shifted slightly to the left as it was soaked in increasingly concentrated trehalose solutions (**Figure 3.8b**). This suggests a slight flexibility of the UiO-66 framework. Based on the positions of the peaks, the dimensions of the UiO-66 cubic crystal structure can be calculated. The empty UiO-66 material had a unit cell length of 20.5 Å, and increased with increasing loading concentrations up to 2 % of the original length (i.e. 20.9 Å) for the material loaded in 500 mg/mL of trehalose.

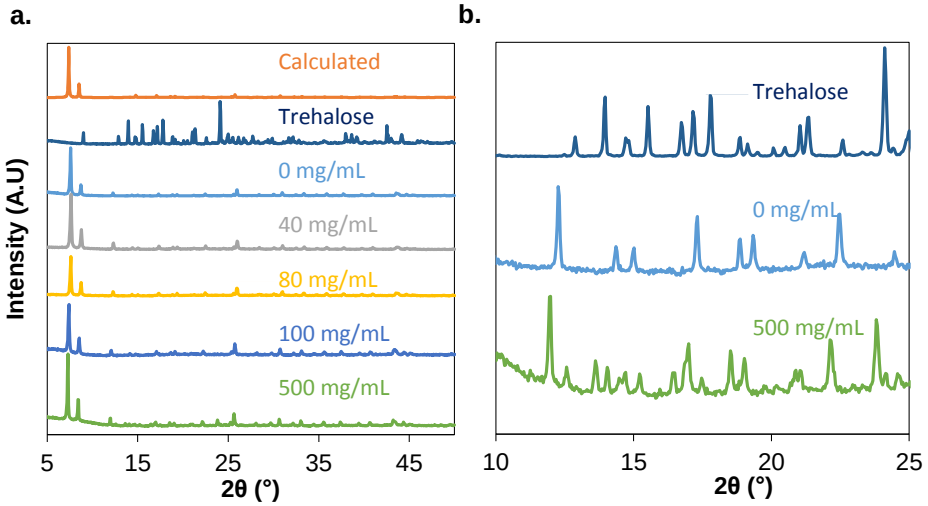

Figure 3.8. (a) PXRD patterns of trehalose, calculated UiO-66, and UiO-66 loaded in solutions with different trehalose concentrations, and (b) magnified portion of the curves between the angles of 10° and 25°.

The amount of trehalose loaded in the different samples was estimated using TGA. Plots for trehalose, empty UiO-66, and loaded UiO-66 are shown in **Figure 3.9**. All MOF weights were normalised to their dehydrated and desolvated forms, meaning that the weights after loss of solvent were set at 100 %. The weight of trehalose was normalised to that of its dehydrated form. The temperature range shown in the graph is between 170 °C and 600 °C. Empty UiO-66 displayed a significant weight loss due to the loss of benzene rings between 450 °C and 530 °C, and the sample was left with 41 % of the original weight. Pure trehalose dihydrate exhibited two distinct weight losses. The first one, of approximately 9.7 % between 60 °C and 100 °C (not shown on graph), corresponds to the dehydration of the trehalose. This weight loss compares well to the expected 9.5 %, which equates to two molecules of water per molecule of trehalose. The second weight loss occurred between 220 °C and 600 °C and can be attributed to the degradation of trehalose[154]. The trehalose-loaded MOFs displayed three different weight losses that can be attributed to three different events. Between 30 °C and 150 °C, the different solvents evaporated (not shown on graph). Between 220 °C and 450 °C, the trehalose degraded. Between 450 °C and 550 °C, the remaining trehalose degraded and the organic linker was lost. The degree of weight loss increased with increasing trehalose loading concentration, indicating higher amounts of adsorbed trehalose. This amount can be estimated by comparing the weight losses of loaded UiO-66 to that of dry and empty MOF ─ specifically, by comparing the relative amounts of ZrO_2 left after degradation of the structure. The trehalose weight loadings

were calculated and ranged from 4 wt % for UiO-66 loaded in 30 mg/mL trehalose to 56 wt % for UiO-66 loaded in 500 mg/mL trehalose.

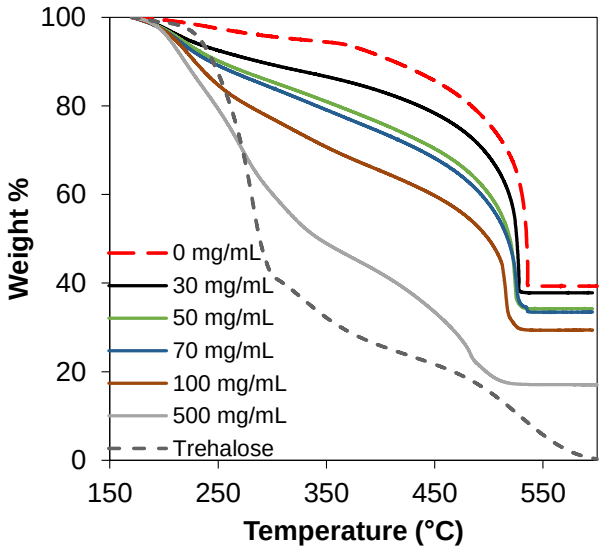

Figure 3.9. TGA plots of trehalose, empty UiO-66, and trehalose-loaded UiO-66 prepared by soaking UiO-66 in different concentrations of aqueous trehalose solutions ranging from 30 to 500 mg/mL. Dashed red and grey lines represent empty UiO-66 and free trehalose respectively. Solid lines represent trehalose-loaded UiO-66.

To corroborate the results of the TGA measurements, the weight loading of trehalose was also determined by soaking trehalose-loaded MOFs in water under stirring for 48 h and measuring the concentration of trehalose in the supernatant after its complete release using the anthrone method, as laid out in Section 2.3.4. To ensure that all the trehalose was released, the MOFs were harvested by centrifugation and re-suspended in fresh water at the end of the experiment. No additional trehalose was released. **Figure 3.10a** shows the calibration curve used to determine trehalose concentrations by the anthrone method. The values were calculated and ranged from 4 to 50 % for loadings done in 30 mg/mL and 500 mg/mL trehalose respectively. An adsorption isotherm was then built to show trehalose weight loading as a function of equilibrium concentration and is shown in **Figure 3.10b**. Both the loadings determined from TGA and from the release experiment were used for comparison. The values determined using both methods were generally in good agreement. Data points between 120 mg/mL and 500 mg/mL would give a better understanding of the shape of the liquid adsorption isotherm, but have not been performed in this study. UiO-66 loaded in 500 mg/mL trehalose was used for the remainder of the studies. Its high loading

(*ca*. 50 wt %) can be useful to deliver large amounts of trehalose inside cells while using a minimal amount of MOF, to allow to reach the required intracellular concentration of 100-200 mM for efficient cryoprotection.

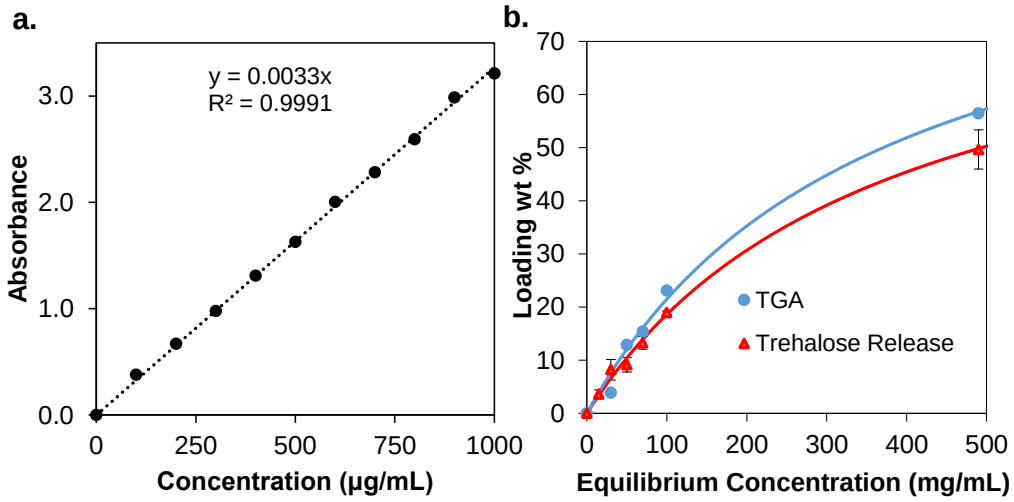

Figure 3.10. (a) Calibration curve used to determine trehalose concentrations using the anthrone method, and (b) liquid-phase adsorption isotherms of trehalose onto UiO-66 determined using data from TGA (blue) and from measuring the concentration of trehalose into the supernatant after complete release in water (red). Error bars represent the standard error of three replicates. When not visible, error bars are too small to be seen.

In order to be suitable for cryopreservation applications, a rapid release of trehalose from the delivery system is required after cellular uptake. In order to study the release of trehalose over time, loaded UiO-66 particles were soaked in PBS, and the trehalose concentration in the supernatant measured at every time point using the anthrone method. PBS is a simple and suitable model for the study, given that similar drug release kinetics were obtained in PBS and in other more complex phosphate media such as cell culture medium supplemented with foetal bovine serum[71]. **Figure 3.11** shows the weight percentage of trehalose released as a function of time. Trehalose release was very fast, with 50 % being released within the first 45 minutes. At 2 h, 80 % of the trehalose was already released, and complete release occurred within 5 hours. The 100 % value in **Figure 3.11** is the experimental value at which no more trehalose release was observed. Slower release would have been expected had trehalose had to diffuse out from within the pores of UiO-66. This fast release further supports the hypothesis that trehalose is mostly adsorbed to the external surface of UiO-66. The hydroxyl and ether groups of trehalose are capable of forming strong hydrogen bonds with the polar functions of UiO-66, such as Zr-OH, and it is hypothesised that this is

how trehalose molecules attach to the external surface of UiO-66, and how they attach to one another. Interestingly, trehalose release was slower than the release of BDC from the UiO-66 structure (**Figure 3.6b**). This could be due to trehalose protecting the MOF surface from attack by the phosphate groups present in PBS. Another explanation could be that the phosphate groups attack the Zr nodes and create an amorphous solid to which trehalose can get adsorbed. In summary, the release study showed that UiO-66 is a suitable candidate for intracellular trehalose delivery.

Normally, one of the desired characteristics of a drug delivery system is its ability to offer controlled release of the entrapped drug. The general tendency has been to increase the release time as much as possible to improve the pharmacokinetics of a drug and reduce the frequency of dosing. Release times in literature have ranged from a couple of hours to a couple of days, with some releases even reaching 30 days[147,155]. However, such long release times are not required in cryopreservation applications, as the goal is to get the delivery system inside the cell and then unload the CPA rapidly. Cells should however be able to take up the loaded MOFs before all the trehalose is released. The exact mechanism of cellular uptake is currently still not known and will further be explored in Chapter 4. However, HeLa cells are known to take up particles with sizes less than 200 nm by endocytosis[46], which in some cases has been shown to occur within a couple of minutes[156]. Trehalose is not completely released from UiO-66 until after 3 h. It is thus very likely that HeLa cells take up the loaded UiO-66 while there is still a significant amount of trehalose loaded.

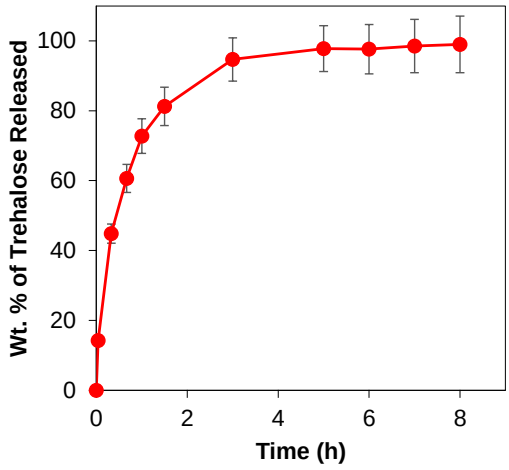

Figure 3.11. Trehalose release from UiO-66 as a function of time. Error bars represent the standard error of three replicates.

3.3.3 In Vitro Testing of Biocompatibility and Cryoprotective Effect

For a biomolecule delivery vehicle to be used in live cells, biocompatibility is a crucial factor to examine. To evaluate the potential use of UiO-66 as a delivery vector for trehalose to the intracellular medium, *in vitro* viability assays were conducted on HeLa cells. The cytotoxicity of UiO-66 and trehalose were evaluated using a 3-(4,5-dimethylthiazol-2-yl)-5-(3-carboxymethoxyphenyl)-2-(4-sulfophenyl)-2H-tetrazolium (MTS) assay. The assay is based on the reduction of MTS tetrazolium compound by viable cells to generate a coloured formazan product. This conversion is thought to be carried out by NAD(P)H-dependent dehydrogenase enzymes in metabolically active cells. HeLa cells were incubated with the MOF and trehalose for 24 h. The results of the MTS assay are shown in **Figure 3.12.** Treatment of the cells with trehalose did not lead to cell death after 24 h incubation with concentrations up to 7.5 mg/mL (**Figure 3.12a**). At 37.5 mg/mL, a moderate decrease in viability was visible (*ca.* 67 %). Concentrations higher than 37.5 mg/mL, or 100 mM, put the cells under great osmotic stress and caused their viability to decrease to near zero levels compared to the untreated control. With UiO-66 (**Figure 3.12b**), cells remained viable up to concentrations of 1.33 mg/mL, after which they started losing viability. From the viability results it is clear that it is the cytotoxicity of UiO-66 that limits how much loaded material can be used to deliver trehalose intracellularly.

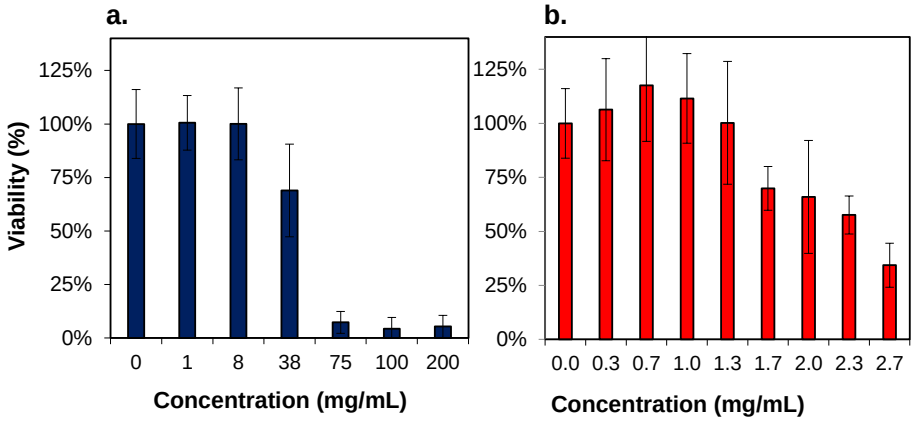

Figure 3.12. MTS viability assay measuring enzymatic metabolic activity of HeLa cells after 24 h incubation with (a) trehalose, and (b) UiO-66. Samples were run in minimum of four replicates. Standard deviations are shown for each given data point.

Having synthesised and characterised the delivery vector after loading it with trehalose, its use as a CPA was investigated. For that, cells were pre-incubated with different conditions for 3 h to allow for enough time for trehalose to be delivered before

freezing. Pre-incubating with 100 mM free trehalose, 0.5 mg/mL trehalose-loaded MOF (TREH@MOF), and a combination of both in growth media was tested, in addition to pre-treating with growth media alone. Pre-treatment with the combination of trehalose and TREH@MOF was done to test whether both intracellular and extracellular trehalose are required for a cryoprotective effect. Additionally, it was thought that the presence of both intracellular and extracellular trehalose would allow to avoid potential osmotic effects. Sample names for the treatments indicate the pre-incubation media used. The pre-incubation solution was then removed and replaced with freezing media (100 mM trehalose in FBS) to avoid freezing the cells in the presence of MOF, after which the cells were slowly cooled to -80 °C (1 °C/min) and then transferred to liquid nitrogen (-196 °C). Both the incubation and freezing media used for the different samples are shown in Table 3.1. Typically, cryopreservation relies on protocols that include the addition of 1.0-2.0 M of penetrating CPAs, such as DMSO, glycerol, and ethylene glycol[157]. For this reason, the efficiency of trehalose-loaded UiO-66 was benchmarked against a positive control (+) of cells frozen in a solution made up of 90 % v/v foetal bovine serum (FBS) and 10 % v/v DMSO. Cells incubated and frozen in growth media without any additives acted as the negative control (-).

Table 3.1. Conditions used to treat cells before freezing.

Sample	Pre-incubation media	Freezing media
MEDIA	Growth media	100 mM trehalose in FBS
TREH	100 mM trehalose	100 mM trehalose in FBS
TREH@MOF	0.5 mg/mL treh@MOF	100 mM trehalose in FBS
TREH + TREH@MOF	100mM Trehalose + 0.5 mg/mL treh@MOF	100 mM trehalose in FBS
Positive control (+)	Growth media	90 % FBS + 10 % DMSO
Negative control (-)	Growth media	Growth media

After freezing, cells were removed from the liquid nitrogen tank and rapidly thawed (within 5 minutes) in a water bath at 37 °C. Rapid thawing is essential for cellular survival as cells may be damaged by the extracellular restructuring of ice masses if thawing is too slow. The thawed cells were then seeded in 96-well plates and allowed to grow for 0 h, 24 h, and 48 h, after which their metabolic activity was measured using the MTS viability assay. **Figure 3.13** shows the enzymatic metabolic activity of HeLa cells 0 h (red), 24 h (blue), and 48 h (yellow) after thawing. The values at every time point were normalised to the positive control of cells pre-incubated in

growth media and frozen in 90 v/v % FBS and 10 v/v % DMSO. A table of values for the data is shown in Table 3.2.

As expected, negative control cells pre-incubated and frozen in the absence of a CPA (in growth media alone) had the lowest survival rate post-thaw, with viability at 6 ± 2 %, 12 ± 2 %, and 7 ± 3 %, at 0 h, 24 h, and 48 h respectively. Cells pre-incubated in growth media and frozen in 100 mM trehalose in FBS (sample 'MEDIA') had a higher survival rate, with 12 ± 2 %, 23 ± 2 %, and 31 ± 5 % still viable after 0 h, 24 h, and 48 h respectively, suggesting that freezing in a 100 mM trehalose in FBS solution provides some protection to cells. Pre-incubating cells with a growth media solution containing 100 mM trehalose (sample 'TREH') did not improve viability compared to pre-incubating in growth media alone (sample 'MEDIA'), indicating that pre-incubation with trehalose did not protect cells during subsequent freezing. When cells were pre-treated with trehalose-containing MOF (sample 'TREH@MOF'), the cell viability was lower than cells pre-incubated with growth media alone (sample 'MEDIA'), with viabilities of 13 ± 4 %, 13 ± 2 %, and 12 ± 3 % at 0 h, 24 h, and 48 h, and were not significantly different than the negative control, indicating a negative effect of the MOF. This is despite **Figure 3.12** showing that UiO-66 is non-toxic at 0.5 mg/mL. This can be explained by the fact that cells might not be able to withstand the combined stresses of freezing and being incubated in the presence of MOFs. However, pre-incubating cells with a combination of trehalose and trehalose-loaded UiO-66 (sample 'TREH + TREH@MOF') led to viabilities that were not significantly different than cells pre-incubated with media (sample 'MEDIA') or a 100 mM trehalose media solution (sample 'TREH'), with values of 11 ± 2 %, 16 ± 2 %, and 28 ± 3 % at 0 h, 24 h, and 48 h respectively. This suggests a protective effect of trehalose that renders cells better able to withstand the stress caused by the presence of MOF.

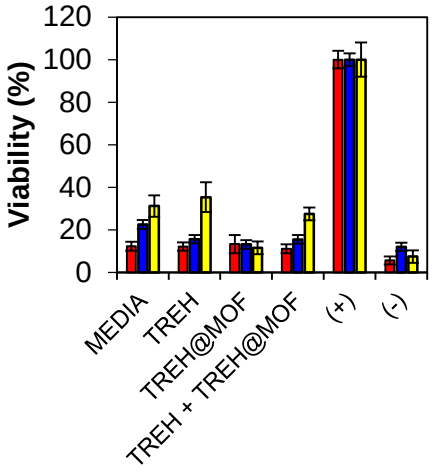

Figure 3.13. Viability of HeLa cells measured using the MTS enzymatic metabolic activity assay at 0 h (red), 24 h (blue), and 48 h (yellow) post-thaw. (+) = positive control; (-) = negative control. Experiments were run three times, with three replicates each time. Standard errors are shown for each given data point.

Table 3.2. Values for the viability of HeLa cells 0 h, 24 h, and 48 h after thawing.

Sample	**Viability (%)**		
	0 h	24 h	48 h
MEDIA	12 ± 2	23 ± 2	31 ± 5
TREH	12 ± 2	16 ± 2	35 ± 7
TREH@MOF	13 ± 4	13 ± 2	12 ± 3
TREH + TREH@MOF	11 ± 2	16 ± 2	28 ± 3
Positive control (+)	100 ± 4	100 ± 3	100 ± 8
Negative control (-)	6 ± 2	12 ± 2	7 ± 3

In order to verify this protective effect, the viability of HeLa cells after incubation with trehalose-loaded UiO-66 for 24 h was tested using the MTS viability assay. The results are shown in **Figure 3.14** and demonstrate that the system was non-toxic up to concentrations of 4 mg/mL (equivalent MOF concentration of *ca.* 2 mg/mL, considering 50 wt % loading), whereas UiO-66 on its own was toxic starting at 1.5 mg/mL. This protective effect may be due to trehalose's ability to stabilise cellular membrane components[158]. In summary, the results showed that trehalose-loaded UiO-66 had no cryoprotective effect on HeLa cells. A possible explanation is that UiO-66 is unable to deliver trehalose into the cytosol, even though the cells take it up. As laid out extensively in Chapter 4, particles taken up by cells can end up trapped in endosomes, which then mature into acidic lysosomes that degrade the MOF along with its cargo,

thus voiding its therapeutic effect. In the case of trehalose, the acidity of lysosomes should not be an issue given that the sugar has been shown to possess extraordinary stability even at pH 3.5 and 100 °C for 24 h[159]. However, the MOF and its cargo could be trapped in the endolysosomal system and recycled out of the cell. In order to test this hypothesis and better understand the cellular uptake of MOFs, the next chapter focuses on elucidating the mechanism of MOF uptake and their final intracellular fate.

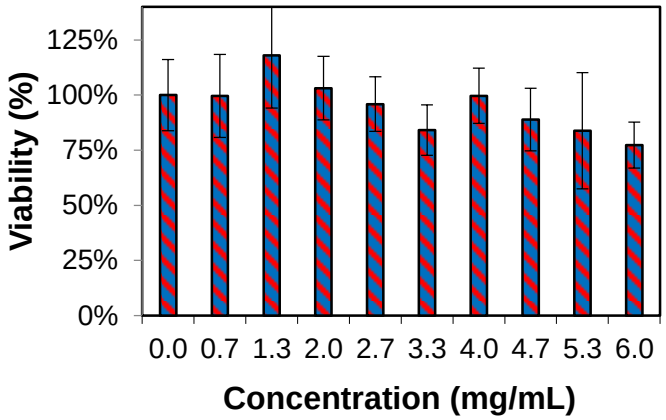

Figure 3.14. Viability of HeLa cells measured using the MTS enzymatic metabolic activity assay after incubation for 24 h with trehalose-loaded UiO-66. Error bars represent the standard deviation of four replicates.

3.4 Conclusions

UiO-66 particles 136 ± 27 nm in size were successfully synthesised and characterised, and PXRD was performed to confirm their crystalline structure. They were found to be stable in water up to the 9 days tested and maintained their crystallinity after this treatment. However, they degraded in PBS within 30 minutes, suggesting that the phosphate groups present in solution competed with the BDC linker for the metal sites.

Trehalose was successfully loaded into UiO-66 by soaking in aqueous trehalose solutions of varying concentrations. The adsorption isotherm of trehalose in UiO-66 showed an increase in the amount of loaded trehalose with increasing loading concentrations. The amount of trehalose loaded reached approximately 50 % of the total weight of the loaded particles. This was confirmed both by TGA and by measuring the total amount of trehalose released when the particles were soaked in water. The obtained high loadings are useful for cryopreservation applications because they allow

for the delivery of large quantities of trehalose inside cells with minimal MOF use. The release of trehalose from UiO-66 in PBS, which is a model for more complex phosphate media, was complete within 3 h, with 50 % being released within the first 30 minutes.

The cytotoxicity of UiO-66 and trehalose was investigated, and it was found that the cytotoxicity of UiO-66 limits the amount of loaded particles that can be used. The concentration of UiO-66 at which the viability of HeLa cells starts to decline (*ca.* 1.5 mg/mL) is nonetheless expected to be high enough for the MOF to be able to deliver large amounts of trehalose intracellularly (100–200 mM).

HeLa cells were frozen using trehalose-loaded UiO-66 as a CPA. However, no protective effect was found when compared to cells frozen using free trehalose or growth media as a CPA. This was hypothesised to be caused by MOFs being entrapped in endosomes, rendering them unable to deliver the trehalose into the cytosol. The next chapter studies the cellular uptake of MOF particles in order to better understand how to design a delivery system that is able to reach its desired intracellular location.

4 Uptake and Intracellular Fate of MOF Nanoparticles

4.1 Introduction

This chapter investigates factors affecting the uptake mechanism of zirconium-based NPs and their subsequent intracellular fate to understand what impedes the release of cargo molecules at the correct intracellular location. This will allow to elucidate the reasons behind the absence of a significant cryoprotective effect when using UiO-66 as a vector to deliver trehalose to the cytosol (**Chapter 3**). Additionally, the study will provide information on suitable approaches to prepare an optimal drug delivery system (DDS) with enhanced endocytosis efficiency and improved ability to avoid lysosomal entrapment. **Section 4.1.1** describes the importance of studying the main cellular uptake mechanisms of MOF particles. **Section 4.1.2** then discusses the main cellular internalisation pathways and relates them to the final intracellular fate of NPs.

4.1.1 Importance of Understanding Endocytosis

Optimal MOFs for drug delivery need to be versatile to be able to carry and release different compounds. However, one of the main limitations to their translation to clinical drug delivery applications is the limited number of studies describing their entry into cells[97,151–153]. To be efficient as a DDS, a MOF needs to be able to penetrate into

cells and, more crucially, release its cargo molecules in the correct intracellular location. While small molecules are able to enter cells by passive diffusion, NPs usually require an energy-dependent process known as endocytosis, a mechanism present in all eukaryotic cells[160–163]. Importantly, the fate of the NPs and hence their therapeutic effect after entering the cell is dependent on the endocytic pathways they enter through. However, no general guidelines for MOF particle internalisation have been established due to the inherent complexity of endocytosis as a mechanism, with a number of factors affecting cellular uptake. For instance, the rate of uptake and pathway selection is extremely cell line dependent. Additionally, characteristics specific to the particles being taken up, such as size, shape, and surface chemistry all play a significant role in the cellular uptake mechanism[164,165]. For instance, the cellular uptake of polystyrene NPs by human colon adenocarcinoma cells was shown to be optimally efficient for 100 nm particles[166]. Conversely, Chithrani *et al.* showed that gold NPs 50 nm in size were internalised more efficiently in HeLa cells[167]. A number of studies have shown that positive surface charges increase particle uptake due to electrostatic attractions to the slightly negatively charged cell membrane[168,169]. Understanding MOF particle interactions with cells is therefore critical to optimise these materials as DDSs.

4.1.2 Endocytosis Pathways and Final Intracellular Fate of Particles

Active cell uptake can be divided into two main types: phagocytosis, which relates to the ingestion and degradation of large particles (≥ 0.5 µm) by specific cell types such as neutrophils, monocytes, and macrophages[170–172]; and pinocytosis, used by cells to internalise surrounding fluid along with soluble molecules and particles[164]. Pinocytosis, or what is more commonly known as endocytosis, can further be classified into three main endocytic pathways: (i) macropinocytosis; (ii) *clathrin*-dependent endocytosis; and (iii) *caveolae*-dependent endocytosis[172,173]. Several *clathrin*- and *caveolae*-independent endocytosis pathways also exist[174,175], but will not be discussed in greater detail as they are less significant and their mechanisms less extensively described in the scientific literature[163,176]. Macropinocytosis is a nonspecific process present in almost all cell types and refers to the uptake of large amounts of extracellular fluid along with any particles that are present in it. Fluid contents are taken up in 0.5–1.0 µm vesicles in the same concentration as in the surrounding medium[162]. Receptor-mediated endocytosis, and in contrast to macropinocytosis, allows for the uptake of specific macromolecules in a concentrated form[177]. *Clathrin*-dependent endocytosis is

the most well described receptor-mediated endocytosis pathway. In *clathrin*-mediated endocytosis, receptors are responsible for cargo recognition, followed by the formation of *clathrin*-coated vesicles, which are usually up to 200 nm in size. These vesicles then fuse with early endosomes, mature into late endosomes, and then merge with lyososomes, leading to the hydrolysis of the DDS and its cargo, thus nullifying its therapeutic effect[178]. *Caveolae*-dependent endocytosis is associated with the formation of lipid raft-enriched flask-shaped invaginations coated with *caveolin*, approximately 60–80 nm in diameter. Particles taken up through this pathway can then be delivered to different intracellular locations. For example, and similarly to *clathrin*-dependent endocytosis, the vesicles can fuse with endosomes and mature into lysosomes for further degradation. Notably, particles taken up through this pathway can also be delivered into pH neutral *caveolin*-containing endosomes, termed caveosomes, which can then release their contents into the cytosol or in other intracellular locations. This means that particles taken up by *caveolae*-mediated endocytosis can potentially avoid lysosomal degradation along with their cargo[179–181].

Because particles penetrating cells through different endocytosis routes have different final intracellular fates, it is important to consider the factors that affect cellular uptake pathways when designing a MOF DDS, namely surface chemistry and particle size. In this chapter, the trafficking and final intracellular fate of MOFs was investigated. A range of Zr-based MOFs with different surface chemistries was studied. Surface chemistry was controlled either by linker functionalisation or by post-synthetic attachment of surface moieties. In order to avoid the presence of modulators that could affect the surface chemistry, particle size of the MOFs with functionalised organic linkers was not controlled/tuned. To allow for comparison, a range of UiO-66 MOFs with different particle sizes was included in the study. This range of materials also allowed to understand the effect of MOF particle size on cellular uptake. In order to investigate the endocytosis pathways used by these particles, different endocytosis pharmacological inhibitors were used. Cells were imaged using confocal microscopy to determine the final intracellular location of some of these MOFs. The therapeutic effect of drug-loaded MOFs was assessed using the MTS viability assay in order to correlate the results to the cellular uptake findings.

4.2 Collaborative Work

MOFs with functionalised linkers (Zr-L2 to Zr-L6) as well as MOFs surface-modified by post-synthetic attachment of biomolecules (Zr-L1-FA, Zr-L1-Hep, Zr-L1-Biot, Zr-L1-Lact, Zr-L1-PNIPAM, Zr-L1-PEG550, and Zr-L1-PEG2000) were synthesised at the School of Chemistry, University of Glasgow, by Dr. Isabel Abanades-Lazaro and Dr. Ross Marshall under the supervision of Dr. Ross Forgan's group. Synthesis of the range of Zr-L1 with different particle sizes was done by Mr. Gerard Boix and Dr. Inhar Imaz from Dr. Daniel Maspoch's group (Catalan Institute of Nanoscience and Nanotechnology ICN2, CSIC and The Barcelona Institute of Science and Technology, Campus UAB, Spain). Endocytosis efficiencies and pathway inhibition studies on Zr-L2 to Zr-L6 were performed by Dr. Claudia Orellana-Tavra under the supervision of Dr. David Fairen-Jimenez (Department of Chemical Engineering and Biotechnology, University of Cambridge). Confocal images of Zr-L2 and Zr-L3 were done by Dr. Claudia Orellana-Tavra. SEM was performed at the Department of Physiology, University of Cambridge by Dr. Jeremy Skepper.

4.3 Results & Discussion

4.3.1 Effect of Size on Cellular Uptake by HeLa Cells

As discussed in **Section 4.1**, the MOFs with different linker functionalities included in the study also presented different particle sizes. Controlling their size would have meant the addition of modulators, which would have further altered the surface chemistry, making it difficult to isolate the effect of the functionalised linkers on the cellular uptake behaviour. To be able to discriminate between the role of surface chemistry and particle size on the endocytosis pathways and uptake efficiencies, the present analysis was split to study both effects separately. As a reference for the surface chemistry analysis, the effect of particle size on cellular uptake using a broad range of sizes was first investigated. A series of UiO-66 samples with different particle sizes was used: 50, 75, 92, 260, and 652 nm; these structures were named $_x$Zr-L1, where *x* is the particle size (**Table 4.1**).

Table 4.1. Colloidal analysis of Zr-L1 samples of different particle sizes (i.e. *x*Zr-L1) as well as their calcein uptakes.

MOF	Particle size (nm)[a]	Effective diameter (nm)[b]		Polydispersity Index		Z-Potential (mV)		Calcein (wt.%)
		PBS	Growth media	PBS	Growth media	Water	Growth media	
$_{50}$Zr-L1	50 ± 2	517 ± 40	238 ± 11	0.507	0.429	0.5 ± 0.1	-9.5 ± 0.2	2.7
$_{75}$Zr-L1	75 ± 3	575 ± 16	480 ± 21	0.581	0.479	12.3 ± 0.4	-10.2 ± 0.2	2.2
$_{92}$Zr-L1	92 ± 2	210 ± 2	161 ± 1	0.411	0.207	14.2 ± 0.4	-11.2 ± 0.3	2.2
$_{260}$Zr-L1	260 ± 21	328 ± 13	272 ± 12	0.295	0.167	18.9 ± 0.6	-10.3 ± 0.2	1.3
$_{652}$Zr-L1	652 ± 23	1637 ± 77	874 ± 105	0.373	0.262	8.5 ± 0.2	-8.7 ± 0.1	0.4

Figure 4.1 presents the PXRD patterns for the MOFs compared with the patterns predicted from single crystal structures. The positions of the main peaks in all the synthesised structures at 2θ = 7.4°, 8.6°, and 12.1° matched those in the simulated structure. Additionally, other observable peaks above 2θ = 12.1° were also in agreement with the simulated structure, indicating successful synthesis of UiO-66 for all materials.

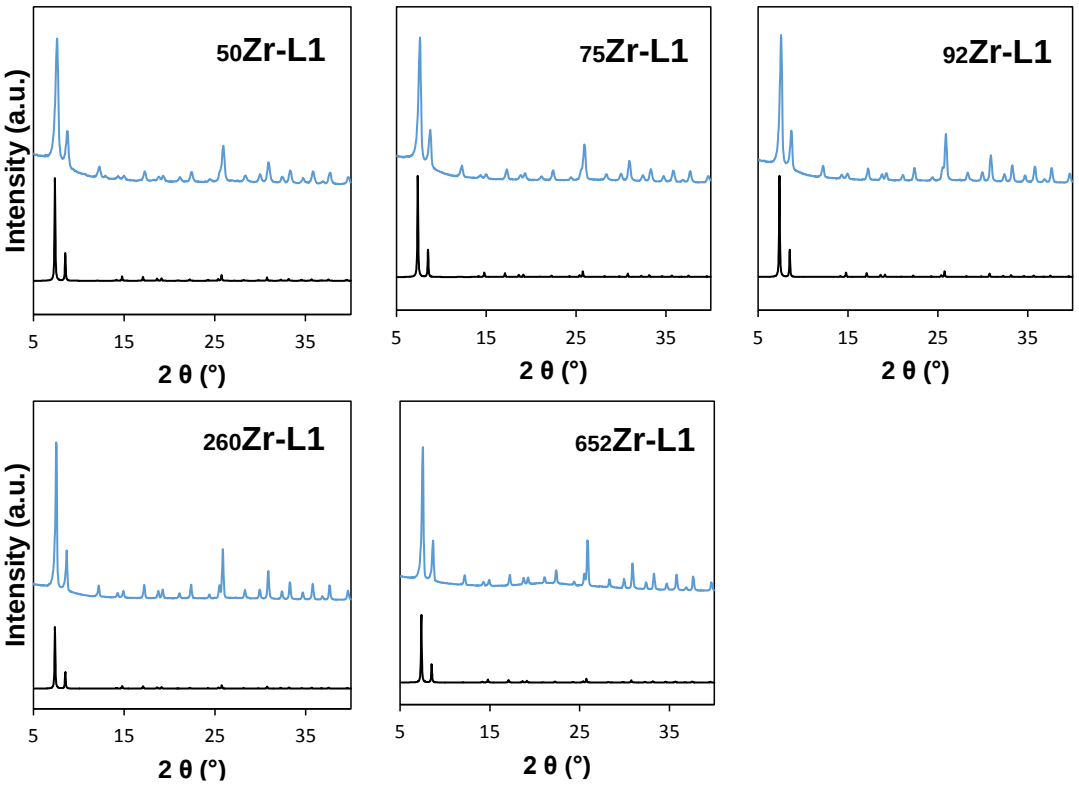

Figure 4.1. PXRD patterns of $_x$Zr-L1 MOFs compared with their calculated pattern. Colour code of patterns: black, calculated; and blue, synthesised. Sample names are shown on top of patterns.

SEM images were acquired in order to determine particle sizes. **Figure 4.2a** displays images of the $_x$Zr-L1 MOFs. Mean particle sizes were determined, averaging across 100 particles per sample. The sizes are shown in **Table 4.1**, and ranged from 50-652 nm. **Figure 4.2b** shows the particle size distribution for all five $_x$Zr-L1 particles, and indicates a narrow distribution of particle sizes. This is further reflected in the low relative standard deviations, ranging between 2.1–8.0 %, as can be determined from **Table 4.1**. Such a narrow distribution was necessary in order to properly study the effect of particle size on cellular uptake.

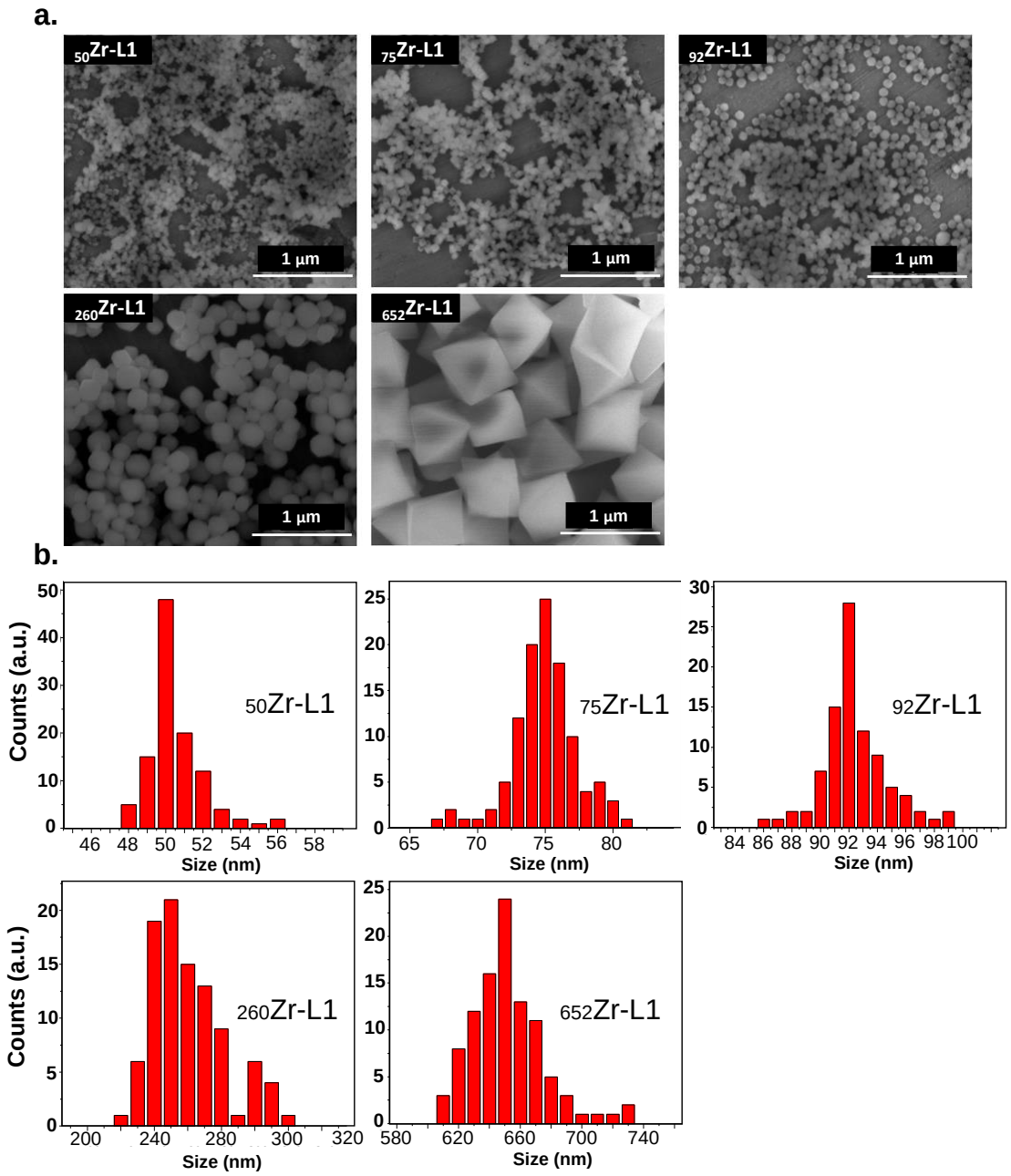

Figure 4.2. (a) SEM images of UiO-66 with different particle sizes ($_x$Zr-L1), and (b) particle size distribution of $_x$Zr-L1 particles as determined from SEM images. A minimum of 100 particles were counted. Scale bar sizes provided on images.

Since the physicochemical properties of MOFs, and of NPs in general, are affected by the media in which they are present, their colloidal properties were determined: hydrodynamic size in PBS and growth media, zeta potential in water and growth media, all at pH 7.4. The hydrodynamic diameter is the effective size that cells "observe" in solution. The zeta potential is the effective surface potential at the hydrodynamic "shear surface" close to the solid-liquid interface. **Table 4.1** shows the

hydrodynamic diameter of all the $_{x}$Zr-L1 particles in PBS and growth media. The degree of aggregation was more pronounced in PBS than in growth media. For example, the hydrodynamic diameter of $_{50}$Zr-L1 was more than double the size in PBS compared to growth media. The hydrodynamic diameters in growth media indicate aggregation was only significant for the smaller particle size Zr-L1 samples. A decrease in polydispersity index (PdI) was also observed, and ranged from 16 % for $_{50}$Zr-L1 to 50 % for $_{92}$Zr-L1. MOFs are susceptible to aggregation in aqueous solvents due to their varying hydrophobicities[150]. However, the formation of a "protein corona"[149] on the external surface of the MOF particles, resulting from the adsorption of different kinds of proteins from the serum present in growth media, might be the reason for their lower susceptibility to aggregation compared to PBS and also the negative zeta potentials measured in media compared to water.

To allow their intracellular detection using flow cytometry and confocal microscopy, the MOF particles were loaded with the fluorescent molecule calcein. Calcein was selected because of its hydrophilic character, which makes it unable to cross the cell membrane and thus requires a DDS to be transported through it[147,151]. The amounts of calcein loaded in the $_{x}$Zr-L1 MOFs are presented in **Table 4.1**. They ranged between 0.4 and 2.7 wt % for $_{652}$Zr-L1 and $_{50}$Zr-L1 respectively. Calcein loading decreased with increasing particle size. Since smaller particles have higher external surface areas compared with larger particles, this suggests that calcein mostly adsorbs to the external surface or to potential defects or roughness. This is supported by the fact that calcein (13 Å) is too large to fit through the Zr-L1 windows (5–7 Å).

Having confirmed the successful synthesis and loading of calcein into the range of $_{x}$Zr-L1 particles, their uptake efficiency by HeLa cells was then investigated. **Figure 4.3** shows the normalised intracellular fluorescence, measured by flow cytometry, of HeLa cells incubated for 1.5 h with varying amounts of $_{x}$Zr-L1 particles. The mass ratios of the different MOFs were chosen in such a way to keep the amount of calcein constant. An equal amount of free calcein was used as a control. $_{50}$Zr-L1 presented the highest intracellular fluorescence, and therefore, all the values were normalised against it. Although calcein is considered a cell impermeable dye, a low calcein uptake was observed, 17 % in comparison with $_{50}$Zr-L1 uptake. This effect has been seen with calcein previously, and has also been observed for other impermeable dyes, which are internalised by endocytosis[142,147,182]. For $_{x}$Zr-L1 particles, uptake efficiency decreased with increasing particle size, with $_{50}$Zr-L1 having the highest

efficiency (100 ± 6 %) and $_{260}$Zr-L1 having the lowest (58 ± 3 %). The uptake efficiencies of $_{75}$Zr-L1 (75 ± 5 %) and $_{92}$Zr-L1 (82 ± 5 %) were not significantly different. In the case of $_{652}$Zr-L1, the amount of calcein entering the cell was not significantly different from free calcein (18 ± 1 % vs 17 ± 1 %), showing that a negligible amount of MOF entered the cells, likely due to particle size being too large for cellular uptake.

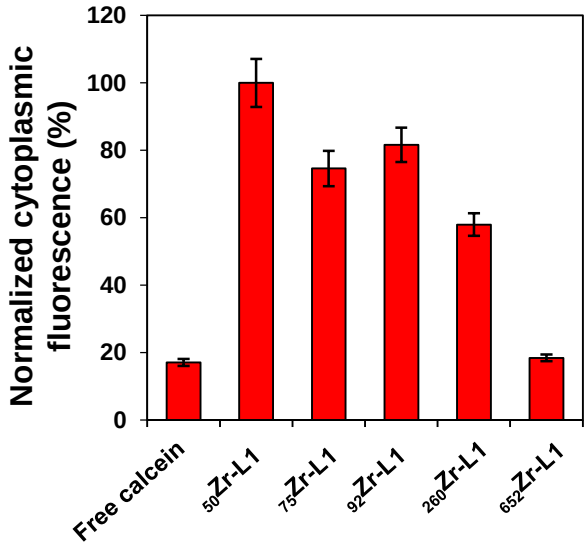

Figure 4.3. Normalised intracellular fluorescence of HeLa cells incubated with Zr-L1 of different particle sizes. Different concentrations of MOF were used to keep the amount of calcein constant across all samples. Error bars represent the standard error of at least 3 replicates.

In flow cytometry, cells or particles passing through the laser beam scatter light, which is detected as forward scatter (FS) and side scatter (SS). FS correlates with cell size and SS is proportional to the granularity of the cells. In this manner, cell populations can often be identified based on size and granularity alone. The fact that $_{652}$Zr-L1 was too large to enter cells was confirmed by the change in the SS versus FS plot when cells were incubated with $_{652}$Zr-L1 (**Figure 4.4**). HeLa cells with normal size and granularity mostly fell within the gate seen in **Figure 4.4a** (93.3 %). When cells were incubated with $_{652}$Zr-L1, there was a significant increase in side scatter (**Figure 4.4b**), indicating an increase in granularity due to MOFs adhered to the outside of the cells. Only 22.7 % of cells remained in the gate where healthy HeLa cells should be, and within this population there was negligible fluorescence, indicating that an insignificant amount of MOF was taken up by cells. In contrast, cells incubated with $_{260}$Zr L1 had normal side scatter (**Figure 4.4c**), with 91.1 % of cells falling within the

gate, indicating that the granularity of the cells was normal and hence that there was no MOF adhered to the outer cellular membrane.

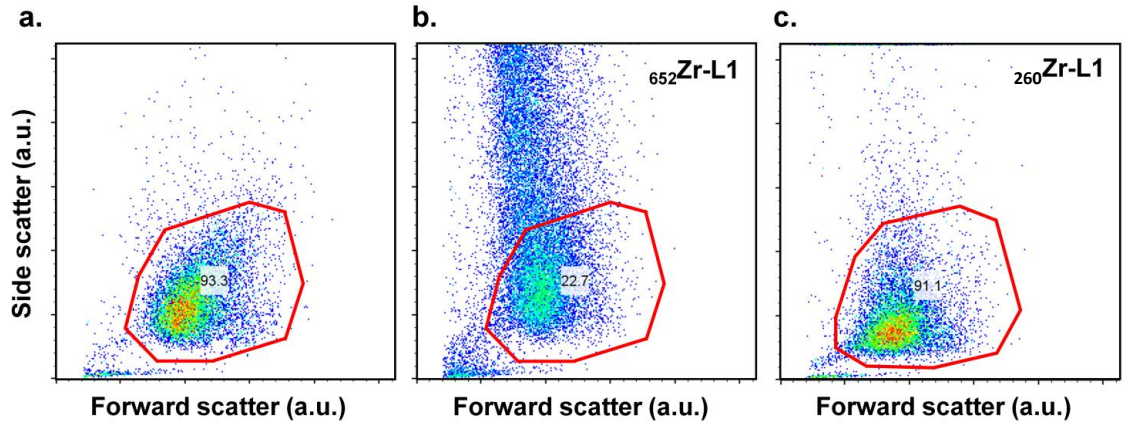

Figure 4.4. Side scatter versus forward scatter plots obtained from fluorescence-activated cell sorting (FACS) of (a) HeLa cells, (b) HeLa cells incubated with $_{652}$Zr-L1, and (c) HeLa cells incubated with $_{260}$Zr-L1. Solid red line shows the gate around morphologically normal HeLa cells. The numbers indicate the percentage of cells within that gate.

The endocytic pathways for the internalisation of $_{x}$Zr-L1 by HeLa cells were then studied using different pharmacological inhibitors. First, sucrose and chlorpromazine were used to independently inhibit *clathrin*-mediated endocytosis. Sucrose scatters *clathrin* matrices on the cell membrane, whereas chlorpromazine inhibits *clathrin*-coated pit formation by reversibly translocating *clathrin* and its adaptor proteins from the plasma membrane to intracellular vesicles[171,183]. Second, nystatin, a polyene antibiotic that sequestrates cholesterol molecules from the cell membrane, was used to inhibit *caveolae*-mediated endocytosis[183]. Finally, rottlerin was used to hinder macropinocytosis by inhibiting kinase proteins[184]. Since the inhibition of one particular endocytic pathway may trigger compensatory uptake mechanisms with time[183], the internalisation of the particles was assessed after a short exposure time to the endocytosis inhibitors (2 h). **Figure 4.5** shows HeLa cells' internal fluorescence after incubation with $_{x}$Zr-L1 particles in the presence of the different endocytic inhibitors. $_{652}$Zr-L1 was excluded from the analysis because it is too large to be taken up by cells. **Table A2.1** (Appendix) shows the values for each sample. To determine if the differences were statistically significant, every value was compared to the control at 37 °C using one-way analysis of variance (ANOVA) followed by Dunnett's test to adjust for multiple comparisons. At 4 °C, cellular uptake of the MOFs was significantly reduced by *ca.* 85 %. At this temperature, the metabolic activity of a cell is significantly

reduced[183], confirming that the particles were taken up by energy-dependent endocytosis and not by passive diffusion.

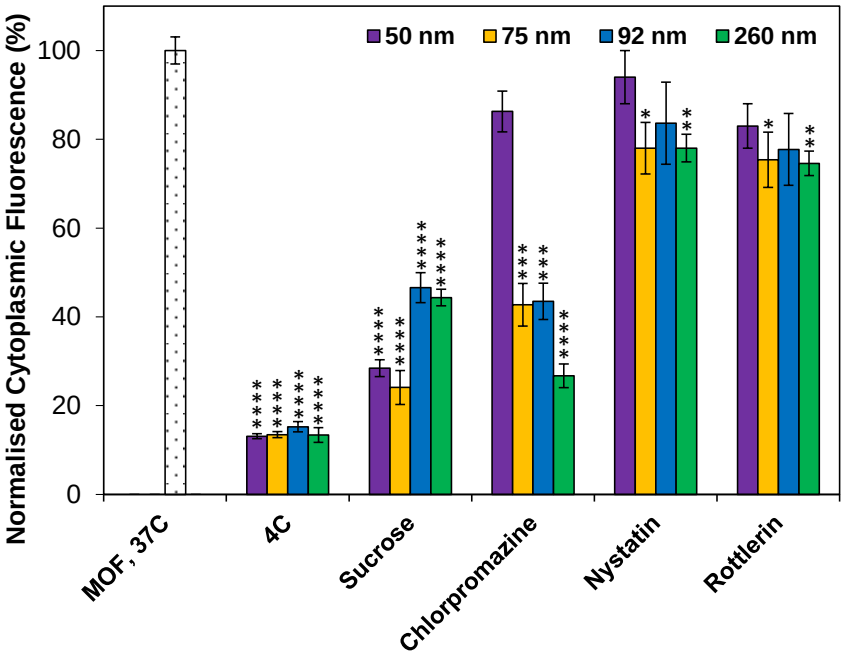

Figure 4.5. Effects of pharmacological endocytosis inhibitors on the uptake of Zr-L1 with different particle sizes, measured by flow cytometry. Error bars represent the standard error of at least 3 replicates. Asterisks indicate statistical significance, determined by one-way ANOVA, of normalised intracellular fluorescence of HeLa cells treated with each MOF and different pharmacological inhibitors compared with control value (ns $P > 0.05$, * $P \leq 0.05$, ** $P \leq 0.01$, *** $P \leq 0.001$, **** $P \leq 0.0001$).

For $_{50}$Zr-L1, particle uptake decreased significantly to 29 % when cells were treated with hypertonic sucrose. Despite the fact that sucrose is considered an inhibitor of *clathrin*-mediated endocytosis[185,186], there is evidence suggesting that it has some effect on non-*clathrin*-mediated endocytosis pathways[187,188]. Given that there is no evidence that chlorpromazine affects *caveolae*-mediated endocytosis or other endocytic pathways[183], it was used to confirm the results obtained with sucrose. For chlorpromazine, the uptake decreased only moderately to 86 %, although this was not statistically different from the control at 37 °C. The fact that sucrose affected uptake while chlorpromazine did not suggests that the main uptake routes of $_{50}$Zr-L1 did not involve *clathrin*-mediated pathways, and that, in this case, sucrose was inhibiting non-*clathrin*-mediated endocytosis pathways. Similarly, $_{50}$Zr-L1 particle uptake moderately decreased to 94 and 83 % when cells were treated with nystatin and rottlerin,

respectively. Again, this was not statistically different from the control at 37 °C. This indicates that the main routes of entry of $_{50}$Zr-L1 did not involve *clathrin*-or *caveolae*-mediated endocytosis, or macropinocytosis, but *clathrin*- and *caveolae*- independent endocytosis. For $_{75}$Zr-L1 and $_{92}$Zr-L1, similar levels of inhibition by chlorpromazine, nystatin, and rottlerin were observed, decreasing to *ca.* 45, 84, and 78 %, respectively, for both MOFs. However, the signals for these MOFs when treated with nystatin and rottlerin were not statistically significantly different from the control, indicating that they mainly entered the cell through *clathrin*-mediated endocytosis. In the case of $_{75}$Zr-L1, the decrease when treated with nystatin and rottlerin was slightly greater than that observed for $_{92}$Zr-L1 and showed some statistical significance, suggesting some uptake by *caveolae*-mediated endocytosis and macropinocytosis. For $_{260}$Zr-L1, the decrease in fluorescence intensity when treated with nystatin and rottlerin was the same as $_{75}$Zr-L1 (down to 78 % and 75 % respectively) and was statistically significant. However, an even larger decrease in intensity was observed for chlorpromazine, suggesting that, for $_{260}$Zr-L1, *clathrin*-mediated endocytosis was again the main entry pathway. Given that the hydrodynamic diameter is the effective size of the particles that cells observe in solution, the DLS results were also correlated to the data. As can be seen in Figure 4.5, $_{50}$Zr-L1 and $_{260}$Zr-L1, which have similar hydrodynamic diameters of 238 ± 11 nm and 272 ± 12 nm respectively (Table 4.1), are taken up differently in cells. While the hydrodynamic diameter might have an effect, it is not the only one. The endocytosis routes of entry are likely dependent on a combination of factors including physical size, hydrodynamic diameter, and surface chemistry that are difficult to isolate within the constraints of this study.

Table A2.2 (Appendix) summarises the statistical significance for comparison between the intracellular fluorescence of the different MOFs treated with a given inhibitor. The results show that there was no statistically significant difference between the normalised intracellular fluorescence of the Zr-L1 MOFs of different sizes when treated with nystatin (i.e., for *caveolae*) and rottlerin (i.e., macropinocytosis). This was despite the fact that decreases in fluorescence for $_{75}$Zr-L1 and $_{260}$Zr-L1 with these inhibitors were statistically significant when compared to the control at 37 °C. In summary, while the results in **Figure 4.5** suggested minor uptake by the *caveolin*-mediated pathway for $_{75}$Zr-L1 and $_{260}$Zr-L1 particles, indicating a potential ability to escape lysosomal degradation, **Table A2.2** (Appendix) showed that cells treated with the different MOFs and nystatin (*caveolin* pathway inhibited) do not have statistically

significant differences in uptake when compared to each other. Taken together the results suggest that particle size plays a minor role in determining the endocytic pathways Zr-L1 particles go through. The following sections will investigate whether surface chemistry plays a more important role.

4.3.2 Effect of Surface Chemistry on Cellular Uptake by HeLa Cells

Following the analysis of the role of particle size on the internalisation of the MOF particles, the role of surface chemistry was investigated. A range of Zr-based MOFs with different surface chemistries was studied. Surface chemistry was controlled either by linker functionalisation or by post-synthetic attachment of surface moieties. As mentioned in **Section 4.1.2**, particles synthesised using functionalised linkers had different sizes. The findings from **Section 4.3.1** showing the role of particle size on the internalisation pathways can be used to rationalise the results obtained with the MOFs with functionalised linkers. For the post-synthetically modified MOFs, the particle size remains the same given that the same mother batch is used to attach different functionalities.

To prepare the MOFs with functionalised linkers, a range of UiO-66-like materials was prepared by substituting the original BDC linker with functionalised linkers as well as extended linkers. **Figure 4.6a** shows the six different linkers (L1-L6) utilised to build the Zr-based MOFs, herein termed Zr-L1 to Zr-L6. L1 is BDC, used for UiO-66; L2-L4 are BDC functionalised with ─Br, ─NO_2, and ─NH_2, respectively; and L5 and L6 (naphthalene-2,6-dicarboxylic acid and 4,4'-biphenyldicarboxylic acid, respectively) are extended linkers. ─Br and ─NO_2 in L2 and L3 respectively are electron-withdrawing groups, whereas ─NH_2 in L4 is an electron-donating group. This allowed to study the effect of electron density at the surface of the MOFs while keeping the linker length fixed. L5 and L6 have similar chemical properties as L1, and therefore allowed to study the effect of linker size on cellular uptake. To prepare the post-synthetically modified MOFs, different surface reagents were used: folic acid (FA), vitamin B_7 biotin (Biot), and a negatively charged anticoagulant, heparin (Hep). These three molecules were chosen because they are known to have biological properties in binding and targeting, and possess carboxylic acid functionalities that allowed them to be coordinated to UiO-66 surfaces. Additionally, three protecting polymers, poly-L-lactide (Lact; $M_n \approx 2{,}000$), poly-N-isopropylacrylamide (PNIPAM; $M_n \approx 15000$), and poly(ethylene glycol) (PEG) were clicked to UiO-66 surfaces. PEG550 (average

M_n = 550) and PEG2000 (average M_n = 2000) were both tested. The six surface moieties were named Zr-L1-*func*, where *func* is the functionality attached, and are shown in **Figure 4.6b**.

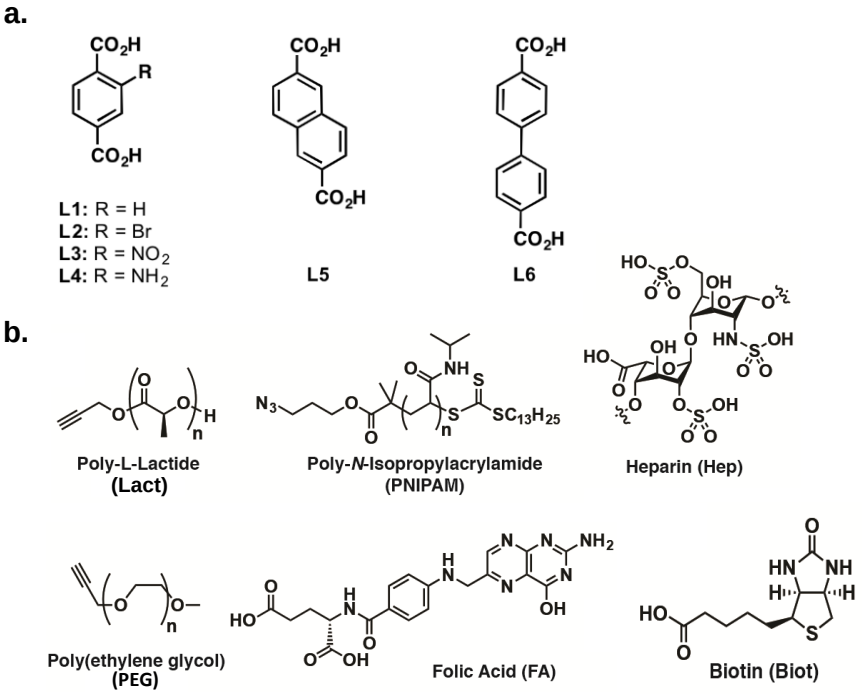

Figure 4.6. Chemical structures of (a) the organic linkers used to synthesise Zr-based MOFs with functionalised linkers, and (b) the surface functionalities attached to Zr-L1.

Table 4.2. Colloidal analysis of Zr-based MOF samples with different surface chemistry as well as their calcein uptakes.

MOF	Particle size (nm)[a]	Effective diameter (nm)[b]		PdI		Z-Pot (mV)		Calcein wt.%
		PBS	GM[e]	PBS	GM[e]	Water	GM[e]	
Zr-L2	211±11/371±38[c]	709±13	237±26	0.242	0.361	36.5±0.2	-8.7±0.3	0.4
Zr-L3	>400[d]	961±16	596±18	0.412	0.411	23.4±0.9	-10.4±0.4	0.3
Zr-L4	129±19/266±34[c]	828±84	165±1	0.282	0.151	42.7±0.5	-11.5±0.4	0.7
Zr-L5	78±3	1319±247	86±13	0.392	0.397	8.0±0.3	-10.8±0.7	1.0
Zr-L6	115±12/255±14[c]	12742±331	137±25	0.488	0.445	-5.8±0.3	-8.8±0.6	6.3
Zr-L1	143±31	1494±122	1196±6	0.575	0.723	N/A	-11.0±0.2	17.9
Zr-L1-FA	168±26	1151±42	539±58	0.564	0.749	N/A	-10.4±0.2	9.8
Zr-L1-Biot	175±17	772±7	275±31	0.380	0.962	N/A	-10.3±0.9	12.8
Zr-L1-Hep	157±34	904±91	905±23	0.373	0.606	N/A	-11.1±0.1	13.0
Zr-L1-Lact	177±25	538±5	402±13	0.335	0.41	N/A	-10. 7±0.4	6.9
Zr-L1-PNIPAM	177±24	837±37	538±44	0.287	0.587	N/A	-11.4±0.3	8.0
Zr-L1-PEG550	160±23	1023±96	890±93	0.874	0.952	N/A	-10.9±0.6	13.3
Zr-L1-PEG2000	173±37	420±98	366±6	0.466	0.523	N/A	-10.3±0.6	10.3

[a]Measured by SEM. [b]Measured by DLS. [c]Two different populations of particle sizes were present.
[d]Population too heterogeneous to determine particle size. [e]GM=growth media

Figure 4.7 shows the SEM images of the functionalised Zr-L1 derivatives (Zr-L2─Zr-L6) and of the post-synthetically modified Zr-L1 particles. **Table 4.2** shows the particle sizes, ranging from 78 to > 400 nm for Zr-L2─Zr-L6, and from 160 to 177 nm for the post-synthetically modified Zr-L1 particles. The Zr-L2 through Zr-L6 complexes varied drastically in size, and some even had two populations of particle size (Zr-L2, Zr-L4, and Zr-L6). To avoid changing the surface chemistry beyond the effects of the functionalised linkers by adding modulators to the synthesis reaction, particle size could not be controlled. However, the inclusion of a range of Zr-L1 MOFs with different particle sizes allowed for comparison. As for the post-synthetically modified Zr-L1 particles, they all had approximately the same particle size, given that they were the result of the attachment of different surface moieties to the same mother structure. This is reflected in the values shown in **Table 4.2**, which were not significantly different when the standard deviations were taken into consideration.

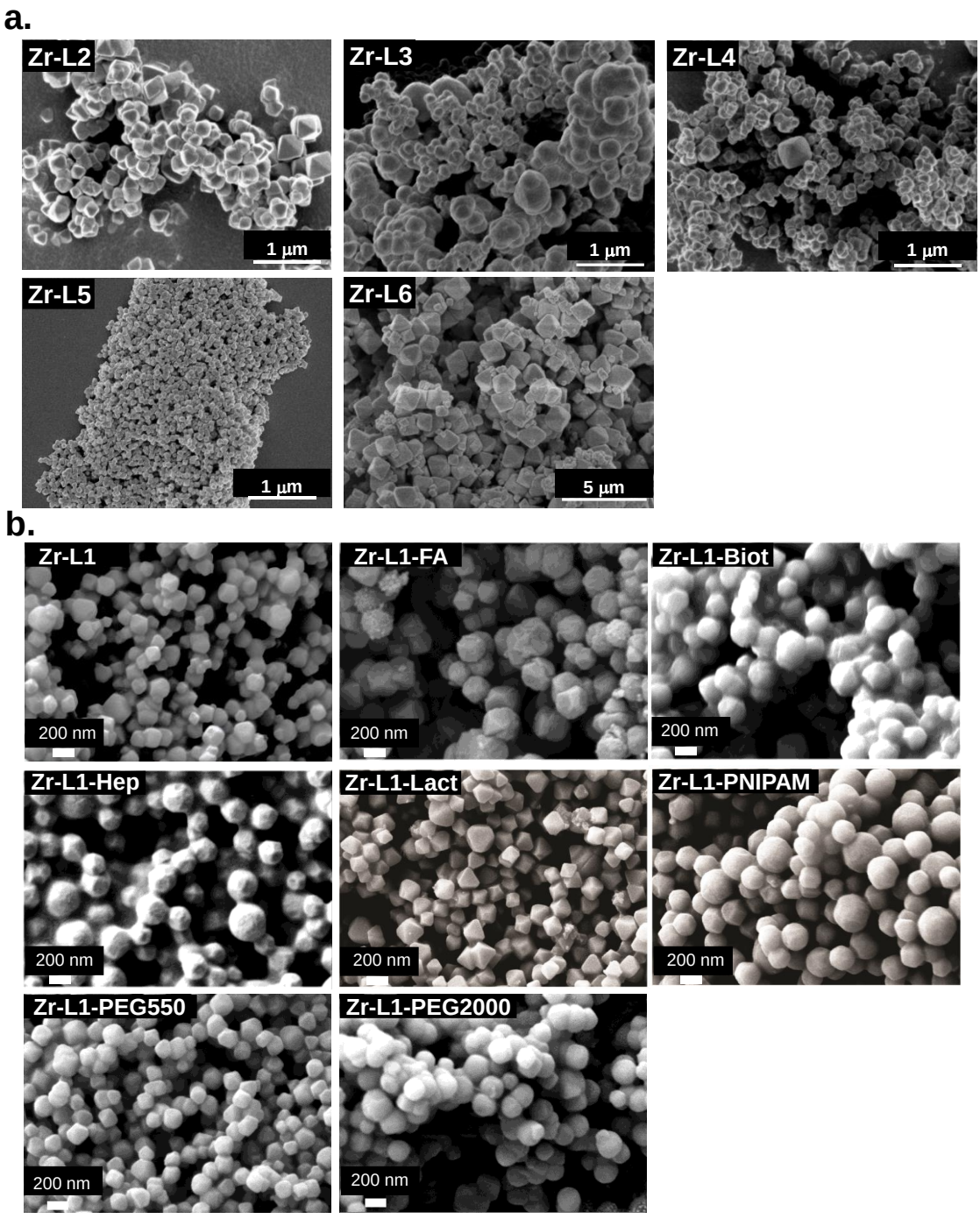

Figure 4.7. SEM images for a. Zr-based family, Zr-L2─Zr-L6 and b. post-synthetically modified Zr-L1-*func* particles.

The hydrodynamic diameter of the particles was then determined in PBS and growth media, at pH 7.4. For all the particles, the hydrodynamic diameters in PBS were higher than in growth media, suggesting a higher degree of aggregation in the former, although the polydispersity index (PdI) for some of the particles was higher in growth media (Zr-L2 and Zr-L1-*func*). In some cases, the particles displayed significant aggregation in growth media, with Zr-L1-Biot for example having a PdI of 0.962. The

post-synthetically modified Zr-L1-*func* particles aggregated more than the family of Zr-based MOFs (Zr-L2─Zr-L6), as indicated by their higher PdIs. This is likely due to the different modulators used for both families of MOFs. The colloidal stability and properties of MOFs are highly dependent on the modulator conditions utilised in the synthesis, with modulators at different concentrations and pK_a leading to the formation of more or less defects in the crystals, which in turn alter the surface chemistry of MOFs and enhance or degrade their colloidal stability[80]. Interestingly, the colloidal stability of post-synthetically modified particles Zr-L1-*func* was enhanced after functionalisation compared to the mother sample Zr-L1. For Zr-L1-PEG2000 specifically, the colloidal stability of the particles was drastically improved, with the PdI in PBS and growth media decreasing to 0.466 and 0.523 from 0.575 and 0.723 respectively. The effective diameter of the particles also decreased from 1494 ± 122 nm and 1196 ± 6 nm to 420 ± 98 nm and 366 ± 6 nm in PBS and growth media respectively. This could be due to the effect of steric stabilisation by the long PEG chains. The zeta potential values for the different particles are also given in **Table 4.2**. The surface potential of MOF particles depends on the chemistry of the linker used and the surface density of metal clusters. The modulator used can also play a role. The MOFs with functionalised linkers (Zr-L2─Zr-L4) have similar linker lengths and hence comparable metal cluster surface densities. The difference in surface chemistry arises from the functional groups attached to the terephthalate. Zr-L3, containing the functional group with the most electron-withdrawing group (─NO_2) has the lowest zeta potential of the MOFs with functionalised linkers. The ─Br group in L2 is slightly less electron-withdrawing than ─NO_2 and gives Zr-L2 particles with a higher zeta potential of 36.5 mV. The electron-donating ─NH_2 group in L4 gives Zr-L4 particles with the highest zeta potential of 42.7 mV. For the MOFs with extended linkers (Zr-L5─Zr-L6), the surface density of metal clusters is lower than with the functionalised linkers. This could be why much lower zeta potentials are observed compared with the functionalised linkers, and why Zr-L6, with the longest linker, has a lower zeta potential than Zr-L5 (-5.8 mV vs 8.0 mV).

The amounts of calcein loaded in all the MOFs are presented in **Table 4.2**. For Zr-L2 through Zr-L6, values ranged between 0.3 and 6.3 wt %. These particles were loaded using the same protocol as with $_x$Zr-L1 particles, which means the loadings between the two families of MOFs can be compared. Loadings for $_x$Zr-L1 can be found in **Table 4.1**. As mentioned in **Section 4.3.1**, for $_x$Zr-L1 particles, the amount of loaded calcein decreased with increasing particle size due to the decreasing available external

surface area to adsorb to. In the case of the functionalised MOFs (i.e. Zr-L2─Zr-L4), the loading values were generally lower compared to the non-functionalised $_{x}$Zr-L1 particles, even for particles similar in size such as $_{260}$Zr-L1 (260 nm; 1.3 wt %) and Zr-L4 (266 nm; 0.7 wt %). In the case of Zr-L6, i.e. the MOF with the longest linker and therefore the largest cavities, the amount increased to *ca.* 6 wt %, suggesting some additional adsorption in the internal porosity as well as the outer surface. Calcein loadings for the post-synthetically modified Zr-L1-*func* particles were considerably higher due to using a higher calcein concentration during the loading process. For all the daughter samples, the calcein loading was lower than for the mother sample (Zr-L1; 17.9 %). This was expected, given that the addition of surface moieties increases the total weight of the particles, diluting the weight of calcein. In all cases, loading values were sufficiently high to detect the MOFs through flow cytometry and confocal microscopy. Additionally, both the calcein and the surface agents were shown to coexist at the MOF surface in a published study investigating these materials[153].

4.3.2.1 Cellular Uptake of Zr-Based Family of MOFs with Functionalised Linkers

The internalisation efficiency of the Zr-based family of MOFs (Zr-L2─Zr-L6) was assessed using flow cytometry. **Figure 4.8** presents the normalised internal fluorescence of HeLa cells after treatment with the functionalised MOFs for 1.5 h in the presence of endocytic inhibitors. Different calcein concentrations were used as controls for each MOF so that they were equivalent to the loaded amount in the respective MOF. Unlike for the $_{x}$Zr-L1 particles with different sizes, using a different calcein concentration for each MOF was necessary because the different MOFs had very different loadings, up to an order of magnitude higher for Zr-L6 (6.3 wt %) for example. Particle sizes are shown beneath the MOF names, and zeta potential values are shown on top of each bar. The highest percentage change compared to free calcein was set as 100 % (Zr-L3), and the rest of the values normalised accordingly. Zr-L3 was internalised the most efficiently, followed by Zr-L2 and Zr-L4. Zr-L5 and Zr-L6 were the least efficiently internalised MOFs. Interestingly, the trend of decreasing efficiencies with increasing particle sizes that was observed with $_{x}$Zr-L1 did not apply to Zr-L2─Zr-L6, confirming the importance of surface chemistry. Further confirming this is the fact that, with the exception of $_{652}$Zr-L1 which was too large to be taken up by cells, the variability in uptake efficiency for $_{x}$Zr-L1 particles was low, whereas for Zr-L2─Zr-L6 the variability was much larger.

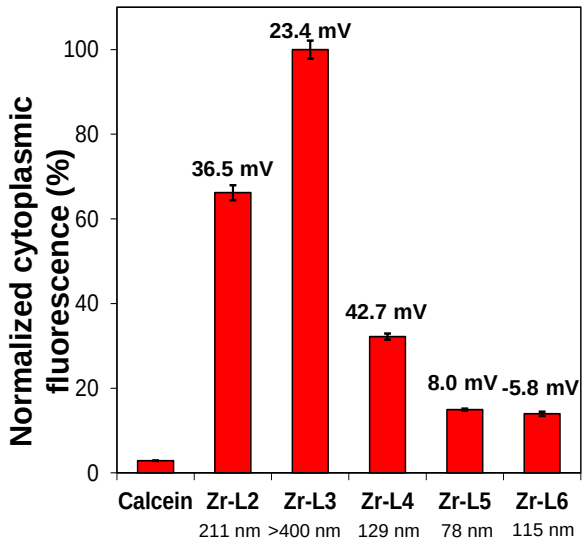

Figure 4.8. Normalised intracellular fluorescence of HeLa cells incubated with Zr-L2 to Zr-L6. Zeta potential values shown at the top of bars, particle size at the bottom. Error bars represent the standard error of at least 3 replicates.

For the MOFs with functionalised BDC linkers (i.e., ─Br, ─NO_2, and ─NH_2, for Zr-L2, Zr-L3, and Zr-L4, respectively), cellular uptake was inversely related to zeta potential. Zr-L2, which had the highest uptake, had a zeta potential of 23.4 mV, followed by Zr-L2 (36.5 mV) and Zr-L3 (42.7 mV). The MOFs with extended linkers (i.e., Zr-L5 and Zr-L6) had low zeta potentials of 8.0 and -5.8 mV, respectively, which might explain why they were not significantly taken up by the cells. As discussed in **Section 4.1.1**, studies have shown that positive surface charges increase particle uptake in both phagocytic and non-phagocytic cells due to electrostatic attractions to the slightly negatively charged cell membrane[168,169]. Interestingly, **Table 4.2** shows that the zeta potential values for all the MOFs in media converged to around -10 mV, which is the zeta potential measured for growth media, confirming again the "protein corona" formation around the external surface of the particles.

The influence of endocytosis inhibitors on the cellular uptake of Zr-L2─Zr-L6 was then analysed. **Figure 4.9** shows the intracellular fluorescence of HeLa cells after incubation with each MOF in the presence of the pharmacological inhibitors (the specific value for each column is shown in the Appendix, **Table A2.1**). To determine if the differences were statistically significant, every value was compared to the control at 37 °C using one-way analysis of variance (ANOVA) followed by Dunnett's test to adjust for multiple comparisons. For all the MOFs, cellular uptake at 4 °C decreased between 74 and 88 % when compared to the control at 37 °C, indicating that the

particles were taken up by energy-dependent endocytosis. For cells incubated with pharmacological inhibitors, and similarly to the endocytosis efficiency discussed above, it was possible to separate the MOFs into two subgroups with regards to the endocytosis pathways used for their internalisation: (i) MOFs with functionalised BDC linkers (Zr-L2─Zr-L4), and (ii) MOFs with extended linkers (Zr-L5 and Zr-L6). The uptake of Zr-L2, Zr-L3, and Zr-L4 decreased to *ca.* 20 % after incubation with the *clathrin*-mediated inhibitors sucrose and chlorpromazine, whereas incubation with nystatin (*caveolae*-mediated endocytosis inhibitor) caused a moderate decrease to *ca.* 70 %. Rottlerin (macropinocytosis inhibitor) decreased the uptake to *ca.* 48 %. Conversely, the uptake of Zr-L5 and Zr-L6 was significantly inhibited, down to *ca.* 42 % compared to the control at 37 °C, when *caveolae*-mediated endocytosis was blocked using nystatin. Inhibition of *clathrin*-mediated endocytosis only had a moderate effect: sucrose decreased uptake to around 65 % whereas chlorpromazine only reduced uptake to around 90 % (no significant difference with the control at 37 °C). Inhibition of macropinocytosis with rottlerin reduced the uptake to around 67 % for the two MOFs. These results suggest that Zr-L2─Zr-L4 underwent preferably *clathrin*-mediated endocytosis whereas Zr-L5 and Zr-L6 were mostly taken up by *caveolae*-mediated endocytosis. The literature offers conflicting data about the selection of endocytic pathways for charged particles, probably because the process is cell-type specific. With HeLa cells, studies have shown that positively charged NPs go through the *clathrin*-mediated pathway whereas negatively charged NPs go through *clathrin*-independent pathways[189,190]. This could explain why the negatively charged Zr-L6 was mostly taken up by *caveolae*-mediated endocytosis.

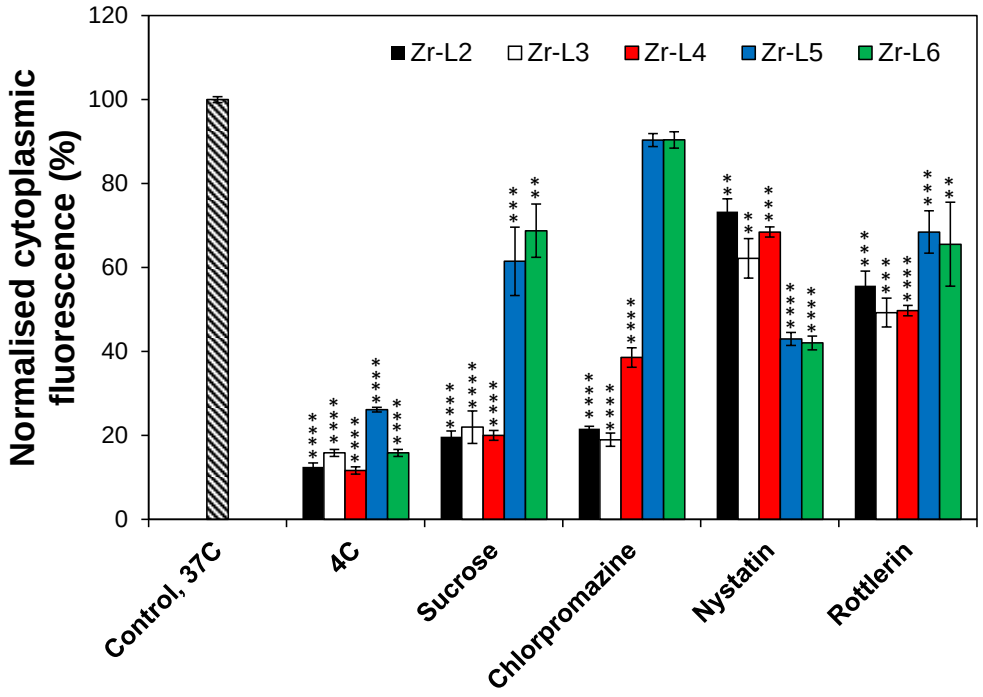

Figure 4.9. Effects of pharmacological endocytosis inhibitors on the uptake of Zr-based family of MOFs compared to a control at 37 °C, measured by flow cytometry. Error bars represent the standard error of at least 3 replicates. Asterisks indicate statistical significance, determined by one-way ANOVA, of normalised internal fluorescence of HeLa cells treated with the Zr-based family of MOFs and different pharmacological inhibitors, compared with the control at 37 °C (ns $P > 0.05$, * $P \leq 0.05$, ** $P \leq 0.01$, *** $P \leq 0.001$, **** $P \leq 0.0001$).

Table A2.3 (Appendix) summarises the statistical significance for comparison between the intracellular fluorescence of the different MOFs treated with a given inhibitor, allowing the statistically significant differences within these two subgroups (Zr-L2─Zr-L4 vs. Zr-L5─Zr-L6) and between them to be determined. Within the group of MOFs with functionalised BDC linkers, the only significant difference ($P \leq 0.01$) was between Zr-L4 on the one hand, and Zr-L2 and Zr-L3 on the other, when treated with chlorpromazine. When treated with nystatin or rottlerin, no statistically significant difference was observed. Within the sub-group of MOFs with extended linkers, no significant difference was observed between Zr-L5 and Zr-L6 for any inhibitor used. Conversely, there were significant differences when comparing the values for Zr-L2, Zr-L3, and Zr-L4, with the values for Zr-L5 and Zr-L6, for sucrose, chlorpromazine, and nystatin. This result further suggests that the cellular uptake behaviour was different between the two sub-groups. The size of the particles could play a minor role in inter-

and intragroup differences. More importantly, the surface chemistry of these particles was affecting the uptake processes. Cell uptake behaviour was less affected by a change in the size of $_x$Zr-L1 in comparison with the change in surface chemistry of the Zr-based family of MOFs. The two sub-groups of MOFs can also be segregated with respect to zeta potential. The MOFs with functionalities (Zr-L2 to Zr-L4) had zeta potentials in the range of 23.4 to 42.7 mV, while the MOFs with extended linkers (Zr-L5 and Zr-L6) had low zeta potentials of 8.0 and -5.8 mV respectively. MOFs with functional groups and thus higher zeta potentials underwent preferably *clathrin*-mediated endocytosis and the MOFs with extended linkers and thus low surface charge were internalized mostly through *caveolae*-mediated endocytosis. $_x$Zr-L1 particles do not have functional groups but their surface charge was slightly greater than Zr-L5 and Zr-L6, which might be due to the higher surface density of clusters on their surface compared to the MOFs with extended linkers. This may explain why $_x$Zr-L1 particles, with a surface charge between that of the functionalized MOFs and that of the extended linker MOFs, went through *clathrin*-mediated endocytosis in addition to *caveolae*-mediated endocytosis, whereas Zr-L5 and Zr-L6 mainly went through *caveolae*-mediated endocytosis. It is noteworthy that all MOFs were internalized by macropinocytosis as it is a non-selective process carried out by cells.

Depending on the type of endocytosis, the internalised carrier and its corresponding cargo are processed and transported to different final intracellular locations[191]. As explained in **Section 4.1.2**, particles that undergo *caveolae*-mediated endocytosis are able to potentially bypass lysosomal degradation. Studies on viruses and bacteria provide strong evidence that they are internalised through this non-acidic, non-digestive pathway[192] and are able to avoid digestion in the lysosomes[193]. Accordingly, one would expect MOFs going through *caveolae*-mediated endocytosis to have a higher chance of avoiding lysosomes and consequently delivering their cargo in other intracellular locations. The intracellular fate of the Zr-based family of MOFs after cellular uptake was investigated. This was done by examining whether the MOFs were found in lysosomes for further acidic degradation. For this purpose, confocal microscopy was used to determine if the particles were in the same intracellular location as a lysosomal marker, LysoTracker-Deep Red. **Figure 4.10a** shows the images of HeLa cells incubated with each MOF for 2 h. For Zr-L2, Zr-L3, and Zr-L4, a high degree of co-localisation was observed between signal from the MOF (green) and LysoTracker-Deep Red, illustrated by the yellow colour in the merged images. For

Zr-L5 and Zr-L6, a moderate degree of overlap between the MOFs and lysosomes can be seen. While some co-localisation is observed (yellow), most signal from the MOF did not overlap with the signal from LysoTracker-Deep Red. In order to quantify the degree of overlap, the Manders' overlap coefficient (MOC) was measured (**Figure 4.10b**). The MOC varies from 0 to 1 for non-overlapping and complete co-localisation, respectively[194,195]. **Figure 4.10b** shows that the results are also divided into two subgroups: (i) Zr-L2─Zr-L4; and (ii) Zr-L5 and Zr-L6. Within the first subgroup, all the MOFs had the same MOC of *ca.* 0.8, with no statistically significant difference between them. Similarly, within the second subgroup, the average MOC was *ca*. 0.4, with no statistically significant difference between Zr-L5 and Zr-L6. Comparing the two subgroups shows that the degree of co-localisation of Zr-L5 and Zr-L6 was on average *ca*. 50 % lower than that of Zr-L2─Zr-L4. This result suggests that a significant quantity of Zr-L5 and Zr-L6 may be able to successfully avoid lysosomes and potentially release their cargo in the cytosol or other organelles.

Based on these results, there seems to be a correlation between the surface chemistry of MOF particles and their cellular uptake behaviour. Particle size seems to play a less prominent role. The results also show that while it is important to consider the uptake efficiency of a particle, it is also crucial to consider the endocytosis pathways it goes through. MOFs entrapped in endosomes or lysosomes do not contribute to the final aim of delivering drugs in the cytosol, even if they are taken up in large quantities. Zr-L3 for instance was the most successful MOF in terms of uptake efficiency; however, it was found mostly localised in lysosomes for further degradation. In contrast, Zr-L5 and Zr-L6, which had the lowest uptake efficiencies, could avoid lysosomes and potentially release their cargo in the cytosol. Orellana-Tavra *et al.* have tested the cytotoxicity of Zr-L1─Zr-L6 loaded with α-cyano-4-hydroxycinnamic acid (α-CHC) and found that there was no significant difference in viability for cells treated with empty and α-CHC-loaded Zr-L1 to Zr-L5, with viability remaining above 80 % for both conditions at any given concentration of MOF. For Zr-L6 however, α-CHC-loaded MOF decreased the viability down to 59 ± 5 % at a MOF concentration of 1 mg/mL, whereas the empty MOF was non-cytotoxic. This once again shows that uptake efficiency is not sufficient on its own to determine therapeutic efficacy. Even though Zr-L3 was more efficient than Zr-L6 at delivering cargo into the cell, it was less therapeutically active than the latter since most of the cargo ended up being degraded in the lysosomes. The results also show that it is not necessarily the amount of drug loaded

in the MOF that determines its efficacy, given that Zr-L1, which had a higher α-CHC loading than Zr-L6, was still less effective at killing cells[151]

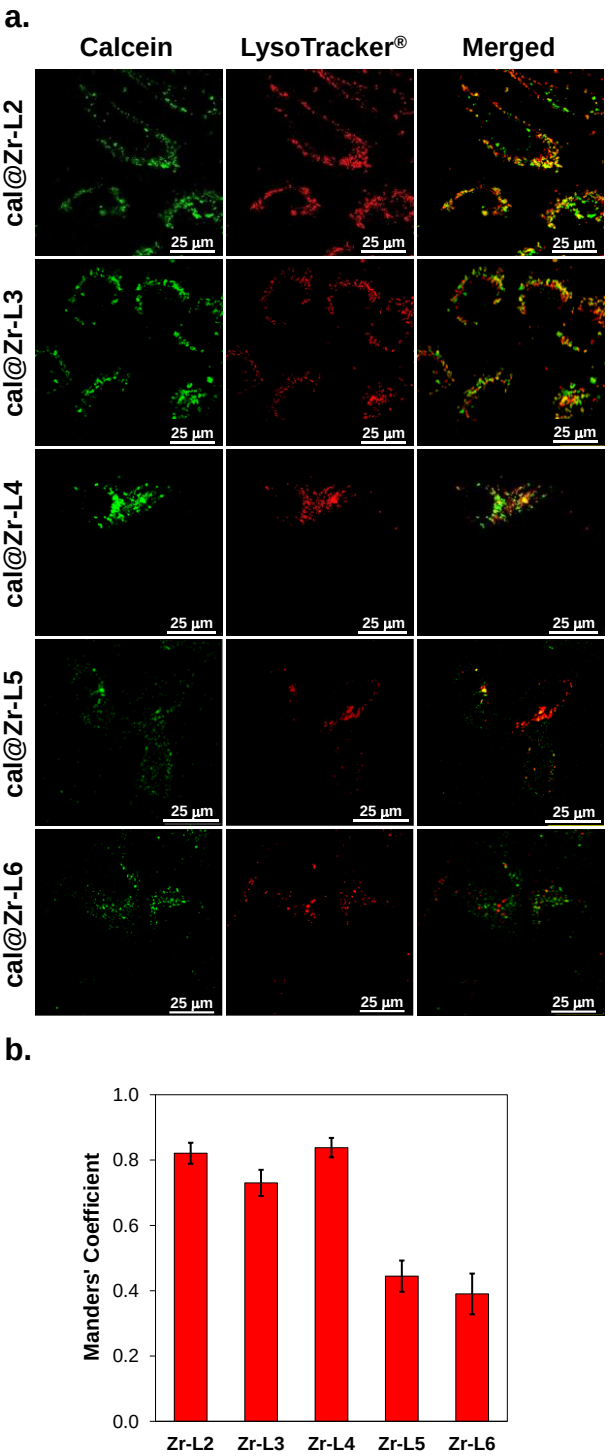

Figure 4.10. Confocal microscopy images of HeLa cells incubated with Zr-based MOFs (Zr-L2─Zr-L6) loaded with calcein (green fluorescence), and Lyso-Tracker Deep Red (red), for 2 h. (b) Manders' overlapping coefficient for all the MOF samples and the lysosomal marker. Error bars represent the standard error of at least 10 independent images.

4.3.2.2 Cellular Uptake of Post-Synthetically Modified Zr-L1 MOFs

Next, the cellular uptake behaviour of the post-synthetically modified Zr-L1-*func* particles was assessed. All the samples were derived from the same batch of Zr-L1, measured to be around 150 nm in size by SEM, thus allowing to isolate the effect of particle size. Through the choice of surface reagents (FA, Biot, Hep, Lact, PNIPAM, PEG500, and PEG2000), the goal was to rationalise the effects of hydrophilicity/hydrophobicity, targeting agents, and surface charge on HeLa cell internalisation pathways and therapeutic efficacy. The uptake efficiency of the surface-modified MOFs was assessed using flow cytometry. **Figure 4.11** shows the normalised intracellular fluorescence of HeLa cells after incubation with 0.5 mg/mL of the different MOFs for 2 h. The data was normalised to Zr-L1 cell internalisation, taking into account the different calcein loadings in every sample. Zr-L1-Biot was poorly internalised (37 ± 1 %), suggesting that biotin coating might not be desirable to enhance particle internalisation. Zr-L1-FA was the most efficiently internalised MOF (184 ± 2 %), followed by Zr-L1-Hep (171 ± 3 %), Zr-L1-PNIPAM (150 ± 1 %), Zr-L1-Lact (141 ± 2 %), Zr-L1-PEG2000 (98 ± 3 %), and Zr-L1-PEG550 (78 ± 3 %). HeLa cells overexpress the folate receptor on their surface[196], which might explain why coating the MOF with FA enhanced cellular uptake efficiency.

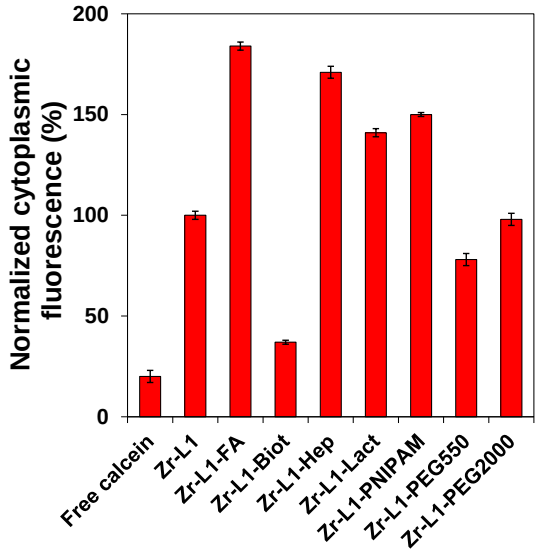

Figure 4.11. Normalised intracellular fluorescence of HeLa cells incubated with post-synthetically surface-modified Zr-L1-*func*. Error bars represent the standard error of at least 3 replicates.

The influence of endocytosis inhibitors on the cellular uptake of the post-synthetically modified MOFs was then analysed. **Figure 4.12** shows the intracellular

fluorescence of HeLa cells after incubation with each MOF in the presence of the pharmacological inhibitors (the specific value for each column is shown in the Appendix, **Table A2.1**). To determine if the differences were statistically significant, every value was compared to the control at 37 °C using one-way analysis of variance (ANOVA) followed by Dunnett's test to adjust for multiple comparisons. For all the MOFs, cellular uptake at 4 °C decreased between 40 and 86 % when compared to the control at 37 °C, indicating that the particles were taken up by energy-dependent endocytosis. The uptake of Zr-L1-Biot only decreased by 28 %, confirming the observations from the previous uptake experiments that it was not efficiently internalised by HeLa cells. For this reason, no further experiments were carried out with this sample. The uptake of uncoated Zr-L1 decreased to 37 ± 4 % and 27 ± 1 % when incubated with chlorpromazine (*clathrin*-mediated endocytosis inhibitor) and sucrose respectively. No effect was observed when cells were inhibited with nystatin (*caveolae*-mediated endocytosis), and only a minor effect was observed when incubated with rottlerin to inhibit macropinocytosis, indicating that Zr-L1 particles were internalised mostly by *clathrin*-mediated endocytosis. When cells were incubated with Zr-L1-FA and nystatin (*caveolae*-mediated endocytosis inhibitor), uptake decreased to 62 ± 2 %, whereas no inhibition was found when *clathrin*-mediated endocytosis was inhibited using chlorpromazine (96 ± 3 %), and only a minor effect (81 ± 5 %) was observed when rottlerin was used to inhibit macropinocytosis. Sucrose decreased the uptake to 36 ± 4 %. As mentioned previously, sucrose is non-specific inhibitor of *clathrin*-mediated endocytosis and can inhibit other pathways. These results indicate that the addition of FA to the surface of Zr-L1 alters cancer cell endocytosis selection pathways from *clathrin*-mediated endocytosis to *caveolae*-mediated endocytosis, and suggest that Zr-L1-FA samples have the potential to be efficient therapeutic DDS. Preferential uptake through *caveolae*-mediated endocytosis could be due to the fact that folate receptors have been reported to often be located within *caveolae* invaginations[196]. For Zr-L1-Hep particles, inhibition with nystatin decreased cellular uptake to 60 ± 1 %, indicating that they were partially internalised by *caveolae*-mediated endocytosis. However, and in contrast to Zr-L1-FA particles, particles were also taken up by *clathrin*-mediated endocytosis, with uptake decreasing to values of 70 ± 2 %. Inhibiting macropinocytosis decreased uptake to 83 ± 3 %; sucrose reduced internalisation to values of 41 ± 4 %.

In the case of the polymer-coated samples, inhibition of *clathrin*-mediated endocytosis using chlorpromazine had no significant effect on Zr-L1-Lact (84 ± 11 %) and Zr-L1-PNIPAM (105 ± 5 %), whereas it greatly reduced uptake down to 27 ± 2 % for both Zr-L1-PEG550 and Zr-L1-PEG2000. Sucrose reduced the uptake of all four particles by 46─72 %. With the exception of Zr-L1-PEG2000, rottlerin moderately decreased the uptake of the particles down to 80─85 %. Inhibition of macropinocytosis decreased the uptake of Zr-L1-PEG2000 to 45 ± 4 %. Using an inhibitor of *caveolae*-mediated endocytosis (nystatin) had no effect on Zr-L1-Lact (106 ± 13 %), Zr-L1-PNIPAM (103 ± 4 %), and Zr-L1-PEG550 (106 ± 3 %). However, it reduced the uptake of Zr-L1-PEG2000 down to 51 ± 2 %, showing that the PEGylated MOF was partially internalised through *caveolae*-mediated endocytosis. This again shows that the Zr-L1 internalisation pathway was significantly affected by the functionality attached to its surface, and the longer PEG chains ($M_n \approx 2{,}000$) allowed the MOFs to partially avoid lysosomal degradation. The amphiphilic nature of Zr-L1-PEG2000, in contrast to the hydrophilic surface of the uncoated sample, is thought to be more compatible with the *caveolae*-mediated route.

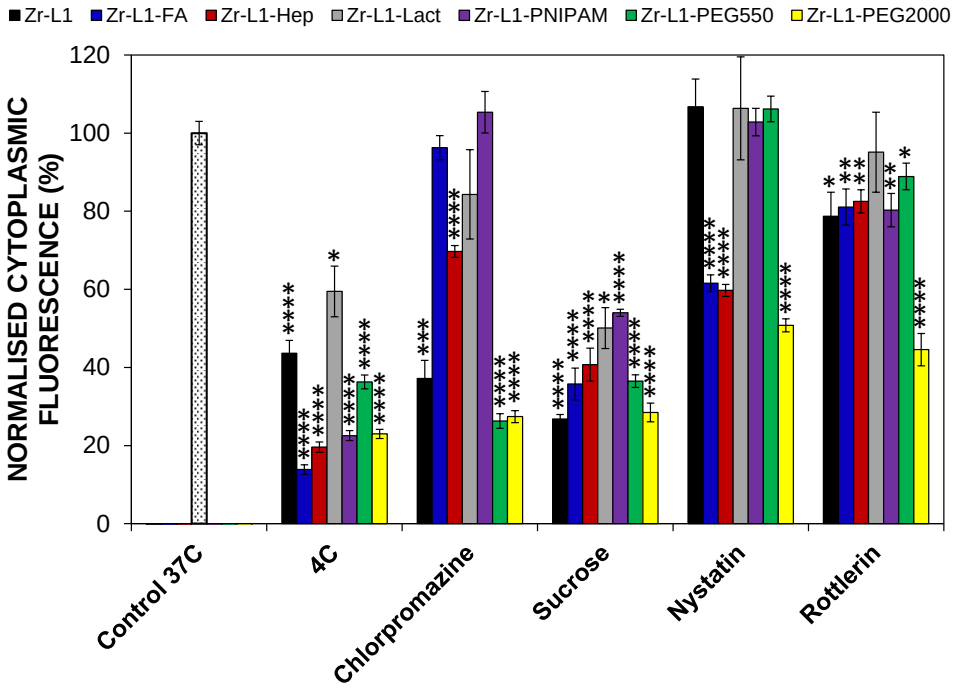

Figure 4.12. Effects of pharmacological endocytosis inhibitors on the uptake of post-synthetically surface-modified Zr-L1-*func* MOFs, measured by flow cytometry. Error bars represent the standard error of at least 3 replicates. Statistical significance was determined by one-way ANOVA and is indicated on top of each column. * $P \leq 0.05$, ** $P \leq 0.01$, *** $P \leq 0.001$, and **** $P \leq 0.0001$.

To investigate the consequences of surface coating on the therapeutic efficacy of the MOF particles, and relate the results to the endocytosis efficiency and uptake pathway studies, a small drug molecule with high metabolic anticancer activity[197,198], dichloroacetate (DCA), was introduced into the MOFs by using it as a modulator that attaches to UiO-66 metal nodes during synthesis[152]. DCA is thought to inhibit pyruvate dehydrogenase kinase (PDK), reversing cancer cell metabolism from aerobic glycolysis to oxidative phosphorylation[197]. The materials were named Zr-L1-DCA-*func*, where *func* is the functionality attached to the surface. The cytotoxicity of the materials was then tested on HeLa cells using the MTS enzymatic activity assay. Abanades-Lazaro *et al.* have shown that incubation with the empty surface-functionalised MOFs for 72 h did not lead to a decrease in HeLa cell viability. The exception was Zr-L1-PNIPAM, which was cytotoxic for concentrations above 0.25 mg/mL[153]. Any decrease in viability with the DCA-loaded materials can therefore be attributed to DCA. The viability of the cells after treatment with the DCA-loaded materials for 72 h is shown in **Figure 4.13** as a function of both MOF and DCA concentrations. Zr-L1-PEG550 was not tested due to an insufficient amount of material. The viability of HeLa cells incubated with non-functionalised Zr-L1-DCA did not decrease at concentrations up to 1 mg/mL MOF, even though this MOF had the highest DCA loading (16.9 wt %). Zr-L1-DCA-FA was toxic to HeLa cells starting at the MOF concentration of 0.75 mg/mL, decreasing the viability down to 74 ± 4 % at a MOF concentration of 1 mg/mL. This is consistent with the finding that Zr-L1-FA particles are taken up mostly by *caveolae*-mediated endocytosis (**Figure 4.12**). Zr-L1-DCA-Lact was more toxic than its folate-covered counterpart, inhibiting cell growth when incubated with 0.75 mg/mL MOF (85 ± 3 %), and killing almost all the cells at 1 mg/mL. This is despite the fact that it had lower uptake efficiency (**Figure 4.11**), was not taken up by *caveolae*-mediated endocytosis (**Figure 4.12**), and had a lower DCA loading as can be seen in **Figure 4.13b**. This could be indicative of its significant internalisation by energy-independent endocytosis, as supported by its high uptake even when cells are incubated at 4 °C. Although empty Zr-L1-PNIPAM was already found to be toxic at concentrations of 0.5 mg/mL and above[153], DCA loading enhanced its toxicity, with Zr-L1-DCA-PNIPAM killing almost all the cells at a MOF concentration of 0.25 mg/mL. Zr-L1-DCA-Biot and Zr-L1-DCA-Hep did not cause any decrease in viability even at MOF concentrations of 1 mg/mL. This is despite the fact that Zr-L1-Hep was shown to partially go through *caveolae*-mediated endocytosis (**Figure 4.12**). Looking at the viability results plotted

against DCA concentration however (**Figure 4.13b**), one can see that it is not possible to compare the toxicity of Zr-L1-DCA-Hep to that of Zr-L1-DCA-FA. This is because the DCA loading in Zr-L1-DCA-Hep was much lower, meaning that the DCA concentration was still within the range in which Zr-L1-DCA-FA was non-toxic. Zr-L1-DCA-PEG2000, which was shown to partially be taken up by *caveolae*-mediated endocytosis, was more toxic than uncoated Zr-L1-DCA, inducing significant cell death at MOF concentrations of 0.75 mg/mL and above (**Figure 4.13a**). It was also more toxic than Zr-L1-DCA-FA, despite having a *ca*. 50 % lower internalisation efficiency (**Figure 4.11**). Once again, the results show that a number of factors need to be considered when designing an efficient DDS, such as drug loading, internalisation efficiency, and endocytosis routes of entry.

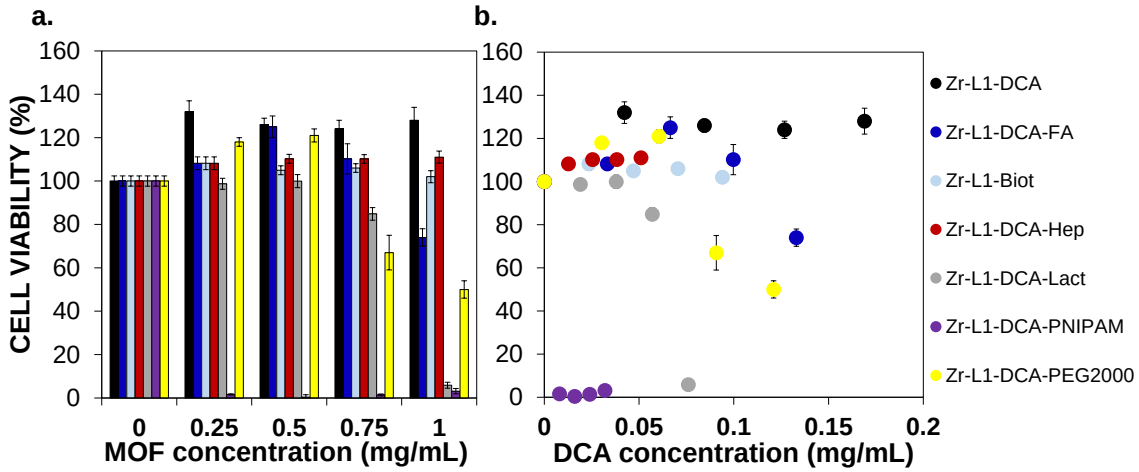

Figure 4.13. MTS viability assay measuring enzymatic metabolic activity of HeLa cells after 72 h incubation with post-synthetically functionalised Zr-L1-DCA-*func* particles. The results were plotted as a function of both DDS and equivalent DCA concentrations. The colour code is the same in both plots. Samples were run in minimum of six replicates. Standard errors are shown for each given data point. For some data points error bars are too small to be seen.

4.4 Conclusions

A range of Zr-based MOFs of different sizes and different surface chemistries were shown to enter cells through different endocytic pathways. It was demonstrated that control of surface chemistry, whether through linker functionalisation or post-synthetic attachment of functionalities, is critical to tune the pathways in which cells take up particles, whereas particle size does not exert a great influence here. It was shown that Zr-L1─Zr-L4 (functionalised BDC linkers), for example, were taken up mostly by *clathrin*-mediated endocytosis and ended up being degraded in the lysosomes, voiding their therapeutic effect. However, Zr-L5 and Zr-L6 (MOFs with extended linkers), although much less efficient at entering cells, were taken up through the *caveolae*-mediated route, enabling them to avoid lysosomal degradation, and to release their cargo in the desired intracellular location. This chapter also demonstrated that post-synthetic surface functionalisation can enhance cellular uptake and tune internalisation pathways to more desirable uptake routes. It was shown for example that FA-coated and PEG2000-coated Zr-L1 particles were more cytotoxic than uncoated ones, as a result of their uptake through the *caveolae*-mediated route. However, it was also found that particles that do not go through that route, such as Zr-L1-Lact, can also be toxic to cells. Additionally, particles that are taken up through the *caveolae*-mediated pathway are sometimes non-toxic to cells due to low drug loadings (Zr-L1-Hep). In summary, it is important to consider multiple factors, such as drug loading, internalisation efficiency, and routes of entry, when identifying suitable candidates for DDSs. Furthermore, while these studies have provided indications as to how to design efficient DDSs *a priori*, selection of suitable DDS candidates still needs to be made on a case by case basis by testing the final therapeutic efficacy of the materials. Guided by the findings of the present study, the next chapter explores the design and synthesis of a UiO-66-based mitochondria-targeted intracellular delivery system.

5 TARGETED INTRACELLULAR DELIVERY TO MITOCHONDRIA

5.1 Introduction

This chapter will assess the mitochondrial targeting ability and *in vitro* therapeutic efficacy of UiO-66 carrying a small drug molecule, dichloroacetate (DCA), and functionalised with a triphenylphosphonium (TPP) targeting moiety. In order to understand the motivation behind targeting mitochondria, **Section 5.1.1** describes these organelles, both at a structural and functional level, with a specific focus on their role in cancer. **Section 5.1.2** describes specific therapeutic targets in mitochondria. **Section 5.1.3** then gives the rationale behind using TPP as a mitochondrial-targeting agent.

5.1.1 Mitochondria in Cancer

Mitochondria play a key role in oncogenesis, and thus constitute promising targets for novel cancer treatments[199]. These maternally-inherited organelles are elongated membrane structures that are 0.5–1 μm in diameter and 1–10 μm in length, and consist of a mitochondrial matrix surrounded by an outer and inner membrane[200]. The outer membrane is highly negative ($\Delta\Psi$ = -150–200 mV), with a proton gradient across the inner membrane. Mitochondria are the energy powerhouse of cells. Non-cancerous mammalian cells normally produce their energy by oxidative phosphorylation

using the electron transport chain in the mitochondrial matrix. Cancerous cells, however, utilise glycolysis, even in the presence of oxygen[201]. This is due in part to a reprogramming of mitochondrial function that increases pyruvate dehydrogenase kinase (PDK) activity, which limits pyruvate uptake necessary for oxidative phosphorylation[202]. Targeting and reverting mitochondrial metabolism to oxidative phosphorylation is therefore an attractive strategy in cancer treatment.

In addition to regulating cellular metabolism, mitochondria are heavily involved in regulation of cell death, which can also be used as a therapeutic target in cancer therapy. Indeed, evasion of cell death is a trademark feature of cancer[203], and is a determining factor in tumour cell populations' ability to expand in numbers[204]. This is why activating the cell death machinery, and more specifically apoptosis, is an attractive target in cancer treatment. Apoptosis mostly involves proteases known as caspases, which are only activated when cell death is triggered. Once activated, caspases trigger a cascade of events that lead to the controlled demolition of cellular components[205]. Until then, they are held in check by inhibitors that act on them directly, or by inhibition and/or sequestration of their activators[206]. Permeabilisation of the mitochondrial outer membrane (MOM) causes the release of activators, namely cytochrome C, into the cytosol, where they trigger the caspase cascade, making treatment strategies that cause mitochondrial permeabilisation attractive[207–209]. This is especially true given that cancer cell mitochondria are structurally and functionally different than their normal counterparts, and are more susceptible to mitochondrial perturbations[210], making mitochondrial targeting a means to also selectively target cancer cells.

5.1.2 Therapeutic Targets in Mitochondria

As described in the previous section, mitochondrial defects are heavily involved in cancer. The correction of cancer-associated mitochondrial defects/dysfunctions and the reactivation of cell death programmes by pharmacological agents that induce mitochondrial membrane permeabilisation is therefore an attractive strategy for cancer treatments[207,208]. A number of drugs that are thought to act on the mitochondria have been discovered, developed, and investigated. They act on different targets, which will be discussed next.

5.1.2.1 Modulators of the B-cell Lymphoma Protein 2 (BCL-2) Protein Family

The BCL-2 family of proteins regulates the permeabilisation of the MOM and therefore acts as a gatekeeper in the apoptotic process. The family can be divided into three functional groups: anti-apoptotic proteins such as BCL-2, pro-apoptotic effectors such as BAX, BAK, and BOK, and pro-apoptotic activators such as BID, BAD and BIM. Effectors are proteins closely associated with the mitochondrial membrane, and when stimulated by activators promote the formation of pores in the mitochondrial membrane[211,212]. Anti-apoptotic proteins interact directly with pro-apoptotic effectors and activators to inhibit their effect[213]. This dynamic balance helps determine whether the cell initiates apoptosis[211]. A number of treatments targeting the BCL-2 family have shown great promise - most notably, ABT-737, which predominantly binds to and antagonises BCL-2, thus shifting the balance in favour of pro-apoptotic proteins[214–218]. Other treatments with a similar mechanism of action, such as Gossypol (AT-101), or Obatoclax (GX15-070), have shown significant potential[219,220].

5.1.2.2 Agents Targeting the Permeability Transition Pore Complex (PTPC)

The PTPC is a highly dynamic supramolecular system for which the exact structural identity is poorly understood[206]. It is formed of a number of constituents that can exist in multiple isoforms. These constituents are embedded across the mitochondrial membrane and into the mitochondrial matrix. Under physiological conditions, the PTPC exists in a low-conductance state, thereby allowing the controlled exchange of small solutes between the cytosol and the mitochondrial matrix. This low-conductance state is favoured by its interaction with anti-apoptotic BCL-2 proteins[221]. Drugs that can interact with the PTPC and cause it to assume a high-conductance state can cause the deregulated entry of small solutes into the mitochondrial matrix, driven by electrochemical forces. This in turn causes the immediate dissipation of $\Delta\Psi$ and osmotic swelling of the mitochondrial matrix, which ultimately leads to MOM permeabilisation and subsequent apoptosis[222,223].

5.1.2.3 Targeting Mitochondrial Metabolism

As mentioned in **Section 5.1.1**, approaches that reverse the hyperglycolytic state of cancer cells and prime them for cell death are attractive strategies for cancer treatment. DCA is a small molecule reported to have anti-cancer effects through its inhibition of pyruvate dehydrogenase kinase (PDK). This reverses cancer cell metabolism from aerobic glycolysis to oxidative phosphorylation[197]. This shift is

accompanied by a downregulation of the abnormally high mitochondrial membrane potential, reduced proliferation, and increased apoptosis of cancerous cells[224].

5.1.3 Triphenylphosphonium (TPP) as a Mitochondrial Targeting Agent

As discussed in **Section 5.1.2**, there are a number of therapeutic agents which can act on various components of the mitochondria. Finding a way to deliver these agents specifically to mitochondria could lead to more precise and effective cancer treatments. Emerging research in cancer therapy is focused on using the capacity of mitochondria-targeted cations (MTCs) to accumulate in mitochondria as a targeting approach[225–227]. Triphenylphosphonium (TPP) is one such MTC that has a number of advantages over other mitochondria-targeting agents: it has both lipophilic and hydrophilic properties, making it stable in aqueous media and able to cross biological membranes, has low reactivity with cellular components, and is relatively safe in humans, meaning it has high clinical potential and translational significance[228]. It is known to accumulate readily in the mitochondrial matrix of living cells − up to 100−1000 fold compared to the extracellular matrix − driven by the mitochondrial membrane potential[197].

The use of TPP-conjugated bioactive molecules in mitochondrial biology was pioneered and refined by Murphy and colleagues[229–231]. TPP was used to deliver probes, antioxidants, and pharmacological agents to mitochondria, with most approaches consisting of linking the active ingredient to TPP with a covalent bond in 1:1 stoichiometry. Representative examples are Mito-Doxorubicin (doxorubicin linked to TPP)[232], MitoQ (ubiquinone attached to TPP)[233], and Mito-Dicholoracetate (DCA conjugated to TPP)[234]. Another approach is to use mitochondria-targeting vesicles to deliver therapeutic cargo. This is typically done by functionalising the surface of particles carrying drug molecules with TPP. The advantage of such an approach compared to covalently linking TPP to drug molecules is the possibility of overcoming obstacles related to the use of free drugs, such as poor solubility, short half-lives *in vivo*, and non-selective biodistribution. A number of such nanocarriers have been developed and tested. TPP-modified liposomes for example have been used to deliver a wide range of bioactive molecules to mitochondria, and were shown to accumulate there[235,236]. TPP-functionalised polymeric dendrimers have also been shown to improve mitochondrial drug delivery[237]. These carriers have pitfalls that can be overcome using MOFs, as outlined in **Section 1.2.3**.

This chapter explores the design of DCA-loaded, TPP-functionalised UiO-66 particles, and investigates their therapeutic effect. The rationale behind using DCA as the therapeutic drug molecule was that it is also an excellent modulator of MOF crystal growth, and can be incorporated into the DDS by coordinating to the Zr-oxo clusters of UiO-66. Indeed, its lower pKa value (1.96) compared to the pKa of BDC (3.54 and 4.46) means that it can be attached to Zr positions in substantial amounts, even in the presence of other functionalised modulators. Its use as a modulator gives particles with good colloidal stability and reproducible control of particle size, as demonstrated in **Chapter 4**. Its cytotoxic effect will only be observed if MOFs are able to deliver cargo into the cytosol and subsequently reach the mitochondria. This allows experimental confirmation that therapeutically active DCA-loaded MOFs have been successfully internalised in a way that results in the DDS being localised in the cytosol, potentially reaching mitochondria, rather than in the lysosomes. As such, DCA is an excellent mechanistic probe for the therapeutic efficiency and cellular internalisation of MOFs. TPP was used as a targeting agent and is shown below to greatly increase the efficacy of the DDS.

5.2 Collaborative Work

Materials in this chapter were synthesised and characterised in collaboration with Dr Isabel Abanades-Lazaro from Dr. Ross Forgan's group at the School of Chemistry, University of Glasgow. Super-resolution microscopy was done in collaboration with Marcus Fantham from Professor Clemence Kaminski's group at the Department of Chemical Engineering and Biotechnology, University of Cambridge.

5.3 Results & Discussion

5.3.1 Synthesis and Characterisation of Mitochondria-Targeting DDS

To find candidate UiO-66 derivative MOFs that are suitable for drug delivery and that have optimal mitochondrial targeting properties, synthesis and characterisation of a range of UiO-66 materials containing DCA and TPP was performed. This section describes their assessment for suitability based on a number of factors, such as DCA and TPP incorporation, size, colloidal stability, and *in vitro* efficacy.

5.3.1.1 Functionalisation with TPP by Coordination Modulation

This present section investigates the suitability of targeted UiO-66 derivative MOFs prepared in a one-pot synthesis, through incorporation of (4-carboxybutyl)triphenylphosphonium and/or DCA (structures shown in **Figure 5.1**) by coordination modulation, i.e. by using them as modulators during synthesis, as described in **Section 2.2.1.3**. A version of TPP containing a carboxylic acid functionality was chosen to allow it to coordinate to the metal nodes. The resulting particles were termed DCA_x-TPP_y-UiO-66, where *x* and *y* are the molar equivalents relative to the linker in the initial reaction conditions of DCA and TPP, respectively. Where only DCA was used as a modulator, the materials were named DCA_x-UiO-66. Similarly, materials synthesised with only TPP as a modulator were termed TPP_y-UiO-66.

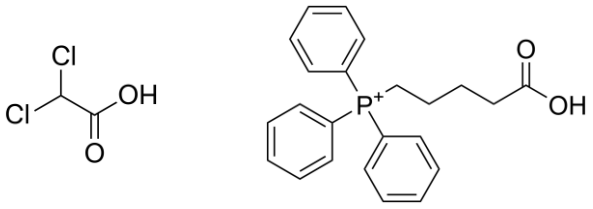

DCA **TPP**

Figure 5.1. Chemical structure of DCA (drug) and TPP (targeting agent), used as modulators in the synthesis of UiO-66.

PXRD was used to confirm the successful synthesis of the UiO-66 based MOFs by comparing their patterns with those obtained from single crystal X-ray structures. **Figure 5.2** shows the patterns for all the synthesised MOFs along with the calculated pattern. The positions of the main peaks in all the synthesised structures at $2\theta = 7.4°$, 8.6°, and 12.1° perfectly match those in the simulated structure. Additionally,

other observable peaks above $2\theta = 12.1°$ are also in agreement with the simulated structure, indicating successful synthesis of UiO-66 for all materials.

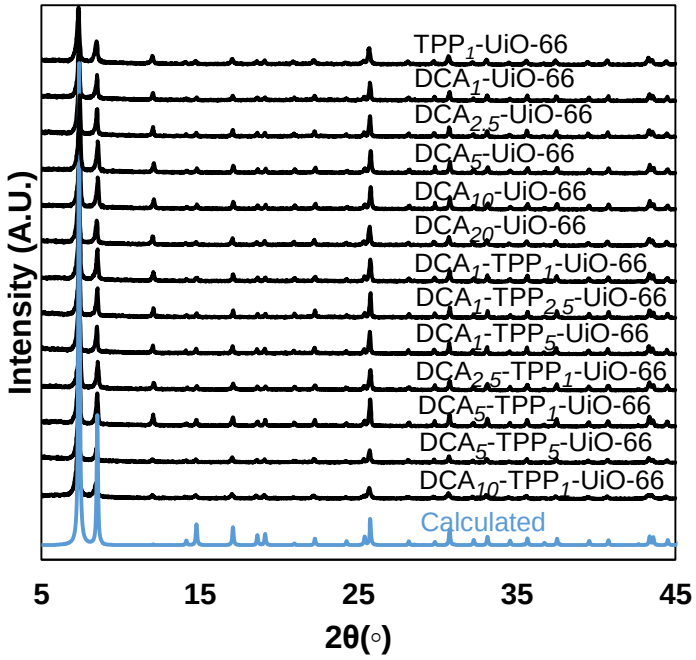

Figure 5.2. PXRD patterns of synthesised MOFs compared with their calculated pattern. Colour code of patterns: blue, calculated; and black, synthesised. Sample names are shown on top of patterns.

TGA of the synthesised samples was performed to estimate the attachment of both DCA and TPP. **Figure 5.3** shows the thermal degradation profiles of DCA$_x$-TPP$_y$-UiO-66 samples (black), TPP in its free form (purple) and UiO-66 synthesised with benzoic acid as a modulator – UiO-66 not containing any DCA or TPP, named UiO-66 (blue). The first derivative of the DCA$_x$-TPP$_y$-UiO-66 profile is shown in red. TGA of DCA in its free form was not possible due to practical limitations, DCA being a highly acidic substance in liquid form that cannot be placed in a pan for measurement. However, its decomposition temperature has been reported as 194 °C[238]. The results show that the decomposition of TPP in its free form occurred between 280 °C and 330 °C. The noticeable decomposition step in the same temperature range for all the DCA$_x$-TPP$_y$-UiO-66 samples can therefore be attributed to the loss of TPP from the structure. Based on the magnitudes of weight loss, the relative amounts of TPP in the different samples can be estimated. TPP$_1$-UiO-66 and DCA$_1$-TPP$_1$-UiO-66 for example showed smaller weight losses than DCA$_{10}$-TPP$_1$-UiO-66, suggesting lower TPP weight loadings. However, and based on the concentrations of the modulators

during synthesis, the opposite results were expected, i.e. TPP_1-UiO-66 and DCA_1-TPP_1-UiO-66 were expected to have more TPP in the MOF structure than DCA_{10}-TPP_1-UiO-66. The rationale behind this was that DCA and TPP compete for coordination to the metal nodes during crystal formation, meaning that with less competition from DCA, the same concentration of TPP (1 eq) would yield particles with higher TPP loadings. This discrepancy suggests that DCA might also be decomposing in the 280–330 °C range, and that TGA is not an adequate tool to quantify the weight loadings of both molecules due to the overlap.

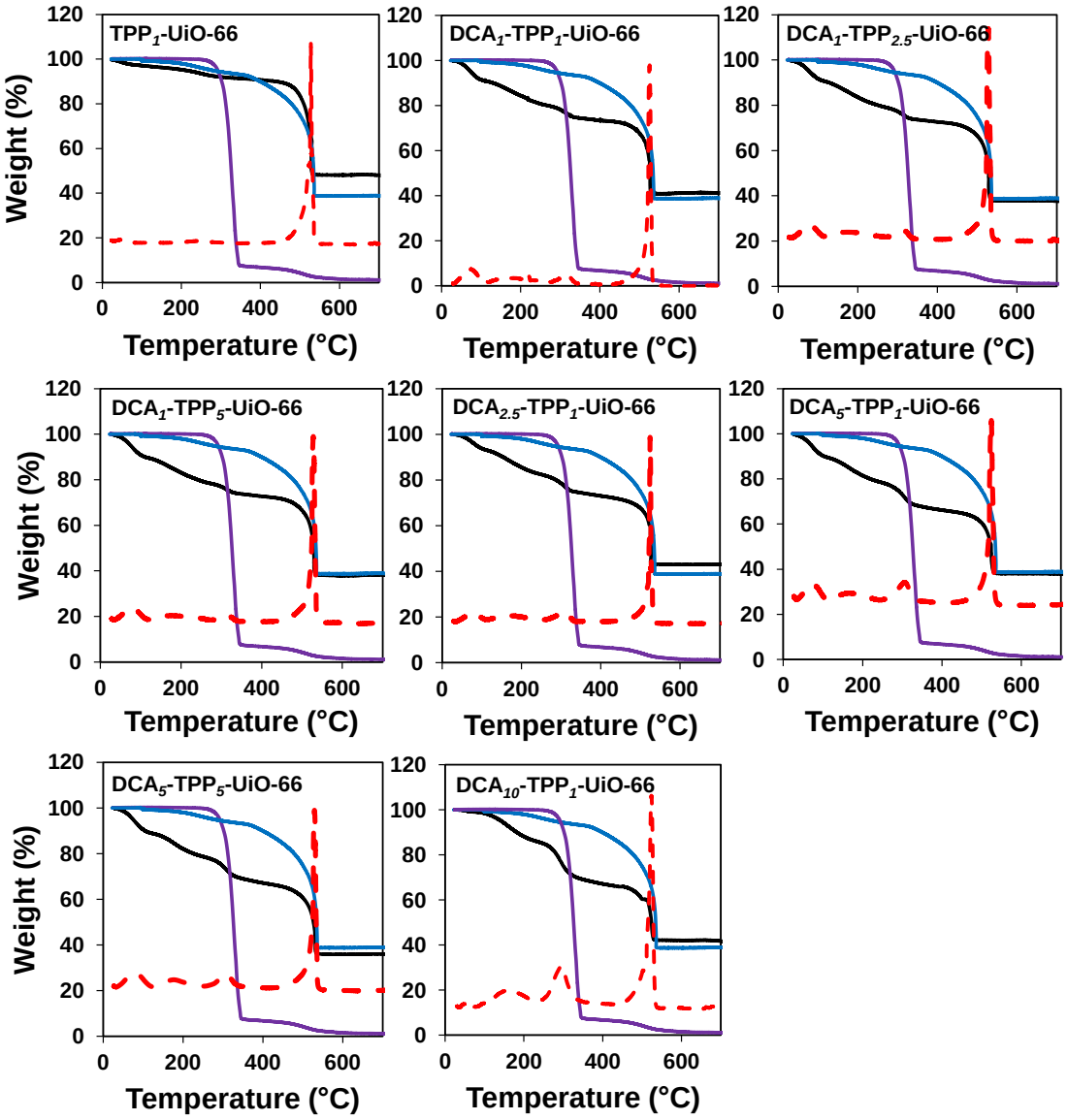

Figure 5.3. TGA of DCA_x-TPP_y-UiO-66 (black), UiO-66 (blue), and free TPP (purple), under air. The red dotted line represents the first derivative of the TGA plot of DCA_x-TPP_y-UiO-66.

To confirm that DCA also decomposes in the 280–330 °C range, TGA was performed on DCA_{10}-UiO-66, which does not contain any TPP. As can be seen in **Figure 5.4**, a decomposition step also occurs at temperatures around 280–330 °C even though the decomposition temperature of DCA in its free form is 194 °C. This shows that the decomposition of DCA when in the UiO-66 structure is different than when it is in its free form, suggesting that DCA is attached to the structure through coordination to the metal nodes rather than simply being adsorbed in the pores. This also suggests that the weight loss observed at 280-330 °C with the DCA_x-TPP_y-UiO-66 samples is due to the decomposition of both TPP and DCA at those temperatures, making it challenging to estimate the individual weight loadings from TGA.

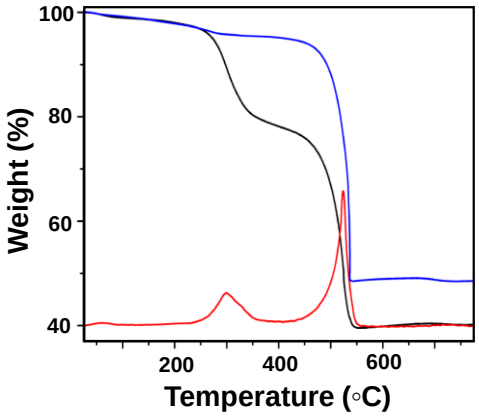

Figure 5.4. TGA of DCA_{10}-UiO-66 (black) and UiO-66 (blue) under air.

To better determine loading, another method was assessed. The chlorine atoms in DCA and the phosphorous atom in TPP allowed the quantification of these two molecules by ICP-OES. **Table 5.1** presents the values of DCA and TPP loadings in DCA_x-TPP_y-UiO-66 samples after deduction of the chlorine and phosphorus content of a blank sample of UiO-66, as well as their colloidal properties. DCA loadings ranged between 7.7 and 15.1 % for DCA_1-TPP_5-UiO-66 and DCA_5-TPP_5-UiO-66 respectively. TPP loadings ranged between 0 and 2.3 % for DCA_{10}-TPP_1-UiO-66 and DCA_5-TPP_5-UiO-66 respectively. DCA weight loadings were an order of magnitude higher than those of TPP, even though TPP is heavier than DCA (363 g/mol vs. 128 g/mol). This is explained by the difference in acidity between the two modulators. The lower pKa of DCA (1.96) means that it will be deprotonated more easily in the reaction mixture and hence compete much better than TPP (pKa = 4) for coordination to the metal nodes. For the DCA_x-UiO-66 samples, the incorporation of DCA into the MOF structure generally increased with increasing DCA concentration during synthesis,

from 6.7 wt % for DCA$_1$-UiO-66 to 46.8 wt % for DCA$_{20}$-UiO-66. For DCA$_x$-TPP$_y$-UiO-66 samples, it was expected that increasing the concentration of DCA for example while maintaining the concentration of TPP fixed would increase the level of DCA incorporation and reduce that of TPP, and *vice versa*. This is what was observed. For example, at a fixed TPP concentration of 1 eq, DCA incorporation increased with increasing modulator concentration, from 8.0 wt % for DCA$_1$-TPP$_1$-UiO-66 to 15.1 wt % for DCA$_{10}$-TPP$_1$-UiO-66, while TPP incorporation decreased from 0.8 wt % to 0 wt %. Similarly, fixing the DCA concentration and increasing the TPP concentration increased the amount of TPP incorporated in the MOF structure as well. However, and surprisingly, when going from using only DCA as a modulator to using both DCA and TPP, the attachment of DCA was improved. For example, DCA$_1$-TPP$_1$-UiO-66, DCA$_1$-TPP$_{2.5}$-UiO-66, and DCA$_1$-TPP$_5$-UiO-66 all have higher DCA loadings than DCA$_1$-UiO-66. This is counter-intuitive, as there should be fewer opportunities for DCA to coordinate to the zirconium nodes if TPP is present in the reaction mixture, as discussed before.

Table 5.1. Colloidal analysis of DCA$_x$-TPP$_y$-UiO-66 samples as well as their DCA and TPP loadings.

MOF	Particle size (nm)[a]	Effective diameter (nm)[b]	PdI	Z-Pot (mV)[c]	DCA (wt.%)	TPP (wt.%)
TPP$_1$-UiO-66	333 ± 175	2232 ± 438	0.67	-1.3 ± 0.2	0	1.2
DCA$_1$-UiO-66	236 ± 51	1524 ± 113	0.58	28.8 ± 0.9	6.7	0
DCA$_{2.5}$-UiO-66	139 ± 51	348 ± 4	0.21	35.5 ± 0.4	6.1	0
DCA$_5$-UiO-66	115 ± 48	308 ± 1	0.17	35.3 ± 0.4	10.0	0
DCA$_{10}$-UiO-66	81 ± 27	257 ± 1	0.17	35.4 ± 0.6	15.5	0
DCA$_{20}$-UiO-66	683 ± 27	4169 ± 706	1.00	31.5 ± 0.8	46.8	0
DCA$_1$-TPP$_1$-UiO-66	255 ± 108	5289 ± 367	0.73	48.2 ± 1.1	8.0	0.8
DCA$_1$-TPP$_{2.5}$-UiO-66	171 ± 52	4131 ± 78	0.70	43.0 ± 0.7	8.5	0.7
DCA$_1$-TPP$_5$-UiO-66	167 ± 46	2301 ± 130	0.64	44.2 ± 0.9	7.7	1.4
DCA$_{2.5}$-TPP$_1$-UiO-66	178 ± 64	4760 ± 205	0.47	33.4 ± 0.6	12.1	0.9
DCA$_5$-TPP$_1$-UiO-66	171 ± 36	913 ± 29	0.50	40.2 ± 0.3	14.5	0.5
DCA$_5$-TPP$_5$-UiO-66	131 ± 51	660 ± 26	0.51	42.2 ± 0.4	13.0	2.3
DCA$_{10}$-TPP$_1$-UiO-66	81 ± 18	323 ± 1	0.19	36.8 ± 0.7	15.1	0

[a]Measured by SEM – errors represent standard deviation of 100 particle sizes. [b]Measured by DLS in water. [c]Measured in water

Having confirmed the synthesis of the DDSs and the successful incorporation of DCA and TPP into them, SEM images were acquired in order to determine particle

size distributions. **Figure 5.5** displays these images. Mean particle sizes were determined, averaging across 100 particles per sample. The results are shown in **Table 5.1**, along with the standard deviations. Sizes ranged from 81–683 nm for DCA_{10}-UiO-66 and DCA_{20}-UiO-66 respectively. Generally, increasing the concentration of DCA gave smaller particle sizes. For example, for particles synthesised without TPP (DCA_x-UiO-66), increasing the concentration of DCA from 1 to 10 eq in the synthesis decreased particle size from 236 nm to 81 nm. When the DCA concentration was further increased to 20 eq however, the particle size jumped to 683 nm. Modulators of MOF crystal growth act by competing with the organic linker for coordination to the zirconium nodes. They have two antagonistic and co-occurring effects, promoting crystal growth by preventing nucleation through coordination to zirconium in solution, and limiting crystal growth by capping zirconium nodes on the surface of already formed particles. Within the range 1–10 eq, it seems that the capping effect of DCA is more dominant than the nucleation-preventing one for DCA_x-UiO-66 particles. Looking at the particles synthesised with both DCA and TPP as modulators, the same trend can be observed – fixing the TPP concentration and increasing DCA concentration led to smaller particle sizes. With the exception of DCA_{20}-UiO-66, all the samples were within the correct size range for cellular uptake, indicating their suitability for delivery applications.

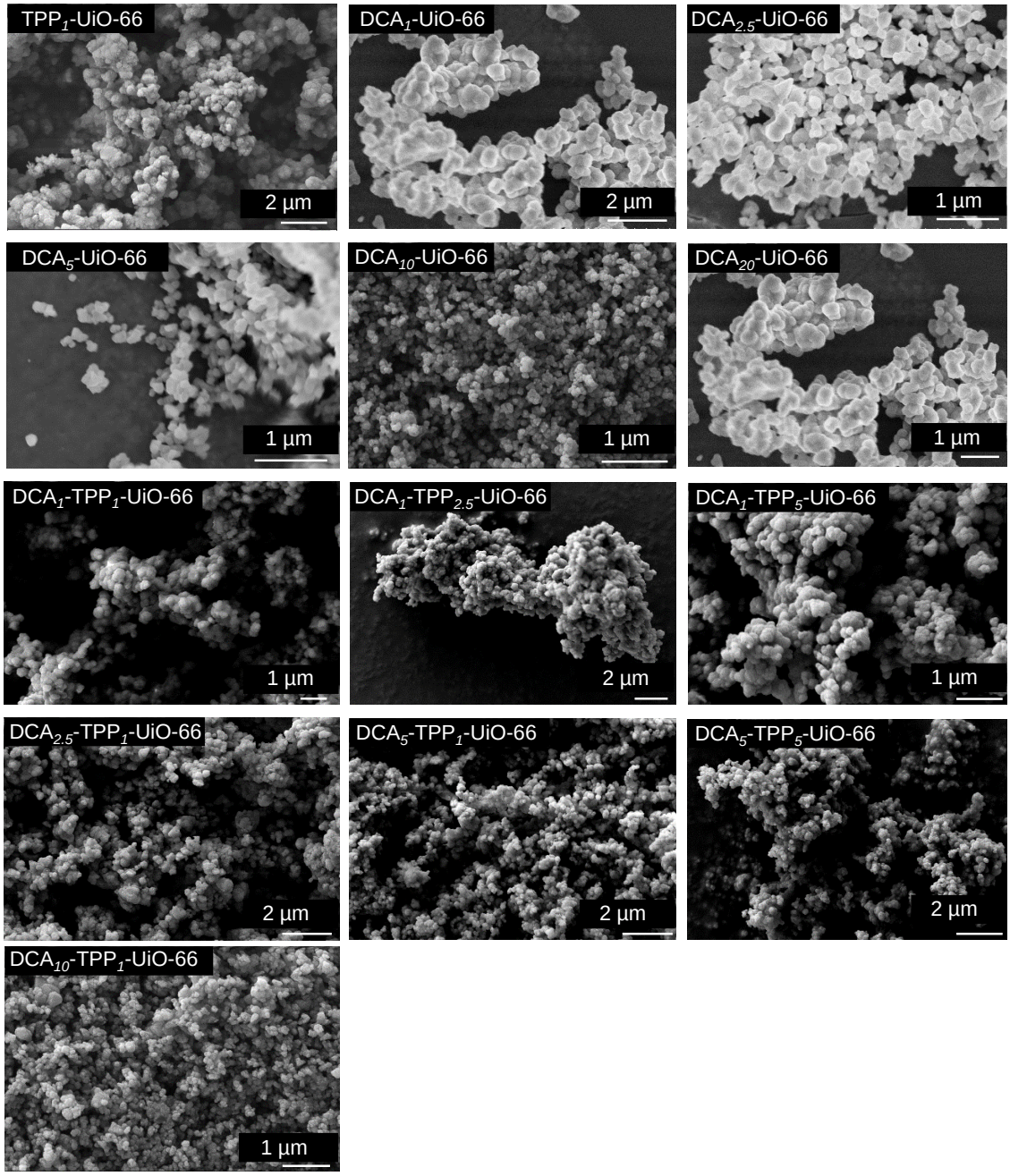

Figure 5.5. SEM of synthesised DCA_x-TPP_y-UiO-66 particles. Scale bar sizes provided on figure.

To better visualise the effect of modulator concentration on particle size, the latter was plotted as a function of DCA and TPP concentration (**Figure 5.6**). For all materials the concentration of DCA ranged from 0 to 10 eq, and the concentration of TPP ranged from 1 to 5 eq. For a fixed amount of TPP, increasing the concentration of DCA reduced particle size. For example, with 1 eq of TPP, the particle size decreased from 333 nm to 81 nm as the DCA concentration was increased from 0 to 10 eq. Additionally, a narrower particle size distribution was observed with increasing DCA

concentration, with the relative standard deviation of particle size decreasing from 53 % for TPP$_1$-UiO-66 (333 ± 175 nm), to 22 % for DCA$_{10}$-TPP$_1$-UiO-66 (81 ± 18 nm). The same trend was observed when fixing the TPP concentration at 5 eq and increasing the DCA concentration, e.g. particle size decreased from 167 nm for DCA$_1$-TPP$_5$-UiO-66 to 131 nm for DCA$_5$-TPP$_5$-UiO-66. When the DCA concentration was fixed and the TPP concentration increased, particle size increased when going from 0 to 1 eq TPP, but then decreased as the TPP concentration further increased. For example, fixing the DCA concentration at 1 eq and increasing TPP concentration from 0 to 1 eq increased particle size from 236 nm to 255 nm. When the TPP concentration was further increased, to 2.5 eq and 5 eq, particle size then decreased to 171 nm and 167 nm respectively. The jump in size when adding TPP to the reaction was observed for all the materials, except for particles synthesised with 10 eq DCA, i.e. DCA$_{10}$-UiO-66 and DCA$_{10}$-TPP$_1$-UiO-66, which had the same size of 81 nm. This suggests that for DCA$_{10}$-TPP$_1$-UiO-66, TPP had no role in the modulation of crystal growth, likely due to its inability to compete with high concentrations of DCA for attachment to the Zr nodes. The fact that no TPP was detected by ICP-OES in DCA$_{10}$-TPP$_1$-UiO-66 further confirms this.

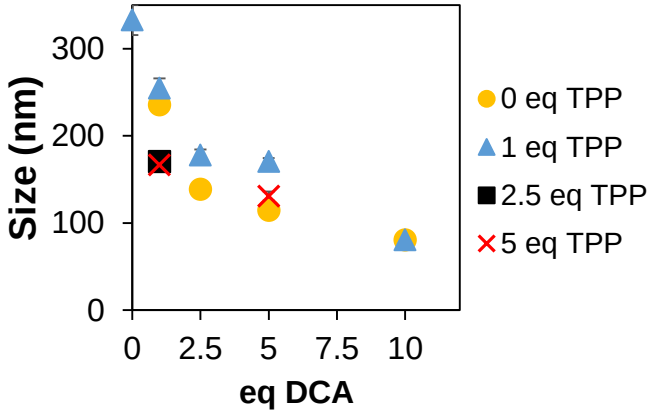

Figure 5.6. DCA$_x$-TPP$_y$-UiO-66 particle sizes determined from SEM as a function of DCA and TPP concentrations used in synthesis. Error bars represent the standard error of at least 100 size measurements. Where not visible, error bars are too small to be seen.

In addition to the particle size, colloidal stability is an important parameter to consider for intracellular delivery applications, as particles that aggregate cannot be taken up by cells. The zeta potential is an indicator of colloidal stability, as it determines inter-particle interactions, promoting or preventing attraction and aggregation. It also determines particle interaction with cells, determining uptake efficiency and endocytosis routes of entry as discussed in **Chapter 4**. The zeta potential was measured for all the

samples, and the results are shown in **Table 5.1**. Zeta potentials of DCA_x-UiO-66 particles synthesised without TPP ranged from 28.8 mV to 35.5 mV. $DCA_{2.5}$-UiO-66, DCA_5-UiO-66, and DCA_{10}-UiO-66 all had the same zeta potential at around 35.5 mV. DCA_1-UiO-66 and DCA_{20}-UiO-66 had lower zeta potentials at 28.8 mV and 31.5 mV respectively. Synthesis of DCA_x-TPP_y-UiO-66 with DCA and TPP as co-modulators gave particles with a wide range of zeta potentials, spanning 33.4 mV to 48.2 mV. It is noteworthy that all the particles had zeta potentials higher than +25 mV, suggesting that they are all colloidally stable in water[239]. Additionally, particles synthesised using TPP as a co-modulator had higher zeta potentials than particles synthesised using only DCA. This could be due to the increased number of defects in the crystal structure when using TPP as a co-modulator. The higher potentials suggest better colloidal stability for particles synthesised with TPP as a co-modulator.

To confirm the colloidal stability of the synthesised MOF particles, their hydrodynamic diameter was measured in water. The hydrodynamic diameter represents the effective particle size that cells 'observe' in solution. The results are shown in **Table 5.1**, and plotted in **Figure 5.7** as a function of DCA and TPP concentrations. Generally, the hydrodynamic diameter followed the same trend as particle size for all the samples. The exception was when going from 0 to 1 eq DCA at a fixed concentration of 1 eq TPP, where the hydrodynamic diameter greatly increased from 2,232 nm to 5,289 nm (**Figure 5.7**), whereas particle size was shown to decrease (**Figure 5.6**). This indicates that the addition of low concentrations of DCA makes particles less colloidally stable than ones synthesised with 1 eq of TPP alone. Synthesis with high concentrations of DCA however created particles that showed little aggregation, with DCA_{10}-TPP_1-UiO-66 for example having a hydrodynamic diameter of 323 nm, compared to 5,289 nm for DCA_1-TPP_1-UiO-66. For samples synthesised with only DCA as a modulator in the concentration range 1–10 eq, increasing the DCA concentration yielded particles that had smaller hydrodynamic diameters. The hydrodynamic diameter decreased from 1,524 nm to 257 nm as the concentration of DCA increased from 1 to 10 eq. With further increase of DCA concentration to 20 eq, the hydrodynamic diameter increased greatly to 4,169 nm (result not shown in graph for ease of visualisation), indicating that the particles become highly unstable in water when using high concentrations of DCA. Interestingly, the results show that synthesis with TPP as a co-modulator generally creates particles that are less colloidally stable than particles synthesised with DCA alone, i.e. DCA_x-TPP_y-UiO-66 particles had very

high hydrodynamic diameters and PdIs when compared to DCA$_x$-UiO-66 particles. This is in contrast to the trends predicted from the zeta potential results. Materials such as DCA$_5$-TPP$_5$-UiO-66 that had very high zeta potentials (48.2 mV) were also some of the most colloidally unstable. There generally does not seem to be a relationship between zeta potential and colloidal stability. All the particles had zeta potentials higher than +25 mV, but most of them were unstable. The only sample containing TPP that holds some potential for biological applications in terms of colloidal stability is DCA$_5$-TPP$_5$-UiO-66, even though it displayed some minor aggregation, with a hydrodynamic diameter of 660 nm and a PdI of 0.51. Materials synthesised without TPP such as DCA$_{2.5}$-UiO-66 (348 nm, PdI = 0.21), DCA$_5$-UiO-66 (308 nm, PdI = 0.17), and DCA$_{10}$-UiO-66 (257 nm, PdI = 0.17), are in the correct size range for biological applications and have suitable colloidal stability in water, thus presenting themselves as promising candidates for this application. In summary, the results suggest that incorporation of TPP by coordination modulation is not a suitable approach to create particles that do not aggregate, and that its post-synthetic attachment to colloidally stable DCA$_x$-UiO-66 might be a better alternative.

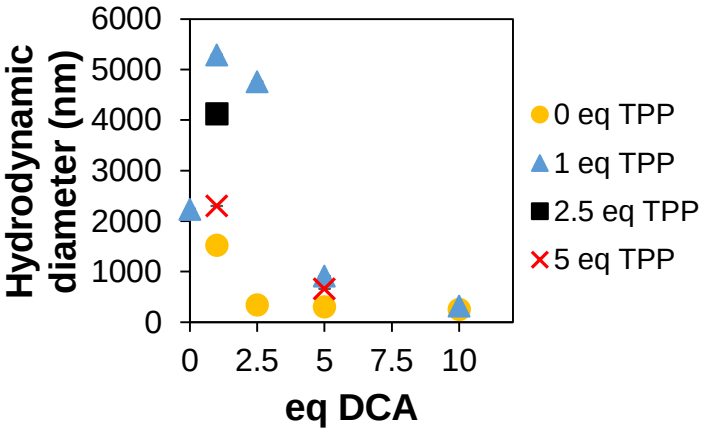

Figure 5.7. DCA$_x$-TPP$_y$-UiO-66 hydrodynamic diameters determined from DLS as a function of DCA and TPP concentrations used in synthesis.

The cytotoxicity of all the materials was tested in order to identify efficacious mitochondrial delivery systems, and relate the results to what was obtained previously regarding DCA and TPP loadings, particle size, and colloidal stability. The effect of the synthesised materials on breast adenocarcinoma MCF-7 cells and on human embryonic kidney HEK-293 cells was assessed by measuring their metabolic activity using an MTS reduction assay. **Figure 5.8** shows the cell viability after 72 h of MOF exposure at various concentrations. The viability values were plotted against both DDS

concentration and equivalent drug (DCA) concentration based on the loading values determined by ICP-OES. Using DCA_{20}-UiO-66 as an example (46.8 wt % DCA loading), in the range 0–1 mg/mL DDS, the equivalent DCA concentration ranged from 0–0.468 mg/mL. The reason for plotting against both the DDS and DCA concentrations is that it was uncertain at that point whether the toxicity was due to DCA alone or whether there were other properties inherent to the DDS such as aggregation, particle size, and charge that were also affecting the efficacy. Results for DCA_x-TPP_y-UiO-66 and DCA_x-UiO-66 were shown on separate graphs because the DCA concentration range for the latter was much higher. **Figures 5.8A, 5.8B, 5.8E, and 5.8F** show the cell viability of both MCF-7 and HEK-293 cell lines after treatment for 72 h with DCA_x-TPP_y-UiO-66 particles. The relative toxicity of the particles was more or less the same whether viability was plotted against DDS or DCA concentration (DCA_{10}-TPP_1-UiO-66 was the least toxic and DCA_1-TPP_1-UiO-66 the most toxic material). For DCA_x-UiO-66 particles, and looking at the results plotted against DCA concentration (**Figures 5.8D and 5.8H**), DCA_{20}-UiO-66 was the least toxic material. However, looking at the results plotted against DDS concentration (**Figures 5.8C and 5.8G**), this same material demonstrated the highest toxicity and led to the lowest cellular viability at all assessed DDS concentrations above 0.25 mg/mL, with viability at the highest concentration (1 mg/mL) of DDS decreasing to *ca*. 12 % and *ca*. 15 % for MCF-7 (**Figure 5.8C**) and HEK-293 (**Figure 5.8G**) cell lines respectively. This can be explained when considering that DCA_{20}-UiO-66 had a very high loading of DCA (46.8 wt %) compared to the rest of the materials, which had DCA loadings in the range 6.7–15.5 wt %. Plots against DCA concentration for both DCA_x-TPP_y-UiO-66 and DCA_x-UiO-66 materials (**Figures 5.8B, 5.8D, 5.8F, and 5.8H**), show that for a given DCA concentration, different materials had different toxicities, indicating that toxicity is not only dependent on the DCA concentration, and that there are other factors such as particle size or colloidal stability that could be affecting toxicity. Toxicity was higher for particles synthesised with a lower concentration of DCA as a modulator (DCA_1-TPP_y-UiO-66 particles were more toxic than $DCA_{2.5}$-TPP_y-UiO-66 particles, which were in turn more toxic than DCA_5-TPP_y-UiO-66 and DCA_{10}-TPP_y-UiO-66 particles), suggesting that there is some property of the DDS that is dependent on the concentration of modulator used that affects toxicity. As discussed in **Chapter 4**, properties affected by modulator concentration such as size and surface chemistry play a key role in determining how

effective a DDS is by influencing the cellular uptake and final intracellular fate of particles. Aggregation could also be a reason for observed toxicity, as the results show a correlation between hydrodynamic size and viability (the more toxic DCA_{1}-TPP_{y}--UiO-66 particles for example had larger hydrodynamic diameters than DCA_{10}-TPP_{y}-UiO-66 particles). An additional factor that could be affecting toxicity is the amount of TPP in the DDS. TPP is the molecule that has an affinity for mitochondria in the delivery system, meaning that larger amounts of incorporated TPP are expected to enhance mitochondrial targeting, thereby increasing the efficacy (cytotoxicity) of the DDS. The weight loading of TPP varied from sample to sample, with materials like DCA_{5}-TPP_{5}-UiO-66, which had the highest amount of incorporated TPP (2.3 wt %), counter-intuitively being one of the least toxic (**Figures 5.8A, 5.8B, 5.8E, and 5.8F**). Although TPP-containing materials were generally more toxic than particles synthesised without TPP (DCA_{10}-UiO-66 and DCA_{5}-UiO-66 were the two least toxic materials on MCF-7 and HEK-293 cell lines, whether plotted against DDS or DCA concentrations), there are too many variables that could be affecting the toxicity of the materials, making it difficult to isolate the effect of TPP as a targeting functionality. In order to eliminate aggregation and particle size as factors that could potentially be affecting the efficacy of the DDS, a different approach to incorporating TPP into the MOF structure was pursued.

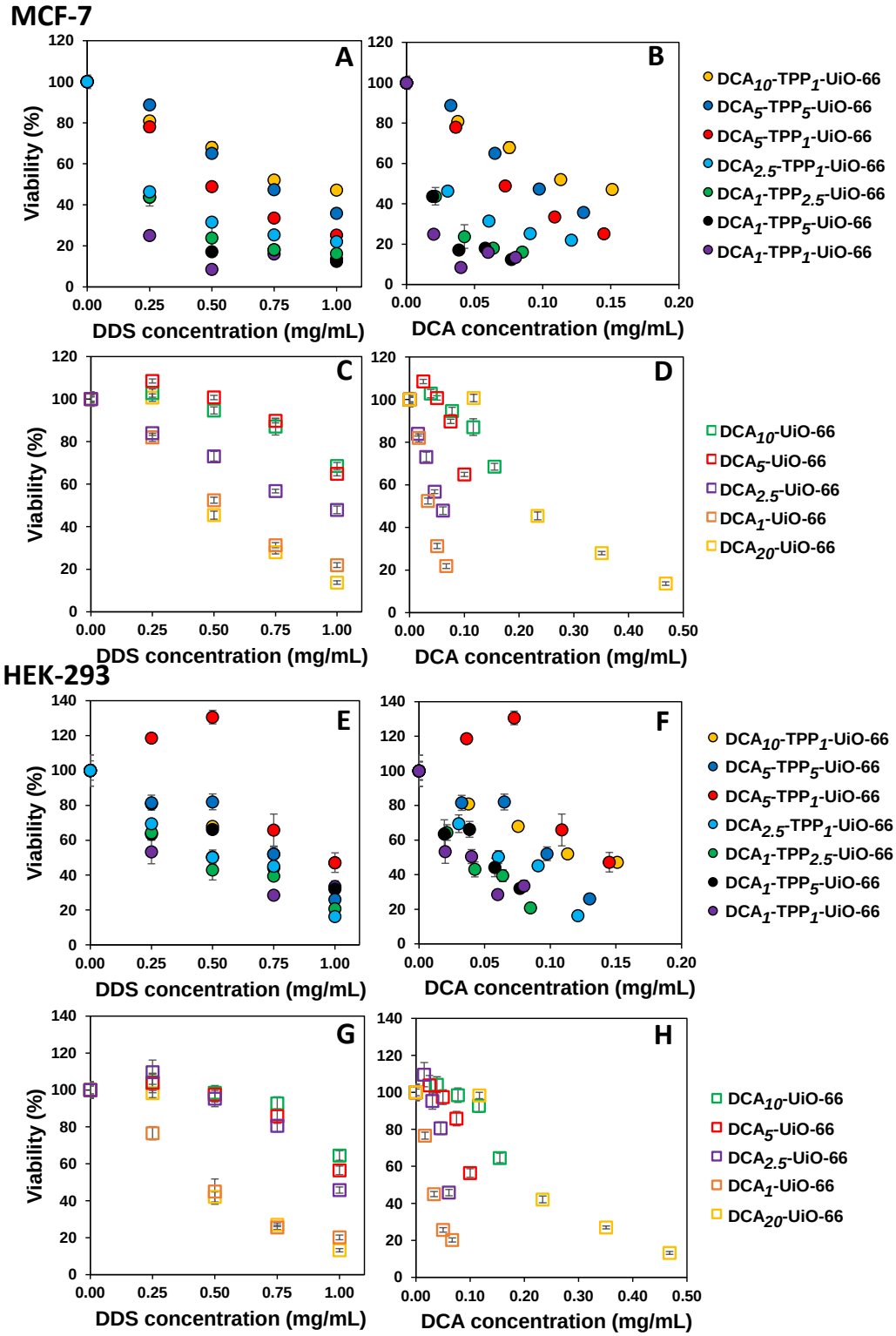

Figure 5.8. MTS viability assay measuring enzymatic metabolic activity of MCF-7 (A-D) and HEK-293 (E-H) cells after 72 h incubation with DCA_x-TPP_y-UiO-66 particles. The results were plotted as a function of both DDS and equivalent DCA concentrations. DCA_x-TPP_y-UiO-66 particles are represented by full circles (A-B-E-F). DCA_x-UiO-66 particles are represented by empty squares (C-D-G-H). Samples were run in minimum of six replicates. Standard errors are shown for each given data point. For some data points error bars are too small to be seen.

5.3.1.2 Functionalisation with TPP by Post-Synthetic Modification

To control the effect of particle size, improve the stability of the particles and eliminate the side effects of aggregation, TPP was post-synthetically attached to the DCA_x-UiO-66 particles which displayed suitable colloidal stability. As mentioned previously, DCA_{10}-UiO-66, DCA_5-UiO-66, and $DCA_{2.5}$-UiO-66 had hydrodynamic diameters of 257 nm, 308 nm, and 348 nm in water respectively, with PdI values ranging from 0.17–0.21. Different amounts of TPP were attached to the external surface of these three MOFs in order to also evaluate the quantity of TPP needed for improved cytotoxicity. **Table 5.2** shows that the resulting particles, named $TPP_{(++)}$@(DCA_x-UiO-66) and $TPP_{(+)}$@(DCA_x-UiO-66) for the high and low levels of TPP respectively, showed a slight increase in hydrodynamic diameter. For comparison, data for DCA_x-UiO-66 is included in **Table 5.2**. For $TPP_{(++)}$@(DCA_{10}-UiO-66) and $TPP_{(+)}$@(DCA_{10}-UiO-66), the hydrodynamic diameter increased by 18 and 23 % respectively relative to DCA_{10}-UiO-66, with PdI values increasing to 0.29 and 0.28. For $TPP_{(++)}$@(DCA_5-UiO-66) and $TPP_{(+)}$@(DCA_5-UiO-66), the diameter increased by 28 and 15 % respectively relative to DCA_5-UiO-66. PdI values increased to 0.35 and 0.33 respectively. For $TPP_{(++)}$@($DCA_{2.5}$-UiO-66) and $TPP_{(+)}$@($DCA_{2.5}$-UiO-66), the increase in hydrodynamic diameter relative to $DCA_{2.5}$-UiO-66 was by 35 and 40 % respectively, with PdI values of 0.35 and 0.36. Even though the hydrodynamic diameters for all the particles increased to 302–487 nm, they remained within the size range that cells can take up by endocytosis, while still displaying good colloidal stability.

Table 5.2 also shows that the post-synthetic attachment of TPP to the surface of MOFs reduced their zeta potential to the range 7.9–13.3 mV, down from around 35.5 mV for DCA_x-UiO-66 materials. This however, did not affect the colloidal stability of the particles, with particles still having hydrodynamic diameters within the range that cells can take up by endocytosis. Additionally, the post-synthetic attachment of TPP led to particles with TPP loadings (5.3–15.0 wt %) an order of magnitude higher than particles synthesised with TPP as a co-modulator (0.5–2.3 wt %). This is because in co-modulated syntheses, TPP has to compete with DCA and the BDC linker for coordination to the metal nodes. With post-synthetic attachment, TPP can adsorb to the external surface of the MOFs, and even replace some of the DCA or BDC molecules at the surface and coordinate to the zirconium clusters. Basification of the TPP solution before mixing with the MOF solution was done to de-protonate the TPP molecules and

allow for coordination with the metal nodes at the surface. TPP is hypothesised to only be found at the surface of UiO-66 because it is too large to fit through the *ca.* 6 Å windows[58].

Table 5.2. Colloidal analysis of samples with TPP post-synthetically attached, as well as their DCA and TPP loadings. (+) indicates samples post-synthetically modified with a TPP:MOF ratio of 1:4. (++) indicates samples modified with a TPP:MOF ratio of 1:1.

MOF	Effective diameter (nm)[b]	PdI	Z-Pot (mV)	DCA wt.%	TPP wt. %
$DCA_{2.5}$-UiO-66	348 ± 4	0.21	35.5	6.1	0
DCA_{5}-UiO-66	308 ± 1	0.17	35.3	10.0	0
DCA_{10}-UiO-66	257 ± 1	0.17	35.4	15.5	0
$TPP_{(+)}$@($DCA_{2.5}$-UiO-66)	487 ± 8	0.36	7.9	0.4	5.3
$TPP_{(++)}$@($DCA_{2.5}$-UiO-66)	471 ± 10	0.35	10	1.5	15.0
$TPP_{(+)}$@(DCA_{5}-UiO-66)	353 ± 5	0.33	13.3	0.4	6.3
$TPP_{(++)}$@(DCA_{5}-UiO-66)	394 ± 6	0.35	12.9	1.2	7.0
$TPP_{(+)}$@(DCA_{10}-UiO-66)	317 ± 7	0.29	15.1	1.3	11.0
$TPP_{(++)}$@(DCA_{10}-UiO-66)	302 ± 2	0.28	9.3	2.2	14.6

[a]Measured by SEM. [b]Measured by DLS.

The cytotoxicity of the post-synthetically modified particles was then tested to determine whether the incorporation of TPP into the DDS increases its efficacy. **Figure 5.9** shows the toxicity of these particles on MCF-7 and HEK-293 cells. Looking at the plots against DDS concentration for MCF-7 cells (**Figures 5.9A, 5.9B, and 5.9C**), it is clear that the addition of even low levels of TPP to the external surface of the MOFs dramatically increased the cytotoxicity of the materials, decreasing the viability at 1 mg/mL of DDS down to around 35, 26, and 23 % for $TPP_{(+)}$@(DCA_{10}-UiO-66) (green solid triangle), $TPP_{(+)}$@(DCA_{5}-UiO-66) (red solid triangle), and $TPP_{(+)}$@($DCA_{2.5}$-UiO-66) (purple solid triangle), respectively. Particles functionalised with high amounts of TPP ($TPP_{(++)}$@(DCA_{x}-UiO-66), solid squares) were slightly more toxic, indicating that very little TPP is needed at the surface for presumed mitochondrial targeting. In order to know the threshold level of TPP needed, $DCA_{2.5}$-UiO-66 was functionalised using a TPP solution that is five times less concentrated than the one used to prepare $TPP_{(+)}$@($DCA_{2.5}$-UiO-66), and its toxicity was tested on MCF-7 cells. The material was named TPP@($DCA_{2.5}$-UiO-66) and is shown in **Figure 5.9C**. After 72 h of incubation, the viability (*ca.* 42 % at 1 mg/mL DDS) decreased to an intermediate level between that of cells treated with

$DCA_{2.5}$-UiO-66 (purple dashed line) and of cells treated with both $TPP_{(+)}$@($DCA_{2.5}$-UiO-66) and $TPP_{(++)}$@($DCA_{2.5}$-UiO-66) (purple solid triangle and square). This suggests that only minute amounts of TPP are needed at the particle surface to observe an effect. When the viability values were plotted against equivalent DCA concentration (**Figures 5.9D, 5.9E, and 5.9F**), the materials displayed more or less the same level of toxicity regardless of the amount of TPP adsorbed on the surface, with viability dramatically decreasing even at low concentrations of DCA. Compared to the non-targeted DCA_x-UiO-66 particles (dashed lines), a much lower concentration of DCA (*ca*. 10-fold lower) was required to observe the same reduction in viability. For HEK-293 cells, **Figures 5.9G, 5.9H, and 5.9I** show that the surface attachment of low levels of TPP (solid triangles) did not increase the toxic effect of the DDS relative to non-functionalised DCA_x-UiO-66 particles (dashed lines), with viability also decreasing to around 60 % at 1 mg/mL DDS. However, when higher amounts of TPP were present at the surface as is the case for $TPP_{(++)}$@(DCA_x-UiO-66) particles (solid squares), the toxicity of the DDS increased significantly. $TPP_{(++)}$@(DCA_{10}-UiO-66), $TPP_{(++)}$@(DCA_5-UiO-66), and $TPP_{(++)}$@($DCA_{2.5}$-UiO-66) particles decreased the viability down to 48, 43, and 32 % respectively, at 1 mg/mL DDS. Viability plots as a function of DCA concentration however show that for a given DCA concentration, cell viability was the same for both $TPP_{(++)}$@(DCA_x-UiO-66) (solid squares) and $TPP_{(+)}$@(DCA_x-UiO-66) (solid triangles) particles, which again suggests that the quantity of surface TPP does not greatly affect the efficacy of the DDS and that only small amounts are needed (**Figures 5.9J, 5.9K, and 5.9L**). Given that the TPP-functionalised and non-functionalised particles have the same physical size and do not aggregate in solution, the increase in efficacy of the DDS can be attributed solely to the addition of TPP to the surface. Given that free TPP is non-toxic up to concentrations of 1 mg/mL (results shown in **Appendix 3, Figure A.3.1**), this increase in efficacy is hypothesised to be through particle direction to mitochondria. It is unclear however whether it is the DCA or MOF that is toxic to cells once the DDS reaches the mitochondria.

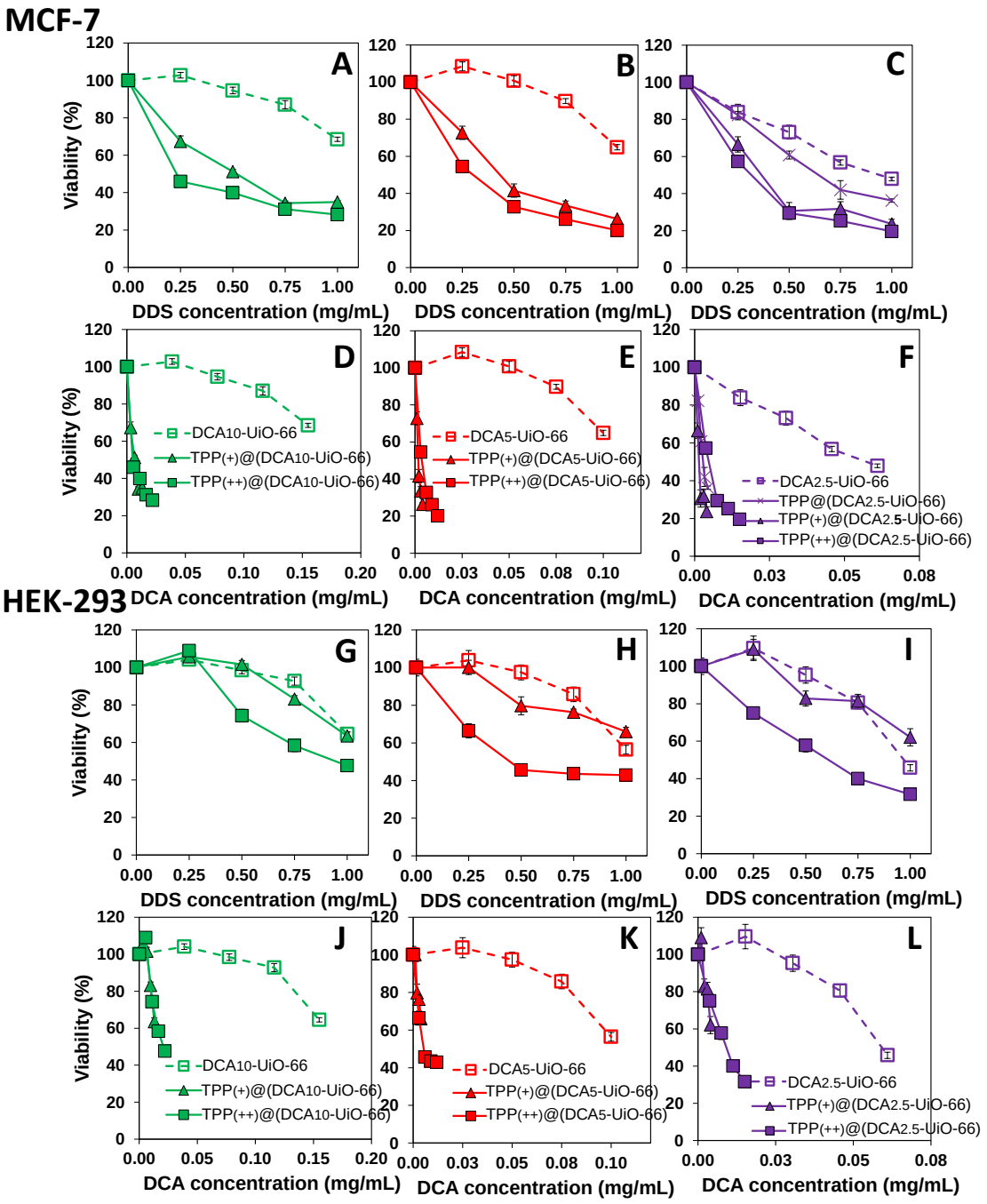

Figure 5.9. MTS viability assay measuring enzymatic metabolic activity of MCF-7 (A-F) and HEK-293 (G-L) cells after 72 h incubation with DCA$_x$-UiO-66 particles to which TPP was post-synthetically attached. The results were plotted as a function of both DDS and equivalent DCA concentrations. DCA$_x$-UiO-66 particles are represented by empty squares. TPP$_{(++)}$@(DCA$_x$-UiO-66) particles are represented by full squares. TPP$_{(+)}$@(DCA$_x$-UiO-66) particles are represented by full triangles. TPP@(DCA$_{2.5}$-UiO-66) is represented by a cross symbol. Samples were run in minimum of six replicates. Standard errors are shown for each given data point. For some data points error bars are too small to be seen. Lines help to guide the eye.

In order to investigate whether the MOF rather than the drug is toxic to cells when directed to mitochondria, UiO-66 with benzoic acid as a modulator was synthesised, TPP was attached to its surface (TPP@UiO-66), and the toxicity of the material was assessed using the MTS assay. Ideally, synthesis of UiO-66 without any modulator would have given the most accurate insight into the inherent toxicity of the particles. However, modulators are necessary for the synthesis of MOFs. Benzoic acid, which is very chemically similar to the terephtalic acid linker, was therefore chosen in order to avoid the use of modulators that would significantly alter the chemical properties of the MOFs, such as trifluoroacetic acid. The results are shown in **Figure 5.10**. Interestingly, UiO-66 synthesised with benzoic acid was found to be toxic, whereas previous results showed that particles synthesised with DCA as a modulator were not. However, the purpose of this experiment was to investigate whether the addition of TPP alters the toxicity of particles that do not contain DCA. For all DDS concentrations, the viability of MCF-7 cells decreased to the same level when incubated with both UiO-66 and TPP@UiO-66, indicating that the addition of TPP does not increase the toxicity of the MOF when it is not loaded with DCA. This supports the hypothesis that the increase in efficacy of the DDS seen in **Figure 5.9** is due to the DCA – or a synergistic effect of the MOF and DCA – and not the MOF alone.

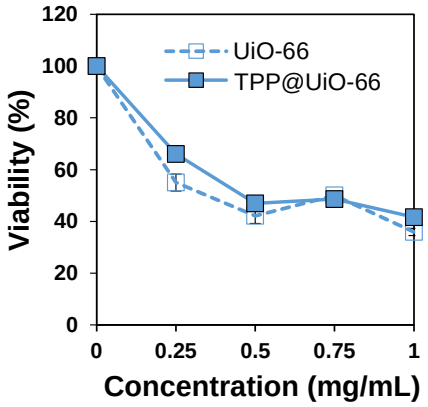

Figure 5.10. MTS viability assay measuring enzymatic metabolic activity of MCF-7 cells after 72 h incubation with UiO-66 and TPP@UiO-66. Samples were run in minimum of six replicates. Standard errors are shown for each given data point. For some data points error bars are too small to be seen. Lines help to guide the eye.

5.3.1.3 Toxicity Time Course Study Using Three Candidate MOFs

For the remainder of the study, three DDSs were chosen for further investigation of mitochondrial targeting abilities. TPP-containing materials functionalised both using coordination modulation and post-synthetic modification were included to study whether different modes of functionalisation lead to systems with different mechanisms of action. From the DDSs synthesised using TPP as a co-modulator, materials that aggregate were discarded from the study – only the colloidally stable DCA_5-TPP_5-UiO-66 was included. From the DDSs with TPP post-synthetically attached, which are all colloidally stable, $TPP_{(++)}$@(DCA_5-UiO-66) was further investigated. DCA_5-UiO-66 was included as a non-targeted control.

To investigate the kinetics of toxicity of the three candidate MOFs, a time course study was performed. **Figure 5.11** shows the viability determined by the MTS assay of MCF-7 and HEK-293 cells at different time intervals between 4 h and 72 h when incubated with various concentrations of the three materials. As with previous results, viability was plotted as a function of both DDS and DCA concentration in order to visualise both the effects of the vector (MOF) and drug (DCA) on cell viability. When studying the viability of MCF-7 cells in terms of total DDS concentration for the two materials containing TPP (solid red squares and blue circles), the toxicity was apparent as early as 4 h. Viability at the highest DDS concentration of 1 mg/mL decreased to 78 % and 66 % for DCA_5-TPP_5-UiO-66 and $TPP_{(++)}$@(DCA_5-UiO-66) respectively. Toxicity increased as time progressed, and stabilised between 8 and 48 h, as evidenced by the lack of change in the viability curves during these time points (viability remained at *ca.* 60 % and *ca.* 50 % at 1 mg/mL between 8 h and 48 h for DCA_5-TPP_5-UiO-66 and $TPP_{(++)}$@(DCA_5-UiO-66) respectively). There was a further decrease in viability at 72 h, with viability decreasing to 36 % and 12 % at 1 mg/mL for both MOFs. DCA_5-UiO-66 on the other hand, which does not contain TPP, remained non-toxic up to 48 h, showing only slight toxicity after 72 h at the highest concentration of 1 mg/mL (*ca.* 63 %).

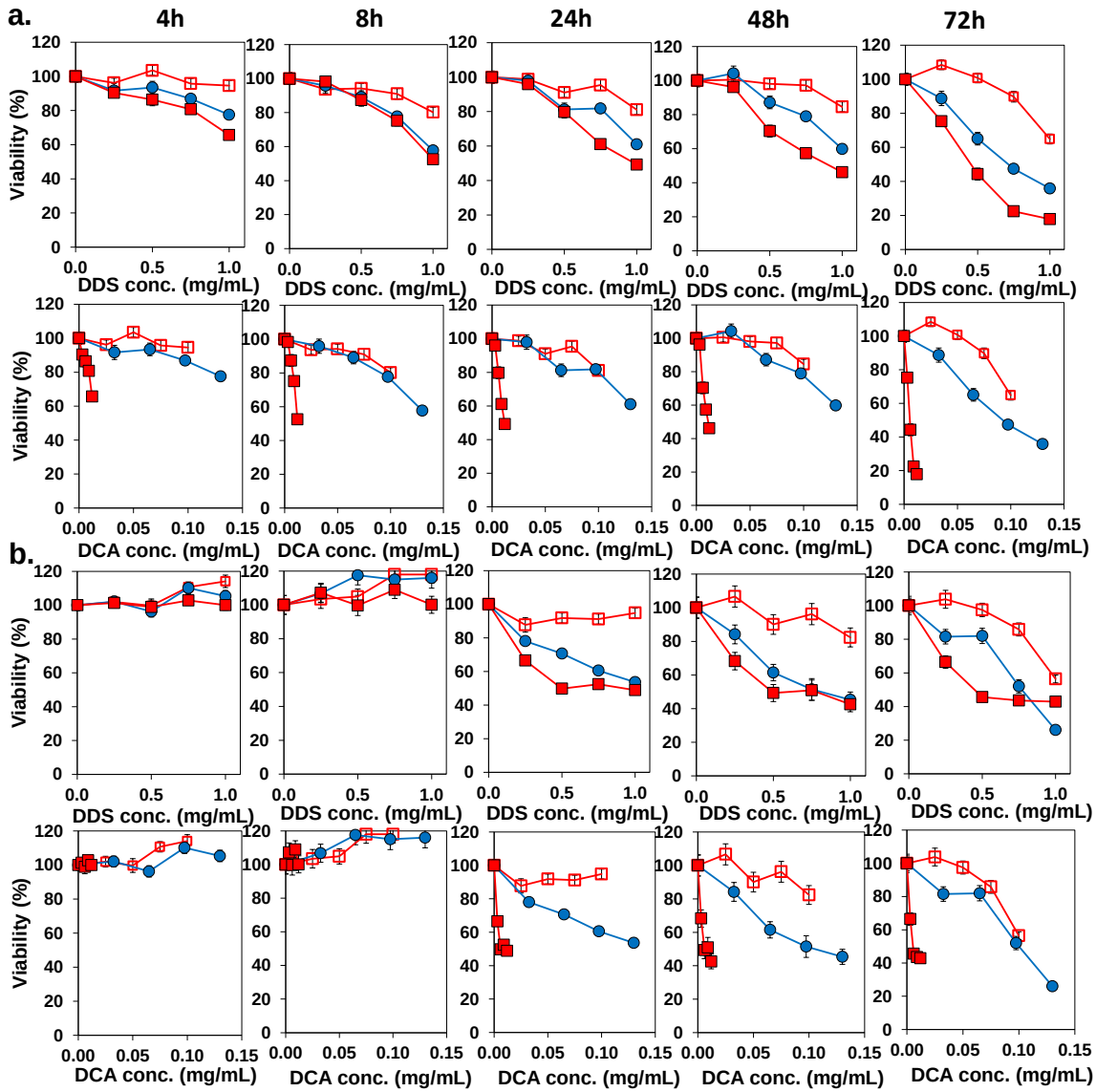

Figure 5.11. MTS viability assay measuring enzymatic metabolic activity of (a) MCF-7 and (b) HEK-293 cells after incubation with DCA_5-UiO-66 (empty red squares), DCA_5-TPP_5-UiO-66 (solid blue circles), and $TPP_{(++)}$@(DCA_5-UiO-66) (solid red squares), for 4 h, 8 h, 24 h, 48 h, and 72 h. The results were plotted as a function of both DDS and equivalent DCA concentrations. Samples were run in minimum of six replicates. Standard errors are shown for each given data point. For some data points error bars are too small to be seen.

When plotted as a function of DCA concentration, the same evolution was observed, with the difference being that $TPP_{(++)}$@(DCA_5-UiO-66) was the most toxic material and caused a sharp decrease in viability of MCF-7 cells even after 4 h of incubation. The toxicity of $TPP_{(++)}$@(DCA_5-UiO-66) was more pronounced when plotted against DCA concentration because the loading of DCA in this sample was much lower than in DCA_5-UiO-66 and DCA_5-TPP_5-UiO-66. While DCA_5-UiO-66

remained non-toxic even at the highest DCA concentration of 0.10 mg/mL (95 % viability), $TPP_{(++)}$@(DCA_5-UiO-66) decreased viability of MCF-7 cells to 90 % at a DCA concentration of 0.003 mg/mL (**Figure 5.11a,** 4 h) . At slightly higher concentrations of 0.012 mg/mL, viability after 4 h was further reduced to 66 %. DCA_5-TPP_5-UiO-66 was also more toxic than DCA_5-UiO-66, although this was only apparent after 72 h when plotted against DCA concentration, with viability at the highest DCA concentration of 0.13 mg/mL decreasing to 36 %. The reason DCA_5-TPP_5-UiO-66 appeared to be more toxic than DCA_5-UiO-66 at all measured time points before 72 h when plotted against DDS concentration was because the former had a higher drug weight loading (13.0 and 10.0 wt % respectively).

For HEK-293 cells (**Figure 5.11b**), DCA_5-UiO-66 was also non-toxic even at high concentrations and long incubation times. Viability only started decreasing at 72 h and at the highest DDS concentration of 1 mg/mL (*ca.* 57 %). For the two materials containing TPP (solid red squares and blue circles), there was a lag in toxicity at 4 h and 8 h when compared to MCF-7 cells, as the viability remained close to 100 % during this time. After this period (at 24 h), viability decreased to *ca.* 50 % at the highest concentrations of both DCA_5-TPP_5-UiO-66 and $TPP_{(++)}$@(DCA_5-UiO-66). Cells incubated with $TPP_{(++)}$@(DCA_5-UiO-66) did not experience any further drop in viability after that, whereas DCA_5-TPP_5-UiO-66 caused a further drop in viability to *ca*. 27 % at the highest concentration of 1 mg/mL at 72 h. This difference in behaviour between both MCF-7 and HEK-293 cell lines in the early and late stages of incubation can be due to a multitude of factors. Different cell lines can respond differently to identical conditions. Agents that induce apoptosis in one cell line might have no effect on the other. In some cases, even if the final result is the same (cell death), the death mechanisms might be different[240]. Even with an identical death mechanism, timelines for the progression of cell death can vary significantly from one cell line to another. For example, DNA fragmentation after apoptosis induction peaked at 6 hours for EL4 cells[241], but at 24 hours for HCE cells[242]. A lesser-known factor that might have an important effect is the cell culture conditions. High cell numbers seem to have a protective effect, with higher doses or longer incubation times required to initiate apoptosis. MCF-7 and HEK-293 cells have different growth rates, with doubling times at approximately 38 h and 24 h respectively, which might explain why the treatments have a much more pronounced effect for MCF-7 cells, especially early on.

In conclusion, the results of the present section (**Section 5.3.1**) have shown that the addition of TPP, whether by coordination modulation or post-synthetic modification, dramatically increases the efficacy of the UiO-66-based DDS. The targeted DDS is fast-acting, with toxicity apparent after 4 h for MCF-7 cells, and 24 h for HEK-293 cells. $TPP_{(++)}$@(DCA_5-UiO-66) is much more efficacious than DCA_5-TPP_5-UiO-66, with approximately 10 times less DCA needed to observe the same decrease in viability. Further *in vitro* studies were undertaken to better elucidate the mechanism of action of the studied DDSs.

5.3.2 Cellular Uptake Analysis Using Microscopy and Flow Cytometry

To confirm that TPP is directing the DDS to the mitochondria as hypothesised, the particles were tracked *in vitro* using light scanning confocal microscopy. For this, a DDS derivative equipped with fluorescent labels was synthesised. It has been shown in **Chapter 4** that the surface chemistry of MOFs plays a big role in determining the endocytosis pathways they go through. To avoid changing the surface chemistry, as is the case with the addition of a supplementary fluorophore, the TPP molecule was modified to have a fluorescent pyrene group (fTPP) following Tomas-Gamasa *et al.*'s protocol[103]. The replacement of one of the phosphonium's phenyl groups with a pyrene allowed to maintain TPP's required hydrophobicity/charge balance for mitochondrial targeting, as well as minimise the surface chemistry change of the DDS. fTPP was then post-synthetically attached to DCA_5-UiO-66, and was named fTPP@(DCA_5-UiO-66). In order to visualise mitochondria, MCF-7 and HEK-293 cells were transfected with CellLight Mitochondria-RFP, BacMam 2.0. This allowed for visualisation of mitochondria independently of mitochondrial membrane potential, as opposed to other more common mitochondrial stains. It also ensured that there was no interaction between the MOFs and the staining fluorophore, which could lead to falsely conclude that the MOFs are co-localised with mitochondria. The nuclei were stained with DRAQ5™. **Figure 5.12** shows the confocal images of MCF-7 and HEK-293 cells after 2 h of incubation with fTPP@(DCA_5-UiO-66) (green). Mitochondria are represented in red, and nuclei in blue. The individual channels are shown for each fluorescent label, as well as the merged images. In the merged images for both cell lines, some co-localisation between fTPP@(DCA_5-UiO-66) and RFP-labelled mitochondria was apparent, as illustrated by the yellow colour (overlap between green and red, shown by white arrows). Additionally, most of the non-overlapping signal originating from

fTPP@(DCA$_5$-UiO-66) was heavily concentrated around the mitochondria. These images suggest that the DDS is being directed to its intended target without necessarily being completely taken up by it, possibly due to the size of the DDS being too large for mitochondrial uptake. Given that the MTS viability studies have shown that a cytotoxic effect is observed using the targeted TPP$_{(++)}$@(DCA$_5$-UiO-66) (**Figure 5.11**), the images suggest that mitochondrial uptake might not be necessary to observe an increase in efficacy of DCA. The mere accumulation of particles near the mitochondria may cause high local concentrations of drug which are toxic.

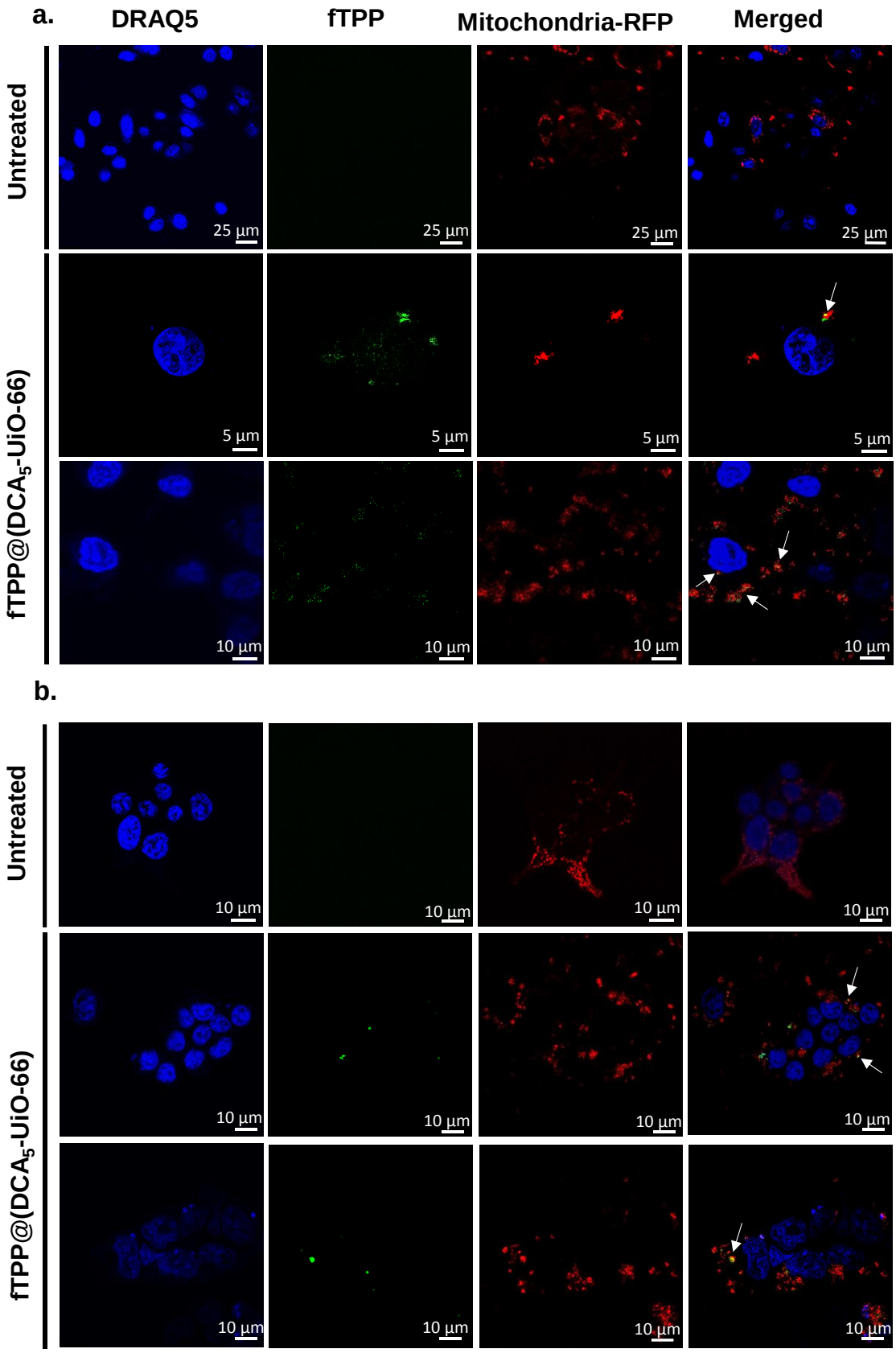

Figure 5.12. Confocal microscopy images of (a) MCF-7 and (b) HEK-293 cells incubated for 2 h with fTPP@(DCA_5-UiO-66) (green). Mitochondria are shown in red, and nuclei are shown in blue. White arrows show overlap between red and green signals.

In order to better visualise the interaction of the DDS with live cells, cells were imaged using structured illumination microscopy (SIM). SIM is a super-resolution microscopy technique that can capture images with a resolution of 100 nm, which is twice that of a traditional diffraction-limited microscope. Such resolution would allow to determine whether there is co-localisation more accurately than using confocal microscopy. The main obstacle with the SIM microscope is that it is incompatible with UV lasers as they can damage the spatial light modulator (SLP). This meant that fTPP, which excites in the UV, could not be used to track the system *in vitro*. $TPP_{(++)}$@(DCA_5-UiO-66) was therefore loaded with the fluorescent molecule calcein. To make sure that the surface chemistry change was minimal and that the DDS retained its main functionality, *i.e*. that calcein did not replace all the TPP at the external surface of the MOFs, the loading was performed in a methanolic calcein solution that also contained TPP at a concentration of 1 mg/mL. The resulting MOF was named cal-$TPP_{(++)}$@(DCA_5-UiO-66). **Figure 5.13** shows 3-colour images of MCF-7 cells in the presence of cal-$TPP_{(++)}$@(DCA_5-UiO-66) after 30 min and 8 h incubation. As with the confocal images, the nuclei were coloured in blue, the mitochondria in red, and the DDSs in green. These images show that the DDS was taken up by cells, as the red-coloured mitochondria and green spots of MOF particles are in focus in the same plane. Additionally, there is evidence that the cells have internalised some MOF even as early as after 30 min of incubation. After 8 h, the image shows that cells have taken up a considerably larger amount of MOF. In terms of localisation of the DDS, it is difficult to decipher from the images whether the MOFs with targeting agent are distributed close to mitochondria. This is because mitochondria are large organelles that occupy up to 25 % of the cytoplasm. However, some interesting mitochondria morphological characteristics, which can be indicative of cellular health[243], were apparent. Healthy cells are expected to have elongated mitochondria that form reticular networks. However, for cells treated with cal-$TPP_{(++)}$@(DCA_5-UiO-66), most mitochondria had a balloon-shaped morphology, and were remarkably short in length.

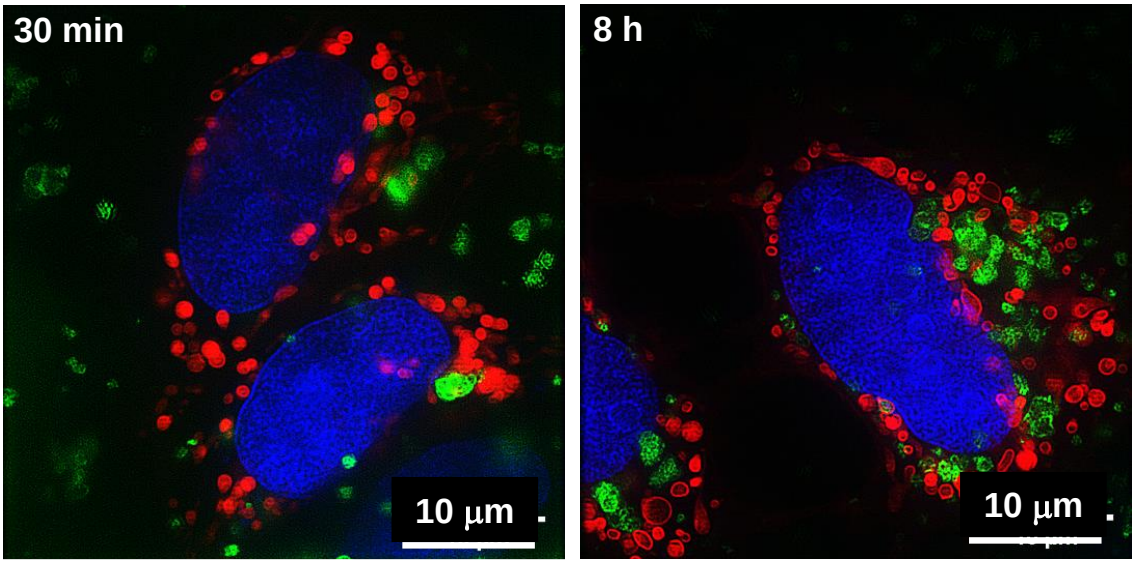

Figure 5.13. SIM images demonstrating cal-TPP$_{(++)}$@DCA$_5$-UiO-66 (green) internalisation into MCF-7 cells after 30 min and 8 h incubation. Mitochondria are coloured in red, nuclei in blue.

In order to probe the effect of the targeted DDS on mitochondrial morphology further, the effect of incubating MCF-7 cells with both targeted and non-targeted DDSs was investigated. For that, DCA$_5$-UiO-66 was also loaded with calcein. This system was named cal@(DCA$_5$-UiO-66). **Figure 5.14** shows 3-colour images of untreated cells, cells in the presence of cal-TPP$_{(++)}$@(DCA$_5$-UiO-66), and cells in the presence of cal@(DCA$_5$-UiO-66) after 8 h of incubation. **Figure 5.14a** shows that untreated cells' mitochondria were elongated and formed reticular networks, as expected. **Figure 5.14c** on the other hand shows that cells incubated with cal-TPP$_{(++)}$@(DCA$_5$-UiO-66) had short, ballon-shaped mitochondria. Incubation with cal@DCA$_5$-UiO-66 (**Figure 5.14b**) caused some mitochondria fragmentation; however, fragmentation was less severe than with cal-TPP$_{(++)}$@(DCA$_5$-UiO-66), and they still remained partially stringy and reticular, as shown by the white arrows in **Figure 5.14b**. By nature, mitochondrial morphology is very dynamic. Depending on cellular requirements, mitochondria are recycled in a dynamic equilibrium between opposing processes of fission and fusion[244]. Fusion produces extended interconnected mitochondria that form reticular networks, while fission produces shorter, balloon-shaped, fragmented mitochondria. Fission is required to control cell quality by replacing damaged mitochondria, and also facilitates apoptosis during high levels of cellular stress[245]. These morphological dynamics as well as the spatial localisation of mitochondria inside the cell are heavily linked to mitochondrial and cellular function, with a good balance of fission and fusion required

to maintain general cellular functionality. Kamogashira *et al.* for example have demonstrated a fundamental interdependence between mitochondrial metabolic activity and its network structure[245]. The fact that fragmentation of mitochondria has increased upon exposure to the targeted DDS indicates an imbalance between fission and fusion (fusion<fission). Some studies[245,246] have demonstrated a direct link between mitochondrial fission and mitochondrial degradation through mitophagy – a mechanism by which impaired or damaged mitochondria are encapsulated in autophagosomes that then fuse with lysosomes where they are degraded. Interestingly, fragmentation of mitochondria – indicating mitochondrial damage – was observed as early as 30 min after incubation with the targeted DDS, as can be seen in **Figure 5.13**.

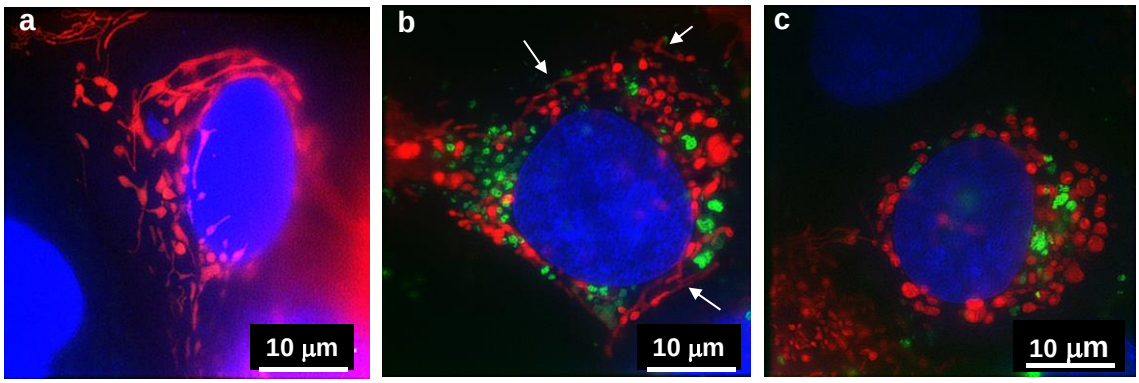

Figure 5.14. SIM images showing MCF-7 cells (a) untreated, (b) treated with cal@DCA_5-UiO-66, and (c) treated with cal-$TPP_{(++)}$@(DCA_5-UiO-66) for 8 h. Mitochondria are coloured in red, MOFs in green, and nuclei in blue. White arrows indicate stringy mitochondria.

In order to quantify fragmentation of the mitochondria, their eccentricity was assessed as described in **Section 2.3.8.1** using a custom designed pipeline for Cell Profiler[106]. Briefly, mitochondria were extracted as objects from the images and run through a plugin to gather information on the extracted objects' size and shape. Representative images showing the mitochondria objects as identified by the Cell Profiler pipeline along with their corresponding original SIM images are shown in **Figure 5.15**.

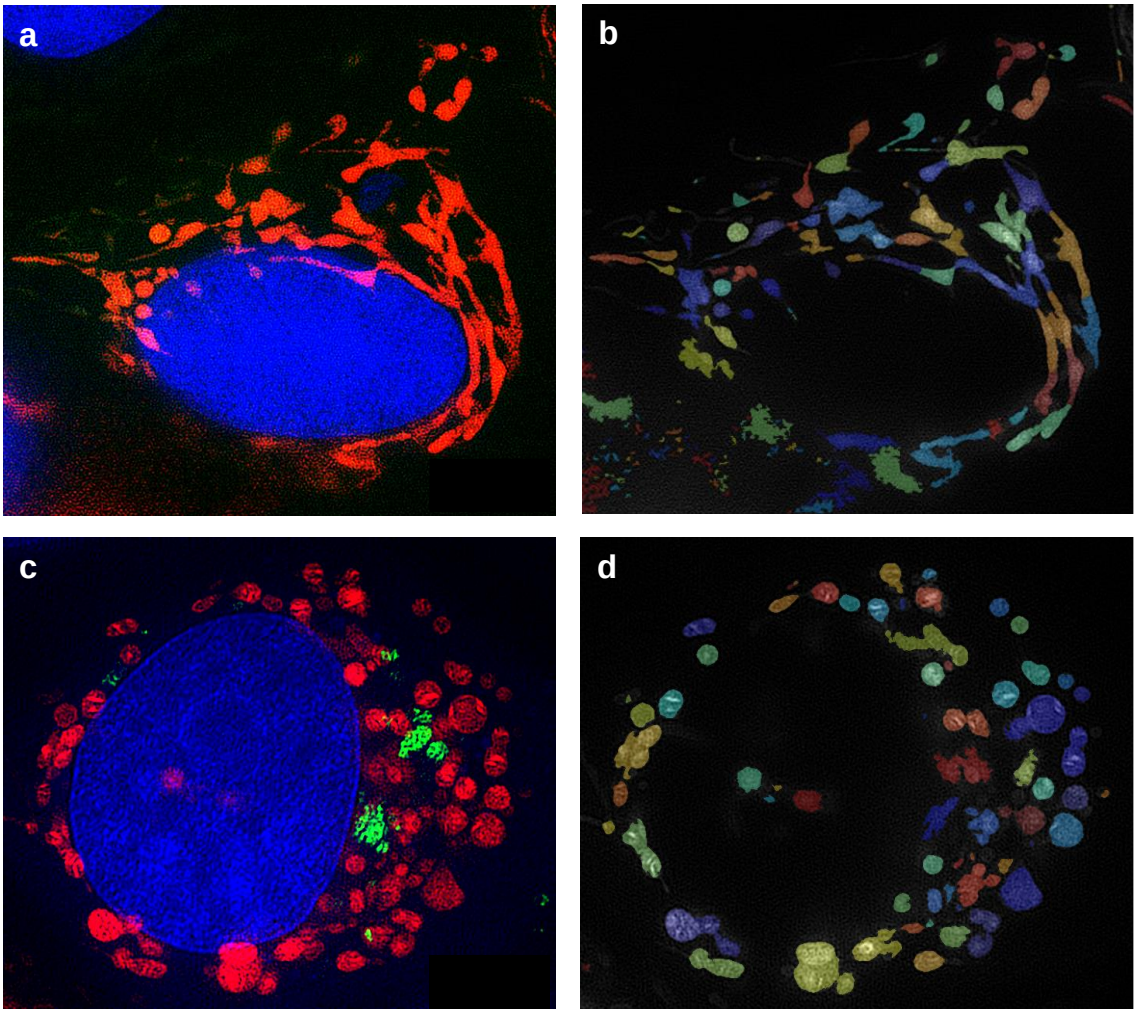

Figure 5.15. Images showing mitochondria shape analysis using Cell Profiler. (a-b) shows an untreated cell, (c-d) show a cell after 8 h of incubation with cal-$TPP_{(++)}$@(DCA_5-UiO-66). (a) and (c) show SIM images with mitochondria in red, MOF in green, and nuclei in blue. (b) and (d) show the mitochondria objects as identified by the Cell Profiler pipeline.

After applying the appropriate filters, data for eccentricity of the objects was analysed. Healthy cells were expected to have more elongated mitochondria whereas damaged ones were expected to have more rounded ones. The objects were assigned eccentricity values between 0 and 1 (the eccentricity of a circle is 0, and that of an ellipse that is not a circle is greater than 0 but less than 1). **Figure 5.16** shows the average eccentricity value for untreated cells, cells treated with cal-$TPP_{(++)}$@(DCA_5-UiO-66) for 30 min and 8 h, and cells treated with cal@(DCA_5-UiO-66) for 8 h. Statistical significance of the change in eccentricity relative to the control was assessed using one-way ANOVA followed by Tukey's test to adjust for multiple comparisons. As expected, healthy cells had the most eccentric mitochondria (0.819 ± 0.010). The fact that the error bars were large is indicative of a

wide distribution of eccentricity, which is consistent with the fact that mitochondria in healthy cells have a dynamic balance between fission and fusion. Cells treated with cal@(DCA$_5$-UiO-66) (no TPP) for 8 h had an average eccentricity of 0.793 ± 0.005, which was not significantly different than the untreated control. For cells treated with cal-TPP$_{(++)}$@(DCA$_5$-UiO-66), the eccentricity of the mitochondria was significantly reduced to 0.768 ± 0.004 after 8 h ($p = 0.0002$), indicating that the TPP-containing DDS had an effect on mitochondrial morphology. Interestingly, treatment with cal-TPP$_{(++)}$@(DCA$_5$-UiO-66) for only 30 min also led to a statistically significant change in mitochondrial eccentricity compared to untreated cells (0.786 ± 0.005, $p = 0.0267$), demonstrating that the system has a very rapid effect on cells. Treatment with the targeted DDS therefore seems to reduce mitochondrial fusion, leading to smaller mitochondrial entities, with the large number of small clusters present in the mitochondrial network attributable to the formation of autophagosomes[247].

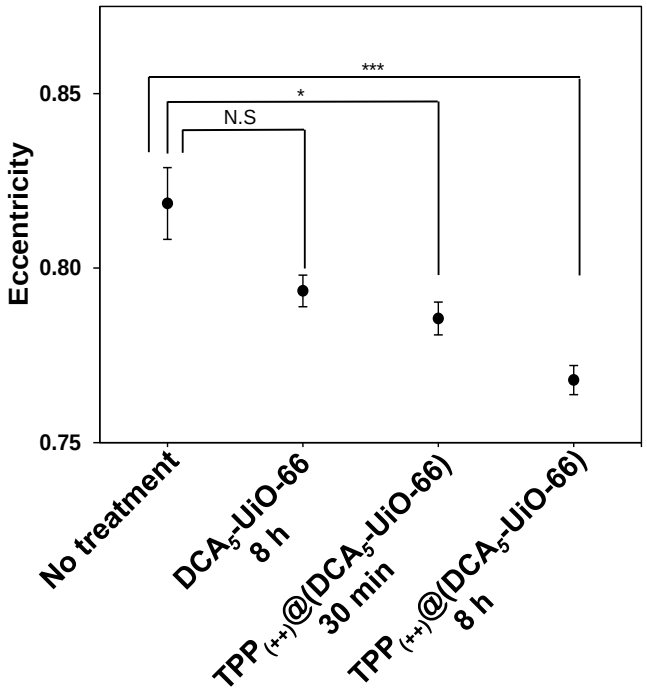

Figure 5.16. Effects of different treatments on the eccentricity of mitochondria in MCF-7 cells. A minimum of 200 mitochondria were studied. Error bars represent the standard error of the mean. Statistical significance was assessed using one-way ANOVA and Tukey's multiple comparisons test.

To understand whether TPP$_{(++)}$@(DCA$_5$-UiO-66) is more toxic than DCA$_5$-UiO-66 due to a difference in cellular uptake mechanism, the uptake pathway by

which MCF-7 cells take up these two MOFs was studied. As discussed extensively in **Chapter 4**, the intracellular fate of particles is dependent on the endocytosis pathway they go through, with particles taken up through *clathrin*-mediated endocytosis ending up being degraded in lysosomes (along with their drug cargo), whereas particles going through *caveolae*-mediated endocytosis can sometimes be released into the cytosol and avoid lysosomal degradation. The endocytosis pathways that the DDSs go through were studied by using pharmacological inhibitors, as described in **Section 2.3.9**, in a set up similar to **Chapter 4**. MCF-7 cells were incubated with either cal-TPP$_{(++)}$@(DCA$_5$-UiO-66) or cal@(DCA$_5$-UiO-66), the same two MOFs visualised with SIM. Sucrose and chlorpromazine were used to independently inhibit *clathrin*-mediated endocytosis, nystatin was used to inhibit *caveolae*-mediated endocytosis, and rottlerin was used hinder macropinocytosis. Cells were also incubated with the DDSs at 4 °C to ensure that uptake was happening through active – and not passive – transport. The intracellular fluorescence was measured using flow cytometry and normalised to a control uptake at 37 °C without inhibitors.

Figure 5.17 shows MCF-7 cells' internal fluorescence after incubation with the two DDSs in the presence of the different endocytic inhibitors. To determine if the differences were statistically significant, every value was compared to the control at 37 °C using one-way analysis of variance (ANOVA) followed by Dunnett's test to adjust for multiple comparisons. Cellular uptake of the MOFs was significantly reduced by *ca.* 80 % for cal@(DCA$_5$-UiO-66) and *ca.* 60 % for cal-TPP$_{(++)}$@(DCA$_5$-UiO-66) when cells were incubated at 4 °C. Cellular metabolism is greatly slowed down at this temperature, which confirms that the particles are taken up by the active mechanism of endocytosis. When incubated with chlorpromazine, particle uptake did not decrease significantly for cal@(DCA$_5$-UiO-66), whereas there was a moderate decrease to 69 % for cal-TPP$_{(++)}$@(DCA$_5$-UiO-66). When incubated with hypertonic sucrose, particle uptake decreased significantly to 28 % and 40 % for cal@(DCA$_5$-UiO-66) and cal-TPP$_{(++)}$@(DCA$_5$-UiO-66) respectively. As mentioned in **Chapter 4**, although sucrose is a known inhibitor of *clathrin*-mediated endocytosis[185], there is evidence suggesting that it is non-specific[187], which might explain why a much larger degree of inhibition was observed when cells were incubated with sucrose as compared to chlorpromazine. Inhibition with nystatin (*caveolae*-mediated endocytosis) showed no statistically significant decrease in intracellular fluorescence with respect to the controls for both cal@(DCA$_5$-UiO-66) and cal-TPP$_{(++)}$@(DCA$_5$-UiO-66). Rottlerin significantly

decreased the uptake of cal@(DCA$_5$-UiO-66) to 56 %, whereas it did not affect the uptake of cal-TPP$_{(++)}$@(DCA$_5$-UiO-66). These results suggest that cal@(DCA$_5$-UiO-66) is internalised mostly by *clathrin*- and *caveolae*- independent endocytosis (mostly macropinocytosis), whereas cal-TPP$_{(++)}$@(DCA$_5$-UiO-66) is internalised mostly by *clathrin*-dependent endocytosis. The literature offers conflicting data about the selection of endocytic pathways for charged particles. However, studies on HeLa cells using charged NPs support *clathrin*-mediated endocytosis for positively charged particles[189], which might explain why adding TPP to the surface of the MOF leads to this internalisation route. With regards to the final intracellular fate of the particles, and as discussed in **Chapter 4**, particles taken up by *clathrin*-dependent endocytosis end up being degraded in lysosomes along with their cargo, voiding their therapeutic effect. However, TPP$_{(++)}$@(DCA$_5$-UiO-66) is clearly able to reach its intended target despite being taken up by *clathrin*-dependent endocytosis, as demonstrated by its toxicity to MCF-7 cells. This could be due to the ability of positively-charged TPP to act as a proton sponge and promote endosomal escape[248] and the subsequent delivery of cargo into the cytosol.

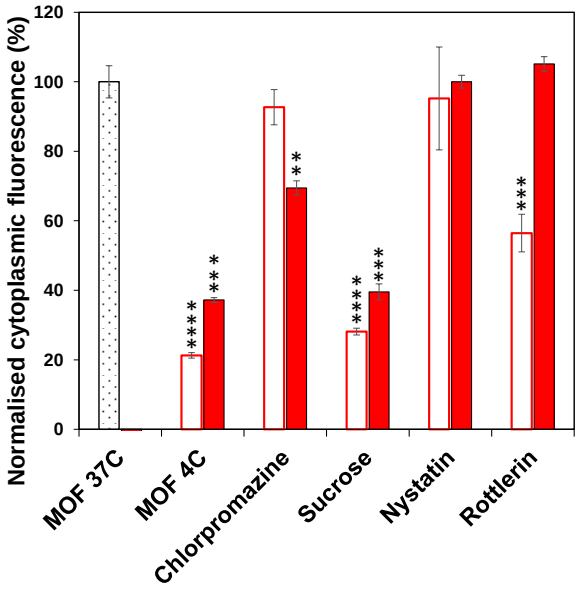

Figure 5.17. Effects of pharmacological endocytosis inhibitors on the uptake of cal@(DCA$_5$-UiO-66) (white bars) and cal-TPP$_{(++)}$@(DCA$_5$-UiO-66) (red bars) by MCF-7 cells, measured by flow cytometry. Samples were run in triplicate. Error bars represent the standard error of the mean. Statistical significance was assessed using one-way ANOVA and Dunnett's multiple comparisons test.

5.3.3 Effects of Treatments on Gene Expression of MCF-7 cells

To uncover the key biophysical and biochemical cellular pathways triggered by the treatments and confirm mitochondrial involvement, microarray analysis was performed on MCF-7 cells after exposure to the treatments for 72 h. It was hoped that the results would produce important information regarding the way in which the transcriptome is altered. The transcriptome is the entire repertoire of RNA transcripts in a species, and represents the fundamental link between information coded in genes (DNA) and the observed phenotype (proteins). Tools for profiling RNA, such as Northern blots, reverse-transcription PCR (RT-PCR), expressed sequence tags (ESTs), and serial analysis of gene expression (SAGE), have been available for years[249]. However, the fast and high-throughput quantification of RNA only became a possibility with the advent of gene expression microarrays[250]. These tools consist of probes that are immobilised on a solid substrate. These probes are complementary to the transcripts whose presence is to be explored. If an RNA strand is complementary to a probe that is present in the microarray, it will bind to it and emit light when excited. Differential expression of a specific bound transcript can then be deduced from differences in fluorescence intensities when comparing two or more samples.

For this study, MCF-7 cells (25,000 cells/cm^2) were exposed to 0.25 mg/mL of DCA_5-UiO-66, DCA_5-TPP_5-UiO-66, and $TPP_{(++)}$@(DCA_5-UiO-66) for 72 h. To optimise the conditions for this experiment, both the RNA final extraction procedure and the selection of previously observed cytotoxic time points were considered. A MOF concentration of 0.25 mg/mL allowed to avoid blockage of the RNA extraction column, and the 72 h time point allowed to observe cytotoxicity as determined by previous MTS studies (**Figure 5.11a**, 72 h). The 72 h time point also gave enough time to provide a wide-ranging overview of cell processes. Cells were also incubated with free DCA at a concentration of 0.25 mg/mL in order to study the effect of using the free drug as opposed to incorporating it in MOF NPs. The range of materials examined using this transcriptomic analysis allowed to compare the effects on gene expression of the free drug (DCA), the non-targeted DDS (DCA_5-UiO-66), and the targeted DDS (both DCA_5-TPP_5-UiO-66 and $TPP_{(++)}$@(DCA_5-UiO-66)), compared to untreated control cells and to each other. Four biological replicates for each condition were analysed.

After RNA extraction and microarray analysis, downstream analysis was performed to study global gene expression. The normalised gene expression data was

investigated using principal component analysis (PCA). PCA clusters the samples in two dimensions, decomposing the variance into several components, and identifies the largest variations in the data as principal components[251]. This allows to obtain a preliminary idea of the clustering of replicates and of different samples relative to each other. **Figure 5.18** shows the PCA of MCF-7 gene expression data. Principal components 1 and 2 are shown. The data allows to make a number of observations. First, biological replicates for each condition generally clustered close to each other. The only exception is one of the replicates of cells treated with DCA, which clustered apart from the other three replicates, and might be an outlier. Second, cells treated with DCA clustered close to untreated cells, suggesting that treatment with DCA induced very small changes in gene expression compared to the control. Third, incubation of MCF-7 cells with DCA_5-UiO-66, TPP_5-DCA_5-UiO-66, and $TPP_{(++)}$@(DCA_5-UiO-66) induced substantial changes in gene expression compared to untreated cells. Fourth, TPP_5-DCA_5-UiO-66 and $TPP_{(++)}$@(DCA_5-UiO-66) clustered together, and away from DCA_5-UiO-66, indicating that the TPP-containing DDSs elicited different responses in MCF-7 cells than DCA_5-UiO-66. In summary, PCA analysis suggests that the treatments can be clustered into three main groups with regards to their effect on gene expression: no treatment and treatment with the free drug in the first group, treatment with the non-targeted DDS in the second, and treatments with the mitochondrially-targeted DDSs in the third.

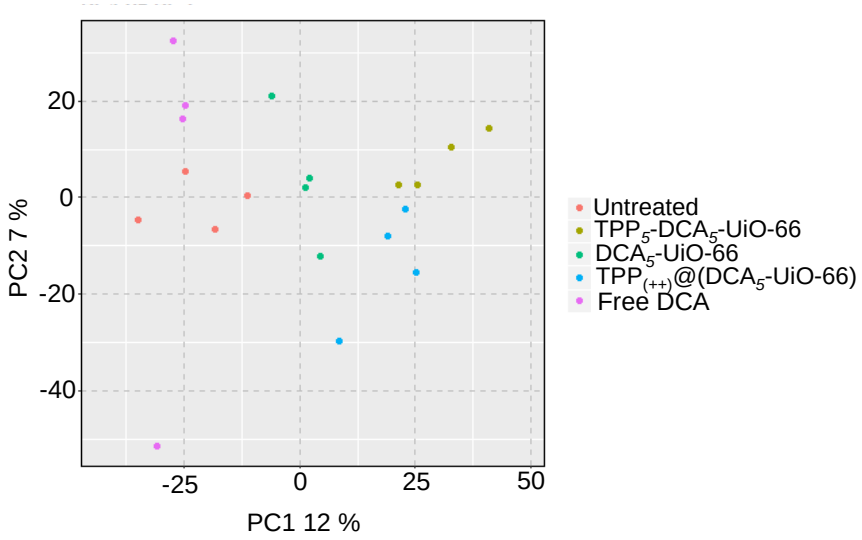

Figure 5.18. Principal component analysis of MCF-7 gene expression data. Principal components 1 and 2 are shown.

The numbers of genes with expression levels significantly changed when comparing treatments to each other are shown in **Table 5.3**. When comparing cells treated with DCA to untreated cells, no differentially expressed genes (DEGs) were detected, whether with a false-discovery rate-adjusted $p < 0.05$ or $p < 0.01$. This indicates that DCA at a concentration of 0.25 mg/mL does not have any apparent effect on the transcriptome after 72 h, i.e. that it does not alter MCF-7 gene expression. Comparing cells treated with DCA_5-UiO-66 to untreated cells reveals the presence of 71 DEGs ($p < 0.05$). This number drops down to 3 DEGs when $p < 0.01$. Remarkably, both mitochondrially-targeted DDSs, i.e. DCA_5-TPP_5-UiO-66 and $TPP_{(++)}$@(DCA_5-UiO-66), induced drastic widespread changes in gene expression profiles. DCA_5-TPP_5-UiO-66 caused significant changes in the expression level of 1,519 genes ($p < 0.05$), of which 821 were up-regulated and 698 were down-regulated, and $TPP_{(++)}$@(DCA_5-UiO-66) affected the expression level of 931 genes, of which 543 were up-regulated and 367 were down-regulated. These results are generally in agreement with the PCA results, showing no differential gene expression compared to the control for DCA-treated cells, only a small number of DEGs in cells treated with DCA_5-UiO-66, and a large gene response elicited similarly by both TPP-containing DDSs.

Table 5.3. Number of differentially expressed genes between cells treated with different conditions.

Comparisons	p<0.05	p<0.01	Total number of genes detected
Untreated vs. DCA	0	0	10702
Untreated vs. DCA_5-UiO-66	70	3	10693
Untreated vs. DCA_5-TPP_5-UiO-66	1519	465	10691
Untreated vs. $TPP_{(++)}$@(DCA_5-UiO-66)	910	358	10725
DCA vs. DCA_5-UiO-66	30	4	10676
DCA vs. DCA_5-TPP_5-UiO-66	987	269	10700
DCA vs. $TPP_{(++)}$@(DCA_5-UiO-66)	616	182	10696
DCA_5-TPP_5-UiO-66 vs. DCA_5-UiO-66	75	3	10687
DCA_5-TPP_5-UiO-66 vs. $TPP_{(++)}$@(DCA_5-UiO-66)	19	10	10678
$TPP_{(++)}$@(DCA_5-UiO-66) vs. DCA_5-UiO-66	103	34	10672

To investigate the overlap in DEGs following the different treatments, Venn diagrams showing the number of genes that were differentially expressed compared to the untreated control were constructed for up-regulated ($p < 0.05$, $FC > 0$) and down-regulated ($p < 0.05$, $FC < 0$) genes separately, and are shown in **Figure 5.19a** and

Figure 5.19b respectively. The diagram was divided according to the type of treatment, and the number of common genes is shown in the overlapping regions. **Figure 5.19a** shows that most of the DEGs up-regulated by DCA_5-UiO-66 (51 genes, 91 %) were also up-regulated by both DCA_5-TPP_5-UiO-66 and $TPP_{(++)}$@(DCA_5-UiO-66), with the targeted systems affecting numerous additional genes (768 and 491 respectively). This supports the idea that the addition of TPP to the MOF increases its efficacy on MCF-7 cells. A comparison of both targeted systems shows that the majority of DEGs up-regulated by $TPP_{(++)}$@(DCA_5-UiO-66) (359 genes, 66.1 %) were also up-regulated by DCA_5-TPP_5-UiO-66, with the latter affecting an additional 462 genes. The large number of overlapping genes suggests that both targeted DDSs affect the cells in a similar manner, but that they also potentially have different mechanisms of action, with DCA_5-TPP_5-UiO-66 and $TPP_{(++)}$@(DCA_5-UiO-66) affecting 462 and 184 unique up-regulated genes respectively. **Figure 5.19b** shows that there are very few down-regulated DEGs for DCA_5-UiO-66 (14 DEGs), whereas for DCA_5-TPP_5-UiO-66 and $TPP_{(++)}$@(DCA_5-UiO-66) this number is much higher (698 and 367 respectively). There is an overlap between 26.1 % of DEGs down-regulated by DCA_5-TPP_5-UiO-66 and 49.5 % of DEGs down-regulated by $TPP_{(++)}$@(DCA_5-UiO-66), corresponding to 182 genes. DCA_5-TPP_5-UiO-66 and $TPP_{(++)}$@(DCA_5-UiO-66) also provoke the differential expression of 510 and 183 unique down-regulated genes respectively, again suggesting different mechanisms of action. In summary, treatment with both targeted DDSs causes wider changes in gene expression than the non-targeted DDS, supporting the results showing the efficacy of TPP as a targeting agent. Additionally, DCA_5-TPP_5-UiO-66 and $TPP_{(++)}$@(DCA_5-UiO-66) affect MCF-7 cells in similar ways as evidenced by the overlap in the large number of up- and down-regulated genes, supporting the clustering of these two samples observed in the PCA plots (**Figure 5.18**).

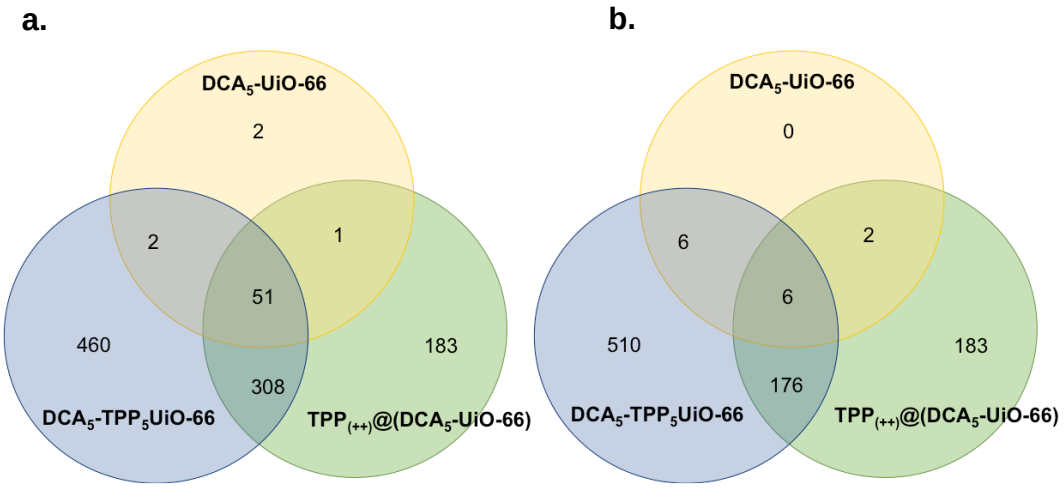

Figure 5.19. Venn diagram analysis of a) up-regulated and b) down-regulated differentially expressed genes in microarrays of MCF-7 cells treated with DCA_5-UiO-66, DCA_5-TPP_5-UiO-66 and $TPP_{(++)}$@(DCA_5-UiO-66) compared to an untreated control.

Further bioinformatics analysis is being done to obtain a holistic view of the transcriptomic dynamics of treated cells in order to give information on what biological processes, cellular components, and molecular functions the differentially expressed genes are involved in. This would hopefully allow to validate what was observed at the functional level.

5.4 Conclusions

A range of UiO-66 materials synthesised using the small drug molecule DCA as a modulator was prepared, and functionalised with the mitochondrial targeting agent TPP. TPP was incorporated into the MOFs either through coordination modulation during synthesis (samples termed DCA_x-TPP_y-UiO-66) or by post-synthetic attachment (termed $TPP_{(+/++)}$@(DCA_x-UiO-66)). SEM images revealed a wide range of particle sizes for the different samples, ranging from 81–683 nm. Samples with TPP post-synthetically attached generally demonstrated better colloidal stability than DCA_x-TPP_y-UiO-66 samples. Among the synthesised samples, two DDSs which were in the correct size range for cellular uptake and were colloidally stable (DCA_5-TPP_5-UiO-66 and $TPP_{(++)}$@(DCA_5-UiO-66)) were further investigated for mitochondrial targeting abilities. Non-functionalised DCA-containing particles (DCA_5-UiO-66) were investigated as a non-targeted control. MTS viability assays showed that DCA_5-UiO-66 did not demonstrate any toxicity up to 72 h, whereas TPP-functionalised particles caused a decrease in viability as early as 4 h after incubation, indicating that TPP

dramatically increases the efficacy of the system. Although they had much lower DCA loadings, particles with TPP post-synthetically attached ($TPP_{(++)}$@(DCA_5-UiO-66)) were more cytotoxic than DCA_5-TPP_5-UiO-66, showing that functionalisation with TPP using post-synthetic modification leads to more efficacious mitochondrial targeting. Confocal microscopy images using post-synthetically modified particles showed that particles accumulate near mitochondria. Super-resolution microscopy images showed significant mitochondrial morphology changes associated with toxicity when incubated with $TPP_{(++)}$@(DCA_5-UiO-66), even after as little as 30 min treatment. Cellular uptake studies showed that both $TPP_{(++)}$@(DCA_5-UiO-66) and DCA_5-UiO-66 showed no uptake through the *caveolae*-mediated route, suggesting an endolysosomal route to degradation within the cell. The observed toxicity of $TPP_{(++)}$@(DCA_5-UiO-66) is nonetheless indicative of its ability to escape endosomes and reach mitochondria. This could be attributed to the TPP acting as a proton sponge and allowing the rupture of endosomes. Microarray analysis was then performed on MCF-7 cells, and showed that cells treated with 0.25 mg/mL of free DCA showed no differentially expressed genes (DEGs) compared to the untreated control, whereas cells treated with non-targeted DCA_5-UiO-66 revealed the presence of 71 DEGs. Remarkably, treatment with both DCA_5-TPP_5-UiO-66 and $TPP_{(++)}$@(DCA_5-UiO-66) caused a dramatic change in gene expression of MCF-7 cells compared to the control, with 1,551 and 931 genes differentially expressed, respectively. Cells treated with DCA_5-TPP_5-UiO-66 and $TPP_{(++)}$@(DCA_5-UiO-66) had an overlap of 359 up-regulated and 182 down-regulated DEGs, suggesting similarities for both targeted systems. However, the two DDSs also caused the differential expression of a large number of unique genes (both up- and down-regulated), which suggests differences in mechanisms of action that could explain the differences in observed toxicities. Identification of key genes and enriched gene ontology (GO) pathways would allow to rationalise the different cellular behaviours upon exposure to the different delivery systems by providing information on what biological processes, cellular components, and molecular functions the differentially expressed genes are involved in.

6 CONCLUSIONS AND FUTURE WORK

6.1 Conclusions

This dissertation evaluated the use of metal-organic frameworks (MOFs) as intracellular delivery vectors, with a specific focus on i) testing the delivery of the cryoprotective disaccharide trehalose to the cytosol, ii) understanding what affects the final intracellular fate of MOF particles and their cargo after cellular uptake, and iii) designing a system capable of targeted delivery to mitochondria. While there is still further research to be done, significant progress has been made in developing this promising material as a targeted intracellular delivery system.

Zirconium-based MOFs were selected for their biocompatibility and high stability, but also for their susceptibility to phosphate attack in aqueous solvents, which causes their breakdown in physiological media. UiO-66 in particular was investigated as an intracellular delivery system of the cryoprotective agent trehalose. Synthesis of the MOF was successful, with the PXRD patterns showing all the main characteristic Bragg peaks as compared to the patterns predicted from single crystal structures. SEM images revealed a mean particle size of 136 ± 27 nm, well within the range that cells can take up by endocytosis. DLS indicated significant aggregation in PBS, which was much less pronounced in growth media, probably due to the formation of a protective 'protein corona' around the particles. Synthesised UiO-66 demonstrated prolonged stability in distilled water, with PXRD patterns showing retention of crystallinity even after 9 days

in solution. Particles were rapidly degraded in PBS however, with *ca.* 90 % of the linker released from the structure after as little as 30 min, and PXRD patterns showing the complete disappearance of Bragg peaks. Trehalose was adsorbed onto the MOFs by soaking in concentrated trehalose solutions, with weight loadings reaching as high as 56 %, as determined by TGA. The numbers were validated by measuring the total amount of trehalose released after soaking the MOFs in water. Time-dependent release of trehalose from the UiO-66 structure in PBS occurred over 5 h, with 50 % being released within the first 45 min. With cellular uptake sometimes taking place within a couple of minutes, enough time is available for the delivery system to reach the cytosol and deliver the trehalose. MTS viability assays showed that the amount of trehalose-loaded MOF that can be safely used is limited by the toxicity of UiO-66, with cellular viability starting to decrease at MOF concentrations of *ca.* 1.5 mg/mL. Cyroprotecting HeLa cells using trehalose-loaded UiO-66 was then tested, and showed no protective effect when compared to cells frozen using free trehalose or growth media as cryoprotective agents. While this can be due to a number of factors, such as insufficient intracellular trehalose concentrations, it was hypothesised that endosomal entrapment of the system after cellular uptake could play a critical role.

The factors that affect the final intracellular fate of MOF particles after uptake were then investigated in order to make sense of the results obtained in the cryopreservation experiments. Specifically, the role of surface chemistry on uptake efficiency and endocytosis routes of entry was explored. For that, a range of MOFs with different surface chemistries was prepared, either by using functionalised organic linkers during synthesis (Zr-L1−Zr-L6), or by functionalising the surface of Zr-L1 particles post-synthesis (Zr-L1-*func*). For samples synthesised using functionalised organic linkers, control of particle size was not possible. In order to isolate the effect of surface chemistry of Zr-L1−Zr-L6 on cellular uptake, a range of UiO-66 particles with different sizes ($_x$Zr-L1) was prepared and used as a reference. It was demonstrated that control of surface chemistry, whether through linker functionalisation or post-synthetic modification, was critical to tune the pathways through which cells take up particles, whereas particle size did not exert a great influence here. Zr-L1−Zr-L4 for example were taken up mostly by *clathrin*-dependent endocytosis, associated with lysosomal degradation, whereas Zr-L5 and Zr-L6 partially went through *caveolae*-mediated endocytosis, and were able to potentially release cargo into the cytosol. Confocal microscopy confirmed this by showing that fluorescent signal from Zr-L2−Zr-L4 was

largely co-localised with signal from lysosomes in HeLa cells, whereas for Zr-L5 and Zr-L6 there was a lot of signal that did not overlap with lysosomes. Post-synthetic surface functionalisation also allowed to tune the internalisation pathways of Zr-L1 and enhance their efficacy. Whereas Zr-L1 particles went mostly through the *clathrin*-mediated route, coating with folic acid and PEG partially redirected the particles towards the *caveolae*-mediated route. This resulted in enhanced efficacy when loaded with the anti-cancer drug DCA, presumably due to the ability to escape lysosomal degradation. Coating with heparin also led to the redirecting of particles towards *caveolae*-mediated endocytosis; however, no toxic effect of drug-loaded particles was observed due to low drug loadings. In summary, the study showed the importance of considering a combination of factors, such as uptake efficiency, drug loading capacity, and endocytosis routes of entry, when designing an efficacious delivery system. The fact that no cryoprotective effect was observed in **Chapter 3** could therefore be explained by the fact that Zr-L1 (UiO-66) was taken up mostly by *clathrin*-mediated endocytosis and ended up being degraded in lysosomes.

The design of a delivery system that is capable of bypassing lysosomal degradation, reaching the cytosol, and also delivering its cargo specifically to mitochondria was then pursued. A range of UiO-66 materials containing DCA as a drug was prepared by using DCA as a modulator during synthesis. The mitochondrial targeting agent TPP was either attached during synthesis by coordination modulation (samples termed DCA_x-TPP_y-UiO-66), or post-synthetically attached to the surface of the MOF (termed $TPP_{(+/++)}$@(DCA_x-UiO-66)). Synthesis of the MOF was successful, with the PXRD patterns showing all the main characteristic Bragg peaks as compared to the patterns predicted from single crystal UiO-66 structures. TGA and ICP-OES demonstrated successful incorporation of both molecules into UiO-66, with DCA and TPP weight loadings ranging from 7.7-15.1 wt % and 0.5-2.3 wt % respectively for DCA_x-TPP_y-UiO-66 particles, and 0.4-2.2 wt % and 5.3-15 wt % respectively for $TPP_{(+/++)}$@(DCA_x-UiO-66). SEM images revealed a wide range of particle sizes for the different samples, ranging from 81-683 nm. Samples with TPP post-synthetically attached generally demonstrated better colloidal stability than DCA_x-TPP_y-UiO-66 samples, and were further investigated using *in vitro* studies. MTS viability assay showed that the attachment of TPP to the surface of DCA_x-UiO-66 dramatically increased its toxicity. Post-synthetically attaching TPP to the surface of UiO-66 without DCA did not alter its toxicity, confirming that it is DCA that is causing the toxic effect.

Confocal microscopy images suggested that the targeted system accumulates near mitochondria. Super-resolution microscopy images showed significant mitochondrial morphology changes associated with toxicity when incubated with the targeted system, even after as little as 30 min treatment. Cellular uptake studies showed that both targeted and non-targeted systems showed no uptake through the *caveolae*-mediated route, suggesting an endolysosomal route within the cell. The fact that a toxic effect is observed for the targeted system is indicative of its ability to nonetheless escape endosomes and reach mitochondria. This could be attributed to the TPP acting as a proton sponge and allowing the rupture of endosomes. Microarray analysis was then performed on MCF-7 cells, and showed that cells treated with 0.25 mg/mL of free DCA showed no differentially expressed genes (DEGs) compared to the untreated control, whereas cells treated with non-targeted DCA_x-UiO-66 revealed the presence of 71 DEGs. Remarkably, treatment with both DCA_5-TPP_5-UiO-66 and $TPP_{(++)}$@(DCA_5-UiO-66) caused a dramatic change in gene expression of MCF-7 cells compared to the control, with 1,551 and 931 genes differentially expressed, respectively.

Overall, MOFs showed great promise for intracellular delivery applications; they achieved high loadings using low amounts of material, had easily tuneable physicochemical properties, and were biocompatible. As these materials are incredibly versatile, their development can further be pushed through synthesis and modification procedures to advance targeted therapeutic delivery. Focus should be placed on targeting and material functionalisation, and encapsulation of larger and more complex biological payloads.

6.2 Future Work

6.2.1 Optimising Cryopreservation Procedure by Allowing Endosomal Escape

As discussed in **Chapter 3**, a possible reason for the absence of cryoprotective effect of trehalose-loaded UiO-66 is endosomal entrapment of the system, which hinders the trehalose from being released into the cytosol. With a better understanding of the factors that affect the final intracellular location of MOF delivery systems, the cryopreservation process can now be attempted using a MOF that is able to escape endosomes. The goal would be to find a MOF that not only can hold large amounts of trehalose, but also be

taken up in sufficiently large quantities, and through desired endocytic pathways. Endosomal escape can also be promoted by the addition of a proton sponge.

6.2.2 Elucidating the Biophysical and Biochemical Pathways Triggered by Nanoparticle Treatment

Microarray analysis identified up to 1,551 genes affected by treatment with the mitochondria-targeting system. Further bioinformatics analysis can be done to obtain a holistic view of the delivery system interaction with the cellular machinery. Transcriptomic dynamics of treated cells can identify key genes and enriched gene ontology (GO) pathways to obtain a comprehensive and objective snapshot of cellular behaviour upon exposure to the delivery system. The analysis could give information on what biological processes, cellular components, and molecular functions the differentially expressed genes are involved in. This would allow to validate what was observed at the functional level in **Chapter 5**, as well as elucidate effects not easily observable at the phenotypical level. The identification of key up- or down-regulated genes enriched in certain pathways would also allow to understand the mechanism of toxicity of the targeted system, by identifying activated cellular death mechanisms or stress-related pathways. It would also allow to determine differences in mechanisms between targeted and non-targeted systems.

6.2.3 Designing a Nucleus-Targeting MOF-based delivery system

The nucleus is a crucial therapeutic target given that it holds the genetic information and transcription machinery of a cell. Some chemotherapeutic drugs such as doxorubicin induce cancer cell apoptosis mainly by oxidative DNA damage and topoisomerase II inhibition in the nucleus[252]. However, cancer cells have strong intracellular resistance mechanisms to hinder the access of drugs to the nucleus, such as over-expression of drug efflux pumps, drug metabolism and detoxification, drug sequestering to acidic compartments, and drug deactivation[253]. As a consequence, only a small fraction of drug present in the cytosol reaches the nucleus in drug-resistant cells. The ability to divert a drug from the endolyososomal route directly to the nucleus is therefore expected to significantly enhance the anticancer efficacy of currently available drugs. Using the knowledge acquired during this thesis, it is now possible to design and synthesise a MOF that is capable of bypassing endosomes/lysosomes. Modifying its surface with a nuclear localisation signal (NLS) could allow to direct it to the nucleus, through the

nuclear envelope which consists of a large number of nuclear pore complexes (NPCs) with a diameter of 20-70 nm. Particle size can be tuned to fit through the NPCs. HIV-1 TAT peptide has been shown to translocate NPs into cell nuclei[254,255]. Its attachment to a biocompatible MOF of the appropriate size could in principle direct the system to the cell nucleus. Attachment could be performed by a water-based carbodiimide mediated reaction, between the exposed amino groups at the surface of MOFs with amino-functionalised organic linkers, and the C-termini of the TAT peptides. The system could also be provided with an imaging functionality by conjugating the fluorescent FITC molecule to the N-terminus of the TAT peptide, thus forming a multi-functional targeted therapy/imaging system.

6.2.4 Using MOFs for CRISPR/Cas9 delivery

CRISPR is a technology for manipulating or editing genes inside cells, and therefore has the potential to cure thousands of human genetic diseases. The CRISPR complex consists of two components: the protein Cas9 and a guide RNA (sgRNA) that provides the template for the required gene modification. Most studies have demonstrated the use of this technology by using gene delivery strategies to generate Cas9 inside cells. This poses problems with regards to off-target effects and unwanted gene editing, due to the required CRISPR genes staying in the host cell after delivery. An alternative strategy has been to deliver Cas9 and sgRNA directly into cells, offering a transient way of editing genes. The main obstacle with this approach is the large CRISPR complex's inability to efficiently reach the nucleus, due to difficulties crossing the cell membrane and escaping endosomal entrapment. MOFs could be designed in a way to carry and deliver Cas9 and sgRNA into the cell cytosol, and possibly directly into the nucleus. This thesis has shown how it is possible to design a MOF-based system that is capable of endosomal escape. As discussed in **Section 6.2.3**, such a system could also be decorated with a nuclear localisation signal that allows it to be taken through the nuclear pore complex and into the nucleus.

7 REFERENCES

(1) Stewart, M. P.; Sharei, A.; Ding, X.; Sahay, G.; Langer, R.; Jensen, K. F. In Vitro and Ex Vivo Strategies for Intracellular Delivery. *Nature* **2016**, *538*, 183–192.

(2) Biswas, S.; Torchilin, V. P. Nanopreparations for Organelle-Specific Delivery in Cancer. *Adv. Drug Deliv. Rev.* **2014**, *66*, 26–41.

(3) Torchilin, V. P. Multifunctional, Stimuli-Sensitive Nanoparticulate Systems for Drug Delivery. *Nat. Rev. Drug Discov.* **2014**, *13*, 813–827.

(4) Yoo, J. W.; Irvine, D. J.; Discher, D. E.; Mitragotri, S. Bio-Inspired, Bioengineered and Biomimetic Drug Delivery Carriers. *Nat. Rev. Drug Discov.* **2011**, *10*, 521–535.

(5) Mintzer, M. A.; Simanek, E. E. Nonviral Vectors for Gene Delivery. *Chem. Rev.* **2009**, *109*, 259–302.

(6) Horcajada, P.; Gref, R.; Baati, T.; Allan, P. K.; Maurin, G.; Couvreur, P.; Ferey, G.; Morris, R. E.; Serre, C. Metal-Organic Frameworks in Biomedicine. *Chem. Rev.* **2012**, *112*, 1232–1268.

(7) Horcajada, P.; Chalati, T.; Serre, C.; Gillet, B.; Sebrie, C.; Baati, T.; Eubank, J. F.; Heurtaux, D.; Clayette, P.; Kreuz, C.; et al. Porous Metal-Organic-Framework Nanoscale Carriers as a Potential Platform for Drug Delivery and Imaging. *Nat. Mater.* **2010**, *9*, 172–178.

(8) Bharti, C.; Gulati, N.; Nagaich, U.; Pal, A. Mesoporous Silica Nanoparticles in

Target Drug Delivery System: A Review. *Int. J. Pharm. Investig.* **2015**, *5*, 124–133.

(9) Bernini, M. C.; Fairen-Jimenez, D.; Pasinetti, M.; Ramirez-Pastor, A. J.; Snurr, R. Q. Screening of Bio-Compatible Metal–organic Frameworks as Potential Drug Carriers Using Monte Carlo Simulations. *J. Mater. Chem. B* **2014**, *2*, 766.

(10) Furukawa, H.; Cordova, K. E.; O'Keeffe, M.; Yaghi, O. M. The Chemistry and Applications of Metal-Organic Frameworks. *Science* **2013**, *341* (6149), 1230444.

(11) Naldini, L. Gene Therapy Returns to Centre Stage. *Nature* **2015**, *526*, 351–360.

(12) June, C. H.; Riddell, S. R.; Schumacher, T. N. Adoptive Cellular Therapy: A Race to the Finish Line. *Sci. Transl. Med.* **2015**, *7* (280), 1–8.

(13) Kim, D.; Kim, C. H.; Moon, J. Il; Chung, Y. G.; Chang, M. Y.; Han, B. S.; Ko, S.; Yang, E.; Cha, K. Y.; Lanza, R.; et al. Generation of Human Induced Pluripotent Stem Cells by Direct Delivery of Reprogramming Proteins. *Cell Stem Cell* **2009**, *4*, 472–476.

(14) Mout, R.; Ray, M.; Yesilbag Tonga, G.; Lee, Y. W.; Tay, T.; Sasaki, K.; Rotello, V. M. Direct Cytosolic Delivery of CRISPR/Cas9-Ribonucleoprotein for Efficient Gene Editing. *ACS Nano* **2017**, *11*, 2452–2458.

(15) Ma, X.; Gong, N.; Zhong, L.; Sun, J.; Liang, X. J. Future of Nanotherapeutics: Targeting the Cellular Sub-Organelles. *Biomaterials* **2016**, *97*, 10–21.

(16) Chou, L. Y. T.; Ming, K.; Chan, W. C. W. Strategies for the Intracellular Delivery of Nanoparticles. *Chem. Soc. Rev.* **2011**, *40*, 233–245.

(17) Hallow, D. M.; Seeger, R. A.; Kamaev, P. P.; Prado, G. R.; LaPlaca, M. C.; Prausnitz, M. R. Shear-Induced Intracellular Loading of Cells with Molecules by Controlled Microfluidics. *Biotechnol. Bioeng.* **2008**, *99* (4), 846–854.

(18) Gurtovenko, A. A.; Anwar, J.; Vattulainen, I. Defect-Mediated Trafficking across Cell Membranes: Insights from in Silico Modeling. *Chem. Rev.* **2010**, *110*, 6077–6103.

(19) Stewart, M. P.; Lorenz, A.; Dahlman, J.; Sahay, G. Challenges in Carrier-Mediated Intracellular Delivery: Moving beyond Endosomal Barriers. *Wiley Interdiscip. Rev. Nanomedicine Nanobiotechnology* **2016**, *8*, 465–478.

(20) Allen, T. M.; Cullis, P. R. Liposomal Drug Delivery Systems: From Concept to

Clinical Applications. *Adv. Drug Deliv. Rev.* **2013**, *65*, 36–48.

(21) Freiberg, S.; Zhu, X. X. Polymer Microspheres for Controlled Drug Release. *Int. J. Pharm.* **2004**, *282*, 1–18.

(22) Lynch, A. L.; Chen, R.; Dominowski, P. J.; Shalaev, E. Y.; Yancey, R. J.; Slater, N. K. H. Biopolymer Mediated Trehalose Uptake for Enhanced Erythrocyte Cryosurvival. *Biomaterials* **2010**, *31* (23), 6096–6103.

(23) Kwon, G. S.; Okano, T. Polymeric Micelles as New Drug Carriers. *Adv. Drug Deliv. Rev.* **1996**, *21*, 107–116.

(24) Hoare, T. R.; Kohane, D. S. Hydrogels in Drug Delivery: Progress and Challenges. *Polymer (Guildf).* **2008**, *49*, 1993–2007.

(25) Bangham, A. D.; Standish, M. M.; Watkins, J. C. Diffusion of Univalent Ions across the Lamellae of Swollen Phospholipids. *J. Mol. Biol.* **1965**, *13*, 238–252.

(26) Gregoriadis, G. The Carrier Potential of Liposomes in Biology and Medicine. *N. Engl. J. Med.* **1976**, *295*, 765–770.

(27) Mudshinge, S. R.; Deore, A. B.; Patil, S.; Bhalgat, C. M. Nanoparticles: Emerging Carriers for Drug Delivery. *Saudi Pharm. J.* **2011**, *19*, 129–141.

(28) Torchilin, V. P. Recent Approaches to Intracellular Delivery of Drugs and DNA and Organelle Targeting. *Annu. Rev. Biomed. Eng.* **2006**, *8*, 343–375.

(29) Klibanov, A. L.; Maruyama, K.; Torchilin, V. P.; Huang, L. Amphipathic Polyethyleneglycols Effectively Prolong the Circulation Time of Liposomes. *FEBS Lett.* **1990**, *268* (1), 235–237.

(30) Torchilin, V. P.; Levchenko, T. S.; Lukyanov, A. N.; Khaw, B. A.; Klibanov, A. L.; Rammohan, R.; Samokhin, G. P.; Whiteman, K. R. P-Nitrophenylcarbonyl-PEG-PE-Liposomes: Fast and Simple Attachment of Specific Ligands, Including Monoclonal Antibodies, to Distal Ends of PEG Chains via P-Nitrophenylcarbonyl Groups. *Biochim. Biophys. Acta - Biomembr.* **2001**, *1511*, 397–411.

(31) Gaucher, G.; Dufresne, M. H.; Sant, V. P.; Kang, N.; Maysinger, D.; Leroux, J. C. Block Copolymer Micelles: Preparation, Characterization and Application in Drug Delivery. *J. Control. Release* **2005**, *109*, 169–188.

(32) Kim, S. C.; Kim, D. W.; Shim, Y. H.; Bang, J. S.; Oh, H. S.; Kim, S. W.; Seo, M.

H. In Vivo Evaluation of Polymeric Micellar Paclitaxel Formulation: Toxicity and Efficacy. *J. Control. Release* **2001**, *72*, 191–202.

(33) Duncan, R. Polymer Conjugates as Anticancer Nanomedicines. *Nat. Rev. Cancer* **2006**, *6*, 688–701.

(34) Khandare, J. J.; Jayant, S.; Singh, A.; Chandna, P.; Wang, Y.; Vorsa, N.; Minko, T. Dendrimer versus Linear Conjugate: Influence of Polymeric Architecture on the Delivery and Anticancer Effect of Paclitaxel. *Bioconjug. Chem.* **2006**, *17*, 1464–1472.

(35) Kuruppuarachchi, M.; Savoie, H.; Lowry, A.; Alonso, C.; Boyle, R. W. Polyacrylamide Nanoparticles as a Delivery System in Photodynamic Therapy. *Mol. Pharm.* **2011**, *8*, 920–931.

(36) Turos, E.; Shim, J. Y.; Wang, Y.; Greenhalgh, K.; Reddy, G. S. K.; Dickey, S.; Lim, D. V. Antibiotic-Conjugated Polyacrylate Nanoparticles: New Opportunities for Development of Anti-MRSA Agents. *Bioorganic Med. Chem. Lett.* **2007**, *17*, 53–56.

(37) Martínez, A.; Iglesias, I.; Lozano, R.; Teijón, J. M.; Blanco, M. D. Synthesis and Characterization of Thiolated Alginate-Albumin Nanoparticles Stabilized by Disulfide Bonds. Evaluation as Drug Delivery Systems. *Carbohydr. Polym.* **2011**, *83*, 1311–1321.

(38) Rampino, A.; Borgogna, M.; Blasi, P.; Bellich, B.; Cesàro, A. Chitosan Nanoparticles: Preparation, Size Evolution and Stability. *Int. J. Pharm.* **2013**, *455*, 219–228.

(39) Willem de Vries, J.; Schnichels, S.; Hurst, J.; Strudel, L.; Gruszka, A.; Kwak, M.; Bartz-Schmidt, K. U.; Spitzer, M. S.; Herrmann, A. DNA Nanoparticles for Ophthalmic Drug Delivery. *Biomaterials* **2018**, *157*, 98–106.

(40) des Rieux, A.; Fievez, V.; Garinot, M.; Schneider, Y. J.; Préat, V. Nanoparticles as Potential Oral Delivery Systems of Proteins and Vaccines: A Mechanistic Approach. *J. Control. Release* **2006**, *116*, 1–27.

(41) Liechty, W. B.; Kryscio, D. R.; Slaughter, B. V.; Peppas, N. A. Polymers for Drug Delivery Systems. *Annu. Rev. Chem. Biomol. Eng.* **2010**, *1*, 149–173.

(42) Park, J.; Fong, P. M.; Lu, J.; Russell, K. S.; Booth, C. J.; Saltzman, W. M.;

Fahmy, T. M. PEGylated PLGA Nanoparticles for the Improved Delivery of Doxorubicin. *Nanomedicine Nanotechnology, Biol. Med.* **2009**, *5*, 410–418.

(43) Rimoli, M. G.; Rabaioli, M. R.; Melisi, D.; Curcio, A.; Mondello, S.; Mirabelli, R.; Abignente, E. Synthetic Zeolites as a New Tool for Drug Delivery. *J. Biomed. Mater. Res. - Part A* **2008**, *11*, 156–164.

(44) Amorim, R.; Vilaça, N.; Martinho, O.; Reis, R. M.; Sardo, M.; Rocha, J.; Fonseca, A. M.; Baltazar, F.; Neves, I. C. Zeolite Structures Loading with an Anticancer Compound as Drug Delivery Systems. *J. Phys. Chem. C* **2012**, *116*, 25642–25650.

(45) Datt, A.; Burns, E. A.; Dhuna, N. A.; Larsen, S. C. Loading and Release of 5-Fluorouracil from HY Zeolites with Varying SiO2/Al2O3 Ratios. *Microporous Mesoporous Mater.* **2013**, *167*, 182–187.

(46) Vivero-Escoto, J. L.; Slowing, I. I.; Trewyn, B. G.; Lin, V. S.-Y. Mesoporous Silica Nanoparticles for Intracellular Controlled Drug Delivery. *Small* **2010**, *6* (18), 1952–1967.

(47) Qu, Q.; Ma, X.; Zhao, Y. Targeted Delivery of Doxorubicin to Mitochondria Using Mesoporous Silica Nanoparticle Nanocarriers. *Nanoscale* **2015**, *7* (40), 16677–16686.

(48) Pan, L.; He, Q.; Liu, J.; Chen, Y.; Zhang, L.; Shi, J. Nuclear-Targeted Drug Delivery of TAT Peptide-Conjugated Monodisperse Mesoporous Silica Nanoparticles. *J. Am. Chem. Soc.* **2012**, *134*, 5722–5725.

(49) Kwon, S.; Singh, R. K.; Perez, R. A.; Abou Neel, E. A.; Kim, H.-W.; Chrzanowski, W. Silica-Based Mesoporous Nanoparticles for Controlled Drug Delivery. *J. Tissue Eng.* **2013**, *4*, 1–18.

(50) He, Q.; Shi, J. Mesoporous Silica Nanoparticle Based Nano Drug Delivery Systems: Synthesis, Controlled Drug Release and Delivery, Pharmacokinetics and Biocompatibility. *J. Mater. Chem.* **2011**, *21*, 5845–5855.

(51) Slowing, I. I.; Vivero-Escoto, J. L.; Wu, C.-W.; Lin, V. S.-Y. Mesoporous Silica Nanoparticles as Controlled Release Drug Delivery and Gene Transfection Carriers. *Adv. Drug Deliv. Rev.* **2008**, *60*, 1278–1288.

(52) Li, H.; Eddaoudi, M.; O'Keeffe, M.; Yaghi, O. M. Design and Synthesis of an

Exceptionally Stable and Highly Porous Metal-Organic Framework. *Nature* **1999**, *402*, 276–279.

(53) Moghadam, P. Z.; Li, A.; Wiggin, S. B.; Tao, A.; Maloney, A. G. P.; Wood, P. A.; Ward, S. C.; Fairen-Jimenez, D. Development of a Cambridge Structural Database Subset: A Collection of Metal-Organic Frameworks for Past, Present, and Future. *Chem. Mater.* **2017**, *29*, 2618–2625.

(54) Yaghi, O. M.; O'Keeffe, M.; Ockwig, N. W.; Chae, H. K.; Eddaoudi, M.; Kim, J. Reticular Synthesis and the Design of New Materials. *Nature* **2003**, *423*, 705–714.

(55) Chui, S. S. Y.; Lo, S. M. F.; Charmant, J. P. H.; Orpen, a G.; Williams, I. D. A Chemically Functionalizable Nanoporous Material [Cu3(TMA)2(H2O)3]n. *Science (80-.).* **1999**, *283*, 1148–1150.

(56) Pan, Y.; Liu, Y.; Zeng, G.; Zhao, L.; Lai, Z. Rapid Synthesis of Zeolitic Imidazolate Framework-8 (ZIF-8) Nanocrystals in an Aqueous System. *Chem. Commun.* **2011**, *47*, 2071–2073.

(57) Férey, G.; Serre, C.; Mellot-Draznieks, C.; Millange, F.; Surblé, S.; Dutour, J.; Margiolaki, I. A Hybrid Solid with Giant Pores Prepared by a Combination of Targeted Chemistry, Simulation, and Powder Diffraction. *Angew. Chemie - Int. Ed.* **2004**, *43*, 6296–6301.

(58) Cavka, J. H.; Jakobsen, S.; Olsbye, U.; Guillou, N.; Lamberti, C.; Bordiga, S.; Lillerud, K. P. A New Zirconium Inorganic Building Brick Forming Metal Organic Frameworks with Exceptional Stability. *J. Am. Chem. Soc.* **2008**, *130*, 13850–13851.

(59) Cunha, D.; Gaudin, C.; Colinet, I.; Horcajada, P.; Maurin, G.; Serre, C. Rationalization of the Entrapping of Bioactive Molecules into a Series of Functionalized Porous Zirconium Terephthalate MOFs. *J. Mater. Chem. B* **2013**, *1*, 1101–1108.

(60) Katz, M. J.; Brown, Z. J.; Colón, Y. J.; Siu, P. W.; Scheidt, K. A.; Snurr, R. Q.; Hupp, J. T.; Farhat, O. K. A Facile Synthesis of UiO-66 , UiO-67 and Their Derivatives. *Chem. Commun.* **2013**, *49* (82), 9449–9451.

(61) Valenzano, L.; Civalleri, B.; Chavan, S.; Bordiga, S.; Nilsen, M. H.; Jakobsen, S.; Lillerud, K. P.; Lamberti, C. Disclosing the Complex Structure of UiO-66

Metal Organic Framework : A Synergic Combination of Experiment and Theory. *Chem. Mater.* **2011**, *23*, 1700–1718.

(62) Cmarik, G. E.; Kim, M.; Cohen, S. M.; Walton, K. S. Tuning the Adsorption Properties of UiO-66 via Ligand Functionalization. *Langmuir* **2012**, *28* (44), 15606–15613.

(63) Marshall, R. J.; Forgan, R. S. Postsynthetic Modification of Zirconium Metal-Organic Frameworks. *Eur. J. Inorg. Chem.* **2016**, *2016* (27), 4310–4331.

(64) Wang, S.; Morris, W.; Liu, A.; Mcguirk, C. M.; Zhou, Y.; Hupp, J. T.; Farha, O. K.; Mirkin, C. A. Surface-Specific Functionalization of Nanoscale Metal-Organic Frameworks. *Angew. Commun.* **2015**, *54*, 14738–14742.

(65) Shearer, G. C.; Chavan, S.; Bordiga, S.; Svelle, S.; Olsbye, U.; Lillerud, K. P. Defect Engineering: Tuning the Porosity and Composition of the Metal-Organic Framework UiO-66 via Modulated Synthesis. *Chem. Mater.* **2016**, *28* (11), 3749–3761.

(66) Horcajada, P.; Serre, C.; Vallet-Regí, M.; Sebban, M.; Taulelle, F.; Férey, G. Metal–Organic Frameworks as Efficient Materials for Drug Delivery. *Angew. Chemie* **2006**, *118* (36), 6120–6124.

(67) Chen, W.; Wu, C. Synthesis, Functionalization, and Applications of Metal-Organic Frameworks in Biomedicine. *Dalt. Trans.* **2018**, *47*, 2114–2133.

(68) Vasconcelos, I. B.; Silva, T. G. Da; Militão, G. C. G.; Soares, T. a.; Rodrigues, N. M.; Rodrigues, M. O.; Costa, N. B. Da; Freire, R. O.; Junior, S. A. Cytotoxicity and Slow Release of the Anti-Cancer Drug Doxorubicin from ZIF-8. *RSC Adv.* **2012**, *2* (25), 9437–9440.

(69) Lucena, F. R. S.; de Araújo, L. C. C.; Rodrigues, M. do D.; da Silva, T. G.; Pereira, V. R. A.; Militão, G. C. G.; Fontes, D. A. F.; Rolim-Neto, P. J.; da Silva, F. F.; Nascimento, S. C. Induction of Cancer Cell Death by Apoptosis and Slow Release of 5-Fluoracil from Metal-Organic Frameworks Cu-BTC. *Biomed. Pharmacother.* **2013**, *67*, 707–713.

(70) He, C.; Lu, K.; Liu, D.; Lin, W. Nanoscale Metal-Organic Frameworks for the Co-Delivery of Cisplatin and Pooled siRNAs to Enhance Therapeutic Efficacy in Drug-Resistant Ovarian Cancer Cells. *J. Am. Chem. Soc.* **2014**, *136* (14), 5181–5184.

(71) Agostoni, V.; Chalati, T.; Horcajada, P.; Willaime, H.; Anand, R.; Semiramoth, N.; Baati, T.; Hall, S.; Maurin, G.; Chacun, H.; et al. Towards an Improved Anti-HIV Activity of NRTI via Metal-Organic Frameworks Nanoparticles. *Adv. Healthc. Mater.* **2013**, *2* (12), 1630–1637.

(72) McKinlay, A. C.; Xiao, B.; Wragg, D. S.; Wheatley, P. S.; Megson, I. L.; Morris, R. E. Exceptional Behavior over the Whole Adsorption-Storage-Delivery Cycle for NO in Porous Metal Organic Frameworks. *J. Am. Chem. Soc.* **2008**, *130* (31), 10440–10444.

(73) Wheatley, P. S.; Butler, A. R.; Crane, M. S.; Fox, S.; Xiao, B.; Rossi, A. G.; Megson, I. L.; Morris, R. E. NO-Releasing Zeolites and Their Antithrombotic Properties. *J. Am. Chem. Soc.* **2006**, *128*, 502–509.

(74) Tamames-Tabar, C.; Cunha, D.; Imbuluzqueta, E.; Ragon, F.; Serre, C.; Blanco-Prieto, M. J.; Horcajada, P. Cytotoxicity of Nanoscaled Metal-Organic Frameworks. *J. Mater. Chem. B* **2014**, *2*, 262–271.

(75) Ruyra, A.; Yazdi, A.; Espín, J.; Carné-Sánchez, A.; Roher, N.; Lorenzo, J.; Imaz, I.; Maspoch, D. Synthesis, Culture Medium Stability, and in Vitro and in Vivo Zebrafish Embryo Toxicity of Metal-Organic Framework Nanoparticles. *Chem. - A Eur. J.* **2015**, *21*, 2508–2518.

(76) Baati, T.; Njim, L.; Neffati, F.; Kerkeni, A.; Bouttemi, M.; Gref, R.; Najjar, M. F.; Zakhama, A.; Couvreur, P.; Serre, C.; et al. In Depth Analysis of the in Vivo Toxicity of Nanoparticles of Porous Iron(iii) Metal–organic Frameworks. *Chem. Sci.* **2013**, *4*, 1597–1607.

(77) He, C.; Liu, D.; Lin, W. Nanomedicine Applications of Hybrid Nanomaterials Built from Metal-Ligand Coordination Bonds: Nanoscale Metal-Organic Frameworks and Nanoscale Coordination Polymers. *Chem. Rev.* **2015**, *115* (19), 11079–11108.

(78) Hermes, S.; Witte, T.; Hikov, T.; Zacher, D.; Bahnmüller, S.; Langstein, G.; Huber, K.; Fischer, R. A. Trapping Metal-Organic Framework Nanocrystals: An in-Situ Time-Resolved Light Scattering Study on the Crystal Growth of MOF-5 in Solution. *J. Am. Chem. Soc.* **2007**, *129*, 5324–5325.

(79) Makiura, R.; Motoyama, S.; Umemura, Y.; Yamanaka, H.; Sakata, O.; Kitagawa, H. Surface Nano-Architecture of a Metal-Organic Framework. *Nat. Mater.* **2010**,

9, 565–571.

(80) Morris, W.; Wang, S.; Cho, D.; Auyeung, E.; Li, P.; Farha, O. K.; Mirkin, C. A. Role of Modulators in Controlling the Colloidal Stability and Polydispersity of the UiO-66 Metal–Organic Framework. *ACS Appl. Mater. Interfaces* **2017**, *9* (39), 33413–33418.

(81) Schaate, A.; Roy, P.; Godt, A.; Lippke, J.; Waltz, F.; Wiebcke, M.; Behrens, P. Modulated Synthesis of Zr-Based Metal-Organic Frameworks: From Nano to Single Crystals. *Chem. - A Eur. J.* **2011**, *17*, 6643–6651.

(82) Rijnaarts, T.; Mejia-Ariza, R.; Egberink, R. J. M.; Vanroosmalen, W.; Huskens, J. Metal-Organic Frameworks (MOFs) as Multivalent Materials: Size Control and Surface Functionalization by Monovalent Capping Ligands. *Chem. - A Eur. J.* **2015**, *21*, 10296–10301.

(83) Guo, H.; Zhu, Y.; Wang, S.; Su, S.; Zhou, L.; Zhang, H. Combining Coordination Modulation with Acid-Base Adjustment for the Control over Size of Metal-Organic Frameworks. *Chem. Mater.* **2012**, *24*, 444–450.

(84) Hoshyar, N.; Gray, S.; Han, H.; Bao, G. The Effect of Nanoparticle Size on *in Vivo* Pharmacokinetics and Cellular Interaction. *Nanomedicine* **2016**, *11* (6), 673–692.

(85) Taddei, M.; Dümbgen, K. C.; Van Bokhoven, J. A.; Ranocchiari, M. Aging of the Reaction Mixture as a Tool to Modulate the Crystallite Size of UiO-66 into the Low Nanometer Range. *Chem. Commun.* **2016**, *52*, 6411–6414.

(86) Marshall, R. J.; Hobday, C. L.; Murphie, C. F.; Griffin, S. L.; Morrison, C. A.; Moggach, S. A.; Forgan, R. S. Amino Acids as Highly Efficient Modulators for Single Crystals of Zirconium and Hafnium Metal–organic Frameworks. *J. Mater. Chem. A* **2016**, *4* (18), 6955–6963.

(87) Wu, H.; Chua, Y. S.; Krungleviciute, V.; Tyagi, M.; Chen, P.; Yildirim, T.; Zhou, W. Unusual and Highly Tunable Missing-Linker Defects in Zirconium Metal − Organic Framework UiO-66 and Their Important E Ff Ects on Gas Adsorption. *J. Am. Chem. Soc.* **2013**, *135*, 10525–10532.

(88) Cliffe, M. J.; Hill, J. A.; Murray, C. A.; Coudert, F. X.; Goodwin, A. L. Defect-Dependent Colossal Negative Thermal Expansion in UiO-66(Hf) Metal-Organic Framework. *Phys. Chem. Chem. Phys.* **2015**, *17*, 11586–11592.

(89) Wang, Z.; Cohen, S. M. Postsynthetic Modification of Metal-Organic Frameworks. *Chem. Soc. Rev.* **2009**, *38*, 1315–1329.

(90) Jiang, W.; Kim, B. Y. S.; Rutka, J. T.; Chan, W. C. W. Nanoparticle-Mediated Cellular Response Is Size-Dependent. *Nat. Nanotechnol.* **2008**, *3*, 145–150.

(91) Jin, H.; Heller, D. A.; Sharma, R.; Strano, M. S. Size-Dependent Cellular Uptake and Expulsion of Single-Walled Carbon Nanotubes: Single Particle Tracking and a Generic Uptake Model for Nanoparticles. *ACS Nano* **2009**, *3* (1), 149–158.

(92) Lu, F.; Wu, S. H.; Hung, Y.; Mou, C. Y. Size Effect on Cell Uptake in Well-Suspended, Uniform Mesoporous Silica Nanoparticles. *Small* **2009**, *5* (12), 1408–1413.

(93) Nel, A. E.; Mädler, L.; Velegol, D.; Xia, T.; Hoek, E. M. V.; Somasundaran, P.; Klaessig, F.; Castranova, V.; Thompson, M. Understanding Biophysicochemical Interactions at the Nano–bio Interface. *Nat. Mater.* **2009**, *8* (7), 543–557.

(94) Sykes, E. A.; Chen, J.; Zheng, G.; Chan, W. C. W. Investigating the Impact of Nanoparticle Size on Active and Passive Tumor Targeting Efficiency. *ACS Nano* **2014**, *8* (6), 5696–5706.

(95) Park, J.; Jiang, Q.; Feng, D.; Mao, L.; Zhou, H. C. Size-Controlled Synthesis of Porphyrinic Metal-Organic Framework and Functionalization for Targeted Photodynamic Therapy. *J. Am. Chem. Soc.* **2016**, *138*, 3518–3525.

(96) Zhu, X.; Gu, J.; Wang, Y.; Li, B.; Li, Y.; Zhao, W.; Shi, J. Inherent Anchorages in UiO-66 Nanoparticles for Efficient Capture of Alendronate and Its Mediated Release. *Chem. Commun.* **2014**, *50* (63), 8779–8782.

(97) Röder, R.; Preiß, T.; Hirschle, P.; Steinborn, B.; Zimpel, A.; Höhn, M.; Rädler, J. O.; Bein, T.; Wagner, E.; Wuttke, S.; et al. Multifunctional Nanoparticles by Coordinative Self-Assembly of His-Tagged Units with Metal-Organic Frameworks. *J. Am. Chem. Soc.* **2017**, *139* (6), 2359–2368.

(98) Wang, W.; Wang, L.; Li, Z.; Xie, Z. BODIPY-Containing Nanoscale Metal-Organic Frameworks for Photodynamic Therapy. *Chem. Commun.* **2016**, *52*, 5402–5405.

(99) Zimpel, A.; Preiß, T.; Der, R. R.; Engelke, H.; Ingrisch, M.; Peller, M.; Ra, J. O.; Wagner, E.; Bein, T.; La, U.; et al. Imparting Functionality to MOF

Nanoparticles by External Surface Selective Covalent Attachment of Polymers. *Chem. Mater.* **2016**, *28*, 3318–3326.

(100) Morris, W.; Briley, W. E.; Auyeung, E.; Cabezas, M. D.; Mirkin, C. A. Nucleic Acid-Metal Organic Framework (MOF) Nanoparticle Conjugates. *J. Am. Chem. Soc.* **2014**, *136* (20), 7261–7264.

(101) Nagata, S.; Kokado, K.; Sada, K. Metal-Organic Framework Tethering PNIPAM for ON-OFF Controlled Release in Solution. *Chem. Commun.* **2015**, *51*, 8614–8617.

(102) Wang, C.; Liu, X.; Chen, J. P.; Li, K. Superior Removal of Arsenic from Water with Zirconium Metal-Organic Framework UiO-66. *Sci. Rep.* **2015**, *5*, 1–10.

(103) Tomas-Gamasa, M.; Martinez-Calvo, M.; Couceiro, J. R.; Mascarenas, J. L. Transition Metal Catalysis in the Mitochondria of Living Cells. *Nat. Commun.* **2016**, *7*, 12538.

(104) Young, L. J.; Ströhl, F.; Kaminski, C. F. A Guide to Structured Illumination TIRF Microscopy at High Speed with Multiple Colors. *J. Vis. Exp.* **2016**, *111*, 1–16.

(105) Müller, M.; Mönkemöller, V.; Hennig, S.; Hübner, W.; Huser, T. Open-Source Image Reconstruction of Super-Resolution Structured Illumination Microscopy Data in ImageJ. *Nat. Commun.* **2016**, *7*, 1–6.

(106) Kamentsky, L.; Jones, T. R.; Fraser, A.; Bray, M. A.; Logan, D. J.; Madden, K. L.; Ljosa, V.; Rueden, C.; Eliceiri, K. W.; Carpenter, A. E. Improved Structure, Function and Compatibility for Cellprofiler: Modular High-Throughput Image Analysis Software. *Bioinformatics* **2011**, *27* (8), 1179–1180.

(107) Carvalho, B. S.; Irizarry, R. A. A Framework for Oligonucleotide Microarray Preprocessing. *Bioinformatics* **2010**, *26* (19), 2363–2367.

(108) Irizarry, R. A.; Hobbs, B.; Collin, F.; Beazer-Barclay, Y. D.; Antonellis, K. J.; Scherf, U.; Speed, T. P. Exploration, Normalization, and Summaries of High Density Oligonucleotide Array Probe Level Data. *Biostatistics* **2003**, *4* (2), 249–264.

(109) Ritchie, M. E.; Phipson, B.; Wu, D.; Hu, Y.; Law, C. W.; Shi, W.; Smyth, G. K. Limma Powers Differential Expression Analyses for RNA-Sequencing and

Microarray Studies. *Nucleic Acids Res.* **2015**, *43* (7), e47.

(110) Benjamini, Y.; Hochberg, Y.; Benjaminit, Y. Controlling the False Discovery Rate: A Practical and Powerful Approach to Multiple Controlling the False Discovery Rate: A Practical and Powerful Approach to Multiple Testing. *Source J. R. Stat. Soc. Ser. B J. R. Stat. Soc. Ser. B J. R. Stat. Soc. B* **1995**, *57* (1), 289–300.

(111) Day, J. G.; Stacey, G. N. *Cryopreservation and Freeze-Drying Protocols*, 2nd ed.; Humana Press, 2007.

(112) Gao, D.; Critser, J. K. Mechanisms of Cryoinjury in Living Cells. *Inst. Lab. Anim. Res.* **2000**, *4* (4), 187–196.

(113) Mazur, P.; Leibo, S. P.; Chu, E. H. Y.; Division, B.; Ridge, O.; Ridge, O. A Two-Factor Hypothesis of Freezing Injury: Evidence from Chinese Hamster Tissue-Culture Cells. *Exp. Cell Res.* **1972**, *71*, 345–355.

(114) Fuller, B. J. Cryoprotectants: The Essential Antifreezes to Protect Life in the Frozen State. *CryoLetters* **2004**, *25* (6), 375–388.

(115) Karow, A. M.; Webb, W. R. Tissue Freezing: A Theory for Injury and Survival. *Cryobiology* **1965**, *2* (3), 99–108.

(116) Watson, R. E.; Wiegand, S. J.; Clough, R. W.; Hoffman, G. E. Use of Cryoprotectant to Maintain Long-Term Peptide Immunoreactivity and Tissue. *Peptides* **1986**, *7* (1), 155–159.

(117) Hopkins, R. A. *Cardiac Reconstructions with Allograft Valves*, 1st ed.; Springer Science and Business Media, 2012.

(118) Sieme, H.; Oldenhof, H.; Wolkers, W. F. Mode of Action of Cryoprotectants for Sperm Preservation. *Anim. Reprod. Sci.* **2016**, *169*, 2–5.

(119) Farrant, J. Water Transport and Cell Survival in Cryobiological Procedures. *Phil. Trans. R. Soc. Lond. B* **1977**, *278*, 191–205.

(120) Lovelock, J. E.; Bishop, M. W. H. Prevention of Freezing Damage to Living Cells by DMSO. *Nature* **1959**, *183* (4672), 1394–1395.

(121) Lovelock, J. E. The Denaturation of Lipid-Protein Complexes as a Cause of Damage by Freezing. *Proc R Soc L. B* **1957**, *147*, 427–434.

(122) Fahy, M. The Relevance of Cryoprotectant Toxicity to Cryobiology. *Cryobiology* **1986**, *13*, 1–13.

(123) Katkov, I. I.; Kim, M. S.; Bajpai, R.; Altman, Y. S.; Mercola, M.; Loring, J. F.; Terskikh, A. V; Snyder, E. Y.; Levine, F. Cryopreservation by Slow Cooling with DMSO Diminished Production of Oct-4 Pluripotency Marker in Human Embryonic Stem Cells. *Cryobiology* **2006**, *53* (2), 194–205.

(124) Wang, H.; Lun, Z.; Lu, S. Cryopreservation of Umbilical Cord Blood-Derived Mesenchymal Stem Cells without Dimethyl Sulfoxide. *Cryo Letters* **2011**, *32* (1), 81–88.

(125) Thaler, R.; Spitzer, S.; Karlic, H.; Klaushofer, K.; Varga, F. DMSO Is a Strong Inducer of DNA Hydroxymethylation in Pre-Osteoblastic MC3T3-E1 Cells. *Epigenetics* **2012**, *7* (6), 635–651.

(126) Cox, M. a; Kastrup, J.; Hrubiško, M. Historical Perspectives and the Future of Adverse Reactions Associated with Haemopoietic Stem Cells Cryopreserved with Dimethyl Sulfoxide. *Cell Tissue Bank.* **2012**, *13* (2), 203–215.

(127) Windrum, P.; Morris, T. C. M.; Drake, M. B.; Niederwieser, D.; Ruutu, T. Variation in Dimethyl Sulfoxide Use in Stem Cell Transplantation: A Survey of EBMT Centres. *Bone Marrow Transplant.* **2005**, *36* (7), 601–603.

(128) Abdelkefi, A.; Lakhal, A.; Moojar, N.; Hamed, L. B.; Fekih, J.; Ladeb, S.; Torjman, L.; Benothman, T. Severe Neurotoxicity Associated with DMSO Following PBSCT. *Bone Marrow Transpl.* **2009**, *44* (5), 323–324.

(129) Benekli, M.; Anderson, B.; Wentling, D.; Bernstein, S.; Czuczman, M.; McCarthy, P. Severe Respiratory Depression after DMSO-Containing Autologous Stem Cell Infusion in a Patient with AL Amyloidosis. *Bone Marrow Transpl.* **2000**, *25* (12), 1299–1301.

(130) Hequet, O.; Dumontet, C.; El-Jaafari-Corbin, A.; Salles, G.; Espinouse, D.; Arnaud, P.; Thieblemont, C.; Bouafia, F.; Coiffer, B. Epileptic Seizures after Autologous Peripheral Blood Progenitor Infusion in a Patient Treated with High-Dose Chemotherapy for Myeloma. *Bone Marrow Transpl.* **2002**, *29* (6), 544.

(131) Sharp, D. M. C.; Picken, A.; Morris, T. J.; Hewitt, C. J.; Coopman, K.; Slater, N. K. H. Amphipathic Polymer-Mediated Uptake of Trehalose for Dimethyl Sulfoxide-Free Human Cell Cryopreservation. *Cryobiology* **2013**, *67* (3), 305–

311.

(132) Clegg, J. S. Origin of Trehalose and Its Significance During Formation of Encysted Dormant Embryos of Artemia Salina. *Comp. Biochem. Physiol.* **1963**, *14*, 135–143.

(133) Madin, K. A. C.; Crowe, J. H. Anhydrobiosis in Nematodes: Carbohydrate and Lipid Metabo Ism during Dehydration. *J. Exp. Zool.* **1975**, *193*, 335–342.

(134) Crowe, J. H.; Hoekstra, F. A.; Crowe, L. M. Anhydrobiosis. *Annu. Rev. Physiol.* **1992**, *54*, 579–599.

(135) Jain, N. K.; Roy, I. Effect of Trehalose on Protein Structure. *Protein Sci.* **2009**, *18* (1), 24–36.

(136) Leslie, S. B.; Israeli, E.; Lighthart, B.; Crowe, J. H.; Crowe, L. M. Trehalose and Sucrose Protect Both Membranes and Proteins in Intact Bacteria during Drying. *Appl. Environ. Microbiol.* **1995**, *61* (10), 3592–3597.

(137) Eroglu, A.; Russo, M. J.; Bieganski, R.; Fowler, A.; Cheley, S.; Bayley, H.; Toner, M. Intracellular Trehalose Improves the Survival of Cryopreserved Mammalian Cells. *Nat. Biotechnol.* **2000**, *18* (2), 163–167.

(138) Eroglu, A.; Toner, M.; Toth, T. L. Beneficial Effect of Microinjected Trehalose on the Cryosurvival of Human Oocytes. *Fertil. Steril.* **2002**, *77* (1), 6–8.

(139) Chen, T.; Acker, J. P.; Eroglu, a; Cheley, S.; Bayley, H.; Fowler, a; Toner, M. Beneficial Effect of Intracellular Trehalose on the Membrane Integrity of Dried Mammalian Cells. *Cryobiology* **2001**, *43* (2), 168–181.

(140) Hunt, C. J. Cryopreservation of Human Stem Cells for Clinical Application: A Review. *Transfus. Med. Hemotherapy* **2011**, *38*, 107–123.

(141) Beattie, G. M.; Crowe, J. H.; Lopez, A. D.; Cirulli, V.; Ricordi, C.; Hayek, A. Trehalose: A Cryoprotectant That Enhances Recovery and Preserves Function of Human Pancreatic Islets After Long-Term Storage. *Diabetes* **1997**, *46*, 519–523.

(142) Oliver, A. E.; Jamil, K.; Crowe, J. H.; Tablin, F. Loading Human Mesenchymal Stem Cells with Trehalose by Fluid-Phase Endocytosis. *Cell Preserv. Technol.* **2004**, *2* (1), 35–49.

(143) Guo, N.; Puhlev, I.; Brown, D. R.; Mansbridge, J.; Levine, F. Trehalose Expression Confers Desiccation Tolerance on Human Cells. *Nat. Biotechnol.*

2000, *18*, 168–171.

(144) Holovati, J. L.; Acker, J. P. Spectrophotometric Measurement of Intraliposomal Trehalose. *Cryobiology* **2007**, *55* (2), 98–107.

(145) Puhlev, I.; Guo, N.; Brown, D. R.; Levine, F. Desiccation Tolerance in Human Cells. *Cryobiology* **2001**, *42* (3), 207–217.

(146) Macrae, C. F.; Bruno, I. J.; Chisholm, J. A.; Edgington, P. R.; McCabe, P.; Pidcock, E.; Rodriguez-Monge, L.; Taylor, R.; Van De Streek, J.; Wood, P. A. Mercury CSD 2.0 - New Features for the Visualization and Investigation of Crystal Structures. *J. Appl. Crystallogr.* **2008**, *41*, 466–470.

(147) Orellana-Tavra, C.; Baxter, E. F.; Tian, T.; Bennett, T. D.; Slater, N. K. H.; Cheetham, A. K.; Fairen-Jimenez, D. Amorphous metal–organic Frameworks for Drug Delivery. *Chem. Commun.* **2015**, *51* (73), 13878–13881.

(148) Shang, L.; Nienhaus, K.; Nienhaus, G. U. Engineered Nanoparticles Interacting with Cells: Size Matters. *J. Nanobiotechnology* **2014**, *12* (5), 1–11.

(149) Nazarenus, M.; Zhang, Q.; Soliman, M. G.; del Pino, P.; Pelaz, B.; Carregal-Romero, S.; Rejman, J.; Rothen-Rutishauser, B.; Clift, M. J. D.; Zellner, R.; et al. In Vitro Interaction of Colloidal Nanoparticles with Mammalian Cells: What Have We Learned Thus Far? *Beilstein J. Nanotechnol.* **2014**, *5* (1), 1477–1490.

(150) Cunha, D.; Yahia, M. Ben; Hall, S.; Miller, S. R.; Chevreau, H.; Elka, E.; Maurin, G.; Horcajada, P.; Serre, C. Rationale of Drug Encapsulation and Release from Biocompatible Porous Metal − Organic Frameworks. *Chem. Mater.* **2013**, *25* (14), 2767–2776.

(151) Orellana-Tavra, C.; Marshall, R. J.; Baxter, E. F.; Abánades-Lázaro, I.; Tao, A.; Cheetham, A. K.; Forgan, R. S.; Fairen-Jimenez, D. Drug Delivery and Controlled Release from Biocompatible Metal–organic Frameworks Using Mechanical Amorphization. *J. Mater. Chem. B* **2016**, *4* (47), 7697–7707.

(152) Abanades-Lazaro, I.; Haddad, S.; Sacca, S.; Orellana-Tavra, C.; Fairen-Jimenez, D.; Forgan, R. S. Selective Surface PEGylation of UiO-66 Nanoparticles for Enhanced Stability , Cell Uptake , and pH-Responsive Drug Delivery. *Chem* **2017**, *2*, 561–578.

(153) Abánades Lázaro, I.; Haddad, S.; Rodrigo-Muñoz, J. M.; Orellana-Tavra, C.; Del

Pozo, V.; Fairen-Jimenez, D.; Forgan, R. S. Mechanistic Investigation into the Selective Anticancer Cytotoxicity and Immune System Response of Surface-Functionalized, Dichloroacetate-Loaded, UiO-66 Nanoparticles. *ACS Appl. Mater. Interfaces* **2018**, *10* (6), 5255–5268.

(154) Raimi-abraham, B. T.; Mo, J. G.; Belton, P. S.; Barker, S. A.; Craig, D. Q. M. Generation and Characterization of Standardized Forms of Trehalose Dihydrate and Their Associated Solid-State Behavior. *Cryst. Growth Des.* **2014**, *14*, 4955–4967.

(155) Teplensky, M. H.; Fantham, M.; Li, P.; Wang, T. C.; Mehta, J. P.; Young, L. J.; Moghadam, P. Z.; Hupp, J. T.; Farha, O. K.; Kaminski, C. F.; et al. Temperature Treatment of Highly Porous Zirconium-Containing Metal-Organic Frameworks Extends Drug Delivery Release. *J. Am. Chem. Soc.* **2017**, *139* (22), 7522–7532.

(156) Oldstone, M. B. A.; Compans, R. W. *Influenza Pathogenesis and Control*, 2nd ed.; Springer, 2014.

(157) Mazur, P. Freezing of Living Cells: Mechanisms and Implications. *Am. J. Physiol.* **1984**, *247* (16), 125–142.

(158) Kaushik, J. K.; Bhat, R. Why Is Trehalose an Exceptional Protein Stabilizer? An Analysis of the Thermal Stability of Proteins in the Presence of the Compatible Osmolyte Trehalose. *J. Biol. Chem.* **2003**, *278* (29), 26458–26465.

(159) Higashiyama, T. Novel Functions and Applications of Trehalose* A Special Topic Issue on the Science of Sweeteners. *Pure Appl. Chem* **2002**, *74* (7), 1263–1269.

(160) Chithrani, B. D.; Chan, W. C. W. Elucidating the Mechanism of Cellular Uptake and Removal of Protein-Coated Gold Nanoparticles of Different Sizes and Shapes. *Nano Lett.* **2007**, *7* (6), 1542–1550.

(161) Gratton, S. E. A.; Ropp, P. A.; Pohlhaus, P. D.; Luft, J. C.; Madden, V. J.; Napier, M. E.; DeSimone, J. M. The Effect of Particle Design on Cellular Internalization Pathways. *Proc. Natl. Acad. Sci. U. S. A.* **2008**, *105* (33), 11613–11618.

(162) Kou, L.; Sun, J.; Zhai, Y.; He, Z. The Endocytosis and Intracellular Fate of Nanomedicines: Implication for Rational Design. *Asian J. Pharm. Sci.* **2013**, *8* (1), 1–10.

(163) Mayor, S.; Pagano, R. E. Pathways of Clathrin-Independent Endocytosis. *Nat. Rev. Mol. Cell Biol.* **2007**, *8* (8), 603–612.

(164) Iversen, T.-G.; Skotland, T.; Sandvig, K. Endocytosis and Intracellular Transport of Nanoparticles: Present Knowledge and Need for Future Studies. *Nano Today* **2011**, *6* (2), 176–185.

(165) Park, J. H.; Oh, N. Endocytosis and Exocytosis of Nanoparticles in Mammalian Cells. *Int. J. Nanomedicine* **2014**, 51–55.

(166) Win, K. Y.; Feng, S.-S. Effects of Particle Size and Surface Coating on Cellular Uptake of Polymeric Nanoparticles for Oral Delivery of Anticancer Drugs. *Biomaterials* **2005**, *26* (15), 2713–2722.

(167) Chithrani, B. D.; Ghazani, A. a.; Chan, W. C. W. Determining the Size and Shape Dependence of Gold Nanoparticle Uptake into Mammalian Cells. *Nano Lett.* **2006**, *6* (4), 662–668.

(168) He, C.; Hu, Y.; Yin, L.; Tang, C.; Yin, C. Effects of Particle Size and Surface Charge on Cellular Uptake and Biodistribution of Polymeric Nanoparticles. *Biomaterials* **2010**, *31* (13), 3657–3666.

(169) Lorenz, M. R.; Holzapfel, V.; Musyanovych, A.; Nothelfer, K.; Walther, P.; Frank, H.; Landfester, K.; Schrezenmeier, H.; Mailänder, V. Uptake of Functionalized, Fluorescent-Labeled Polymeric Particles in Different Cell Lines and Stem Cells. *Biomaterials* **2006**, *27* (14), 2820–2828.

(170) Kumari, S.; Mg, S.; Mayor, S. Endocytosis Unplugged: Multiple Ways to Enter the Cell. *Cell Res.* **2010**, *20* (3), 256–275.

(171) dos Santos, T.; Varela, J.; Lynch, I.; Salvati, A.; Dawson, K. a. Effects of Transport Inhibitors on the Cellular Uptake of Carboxylated Polystyrene Nanoparticles in Different Cell Lines. *PLoS One* **2011**, *6* (9), e24438.

(172) Mellman, I. Endocytosis and Molecular Sorting. *Annu. Rev. Cell Dev. Biol.* **1996**, *12*, 575–625.

(173) Rejman, J.; Oberle, V.; Zuhorn, I. S.; Hoekstra, D. Size-Dependent Internalization of Particles via the Pathways of Clathrin- and Caveolae-Mediated Endocytosis. *Biochem. J.* **2004**, *377* (Pt 1), 159–169.

(174) Conner, S. D.; Schmid, S. L. Regulated Portals of Entry into the Cell. *Nature*

2003, *422* (6927), 37–44.

(175) Doherty, G. J.; McMahon, H. T. Mechanisms of Endocytosis. *Annu. Rev. Biochem.* **2009**, *78* (1), 857–902.

(176) Damm, E. M.; Pelkmans, L.; Kartenbeck, J.; Mezzacasa, A.; Kurzchalia, T.; Helenius, A. Clathrin- and Caveolin-1-Independent Endocytosis: Entry of Simian Virus 40 into Cells Devoid of Caveolae. *J. Cell Biol.* **2005**, *168* (3), 477–488.

(177) Kettler, K.; Veltman, K.; van de Meent, D.; van Wezel, A.; Hendriks, a J. Cellular Uptake of Nanoparticles as Determined by Particle Properties, Experimental Conditions, and Cell Type. *Environ. Toxicol. Chem.* **2014**, *33* (3), 481–492.

(178) McMahon, H. T.; Boucrot, E. Molecular Mechanism and Physiological Functions of Clathrin-Mediated Endocytosis. *Nat. Rev. Mol. Cell Biol.* **2011**, *12* (8), 517–533.

(179) Guo, C.-J.; Wu, Y.-Y.; Yang, L.-S.; Yang, X.-B.; He, J.; Mi, S.; Jia, K.-T.; Weng, S.-P.; Yu, X.-Q.; He, J.-G. Infectious Spleen and Kidney Necrosis Virus (a Fish Iridovirus) Enters Mandarin Fish Fry Cells via Caveola-Dependent Endocytosis. *J. Virol.* **2012**, *86* (5), 2621–2631.

(180) Pelkmans, L.; Kartenbeck, J.; Helenius, A. Caveolar Endocytosis of Simian Virus 40 Reveals a New Two-Step Vesicular- Transport Pathway to the ER. *Nat. Cell Biol.* **2001**, *3*, 473–484.

(181) Gonzalez-Gaitan, M.; Stenmark, H. Endocytosis and Signaling : A Relationship under Development Meeting. *Cell* **2003**, *115*, 513–521.

(182) Orellana-Tavra, C.; Mercado, S. a; Fairen-Jimenez, D. Endocytosis Mechanism of Nano Metal-Organic Frameworks for Drug Delivery. *Adv. Healthc. Mater.* **2016**, *5* (17), 2261–2270.

(183) Ivanov, A. I. *Exocytosis and Endocytosis*, 1st ed.; John M. Walker, Ed.; Human Press, 2008.

(184) Sarkar, K.; Kruhlak, M. J.; Erlandsen, S. L.; Shaw, S. Selective Inhibition by Rottlerin of Macropinocytosis in Monocyte-Derived Dendritic Cells. *Immunology* **2005**, *116* (4), 513–524.

(185) Inal, J.; Miot, S.; Schifferli, J. A. The Complement Inhibitor, CRIT, Undergoes

Clathrin-Dependent Endocytosis. *Exp. Cell Res.* **2005**, *310* (1), 54–65.

(186) Yao, D.; Ehrlich, M.; Henis, Y. I.; Leof, E. B. Transforming Growth Factor-B Receptors Interact with AP2 by Direct Binding to B2 Subunit. *Mol. Biol. Cell* **2002**, *13* (6), 4001–4012.

(187) Carpentier, J. L.; Sawano, F.; Geiger, D.; Gorden, P.; Perrelet, a; Orci, L. Potassium Depletion and Hypertonic Medium Reduce "non-Coated" and Clathrin-Coated Pit Formation, as Well as Endocytosis through These Two Gates. *J. Cell. Physiol.* **1989**, *138* (3), 519–526.

(188) Guo, S.; Zhang, X.; Zheng, M.; Zhang, X.; Min, C.; Wang, Z.; Cheon, S. H.; Oak, M. H.; Nah, S. Y.; Kim, K. M. Selectivity of Commonly Used Inhibitors of Clathrin-Mediated and Caveolae-Dependent Endocytosis of G Protein-Coupled Receptors. *Biochim. Biophys. Acta - Biomembr.* **2015**, *1848*, 2101–2110.

(189) Dausend, J.; Musyanovych, A.; Dass, M.; Walther, P.; Schrezenmeier, H.; Landfester, K.; Maila, V. Uptake Mechanism of Oppositely Charged Fluorescent Nanoparticles in HeLa Cells. *Macromol. Biosci.* **2008**, *8*, 1135–1143.

(190) Harush-frenkel, O.; Debotton, N.; Benita, S.; Altschuler, Y. Targeting of Nanoparticles to the Clathrin-Mediated Endocytic Pathway. *Biochem. Biophys. Res. Commun.* **2007**, *353*, 26–32.

(191) Okamoto, C. T. Endocytosis and Transcytosis. *Adv. Drug Deliv. Rev.* **1998**, *29*, 215–228.

(192) Ferrari, A.; Pellegrini, V.; Arcangeli, C.; Fittipaldi, A.; Giacca, M.; Beltram, F. Caveolae-Mediated Internalization of Extracellular HIV-1 Tat Fusion Proteins Visualized in Real Time. *Mol. Ther.* **2003**, *8* (2), 284–294.

(193) Shin, J.-S.; Abraham, S. N. Caveolae as Portals of Entry for Microbes. *Microbes Infect.* **2001**, *3* (9), 755–761.

(194) Manders, E. M. M., Verbeek, F. J., Aten, J. A. Measurement of Co-Localization of Objects in Dual-Colour Confocal Images. *J. Microsc.* **1993**, *169*, 375–382.

(195) Boltes, S.; Cordelieres, F. P. A Guided Tour into Subcellular Colocalization Analysis in Light Microscopy. *J. Microsc.* **2006**, *224*, 213–232.

(196) Zwicke, G. L.; Mansoori, G. A.; Jeffery, C. J. Targeting of Cancer Nanotherapeutics. *Nano Rev.* **2012**, *1*, 1–11.

(197) Bonnet, S.; Archer, S. L.; Allalunis-Turner, J.; Haromy, A.; Beaulieu, C.; Thompson, R.; Lee, C. T.; Lopaschuk, G. D.; Puttagunta, L.; Bonnet, S.; et al. A Mitochondria-K+Channel Axis Is Suppressed in Cancer and Its Normalization Promotes Apoptosis and Inhibits Cancer Growth. *Cancer Cell* **2007**, *11* (1), 37–51.

(198) Michelakis, E. D.; Webster, L.; Mackey, J. R. Dichloroacetate (DCA) as a Potential Metabolic-Targeting Therapy for Cancer. *Br. J. Cancer* **2008**, *99* (7), 989–994.

(199) Porporato, P. E.; Filigheddu, N.; Pedro, J. M. B.-S.; Kroemer, G.; Galluzzi, L. Mitochondrial Metabolism and Cancer. *Cell Res.* **2017**, *28* (3), 265–280.

(200) Wiemerslage, L.; Lee, D. HHS Public Access. *J. Neurosci. Methods* **2016**, *262*, 56–65.

(201) Voet, D.; Voet, J. G.; Pratt, C. W. *Fundamentals of Biochemistry*, 2nd ed.; John Wiley and Sons, 2006.

(202) Alkarakooly, Z.; Kilaparty, S. P.; Al-anbaky, Q. A.; Khan, M. S. Dichloroacetic Acid (DCA)-Induced Cytotoxicity in Human Breast Cancer Cells Accompanies Changes in Mitochondrial Membrane Permeability and Production of Reactive Oxygen Species. **2014**, 1234–1248.

(203) Fulda, S. Tumor Resistance to Apoptosis. *Int. J. Cancer* **2009**, *124* (3), 511–515.

(204) Hanahan, D.; Weinberg, R. A. The Hallmarks of Cancer. *Cell* **2000**, *100* (1), 57–70.

(205) Mcilwain, D. R.; Berger, T.; Mak, T. W. Caspase Functions in Cell Death and Disease. **2013**, *6*, 1–29.

(206) Fulda, S.; Galluzzi, L.; Kroemer, G. Targeting Mitochondria for Cancer Therapy. *Nat. Rev. Drug Discov.* **2010**, *9*, 447–464.

(207) Armstrong, J. S. Mitochondrial Medicine: Pharmacological Targeting of Mitochondria in Disease. *Br. J. Pharmacol.* **2007**, *151* (8), 1154–1165.

(208) Galluzzi, L.; Larochette, N.; Zamzami, N.; Kroemer, G. Mitochondria as Therapeutic Targets for Cancer Chemotherapy. *Oncogene* **2006**, *25* (34), 4812–4830.

(209) Gogvadze, V.; Orrenius, S.; Zhivotovsky, B. Mitochondria as Targets for Cancer

Chemotherapy. *Semin. Cancer Biol.* **2009**, *19* (1), 57–66.

(210) Kroemer, G.; Pouyssegur, J. Tumor Cell Metabolism: Cancer's Achilles' Heel. *Cancer Cell* **2008**, *13* (6), 472–482.

(211) García-Sáez, A. J. The Secrets of the Bcl-2 Family. *Cell Death Differ.* **2012**, *19* (11), 1733–1740.

(212) Wei, M. C.; Zong, W.; Cheng, E. H.; Lindsten, T.; Ross, A. J.; Roth, K. A.; Macgregor, G. R.; Craig, B.; Korsmeyer, S. J. Proapoptotic Bax and Bak: A Requesite Gateway to Mitochondrial Dysfunction and Death. *Science (80-.).* **2001**, *292* (5517), 727–730.

(213) Llambi, F.; Moldoveanu, T.; Tait, S. W. G.; Bouchier-Hayes, L.; Temirov, J.; McCormick, L. L.; Dillon, C. P.; Green, D. R. A Unified Model of Mammalian BCL-2 Protein Family Interactions at the Mitochondria. *Mol. Cell* **2011**, *44* (4), 517–531.

(214) Konopleva, M.; Contractor, R.; Tsao, T.; Samudio, I.; Ruvolo, P. P.; Kitada, S.; Deng, X.; Zhai, D.; Shi, Y. X.; Sneed, T.; et al. Mechanisms of Apoptosis Sensitivity and Resistance to the BH3 Mimetic ABT-737 in Acute Myeloid Leukemia. *Cancer Cell* **2006**, *10* (5), 375–388.

(215) Oltersdorf, T.; Elmore, S. W.; Shoemaker, A. R.; Armstrong, R. C.; Augeri, D. J.; Belli, B. A.; Bruncko, M.; Deckwerth, T. L.; Dinges, J.; Hajduk, P. J.; et al. An Inhibitor of Bcl-2 Family Proteins Induces Regression of Solid Tumours. *Nature* **2005**, *435* (7042), 677–681.

(216) Mason, K. D.; Vandenberg, C. J.; Scott, C. L.; Wei, A. H.; Cory, S.; Huang, D. C. S.; Roberts, A. W. In Vivo Efficacy of the Bcl-2 Antagonist ABT-737 against Aggressive Myc-Driven Lymphomas. *Proc. Natl. Acad. Sci. U. S. A.* **2008**, *105* (46), 17961–17966.

(217) Kim, E. Y.; Jung, J. Y.; Kim, A.; Chang, Y. S.; Kim, S. K. ABT-737 Synergizes with Cisplatin Bypassing Aberration of Apoptotic Pathway in Non-Small Cell Lung Cancer. *Neoplasia (United States)* **2017**, *19* (4), 354–363.

(218) Noll, T.; Schultze-Seemann, S.; Kuckuck, I.; Michalska, M.; Wolf, P. Synergistic Cytotoxicity of a Prostate Cancer-Specific Immunotoxin in Combination with the BH3 Mimetic ABT-737. *Cancer Immunol. Immunother.* **2018**, *67* (3), 413–422.

(219) Radha, G.; Raghavan, S. C. BCL2: A Promising Cancer Therapeutic Target. *Biochim. Biophys. Acta - Rev. Cancer* **2017**, *1868* (1), 309–314.

(220) Liu, G.; Kelly, W. K.; Wilding, G.; Leopold, L.; Brill, K.; Somer, B. An Open-Label, Multicenter, Phase I/II Study of Single-Agent AT-101 in Men with Castrate-Resistant Prostate Cancer. *Clin. Cancer Res.* **2009**, *15* (9), 3172–3176.

(221) Indran, I. R.; Tufo, G.; Pervaiz, S.; Brenner, C. Recent Advances in Apoptosis, Mitochondria and Drug Resistance in Cancer Cells. *Biochim. Biophys. Acta - Bioenerg.* **2011**, *1807* (6), 735–745.

(222) Crompton, M. The Mitochondrial Permeability Transition Pore and Its Role in Cell Death. *Biochem. J.* **1999**, *341*, 233–249.

(223) Desagher, S.; Martinou, J. C. Mitochondria as the Central Control Point of Apoptosis. *Trends Cell Biol.* **2000**, *10* (9), 369–377.

(224) Madhok, B. M.; Yeluri, S.; Perry, S. L.; Hughes, T. a; Jayne, D. G. Dichloroacetate Induces Apoptosis and Cell-Cycle Arrest in Colorectal Cancer Cells. *Br. J. Cancer* **2010**, *102* (12), 1746–1752.

(225) Cheng, G.; Zielonka, J.; McAllister, D.; Hardy, M.; Ouari, O.; Joseph, J.; Dwinell, M. B.; Kalyanaraman, B. Antiproliferative Effects of Mitochondria-Targeted Cationic Antioxidants and Analogs: Role of Mitochondrial Bioenergetics and Energy-Sensing Mechanism. *Cancer Lett.* **2015**, *365* (1), 96–106.

(226) Sassi, N.; Mattarei, A.; Azzolini, M.; Szabo', I.; Paradisi, C.; Zoratti, M.; Biasutto, L. Cytotoxicity of Mitochondria-Targeted Resveratrol Derivatives: Interactions with Respiratory Chain Complexes and ATP Synthase. *Biochim. Biophys. Acta - Bioenerg.* **2014**, *1837* (10), 1781–1789.

(227) Rao, V. A.; Klein, S. R.; Bonar, S. J.; Zielonka, J.; Mizuno, N.; Dickey, J. S.; Keller, P. W.; Joseph, J.; Kalyanaraman, B.; Shacter, E. The Antioxidant Transcription Factor Nrf2 Negatively Regulates Autophagy and Growth Arrest Induced by the Anticancer Redox Agent Mitoquinone. *J. Biol. Chem.* **2010**, *285* (45), 34447–34459.

(228) Zielonka, J.; Joseph, J.; Sikora, A.; Hardy, M.; Ouari, O.; Vasquez-Vivar, J.; Cheng, G.; Lopez, M.; Kalyanaraman, B. Mitochondria-Targeted Triphenylphosphonium-Based Compounds: Syntheses, Mechanisms of Action,

and Therapeutic and Diagnostic Applications. *Chem. Rev.* **2017**, *117* (15), 10043–10120.

(229) Burns, R. J.; Smith, R. A. J.; Murphy, M. P. Synthesis and Characterization of Thiobutyltriphenylphosphonium Bromide, a Novel Thiol Reagent Targeted to the Mitochondrial Matrix. *Arch. Biochem. Biophys.* **1995**, *322* (1), 60–68.

(230) Murphy, M. P. Selective Targeting of Bioactive Compounds to Mitochondria. *Trends Biotechnol.* **1997**, *15* (8), 326–330.

(231) Smith, R. A. J.; Porteous, C. M.; Coulter, C. V.; Murphy, M. P. Selective Targeting of an Antioxidant to Mitochondria. *Eur. J. Biochem.* **1999**, *263* (3), 709–716.

(232) Han, M.; Vakili, M. R.; Soleymani Abyaneh, H.; Molavi, O.; Lai, R.; Lavasanifar, A. Mitochondrial Delivery of Doxorubicin via Triphenylphosphine Modification for Overcoming Drug Resistance in MDA-MB-435/DOX Cells. *Mol. Pharm.* **2014**, *11* (8), 2640–2649.

(233) Kelso, G. F.; Porteous, C. M.; Coulter, C. V.; Hughes, G.; Porteous, W. K.; Ledgerwood, E. C.; Smith, R. A. J.; Murphy, M. P. Selective Targeting of a Redox-Active Ubiquinone to Mitochondria within Cells: Antioxidant and Antiapoptotic Properties. *J. Biol. Chem.* **2001**, *276* (7), 4588–4596.

(234) Pathak, R. K.; Marrache, S.; Harn, D. A.; Dhar, S. Mito-DCA: A Mitochondria Targeted Molecular Scaffold for Efficacious Delivery of Metabolic Modulator Dichloroacetate. *ACS Chem. Biol.* **2014**, *9* (5), 1178–1187.

(235) Boddapati, S. V.; D'Souza, G. G. M.; Erdogan, S.; Torchilin, V. P.; Weissig, V. Organelle-Targeted Nanocarriers: Specific Delivery of Liposomal Ceramide to Mitochondria Enhances Its Cytotoxicity in Vitro and in Vivo. *Nano Lett.* **2008**, *8* (8), 2559–2563.

(236) Biswas, S.; Dodwadkar, N. S.; Deshpande, P. P.; Torchilin, V. P. Liposomes Loaded with Paclitaxel and Modified with Novel Triphenylphosphonium-PEG-PE Conjugate Possess Low Toxicity, Target Mitochondria and Demonstrate Enhanced Antitumor Effects in Vitro and in Vivo. *J. Control. Release* **2012**, *159* (3), 393–402.

(237) Bielski, E. R.; Zhong, Q.; Brown, M.; Da Rocha, S. R. P. Effect of the Conjugation Density of Triphenylphosphonium Cation on the Mitochondrial

Targeting of Poly(amidoamine) Dendrimers. *Mol. Pharm.* **2015**, *12* (8), 3043–3053.

(238) *CRC Handbook of Chemistry and Physics*, 86th ed.; Lide, D. R., Ed.; CRC Press: FL, 2005.

(239) Hunter, R. J. *Zeta Potential in Colloid Science: Principles and Applications*, Revised.; Ottewill, R. H., Rowell, R. L., Eds.; Academic press, 2013.

(240) Belmokhtar, C. A.; Hillion, J.; Segal-Bendirdjian, E. Staurosporine Induces Apoptosis through Both Caspase-Dependent and Independent Mechanisms. *Oncogene* **2001**, *20*, 3354–3362.

(241) Jessel, R.; Haertel, S.; Socaciu, C.; Tykhonova, S.; Diehl, H. a. Kinetics of Apoptotic Markers in Exogeneously Induced Apoptosis of EL4 Cells. *J. Cell. Mol. Med.* **2002**, *6* (1), 82–92.

(242) Härtel, S.; Zorn-Kruppa, M.; Tykhonova, S.; Alajuuma, P.; Engelke, M.; Diehl, H. A. Staurosporine-Induced Apoptosis in Human Cornea Epithelial Cells in Vitro. *Cytom. Part A J. Int. Soc. Anal. Cytol.* **2003**, *55* (1), 15–23.

(243) Shutt, T. E.; McBride, H. M. Staying Cool in Difficult Times: Mitochondrial Dynamics, Quality Control and the Stress Response. *Biochim. Biophys. Acta - Mol. Cell Res.* **2013**, *1833* (2), 417–424.

(244) Frazier, A. E.; Kiu, C.; Stojanovski, D.; Hoogenraad, N. J.; Ryan, M. T. Mitochondrial Morphology and Distribution in Mammalian Cells. *Biol. Chem.* **2006**, *387* (12), 1551–1558.

(245) Kamogashira, T.; Hayashi, K.; Fujimoto, C.; Iwasaki, S.; Yamasoba, T. Functionally and Morphologically Damaged Mitochondria Observed in Auditory Cells under Senescence-Inducing Stress. *npj Aging Mech. Dis.* **2017**, *3* (1), 2.

(246) Mao, K.; Klionsky, D. J. Mitochondrial Fission Facilitates Mitophagy in Saccharomyces Cerevisiae. *Autophagy* **2013**, *9* (11), 1900–1901.

(247) Rambold, A. S.; Kostelecky, B.; Elia, N.; Lippincott-Schwartz, J. Tubular Network Formation Protects Mitochondria from Autophagosomal Degradation during Nutrient Starvation. *Proc. Natl. Acad. Sci.* **2011**, *108* (25), 10190–10195.

(248) Pathak, R. K.; Kolishetti, N.; Dhar, S. Targeted Nanoparticles in Mitochondrial Medicine. *Wiley Interdiscip Rev Nanomed Nanobiotechnol* **2015**, *7* (3), 315–329.

(249) Malone, J. H.; Oliver, B. Microarrays, Deep Sequencing and the True Measure of the Transcriptome. *BMC Biol.* **2011**, *9*, 1–9.

(250) Schena, M.; Shalon, D. Quantitative Monitoring of Gene Expression Patterns with a Complementary DNA Microarray. *Science (80-.).* **1995**, *270* (5235), 467–470.

(251) Ringnér, M.; Ringner, M. What Is Principal Component Analysis? *Nat Biotechnol* **2008**, *26* (3), 303–304.

(252) Mizutani, H.; Tada-Oikawa, S.; Hiraku, Y.; Kojima, M.; Kawanishi, S. Mechanism of Apoptosis Induced by Doxorubicin through the Generation of Hydrogen Peroxide. *Life Sci.* **2005**, *76*, 1439–1453.

(253) Burrow, S. M.; Phoenix, D. A.; Wainwright, M.; Tobin, M. J. Intracellular Localisation Studies of Doxorubicin and Victoria Blue BO in EMT6-S and EMT6-R Cells Using Confocal Microscopy. *Cytotechnology* **2002**, *39*, 15–25.

(254) Patel, S. S.; Belmont, B. J.; Sante, J. M.; Rexach, M. F. Natively Unfolded Nucleoporins Gate Protein Diffusion across the Nuclear Pore Complex. *Cell* **2007**, *129*, 83–96.

(255) Alber, F.; Dokudovskaya, S.; Veenhoff, L. M.; Zhang, W.; Kipper, J.; Devos, D.; Suprapto, A.; Karni-Schmidt, O.; Williams, R.; Chait, B. T.; et al. The Molecular Architecture of the Nuclear Pore Complex. *Nature* **2007**, *450*, 695–701.

8 APPENDICES

APPENDIX 1 STATISTICAL SIGNIFICANCE OF VIABILITY RESULTS AFTER CRYOPRESERVATION FROM CHAPTER 3 158

APPENDIX 2 ENDOCYTOSIS PATHWAY STUDIES RESULTS FROM CHAPTER 4 159

APPENDIX 3 MTS TOXICITY OF DCA, TPP, AND THE COMBINATION OF BOTH FROM CHAPTER 5 161

APPENDIX 1 STATISTICAL SIGNIFICANCE OF VIABILITY RESULTS AFTER CRYOPRESERVATION FROM CHAPTER 3

Table A.1.1 Comparison of the viability of HeLa cells treated with different conditions pre-freezing. Statistical significance, determined by one-way ANOVA (ns $P > 0.05$, * $P \leq 0.05$, ** $P \leq 0.01$, *** $P \leq 0.001$, **** $P \leq 0.0001$).

MOF vs. MOF	0 h	24 h	48 h
Media vs. Treh	ns	ns	ns
Media vs. MOF	ns	*	*
Media vs. Treh + MOF	ns	ns	ns
Media vs. (+)	****	****	****
Media vs. (-)	ns	*	*
Treh vs. Treh + MOF	ns	ns	ns
Treh vs. MOF	ns	ns	*
Treh vs. (+)	****	****	****
Treh vs. (-)	ns	ns	*
Treh + MOF vs. MOF	ns	ns	ns
Treh + MOF vs. (+)	****	****	****
Treh + MOF vs. (-)	ns	ns	*
MOF vs. (+)	****	****	****
MOF vs. (-)	ns	ns	ns
(+) vs, (-)	****	****	****

APPENDIX 2 ENDOCYTOSIS PATHWAY STUDIES RESULTS FROM CHAPTER 4

Table A2.1. Normalized internal fluorescence of HeLa cells incubated with UiO-66 and Zr-based family of MOFs along with different pharmacological inhibitors. The values were normalized to a control incubated with the corresponding MOF in the absence of any inhibitor at 37 °C.

MOF	4 °C	Sucrose	Chlorpromazine	Nystatin	Rottlerin
$_{50}$Zr-L1	13 ± 0.6	29 ± 1.9	86 ± 4.6	94 ± 6	83 ± 5
$_{75}$Zr-L1	14 ± 0.7	24 ± 3.8	43 ± 4.8	78 ± 5.8	75 ± 6.2
$_{92}$Zr-L1	15 ± 1.2	47 ± 3.4	44 ± 4.1	84 ± 9.2	78 ± 8.1
$_{260}$Zr-L1	13 ± 1.7	44 ± 1.9	27 ± 2.7	78 ± 3.1	75 ± 2.8
Zr-L2	13 ± 0.9	20 ± 1.3	22 ± 0.5	73 ± 3	56 ± 3.5
Zr-L3	16 ± 0.9	22 ± 3.9	19 ± 1.6	62 ± 4.7	49 ± 3.4
Zr-L4	12 ± 0.9	20 ± 1.2	39 ± 2.3	68 ± 1.2	50 ± 1.2
Zr-L5	26 ± 0.6	61 ± 8.1	90 ± 1.5	43 ± 1.5	68 ± 5
Zr-L6	16 ± 0.9	69 ± 6.3	90 ± 1.9	42 ± 1.6	66 ± 10
Zr-L1	44 ± 3.3	27 ± 1.1	37 ± 4.7	107 ± 7.1	79 ± 6.1
Zr-L1-FA	14 ± 1.2	36 ± 4.1	96 ± 3.1	62 ± 2.1	81 ± 4.6
Zr-L1-Hep	20 ± 1.3	41 ± 4.2	70 ± 1.5	60 ± 1.5	83 ± 3.0
Zr-L1-Lact	60 ± 6.5	50 ± 5.2	84 ± 11.4	106 ± 13	95 ± 10.2
Zr-L1-PNIPAM	22 ± 1.3	54 ± 0.9	105 ± 5.3	103 ± 3.5	80 ± 4.3
Zr-L1-PEG550	36 ± 1.8	37 ± 1.6	26 ± 1.9	106 ± 3.3	89 ± 3.4
Zr-L1-PEG2000	23 ±1.2	29 ± 2.4	27 ± 1.5	51 ± 1.7	44 ± 4.1

Table A2.2. Comparison of the normalised intracellular fluorescence of HeLa cells treated with each MOF and different pharmacological inhibitors. Statistical significance, determined by unpaired t test (ns $P > 0.05$, * $P \leq 0.05$, ** $P \leq 0.01$, *** $P \leq 0.001$, **** $P \leq 0.0001$).

MOF vs. MOF	Sucrose	Chlorpromazine	Nystatin	Rottlerin
	Clathrin	Clathrin	Caveolae	Macropinocytosis
$_{50}$Zr-L1 vs. $_{75}$Zr-L1	ns	**	ns	ns
$_{50}$Zr-L1 vs. $_{92}$Zr-L1	**	**	ns	ns
$_{50}$Zr-L1 vs. $_{260}$Zr-L1	**	***	ns	ns
$_{75}$Zr-L1 vs. $_{92}$Zr-L1	*	ns	ns	ns
$_{75}$Zr-L1 vs. $_{260}$Zr-L1	**	*	ns	ns
$_{92}$Zr-L1 vs. $_{260}$Zr-L1	ns	*	ns	ns

Table A2.3. Comparison of the normalised intracellular fluorescence of HeLa cells treated with each MOF and different pharmacological inhibitors. Statistical significance, determined by unpaired t test (ns $P > 0.05$, * $P \leq 0.05$, ** $P \leq 0.01$, *** $P \leq 0.001$, **** $P \leq 0.0001$). Rottlerin (macropinocytosis) has not been included because all the results show no significance.

MOF vs. MOF	Sucrose	Chlorpromazine	Nystatin
	Clathrin	Clathrin	Caveolae
Zr-L2 vs. Zr-L3	ns	ns	ns
Zr-L2 vs. Zr-L4	ns	**	ns
Zr-L3 vs. Zr-L4	ns	**	ns
Zr-L2 vs. Zr-L5	**	****	***
Zr-L2 vs. Zr-L6	***	****	****
Zr-L3 vs. Zr-L5	**	****	**
Zr-L3 vs. Zr-L6	***	****	**
Zr-L4 vs. Zr-L5	**	****	***
Zr-L4 vs. Zr-L6	***	****	***
Zr-L5 vs. Zr-L6	ns	ns	ns

APPENDIX 3 MTS TOXICITY OF DCA, TPP, AND THE COMBINATION OF BOTH FROM CHAPTER 5

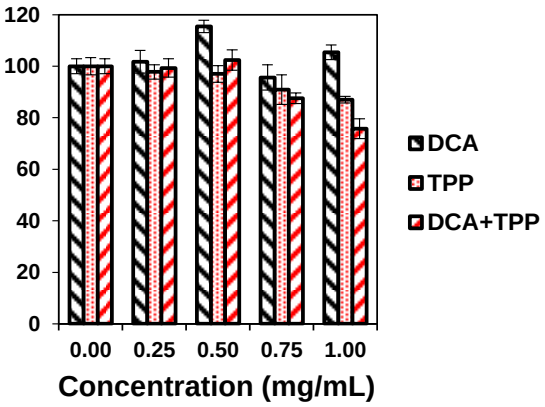

Figure A.3.1. Viability of MCF7 cells as determined by the MTS assay after incubation with DCA, TPP, and a combination of both for 72 h.